



# Bioinspired photonic cellulose films

Axel Fouques

## ► To cite this version:

Axel Fouques. Bioinspired photonic cellulose films. Polymers. Université Grenoble Alpes [2020-..], 2020. English. NNT : 2020GRALV044 . tel-03484314

**HAL Id: tel-03484314**

**<https://theses.hal.science/tel-03484314>**

Submitted on 17 Dec 2021

**HAL** is a multi-disciplinary open access archive for the deposit and dissemination of scientific research documents, whether they are published or not. The documents may come from teaching and research institutions in France or abroad, or from public or private research centers.

L'archive ouverte pluridisciplinaire **HAL**, est destinée au dépôt et à la diffusion de documents scientifiques de niveau recherche, publiés ou non, émanant des établissements d'enseignement et de recherche français ou étrangers, des laboratoires publics ou privés.

## THÈSE

Pour obtenir le grade de

**DOCTEUR DE L'UNIVERSITÉ GRENOBLE ALPES**

Spécialité : **Science des Polymères**

Arrêté ministériel : 25 mai 2016

Présentée par

**Axel FOUQUES**

Thèse dirigée par **Laurent HEUX**, Directeur de Recherche au **CNRS** et co-encadrée par **Silvia VIGNOLINI**, Professeur à l'**Université de Cambridge**.

préparée au sein du **Centre de la Recherche sur les Macromolécules Végétales (CERMAV)**  
dans l'**École Doctorale Chimie et Sciences du Vivant**

## Films de cellulose bio-inspirés à propriétés photoniques

Thèse soutenue publiquement le **16 Décembre 2020** devant le jury composé de :

**Madame Maria Helena GODINHO**

Professeur assistant à l'Universidade Nova de Lisboa, Rapportrice

**Monsieur Michel MITOV**

Directeur de Recherche au CNRS, Rapporteur

**Monsieur Frédéric PIGNON**

Directeur de Recherche au CNRS, Examineur et Président du jury

**Monsieur Aurélien GOURRIER**

Chargé de recherche au CNRS, Examineur

**Madame Teresa LOPEZ-LEON**

Chargée de recherche au CNRS, Examinatrice

**Monsieur Wim THIELEMANS**

Professeur à KU Leuven, Examineur

**Monsieur Laurent HEUX**

Directeur de Recherche au CNRS, Directeur de thèse

**Madame Silvia VIGNOLINI**

Professeur à Cambridge University, Co-encadrante de thèse, invitée

**Monsieur Bruno FRKA-PETESIC**

Assistant de recherche à Cambridge University, invité





**À Geneviève et Laurent.**

*« La douleur infinie de celui qui reste,  
Comme un pâle reflet de l'infini voyage  
Qui attend celui qui part. »  
P. Bottero*



## Table of contents

List of abbreviations (in alphabetical order).....	10
Acknowledgements .....	12
Introduction .....	15
Chapter 1. State of the art .....	19
1.1. Order parameters .....	20
1.2. A brief introduction to colloidal systems .....	22
1.2.1. Brownian motion .....	22
1.2.2. Attractive forces - Van der Waals interactions .....	22
1.2.3. Repulsive forces – Electrostatic and steric repulsion .....	24
1.2.4. Depletion forces .....	27
1.2.5. Colloidal stability versus flocculation .....	28
1.2.6. Kinetic arrest and gelation of colloidal systems .....	29
1.3. A brief introduction to liquid crystals .....	30
1.3.1. Lyotropic and thermotropic liquid crystals .....	30
1.3.2. Different liquid crystalline phases .....	33
1.3.3. The cholesteric liquid crystalline phase .....	34
1.3.3.1. Onsager’s description of the phase transition in hard rods suspensions	34
1.3.3.2. The SLO model: a refinement of Onsager’s calculation for charged rods suspensions .....	36
1.4. Optical properties of the cholesteric phase .....	38
1.4.1. Diffraction gratings .....	38
1.4.2. Bragg reflection in a multilayer assembly .....	39
1.4.3. Theoretical description of the optics of cholesteric phases .....	41
1.5. Cellulose.....	43
1.5.1. Cellulose in nature .....	43
1.5.2. Chemical structure .....	43

1.5.3.	Supramolecular assemblies of cellulose .....	44
1.5.4.	Crystallinity and allomorphs .....	45
1.6.	Cellulose nanocrystals .....	46
1.6.1.	From fibrous materials to colloids .....	46
1.6.2.	Parameters influencing the shape and size of CNCs .....	48
1.6.3.	Polydispersity of CNCs and its statistical description .....	50
1.6.4.	Colloidal stability of CNCs – influence of the type of acid.....	50
1.6.5.	Order of magnitude of colloidal interactions in CNC suspensions.....	51
1.6.6.	Self-assembling properties of CNCs in water.....	52
1.6.6.1.	Characterising the presence of the cholesteric phase .....	53
1.6.6.2.	Parameters influencing the phase diagram of CNCs .....	55
1.6.6.3.	Phase-separation mechanism: Nucleation/growth versus spinodal decomposition .....	58
1.7.	Materials.....	59
1.7.1.	Photonic materials made of cholesteric CNCs.....	60
1.7.1.1.	Controlled dryings .....	60
1.7.1.2.	CNCs as template materials.....	65
1.7.1.3.	Elastomer composites .....	66
1.7.2.	Chiral plasmonic materials .....	67
1.7.3.	Mechanical reinforcement in composites .....	68
Chapter 2.	Materials and methods .....	69
2.1.	Preparation of the CNC suspensions.....	70
2.1.1.	Aqueous CNC suspensions .....	70
2.1.2.	Dispersions in organic apolar solvents .....	71
2.1.3.	Phase diagrams.....	72
2.2.	Field experiments .....	72
2.2.1.	Magnetic field setups .....	72
2.2.2.	Electric field setups.....	75
2.2.3.	Order parameters determination .....	77

2.3.	Polymerisation experiments .....	78
2.3.1.	Experimental setups .....	78
2.3.2.	Sample preparation .....	79
2.3.3.	Inhibitor removal experiments .....	80
2.3.4.	Surface treatment of borosilicate capillaries .....	80
2.4.	Drying experiments .....	81
2.5.	Characterisation techniques.....	82
2.5.1.	<sup>1</sup> H Nuclear magnetic resonance (NMR) .....	82
2.5.2.	Mass spectroscopy .....	82
2.5.3.	Dynamic light scattering (DLS).....	82
2.5.4.	Differential scanning calorimetry (DSC).....	83
2.5.5.	Transmission electron microscopy (TEM) .....	83
2.5.6.	Scanning electron microscopy (SEM) .....	83
2.5.7.	Optical characterisation .....	85
2.5.7.1.	Laser diffraction.....	86
2.5.7.2.	White light diffraction .....	88
2.5.7.3.	Angular-resolved spectroscopy – Goniometry .....	91
2.5.7.4.	Optical microscopy .....	95
Appendix to Chapter two: optimisation of the polymerisation of the neat PS and PMMA matrices .....		96
2.6.	Free-radical polymerisation.....	96
2.7.	Previous works .....	98
2.8.	Fixing the chemical composition of the neat polymer matrices.....	99
2.8.1.	Choice of the initiator .....	99
2.8.2.	Influence of the initiator concentration.....	100
2.8.3.	Influence of the cross-linking .....	102
2.8.4.	Influence of polymerisation inhibitors.....	103
2.8.5.	Thermal analysis .....	105

2.9.	Optical properties of the neat matrices.....	110
2.9.1.	Transparency in “bulk” and glass capillaries.....	110
2.9.2.	Bulk pre-polymerisation .....	112
2.9.3.	Recovering transparency in “capillaries” .....	113
2.10.	Conclusions .....	114
Chapter 3.	Steric stabilisation of CNCs in organic apolar solvents.....	117
3.1.	State of the art .....	118
3.1.1.	Why is it interesting to try to disperse cellulosic materials in organic solvents? .....	118
3.1.2.	On the colloidal stability of CNCs in organic solvents.....	119
3.1.3.	Approaches for the compatibilisation of cellulosic materials in organic apolar solvents and materials .....	120
3.1.4.	Surfactant-stabilised CNCs self-assembly .....	122
3.1.5.	Proportion of CNCs and surfactant in suspension .....	123
3.1.6.	Previous works in CERMAV on the dispersion and self-assembly in monomers .....	124
3.2.	Results .....	125
3.2.1.	Finding a new surfactant for the process .....	125
3.2.1.1.	Mass spectroscopy characterisation of the surfactants .....	125
3.2.1.2.	On the experimental process.....	127
3.2.1.3.	Dispersions in organic apolar solvents .....	128
3.2.1.4.	Self-assembling properties of CNCs stabilised by Surfaline.....	130
3.2.2.	On the viscosity increase of CNC suspensions in organic apolar solvents over time .....	132
3.2.2.1.	Experimental observations.....	132
3.2.2.2.	Possible origins of the viscosity increase over time .....	133
3.2.2.3.	Theoretical modelling of colloidal interactions in suspension .....	135
3.2.3.	Conclusions.....	137
Chapter 4.	Alignment of CNC suspensions in external fields.....	139
4.1.	State of the art: Sensitivity of cellulose nanocrystals to external fields.....	140

4.1.1.	Interaction of single objects with an external field .....	140
4.1.1.1.	Permanent moment of an object .....	140
4.1.1.2.	Induced moment of an object .....	140
4.1.1.3.	Dielectric and diamagnetic anisotropy .....	141
4.1.2.	Experimental alignments of individual cellulose fibres and nanocrystals	141
4.1.2.1.	Electric fields .....	141
4.1.2.2.	Magnetic fields .....	142
4.1.3.	Assessment of the permanent and induced dipoles of CNCs under electric and magnetic fields.....	142
4.1.4.	Experimental alignment of cholesteric phases of CNCs under external fields	144
4.1.4.1.	Electric fields .....	144
4.1.4.2.	Strong magnetic fields .....	146
4.1.4.3.	Weak magnetic fields .....	148
4.1.4.4.	CNC-based materials aligned under magnetic fields.....	149
4.1.4.5.	Most recent works.....	151
4.2.	Results .....	152
4.2.1.	Alignment of CNC suspensions under magnetic fields .....	153
4.2.1.1.	Influence of field intensity on cholesteric textures and alignment .....	153
4.2.1.2.	Nucleation of cholesteric domains in a magnetic field.....	159
4.2.2.	Alignment of CNC suspensions under electric fields .....	163
4.2.2.1.	Alignment with different field geometries .....	163
4.2.2.2.	Quality of the electric field alignment .....	167
4.2.2.3.	Description of the critical transition values .....	168
4.2.2.4.	Electric field cut-off and dynamic colour switching .....	170
4.2.2.5.	Reversibility of the electric field alignment .....	170
4.2.3.	Geometric arguments to explain the behaviour of cholesteric CNCs under electric and magnetic fields.....	172
4.2.4.	Alignment under combined magnetic and electric fields .....	175
4.2.5.	Centimetre scale thickness experiments .....	177
4.3.	Conclusions .....	179
4.3.1.	Alignment experiments under magnetic fields .....	179

4.3.2.	Alignment experiments under electric fields .....	180
4.3.3.	Combining electric and magnetic fields .....	180
4.3.4.	Summary .....	180
Chapter 5.	Iridescent polymer composites .....	183
5.1.	Choice of the polymer matrix.....	184
5.2.	Polymerisation of CNC-polymer composites .....	187
5.2.1.	Isotropic CNC-polymer composites .....	187
5.2.2.	Anisotropic CNC-PS composites.....	188
5.2.3.	Syneresis in CNC-PS composites .....	192
5.2.4.	Anisotropic CNC-PMMA composites .....	194
5.3.	Field-aligned CNC-polymer composites.....	195
5.3.1.	Influence of field alignment on the optical response in PS composites ...	195
5.3.2.	Orientation of cholesteric helices in field-aligned PS composites.....	197
5.3.3.	Distortion of CNC helices under electric field alignment .....	203
5.3.4.	Anchored skin layer in field-aligned composites.....	206
5.3.5.	Influence of the magnetic field alignment on the optical response of PMMA composites	207
5.4.	Characterisation of the optical response of iridescent CNC-polymer composites	208
5.4.1.	Optical response of the composites.....	208
5.4.2.	Pitch measurements in the composites .....	210
5.4.3.	Selectivity in polarisation .....	212
5.4.4.	Quantitative assessment of helices orientation inside the composites.....	213
5.4.5.	Order parameters determination .....	215
5.5.	Conclusions .....	217
5.6.	Perspectives on the mechanical reinforcement properties of the composites ..	219
Chapter 6.	Dryings of CNC suspensions in organic solvents.....	221
6.1.	State of the art: Dryings of CNC suspensions.....	222

6.1.1.	A timeline of the drying process .....	222
6.1.2.	Drying droplets and coffee-ring effect.....	223
6.1.3.	Optimising the suspension state before kinetic arrest.....	225
6.1.4.	A toolbox to reorient cholesteric domains .....	226
6.2.	Results .....	228
6.2.1.	Iterations on the experimental setup .....	228
6.2.1.1.	Slowing down the evaporation with an intermediate layer .....	228
6.2.1.2.	On the saturation of the intermediate layer.....	229
6.2.2.	Evolution of the droplets upon drying .....	230
6.2.2.1.	Concentration of the starting suspension.....	231
6.2.2.2.	Cholesteric domains reorientation inside the droplets.....	232
6.2.2.3.	Final drying step and coffee-ring effects .....	235
6.2.2.4.	Iridescence in reflection.....	237
6.2.2.5.	Polymerisation of the sample before complete drying .....	239
6.2.2.6.	Characterisation of the reflected iridescence .....	241
6.2.3.	Conclusions.....	244
	General conclusion .....	247
	References .....	250

## List of abbreviations (in alphabetical order)

1D, 2D, 3D: 1, 2, 3 dimensions.

AC: alternative current

AFM: atomic force microscopy

AIBN: azobisisobutyronitrile

ATRP: atom transfer radical polymerisation

BNA: Beycostat NA® (surfactant)

ca.: circa

CCD camera: charged coupled device camera

Ch-NCs: chitin nanocrystals

cmc: critical micellar concentration

CNC, CNCs: Cellulose nanocrystals

DLS: dynamic light scattering

DLVO theory: theory jointly proposed by Derjaguin, Landau, Verwey and Overbeek

DMA: dynamic mechanical analysis

DMAPS: dimethylmyristylammonio propane sulphonate

DMF: dimethylformamide

DMSO: dimethylsulphoxide

DP: degree of polymerisation

DSC: differential scanning calorimetry

DVB: divinylbenzene

e.g.: example given

EO (PEO): (poly) ethylene oxide

ESI: electrospray ionisation

ESI-RP: electrospray ionisation reflectron positive

etc: et caetera

FEP: fluoroethylenepropylene polymer

FWHM: full width at half maximum

GBF: “générateur basse fréquence”, Low Frequency Generator

GPC: gel permeation chromatography

HEMA (PHEMA): (poly) hydroxyethyl methacrylate

i.e.: id est

IR: infrared



ITO: indium tin oxide  
 $k_B T$ : thermal energy  
LCP: left circular polarisation  
LED: light emitting diode  
LODP: level-off degree of polymerisation  
MMA: methylmethacrylate  
NMF: N-methylformamide  
NMR: nuclear magnetic resonance  
Obj.: Objective (microscopy)  
PA-6: polyamide 6  
PAAm: polyacrylamide  
PDMS: polydimethylsiloxane  
PEG: polyethyleneglycol  
PEGDMA: polyethyleneglycoldimethylacrylate  
PMMA: polymethylmethacrylate  
POM: polarised optical microscopy  
PS: polystyrene  
PTFE: polytetrafluoroethylene  
PVA: polyvinyl alcohol  
SLO model: model developed by Stroobants, Lekkerkerker and Odjik  
RCP: right circular polarisation  
RGB: red green blue colour code  
TEM: transmission electron microscopy  
TEMPO: (2,2,6,6-Tetramethylpiperidin-1-yl)oxyl  
T-matrix: transfer matrix  
TMPTA: trimethylolpropanetriacrylate  
TMV: tobacco mosaic virus  
SANS: Small angle neutron scattering  
SAXS: small angle X-ray scattering  
(FE-)SEM: (field-enhanced) scanning electron microscopy  
UV: ultraviolet

## Acknowledgements

Conducting this work to its end would not have been possible without the dedication of a number of people and organisations, that I would like to thank hereafter.

My acknowledgements go to the IDEX-Glyco@lps and the ERC SeSaMe for the financial support of my PhD work and the Glyco@lps travel grant that covered part of my travel to ACS Orlando (USA). Many thanks to Carl Bouret from Arkema who kindly supplied the surfactants used in this study. I am grateful to the ICMG characterisation platform for providing access to their facilities.

I would like to warmly thank my two supervisors, Dr. Laurent Heux and Prof. Silvia Vignolini. The past three years have been incredibly rich in both scientific and human insights that they cared sharing me among their other students. I have greatly benefited from their large scientific network, allowing me to meet diverse national and international scientific communities on the topics of cellulose, liquid crystals, photonics *etc.* Not every student is offered the opportunity to travel in multiple places including foreign countries to present his work, and I would like to especially acknowledge their dedication on that topic. I cannot conclude this part without acknowledging Dr. Bruno Frka-Petešić, who could be considered as my third unofficial supervisor during this PhD work. I kept benefiting from the wealth of his scientific knowledge throughout this work, which still astonishes me by its depth. Without a doubt, his vision has influenced this work in multiple aspects. To finish with, I would like to thank these three people for helping me grow as a human being throughout this difficult exercise that tells much about who someone really is.

I would like to acknowledge the people I have been working with on a daily basis in CERMAV and the Melville Laboratory. I would like to warmly thank Jean-Luc Putaux and Christine Lancelon-Pin who performed respectively the TEM and SEM observations of this work, along with the microtome and cryo-cuts. Special thanks to Pierre, Stéphanie, Bruno J., Patrick, Laurent C. and Isabelle who all intervened here and there in the project, bringing their much needed skills. Many thanks to Yotam, Julien and Maëva, the office dream team who were simply wonderful people on top of wise scientific advisors. I would like to acknowledge the work and enthusiasm of the two master interns I had the chance to supervise jointly with Laurent Heux, namely Robin and Sylvain, who had their own projects on scientific topics related to the PhD project (not in the manuscript). I wish to thank the students and postdocs from CERMAV: Claire, Quentin, Lauric, Simon, Robin, Marlène, Tamiris, Raphaël, Clémentine, Wei, Fangbo,

Marie-Alix, Maud and Nora. I think all of them participated in holding a particular working culture in CERMAV and SPG that I appreciated very much. I also wish to thank the PhD students from the Glyco@lps network and from the Research, Company, Innovation label for the shared moments. In the Melville, I would like to thank the people from the Bio-inspired Photonics group for sharing their passion for science throughout the year I spent in Cambridge. Special thanks to the ABCGMTs, who made my stay in Cambridge a memorable experience. I am grateful to Daniel Whitaker for his help on elastomer composites and Clement Chan for his help with setting up spectroscopic microscopy in reflection. I wish all the best to Valerio and Aimee, Andrew and Laurent G., unexpected but much appreciated meets in this journey.

This work would certainly not have been the same without the personal support of my friends and relatives, that I wish to thank hereafter. I will never be able to thank enough S. E. for believing in us two throughout these three years. It has been a long and lonely journey for her as much as it has been for me. Although this choice has not been hers, she coped with the hardships with a stoicism and trust that forces respect. To the lighthouse of my life, with all my love. I wish to thank my family and in-laws for their continuous support in regard to my personal and professional choices. I acknowledge my supportive friends who had me disappear from the Paris area for three long years and kept in touch one way or another.

Finally, I would like to thank the jury members to take the time to assess the quality of my work: Dr. Michel Mitov from CEMES (Toulouse, France) and Dr. Maria Helena Godinho from CENIMAT-I3M (Lisboa, Portugal) as referees and Prof. Wim Thielemans from KU Leuven (Leuven, Belgium), Dr. Theresa Lopez-Leon from Gulliver, ESPCI (Paris, France), Dr. Aurélien Gourrier from LiPhy (Grenoble, France) and Dr. Frédéric Pignon from LRP (Grenoble, France) as examiners.



# **Introduction**

Observing the phenomena in the world surrounding him has long been a powerful driving force for the scientist in the process of innovating. Both knowing that one's research objective is *possible* and that nature has kept optimising it in its own way for million years to yield the result one observes today is inspiring. Would humans have imagined that airplanes could fly if there were not any birds? The approach developed in this work, that could be referred to as bioinspired, participates of a similar trend. It finds its inspiration in the observation of coloured natural structures.

Colour arises in nature both from light absorption by pigments and light interference on ordered structures. These two mechanisms are often present together in the same system. Pigment colouration is the result of the wavelength-selective absorption of light inducing a structural rearrangement in the pigment molecule towards a more stable molecular structure. The final colour displayed corresponds to the wavelengths that have not been absorbed by the material.

Structural colouration arises from a mechanism by which light interferes on a structured material, whose structuration is on a length scale corresponding to optical wavelengths (Kinoshita, Yoshioka, and Miyazaki 2008). Light interference may arise from a variety of structures: diffraction gratings (Vignolini et al. 2015), controlled disorder (Moyroud et al. 2017), photonic crystals and multi-layer structures (Van Blaaderen 1998; Teyssier et al. 2015). Structural colouration is generally angular-dependent and wavelength-selective, conversely to pigment colouration that generally scatter the unabsorbed light in all directions. Among natural structures producing structural colour, we have interested in the helical arrangements that are found in plants (Steiner et al. 2019), fruits (Vignolini et al. 2012) and animals (Neville and Caveney 1969; Natarajan and Gilman 2018; Mitov 2017). They are typically made of cellulose in plants and fruits (Vignolini et al. 2012; Steiner et al. 2019) and of chitin or collagen in animals (Albéric et al. 2018; Nguyen and MacLachlan 2019) often coupled with inorganic minerals. These assemblies show outstanding optical properties (Vignolini et al. 2012; Seago et al. 2009) but also mechanical properties (Weaver et al. 2012; Albéric et al. 2018) that fulfil precise biological functions. These functions span from optical signalling for seed dispersers in fruits (Vignolini et al. 2012) and camouflage in beetles (Seago et al. 2009; Onelli et al. 2017) to mechanical robustness in the plant cell wall and fracture resistance in crustacean shells (Weaver et al. 2012; Nguyen and MacLachlan 2019).

While it is near-impossible to reproduce nature's complexity in man-made materials, it is possible to isolate a limited number of building blocks that retain the main features of natural structures in artificial mimics (Scarangella, Soldan, and Mitov 2020). Discussing plant mimics in more detail, reproducing natural helical structures of cellulose in artificial materials has shown promising results (Almeida et al. 2018). In particular, colloidal rod-like particles obtained from the hydrolysis of the cellulose fibre in strong acids referred to as cellulose nanocrystals (CNCs) are a suitable building block towards this objective (Revol et al. 1992). Their rod-like shape and intrinsic chirality lead to their self-assembly into left-handed helices in suspension. A characteristic distance equal to half the pitch of the helix is repeated throughout the supra-colloidal assembly, yielding spectacular iridescent colour effects whenever this distance is on the order of the wavelength of visible light. In aqueous suspensions, the helical pitch is typically bigger than the visible (Dong and Gray 1997), that is why cholesteric CNC suspensions require controlled drying to produce colourful films. An important research effort has been dedicated to unveil the mechanisms at play during the drying (Gray 2016), highlighting the importance of cholesteric domains orientation control (Frka-Petesic et al. 2019) and yielding at best films reflecting near 100% of the left circular polarisation of light at a chosen wavelength (Zhao et al. 2019). However, these dried photonic films are typically near-100% CNCs and therefore suffer from the brittleness of stiff rods packing, limiting their potential applications.

In this work, an alternative strategy is developed by taking advantage of literature results on the compatibilisation of CNCs in organic apolar solvents using surfactants (Heux, Chauve, and Bonini 2000; Elazzouzi-Hafraoui, Putaux, and Heux 2009) and the associated reduced pitch value, corresponding to an iridescent optical response at high angles of incidence in suspension. This strategy consists of replacing the solvent of these suspensions by monomer mixtures, allowing to make composite materials with cholesteric CNC fillers architectures. Literature showed promising results on the dynamic tuning of the optical properties of CNC cholesteric phases under electric fields (Frka-Petesic, Radavidson, et al. 2017), complementary to the alignment of aqueous CNC suspensions under magnetic fields (Kimura et al. 2005). In that scope, the approach developed in this work is also meant to allow for the alignment of cholesteric suspensions under external fields to take place prior to polymerisation in order to optimise the distribution of cholesteric fillers. The aim is to make iridescent CNC-polymer composites that compare to other literature works and overcome some of the intrinsic limitations of photonic CNC films dried from aqueous suspensions.

To that extent, this manuscript articulates in six chapters. In chapter 1, we present the main characteristics of CNCs along with some background knowledge on several topics of colloidal science, liquid crystals, cellulose and cellulosic materials relevant to the discussions of this work. The second chapter describes how the results of this work have been obtained. The third chapter presents the results on the steric stabilisation of CNCs in organic apolar solvents and monomers. Chapter 4 presents a detailed study on the behaviour of cholesteric CNC suspensions in organic apolar solvents under electric and magnetic fields. It goes beyond literature results, reporting several new features of the electric field alignment and studying in detail the magnetic field alignment of cholesteric CNC suspensions in organic apolar solvents. Chapter 5 presents a strategy to make polymer-CNC composites with retained organisation of the cholesteric fillers. Taking advantage of the results of chapter 4, field-aligned polymer-CNC composites are made, whose optical properties are studied in detail using angular-resolved optical spectroscopy. A different approach is presented in chapter 6, consisting of the drying of CNC suspensions in organic apolar solvents inspired from the literature on aqueous systems. This approach yields iridescent optical responses in reflection in the final films. In conclusion, the perspective is broadened to consider other materials that can be made following this new approach.



# Chapter 1. State of the art

*« After sleeping through a hundred million centuries  
We have finally opened our eyes on a sumptuous planet,  
sparkling with colour, bountiful with life. »  
Nightwish, The greatest show on Earth*

In this first chapter, the general theoretical background of the study is introduced. A short overview of the concepts of order parameters, colloidal chemistry, liquid crystals, optics of cholesteric liquid crystals, cellulose and cellulose nanocrystals necessary to understand this study is presented. We finish with a literature review of materials made out of cellulosic materials. We have chosen to present the literature specific to each chapter in introduction of the corresponding chapters to relate more closely the results of this study. As such, a literature review on the methods to disperse CNCs in organic apolar solvents is presented in chapter 3. In chapter 4, we review the literature on the field alignment of CNCs. In chapter 5, we present a theoretical background of free-radical polymerisation. The chapter 6 finally presents a state of the art on the preparation of CNC films from aqueous suspensions by evaporation induced self-assembly.

## ***1.1. Order parameters***

An order parameter is a measure of the degree of order. It can be referring to positional or orientational order, or have a more abstract significance. In systems transitioning from one phase to another or breaking symmetry, they are commonly used to describe the state of a system. The average orientation of objects with respect to a given direction, without polar constraints (*i.e.* the polar angle  $\theta = 0$  or  $\theta = \pi$  being equivalent) is given by the quadrupolar order parameter  $S_2$ . It is defined as the ensemble average over all considered objects of the second order Legendre polynomial  $P_2(\cos\theta)$ , where  $\theta$  is measured with respect to the average direction of the objects (Mao et al. 2018; De France et al. 2016; Frka-Petesic 2010):

$$S_2 = \langle \frac{3\cos^2\theta - 1}{2} \rangle$$

$\theta$  here is the angle between the director of a given individual object and the average direction of the objects. The quadrupolar order parameter function takes values ranging from +1 to -1/2 when  $\theta$  varies from 0 to  $\pi/2$ . In a purely isotropic distribution of objects,  $\langle \cos^2\theta \rangle = 1/3$ , leading to  $S_2 = 0$ . In a perfectly aligned distribution of objects along the ideal direction of orientation, we have  $\theta = 0$  for all objects, leading to  $\langle \cos^2\theta \rangle = 1$  and  $S_2 = 1$ . In a perfectly anti-nematic distribution of objects with respect to the ideal orientation, we have  $\theta = \pi/2$  for all objects, leading to  $\langle \cos^2\theta \rangle = 0$  and  $S_2 = -1/2$ . Mao et al. in chapter 4 use the Hermans order parameter that is obtained from the integral in intensity of a scattering profile and generalised to correspond to the 3-dimensional order parameter  $P_2(\cos\theta)$ , and will be noted  $P_2$  in this work.

Throughout this work, we use the quadrupolar order parameter to describe two main physical objects:

- The individual alignment of the long axes of CNC rods composing nematic and chiral-nematic phases that have an intrinsic disorder, meaning they do not all perfectly align along the global director  $\mathbf{k}$  of the phase (Schütz et al. 2020). The misalignment can be accurately described by a quadrupolar order parameter  $S_{2,\text{loc}} \sim 0.8 - 0.9$ . In this case,  $\theta$  is defined as the angle between the direction of a given individual CNC rod and the director of the nematic or chiral-nematic phase. The physics of this system is described in more details in the section Different liquid crystalline phases.
- The helical axes of CNC helices have a tendency to align with respect to external electric and magnetic fields, which phenomenon is described extensively in chapter 4. The convention in the definition of the angle  $\theta$  that has been taken in all this work is the following: for electric and magnetic fields alignment,  $\theta$  is defined as the angle between the helical axis of a given helical stack and the direction of the magnetic field. For magnetic fields, CNC helices are expected to align their helical axes along the magnetic field, leading to  $S_2$  values close to +1. For electric field alignment, CNC helices are expected to align their helical axes anti-parallel to the electric field direction, leading to  $S_2$  values close to -0.5.

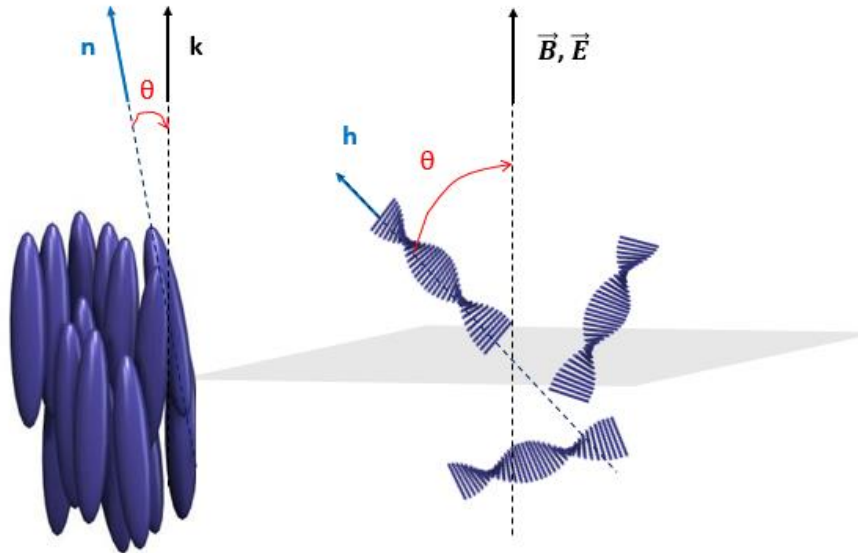


*Figure 1: Definition of the angle  $\theta$  defining the order parameter function  $S_2$  in different example systems of this work. (left) To describe the intrinsic disorder of nematic phases,  $\theta$  is taken as the angle between the director  $\mathbf{n}$  of each rod and the global direction of alignment of the phase  $\mathbf{k}$ . (right) To describe the*

*alignment of CNC helices under electric and magnetic fields,  $\theta$  is taken as the angle between the helical axis of each domain and the direction of the magnetic field.*

## **1.2. A brief introduction to colloidal systems**

A colloidal object is defined as an object big enough so that its interactions with the solvent are averaged, allowing to describe the object with equations such as the one of fluid motion and small enough so that its movement is significantly affected by Brownian motion (thermal agitation). This defines a lower limit at *ca.* 1 nm and an upper limit at *ca.* 10  $\mu\text{m}$  for these objects. They are regrouped into the “colloid” denomination because they are described by the same set of interaction forces, even if they may have as much as four orders of magnitude differences in size. Cellulose nanocrystals belong to this category, which explains why we describe the interactions involved in these systems. The following section provides only a brief introduction on colloidal systems, while the interested reader will find more on this topic in Israelachvili’s seminal book *Intermolecular and surface forces* (Findenegg 1986).

### **1.2.1. Brownian motion**

The molecules composing a solvent at rest are permanently agitated by a thermal energy  $E_{\text{Brownian}} = k_B T$ , where  $k_B$  is the Boltzmann constant and  $T$  is the temperature. A colloidal particle immersed in this solvent is therefore constantly hit by solvent molecules, exchanging part of their momenta to the colloidal particle, effectively thermalizing and communicating to it the same average kinetic energy, equal to  $E_{\text{Brownian}}$ . Brownian motion refers to the global movement of the colloidal particle resulting from the contribution of the collisions with all solvent molecules. A first important consequence of this phenomenon is that a colloidal particle will explore a broad range of configurations, taken in the sense of statistical thermodynamics, powered by Brownian motion. A second important consequence is on the determination of colloidal interactions that matter in the system: one shall compare them to  $k_B T$ . If  $E_{\text{interaction}} < k_B T$ , Brownian motion will dominate the effect of that interaction, which can therefore be neglected. If  $E_{\text{interaction}} \gg k_B T$ , Brownian motion will not be able to counteract the effect of the interaction, leading to a modification of the overall state of the suspension.

### **1.2.2. Attractive forces - Van der Waals interactions**

Let us first consider a gas of molecules. These molecules interact with each other through their possible dipolar moment, and certainly through their induced dipole due to local modifications of their close environment. Van der Waals forces describe the contributions of

the induced dipole-induced dipole, the permanent dipole-induced dipole and the permanent dipole-permanent dipole interactions – respectively the London, Debye and Keesom forces. A characteristic of dipole-dipole interactions is that these forces are often attractive and their potential energy decreases as a power sixth of the distance separating the dipoles. How does this dependence evolve from molecules to colloids?

It is possible to do a geometric calculation (Hiemenz 1972) to derive the potential energy of interaction in the case of two colloidal particles by integrating over all the interactions between the molecules they are made of. However, the geometric shape of the particles and their mutual orientation determines the value of the exact integral. The result gives us the power dependence of the square of the distance  $r$  in between two infinite surfaces, which is a good approximation of particle surfaces in the limit where  $r$ , the edge-to-edge interparticle distance, is much lower than the size of the particles.

$$\varphi_{\text{VdW}(\text{colloids})} = -\frac{A}{12 \pi r^2} \text{ (in J/m}^2\text{)}$$

where  $A$  is the Hamaker constant in J, specific to the particle and the solvent composition. For the case of two spheres of radius  $R$ , we can also derive the resulting van der Waals interaction energy as:

$$\varphi_{\text{VdW}(\text{spheres})} = -\frac{A R}{12 r} \text{ (in J)}$$

The Hamaker constant can be approximated using the Lifshitz theory as (Findenegg 1986) p.258:

$$A = \frac{3}{4} kT \left( \frac{\varepsilon_1 - \varepsilon_3}{\varepsilon_1 + \varepsilon_3} \right) \left( \frac{\varepsilon_2 - \varepsilon_3}{\varepsilon_2 + \varepsilon_3} \right) + \frac{3h}{4\pi} \int_{\nu_1}^{\infty} \left( \frac{\varepsilon_1(i\nu) - \varepsilon_3(i\nu)}{\varepsilon_1(i\nu) + \varepsilon_3(i\nu)} \right) \left( \frac{\varepsilon_2(i\nu) - \varepsilon_3(i\nu)}{\varepsilon_2(i\nu) + \varepsilon_3(i\nu)} \right) d\nu$$

$$\nu_1 = \frac{2\pi kT}{h}$$

Order of magnitudes estimate the Hamaker constant at  $10^{-20}$  J, comparable to Brownian motion. As such, Van der Waals interactions may have a significant effect on colloidal suspensions. Moreover, Van der Waals potentials are very short range interactions between atoms and molecules because of the power minus sixth dependence, but are longer range interactions between spherical colloidal particles due to the  $1/r$  dependence.

These forces are always present in colloidal suspensions because at least induced dipole-induced dipole interactions are present, do not depend on the nature of the particle involved and are always attractive in the case of colloids. They are often – and will be in this work – the only attractive forces involved in colloidal systems. Remembering that Brownian motion allows colloidal particles to explore all possible configurations continuously, one can forecast that two given particles will sooner or later be in range of interacting through Van der Waals forces. Without any repulsive forces to counteract the attraction, colloidal particles are going to aggregate in large clusters in a process referred to as flocculation. This process is considered irreversible, because the Van der Waals potential energy is ever increasing as the particles come closer one from another, increasing hyperbolically as particles get closer to one another.

### 1.2.3. Repulsive forces – Electrostatic and steric repulsion

A couple of repulsive forces are available to counteract the influence of Van der Waals forces and stabilise colloidal systems, namely electrostatic and steric repulsion.

Electrostatic repulsion arises when colloidal particles bear charges. These charges release their counter-ions upon solvation, therefore creating an electrostatic potential that attracts ions of opposite charge and yield an uneven distribution of positive and negative ions in the immediate vicinity of the particles. In aqueous solvents, the DLVO theory describes quantitatively the charge repartition and the shape of the electrostatic potential in the immediate vicinity of the particle (Findenegg 1986; Derjaguin and Kussakov 1939; Derjaguin and Landau 1941; Verwey, Overbeek, and Van Nes 1948). This model solves the Poisson-Boltzmann equation on the electrostatic potential and predicts an exponential decay of the concentration of counter-ions and electrostatic potential over the same characteristic length  $\kappa^{-1}$ , referred to as the Debye length:

$$\kappa^{-1} = \sqrt{\frac{\varepsilon_0 \cdot \varepsilon \cdot k_B \cdot T}{\sum_i \rho_{\infty,i} \cdot e^2 \cdot z_i^2}}$$

where  $\varepsilon_0$  and  $\varepsilon$  are the dielectric permittivities of respectively the void and the solvent,  $\rho_{\infty,i}$  is the concentration of ion  $i$  at infinite distance from the charged surface,  $e$  is the elemental charge and  $z_i$  is the valence of ion  $i$ . Interestingly, the repartition of the counter-ions in suspension only depends on the suspension properties, its solvent and ion content. This expression simplifies in the case of a solvent electrolyte composed of monovalent ions such as NaCl, KCl *etc.* contributing to a total ionic strength I:

$$\kappa^{-1} = \frac{0.304}{\sqrt{I}} \text{ nm}$$

This simplified expression corresponds to very practical uses, in which experimenter is able to tune the strength of the electrostatic repulsion by playing with the monovalent ion concentration. To give some order of magnitudes:

For a NaCl solution at  $10^{-4} \text{ M}$ ,  $\kappa^{-1} \sim 30 \text{ nm}$ .

For a NaCl solution at  $10^{-3} \text{ M}$ ,  $\kappa^{-1} \sim 10 \text{ nm}$ .

For a NaCl solution at  $10^{-1} \text{ M}$ ,  $\kappa^{-1} \sim 1 \text{ nm}$ .

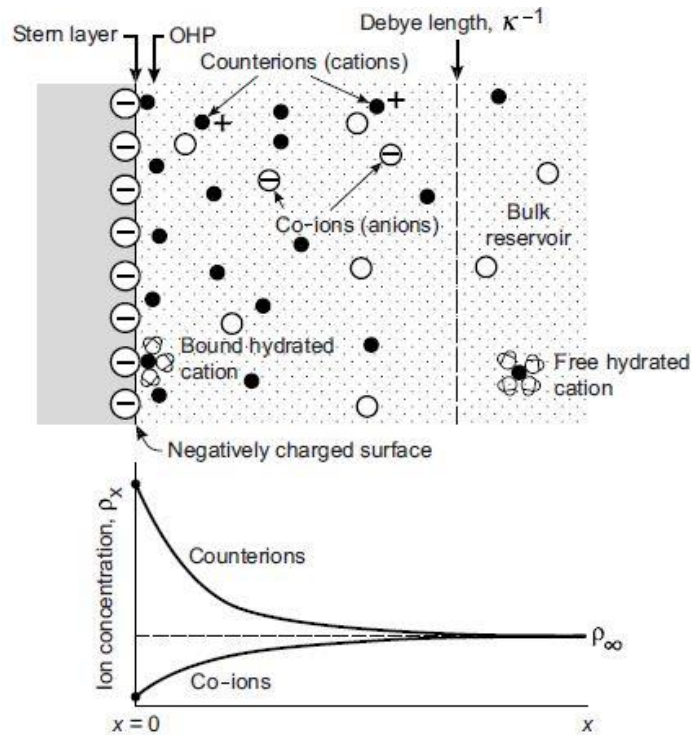


Figure 2: Schematic of the ion repartition in the immediate vicinity of the charged colloidal surface and plot of the ion concentration as a function of the distance to the charged surface. The first layer of counter-ions is tightly bound to the surface and referred to as the Stern layer, whereas the subsequent layers of ions are able to move and referred to as the diffuse electric double layer, of characteristic thickness  $\kappa^{-1}$ . Adapted from Israelachvili's book, "Intermolecular and Surface Forces", p.307.

Back to the concept of electrostatic repulsion, one has to keep in mind that the electrostatic potential decreases exponentially from the surface of the colloidal particle over a characteristic distance  $\kappa^{-1}$ . If we consider two particles with their electrostatic double layers trying to approach one another, these particles will encounter an ever increasing repulsion starting at a distance on the order of  $2 \cdot \kappa^{-1}$  as a result of the overlap of their electrostatic potential. A good way of viewing charged colloids dispersed in suspension is to consider that these colloids

occupy an effective volume made of their actual volume plus an additional volume corresponding in first approximation to their electric double-layer. This volume is excluded to other colloidal particles, therefore resulting in a higher effective volume fraction of particles.

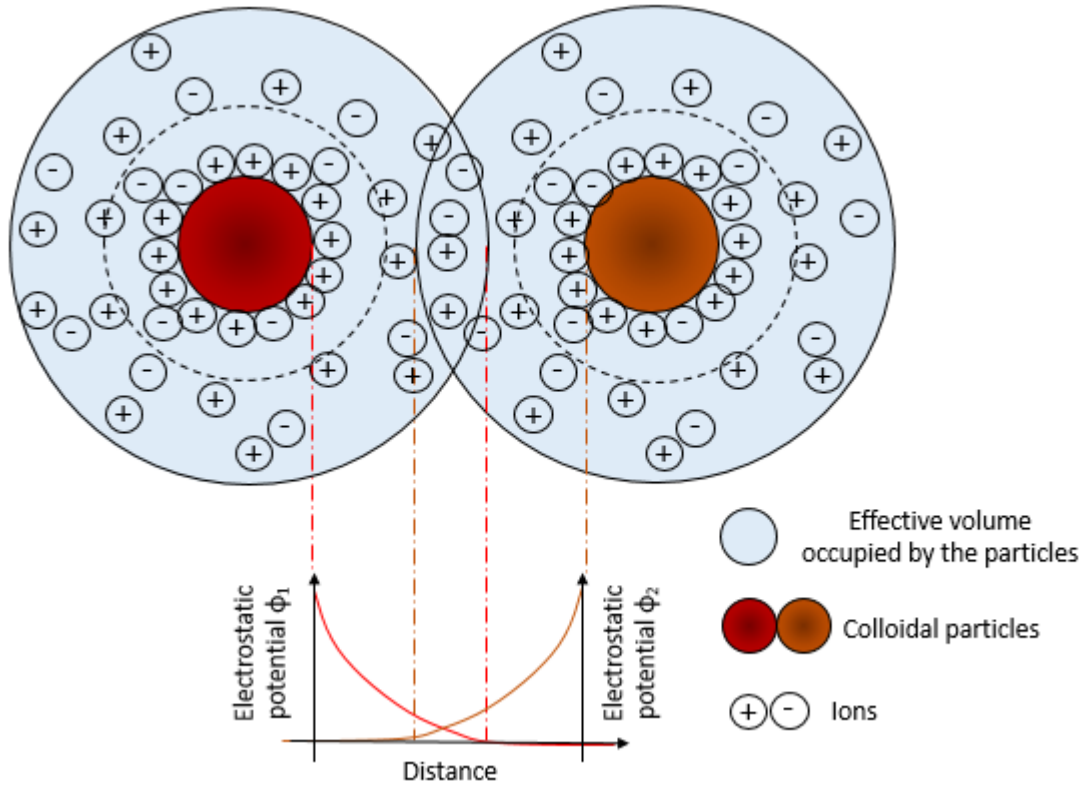


Figure 3: Schematic view of the electrostatic interaction between two charged colloidal particles. Whenever the diffuse electric layer of each particle interpenetrates, particles repel each other because of their non-zero electrostatic potential. This defines an effective larger volume occupied by charged colloidal particles labelled in light blue on the figure.

Steric interaction is the third main force observed in colloidal interactions and is in majority repulsive. This interaction is taken into account whenever the approach of two colloidal particles below a certain inter-particle distance is hindered by the presence of another material in-between the particles. The repulsive potential can take various forms depending on how soft and compressible this material is. When the inter-particle material is a solid, the repulsive potential will typically take the form of a hard-sphere repulsion. When the material is an adsorbed layer such as a surfactant bilayer, the repulsive potential is also quite sharp but does depend on the mechanical properties of the bilayer through its compressibility (Cowley et al. 1978). Whenever the material is grafted polymer chains, the energy cost of forcing polymer chains to adopt certain conformations can be quantitatively calculated from the entropic elasticity of the polymer chains. One can therefore construct a repulsive potential from the entropic energy loss of the polymer chains for any inter-particle distance. In the regime of weak



deformations, the response of compressed polymer chains is fully elastic, equivalent to a mass-spring system of stiffness  $k = \frac{3 \cdot k_B \cdot T}{n \cdot L^2}$ , where  $n$  is the degree of polymerisation of the chain and  $L$  the approximate length of a monomer unit (Morbidelli\_ETH\_Zürich\_course). In this reference paper, the steric potential is derived from the free energy of grafted polymer chains (Evans and Napper 1973).

There are at the end as many repulsive potentials as numbers of materials and supramolecular assemblies, and the general label “steric repulsion” hides this huge diversity. For this reason, quantitative calculations of steric potentials are often challenging to conduct.

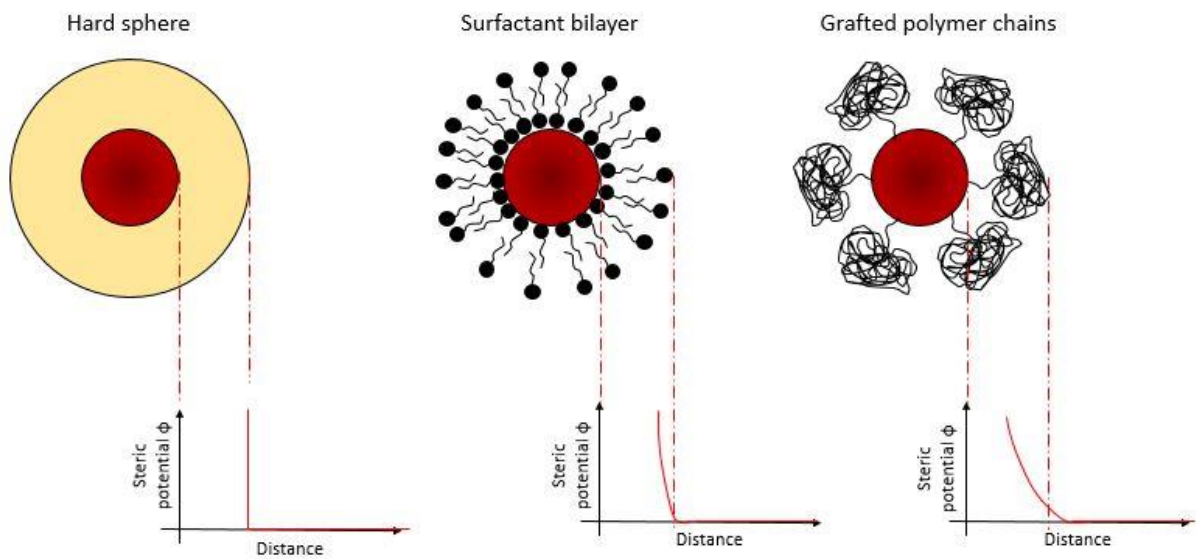


Figure 4: Schematic drawings of the steric repulsion potentials in the case of solid coatings (hard spheres), surfactant bilayer adsorption and grafted polymer chains in the mushroom regime.

#### 1.2.4. Depletion forces

Depletion interactions are forces of entropic origin that are often attractive but can also be repulsive depending on the situation (Asakura and Oosawa 1954). Whenever a polymer of radius of gyration  $R_g$  is added to a suspension of colloidal particles, a layer of thickness  $R_g$  is not accessible to polymer chains on the surface of the particles. When two colloidal particles come close one from another, they overlap this excluded volume. By sticking together, they will contribute in reducing the overall excluded volume to polymer chains as in Figure 5, therefore increasing the entropy of polymer chains. For this reason, the strength of this interaction scales with the concentration in depletants. While depletion forces are not directly involved in this work, we mention them here as they constitute the last important colloidal

interaction and can have a transient role during polymerisation processes of colloidal suspensions.

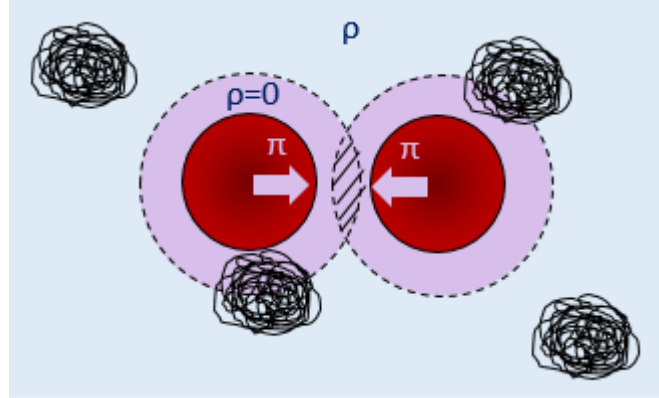


Figure 5: Schematic view of particles attraction through depletion interactions. Because of the presence of polymer chains (black) that cannot enter the excluded volume (purple) in between two colloidal particles (red), particles feel an osmotic pressure  $\pi$  (purple arrow) that tends to stick them together whenever their excluded volume overlap (dashed black area).

### 1.2.5. Colloidal stability versus flocculation

The stability of colloidal suspensions results from the balance of attractive and repulsive forces. A graphical representation of this balance consists in plotting the potential energies of each interaction and the resulting total interaction potential as a function of the interparticle distance as done in Figure 6. Whenever attractive Van der Waals forces dominate massively, particles stick to each other and form large colloidal clusters upon flocculation. This is typically the case when the total interaction potential only takes values in the  $]-\infty; -k_B T[$  region. Whenever repulsive forces dominate massively, particles are repelled from each other at any distance and the suspension is colloidally stable (corresponding total interaction potential not shown in Figure 6).

Whenever repulsive forces are on the same order of magnitude than attractive forces, the total potential energy curve has a deep primary minimum at short distances corresponding to the irreversible aggregation under the action of Van der Waals forces, and sometimes an additional shallow secondary minimum at distances on the order of  $2 \cdot r + 10 \cdot \kappa^{-1}$  separated by a positive peak of the interaction potential around  $2 \cdot r + 2 \cdot \kappa^{-1}$  due to the different scaling of Van der Waals and electrostatic forces. Given particles can fluctuate around their equilibrium position by an energy on the order of  $k_B T$ , how the height of the energy barrier compares with  $k_B T$  is what determines the colloidal stability of the system. Tuning electrostatic repulsion with

ionic strength therefore allows one to determine the threshold for colloidal stability, when the energy barrier is on the order of several  $k_B T$ .

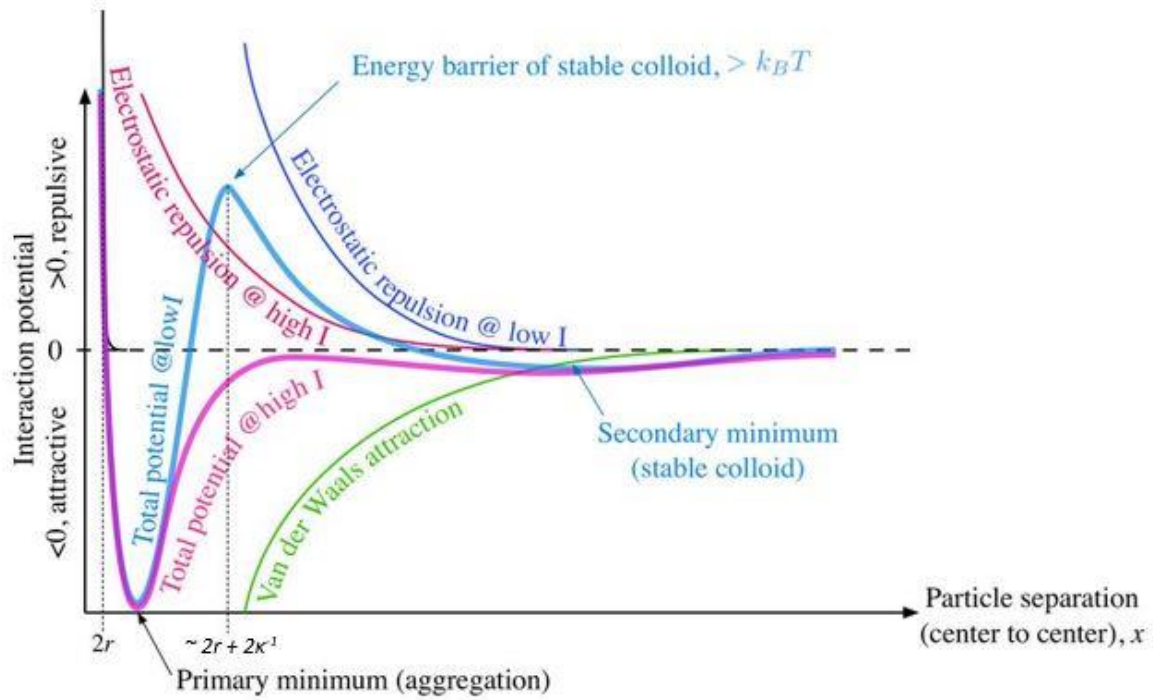


Figure 6: Potential energies of the attractive, repulsive and total interaction forces at low and high ionic strength as a function of the centre-to-centre interparticle distance illustrating colloidal stability. At low ionic strength, electrostatic repulsion (dark blue) dominates over Van der Waals interactions (green), resulting in an energy barrier (light blue) between the primary and secondary minimum significantly higher than  $k_B T$  keeping particles apart. At high ionic strength, Van der Waals interactions dominate over the electrostatic repulsion (red), resulting in a fully attractive total potential (pink) responsible for the flocculation. Adapted from Schütz et al, Crystals 2020.

### 1.2.6. Kinetic arrest and gelation of colloidal systems

Kinetic arrest corresponds to a crowded enough environment so that the state of the system can no longer reach its lowest energy state described by the Gibbs free energy  $G = U - TS + PV$  at given temperature  $T$ , pressure  $P$  and chemical potentials  $\mu_i$  of the system. Glass is a good example of a kinetically arrested system that has been locked into its high-temperature structure. In colloidal suspensions, there are two main types of arrested structures formed when kinetic arrest occurs: when repulsive colloidal interactions dominate over attractive interactions, the arrested suspension is referred to as a colloidal glass or a Wigner glass. The structure is arrested due to a jamming effect because particles have no space to move. Diluting this system will essentially make the system recover its mobility and dispersion properties. When attractive colloidal interactions dominate over repulsive interactions, a gel is formed upon percolation of colloidal particles' aggregates throughout the sample. Diluting such a system will not allow the

system to recover its mobility and dispersion properties because aggregates will remain in suspension, although the percolation can be disrupted by the dilution. Figure 7 reproduces a schematic drawing of the microstructures of colloidal glass and percolated gels on the example of laponite nanorods (Tanaka, Meunier, and Bonn 2004).

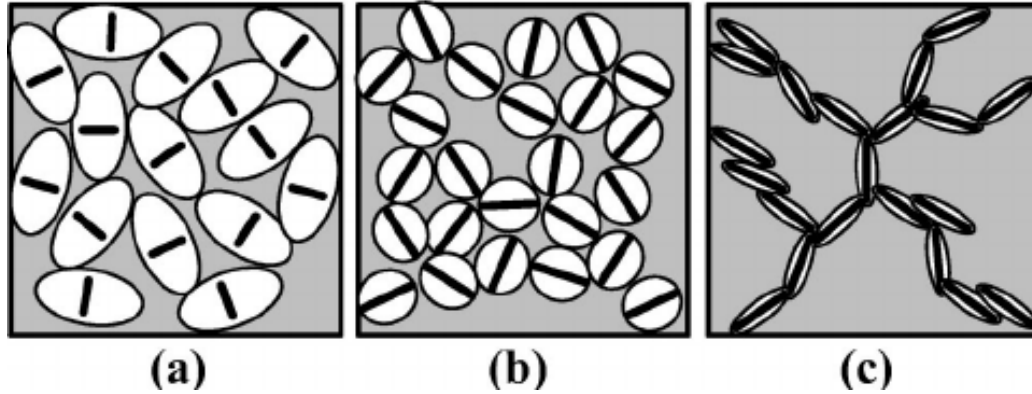


Figure 7: Schematics of different microstates of gels on the example of laponite nanorods. The rods are drawn in full black and circled by the range of their repulsive electrostatic interaction. a) Colloidal glass or Wigner glass observed when the system is dominated by the electrostatic repulsion. b) Intermediate state where attractive and repulsive colloidal interactions balance out. Colloids can still move around. c) Percolated gel observed when attractive interactions dominate over repulsive interactions. Reproduced from Tanaka et al, PRE 2004, 69, 031404.

### 1.3. A brief introduction to liquid crystals

While solids are characterized by a 3-dimensional positional periodicity and a fixed mutual orientation of atoms or molecules, liquids show an absence of long-range positional or orientational order; atoms or molecules exchange neighbours over time and the overall arrangement is constantly changing. Liquid crystals are an intermediate type of phases, often called mesophases, that present a behaviour intermediate between liquids and solids. Only a partial order is observed, corresponding to only some degrees of freedom (*e.g.* orientational), while other degrees of freedom are maintained (*e.g.* positional). These phases result from the spontaneous phase transition from isotropic to an anisotropic distribution of matter due to the system willing to maximise its free energy. In this section, we aim to give a short overview of liquid crystals and introduce the concepts of liquid crystals relevant to this work. For a more in-depth introduction, the reader is invited to refer to de Gennes' seminal book *Physics of Liquid Crystals* (De Gennes and Prost 1993).

#### 1.3.1. Lyotropic and thermotropic liquid crystals

There are two main families of liquid crystals, namely thermotropic and lyotropic liquid crystals. In thermotropic liquid crystals, the phase transition is triggered by temperature, giving

rise to an additional phase before fusion/crystallisation takes place. This is due to contrasts in rigidity-flexibility in the chemical structure of the molecules that depend on the temperature. Famous examples of molecules giving rise to thermotropic liquid crystals are 5CB and 7CB reproduced in Figure 8, in which the biphenyl moiety is rigid whereas the pending C5 chain is flexible. Thermotropic liquid crystals are typically limited to molecular liquid crystals and will not be further developed in this work.

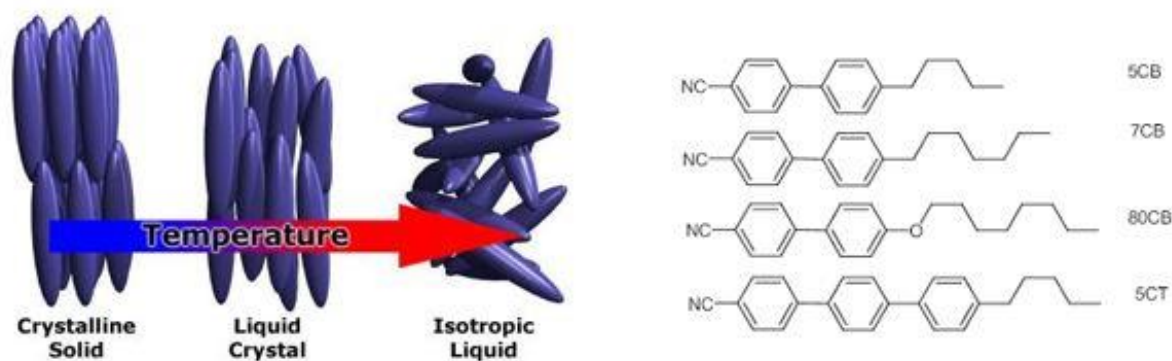


Figure 8: (left) Thermotropic liquid crystals appear as an additional phase between regular solids and liquids. (right) Molecular structures of classical mesogens giving birth to thermotropic liquid crystal phases. Note the contrast of flexibility in this structure between the rigid biphenyl/triphenyl moiety and the flexible pending chain. Credits to Barret research group, McGill University and Barros et al, Central European Journal of Chemistry 2011.

In lyotropic liquid crystals, anisotropic phases arise from changes in concentration of molecules or particles. A very classical example of a lyotropic liquid crystal phase transition is the critical micellar concentration (cmc) above which the excess of amphiphilic molecules self-assemble into micelles, although no macroscopic phase separation is observed in that case. Other types of amphiphilic mesophases can also be considered liquid crystalline, as well as block copolymer solutions. More importantly, suspensions of rod-like particles of extremely various chemical composition and dominant repulsive colloidal interactions also behave uniformly as lyotropic liquid crystals as highlighted in Figure 9. Numerous inorganic nanoparticles (Sonin 1998) such as goethite  $\text{FeOOH}$ , vanadium pentoxide  $\text{V}_2\text{O}_5$ , boehmite  $\text{AlOOH}$  (Zocher and Török 1960), gold nanorods (Pérez-Juste et al. 2005),  $\text{Li}_2\text{Mo}_6\text{Se}_6$  and  $\text{UO}_2\text{F}_2$  have rod-like shapes leading to lyotropic liquid crystallinity. Organic rod-like shaped nanoparticles are less common because there are no straight-forward bottom-up approaches to make them. They are mostly obtained by controlled top-down strategies on high aspect ratios starting materials such as fibres (Elazzouzi-Hafraoui et al. 2008; Belamie, Davidson, and Giraud-Guille 2004). This will be the case in this work, where cellulose nano-rods are obtained from the controlled hydrolysis of high aspect ratio cellulose fibres. Living organisms presenting



elongated shapes have also been evidenced to yield lyotropic liquid crystalline phases: in viruses (TMV, fd-viruses) (Grelet and Fraden 2003), microtubules (Lydon 2006), lipid membranes (Jewell 2011), and proteins (Brecher et al. 1976). In viruses, liquid crystal ordering allows for efficient collective motion. In lipid membranes, liquid crystalline ordering has allowed for compartmentalisation of complex living organisms, allowing different parts to be assigned to different biological functions in a highly out-of-equilibrium state.

To conclude on the diversity of molecules, nanoparticles and living organisms able to spontaneously exhibit liquid crystalline phases, it appears clear that the starting material referred to as “mesogen” has to present a non-trivial shape for the system to distribute in an anisotropic fashion. Elongated molecules or colloids, disk and pyramidal shapes as well as contrasts in the molecular structure – *e.g.* flexibility/rigidity, hydrophobic/hydrophilic – are likely to give birth to liquid crystalline phases.

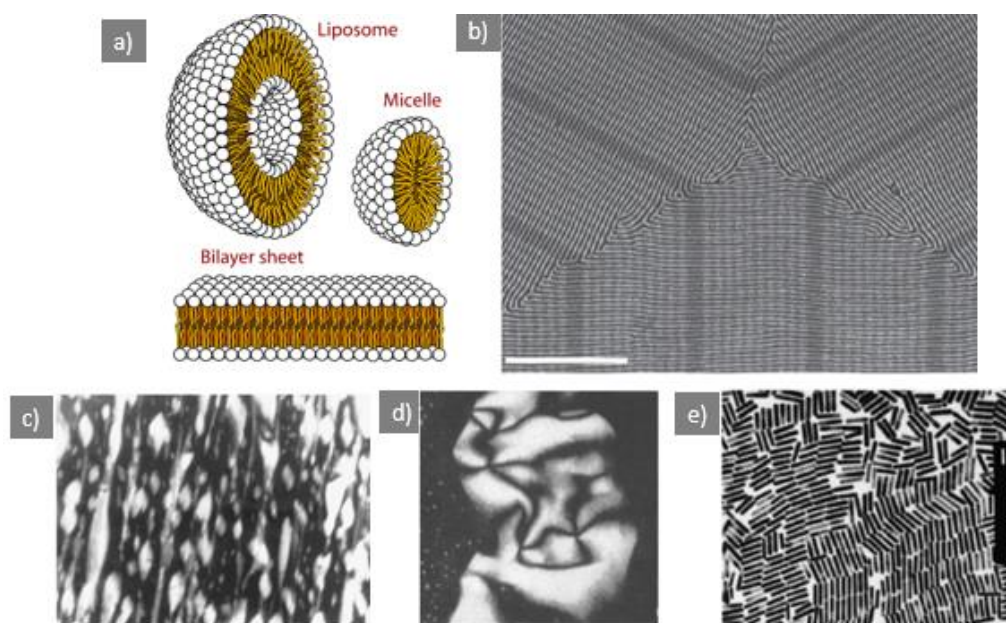


Figure 9: a) Schematics of different amphiphilic mesophase assemblies. b) Self-assembly of block copolymers SD16 and SD45 on a Y-junction template. Scale bar is 500 nm. Adapted from Tavakkoli et al, *Nature Comm.* 2016. c) Polarized optical microscopy image showing spherical germs (tactoids) of vanadium pentoxide  $V_2O_5$ . Adapted from Sonin, J. *Mater. Chem.* 1998. d) Schlieren textures characteristic of a nematic phase observed in suspensions of boehmite  $AlOOH$ . Adapted from Sonin J. *Mater Chem.* 1998. e) TEM image of a suspension of gold nanorods, scale bar is 50 nm. Adapted from Perez-Juste et al, *Coordination Chemistry Reviews* 2011. f) SEM image of a film of *Flavobacterium IR1* where bacteria at close packing exhibit nematic ordering. Adapted from Schertel et al, *J. R. Soc. Interface* 2020.

### 1.3.2. Different liquid crystalline phases

There are various ways for matter to arrange with a disorder intermediate between liquids and solids, corresponding to different liquid crystalline phases.

The smectic phase consists of well-defined and regularly distributed 2D-layers of objects (Figure 10a and b). There is a vertical positional order, but no positional order in the horizontal plane. In the smectic A phase, objects have their director pointing perpendicularly to the layer whereas in smectic C phases, the director is tilted with respect to this direction. This phase mostly originates from mesogens with kinks in their chemical structure. The smectic C\* phase is the chiral version of the smectic C phase, in which chirality makes the director undergo a precession around the normal of the layer at constant tilt angle from one layer to the next.

Another possible arrangement of mesogens is the nematic phase (Figure 10c), in which the directors of the mesogens tend to align along a common direction  $\mathbf{k}$ . The organisation of the phase remains liquid-like, with no long-range positional order in any direction of space. It is important to note that there is still disorder in the arrangement of the direction along the nematic axis, for which the schematic of Figure 10c may be misleading. A good assessment of the disorder in the orientation of the directors is to look at the order parameter of the director with respect to the nematic direction  $\mathbf{k}$ , which tends to be on the order of  $S_{2,loc} \sim 0.8 - 0.9$  (Schütz et al. 2020) depending on the system considered. The chiral-nematic or cholesteric phase is the chiral version of the nematic phase, in which the directors no longer point towards a single direction. Chirality makes the nematic direction  $\mathbf{k}$  undergo a continuous rotation around a given axis, leading to a helical distribution of the directors in space. The axis of rotation is therefore referred to as the helical axis and noted  $\mathbf{h}$ . In a layer perpendicular to the helical axis, mesogens have their directors pointing in the same direction, corresponding locally to a nematic phase.

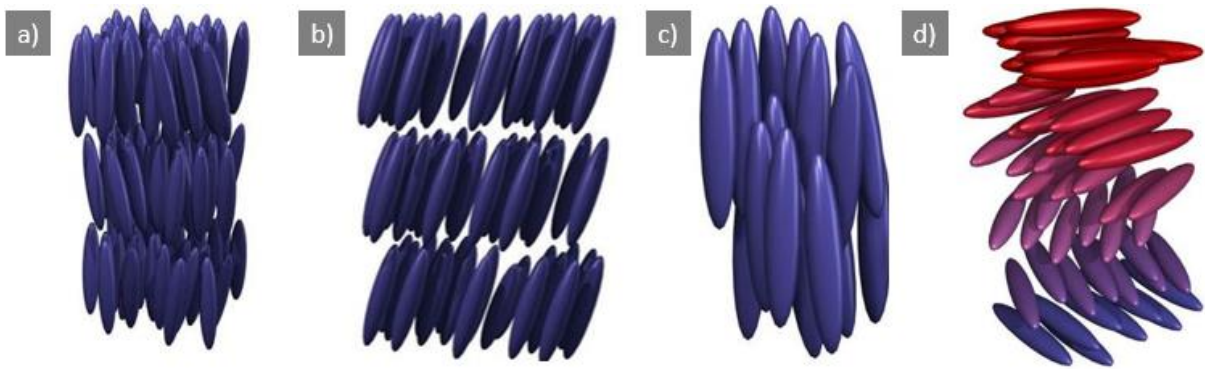


Figure 10: Schematics of the objects repartition in a variety of liquid crystalline phases. a) Smectic A and b) smectic C phases. There is a vertical positional order, but no positional order in the horizontal

plane. c) The nematic phase shows an orientational order, but no positional order. d) Chiral-nematic or cholesteric phase, in which the director undergoes a continuous rotation around an axis, leading to a helical distribution of the directors. Credits to Barret research group, McGill University.

Once again, Figure 10d) sketches the *average* direction of the directors of the cholesteric phase, but there is an intrinsic disorder in the orientation of the directors within each layer exactly alike the nematic phase, with  $S_{2,loc} \sim 0.8 - 0.9$ . A realistic description of the cholesteric phase consists in describing it as a big mess of mesogens, those mesogens having their director  $\mathbf{n}$  pointing more or less in the average direction  $\mathbf{k}$  within a layer perpendicular to the helical axis – being quantitatively described by  $S_{2,loc}$  –, and this average direction of orientation  $\mathbf{k}$  is continuously rotating around the helical axis in a helical trajectory. Lagerwall's group (Schütz et al. 2020) recently sketched the director field versus the orientation of the individual mesogens of the cholesteric phase reproduced in Figure 11, which is a good picture to bear in mind.

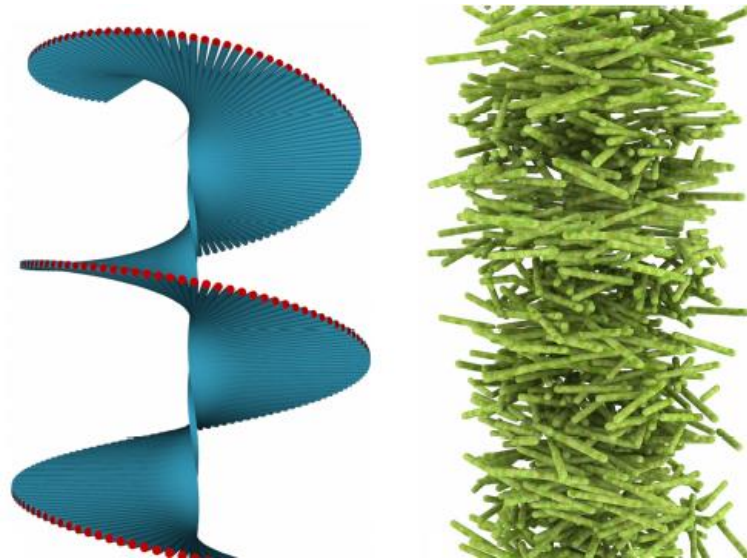


Figure 11: (left) Plot of the director field  $\mathbf{k}$  of the cholesteric phase, defined as the average direction of the mesogens. (right) Realistic vision of the cholesteric phase, in which the mesogens themselves are plotted and their disorder in orientation is accounted for with  $S_{2,loc} \sim 0.8 - 0.9$ . It is much harder to distinguish regularity in the arrangement of the rods, although there is one. Adapted from Schütz et al, *Crystals* 2020, 10, 3, 199.

### 1.3.3. The cholesteric liquid crystalline phase

#### 1.3.3.1. Onsager's description of the phase transition in hard rods suspensions

Colloidal suspensions of anisotropic objects have been described by Onsager (Onsager 1949). He predicted that nano-rods would organize in a nematic (or chiral-nematic) liquid crystalline phase above a threshold concentration for entropic reasons. Let us first understand



qualitatively this phase transition, before we describe it quantitatively by writing the free energy of the system.

Nano-rods are willing to maximise their disorder in suspension according to the second law of thermodynamics, *i.e.* maximise their configurational entropy. One can figure out that increasing the concentration of rods in suspension will eventually lead to a jammed situation, similar to a Wigner glass, where rods are so close and intricate with each other that none of them is able to move anymore. Before this situation happens, rods prefer to align their long axis in the same direction to free their movement in the two-dimensional space perpendicular to their long axis. By doing so, each rod only occupies the area of its cross-section in this plane and suppresses the overlap observed with random packing. To put more precise words on it, the entropy of each rod can be decomposed in two terms, corresponding to their rotational and translational entropies. In a packed assembly of isotropic rods, both translational and rotational entropies decrease quickly as rods get closer to the jamming threshold. By arranging in a nematic phase, rods sacrifice their last rotational degrees of freedom, but retrieve their translational degrees of freedom beyond the jamming threshold of the isotropic arrangement. In a suspension of freely rotating rods, the total entropy per rod is then maximised by spontaneously aligning in a common direction, occurring when the volume fraction reaches a threshold dictated by the aspect ratio of the particles.

The mathematical derivation of Onsager has been initially proposed for infinitely long rods, whereby only the pair interaction hard-rod potential has been considered. He looked at the distribution function describing the orientation of the long axis of hard rods in suspension, for which he constructed solution-functions maximising the free energy of the system. The free energy has three terms contributing, that depend both on the volume fraction in particles and the excluded volume surrounding the particles  $b = \frac{\pi}{4} \cdot L^2 \cdot D$ ,  $L$  being the length and  $D$  the diameter of the particle (equation 61 of the reference paper). So by taking into account the condition of maximising the free energy of the system, Onsager relates the volume fraction in particles to the other parameters under a set of hypotheses that include the limit of big aspect ratios  $L \gg D$ , ending up with the following condition:

$$\varphi_{i,0} = 3.34 \cdot D/L$$

$$\varphi_{a,0} = 4.49 \cdot D/L$$

where  $\varphi_{i,0}$  is the volume fraction at which the anisotropic phase appears and  $\varphi_{a,0}$  is the volume fraction at which the isotropic phase disappears (equation 96 of the reference paper). In other terms, his calculation predicts that suspensions of anisotropic hard rods transition into a nematic liquid crystalline order above a threshold volume fraction that only depends on the aspect ratio of the rods. A biphasic domain where both the isotropic and anisotropic phases coexist is also predicted in his calculation. Throughout this biphasic domain, the isotropic phase has a volume fraction fixed at  $\varphi_{i,0}$  and the anisotropic phase has a volume fraction fixed at  $\varphi_{a,0}$ . In a perfectly monodisperse system, changes in the overall volume fraction of the suspension  $\varphi$  only result in modifications of the relative volumes of isotropic and anisotropic phases; this point is important to bear in mind.

Onsager's theory is strong in the sense that it predicts the phase transition to a nematic phase, the coexistence region and that the critical concentrations only depend on the aspect ratio of the particles with considerations on the entropy of the system. Its limitations are that it does not accurately predict the experimental values observed for the phase transition, in part because electrostatic interactions are not taken into account. This point is addressed in the next section. Relatively strong hypotheses such as the high aspect ratio  $L \gg D$  of the particles are also made on the course of the calculation.

### ***1.3.3.2. The SLO model: a refinement of Onsager's calculation for charged rods suspensions***

Onsager mentions in his 1949 paper the need of taking electrostatic interactions into account for charged rods suspensions in the form of an effective diameter  $D_{\text{eff}} = D + \delta$  where  $\delta$  is the thickness of the electric double layer, leading to the following expression for the excluded volume:

$$b = \frac{\pi}{4} \cdot L^2 \cdot (D + \delta)$$

His approach is however incomplete, as proven by the development of Stroobants, Lekkerkerker and Odijk (Stroobants, Lekkerkerker, and Odijk 1986), nowadays referred to as the SLO theory. They consider an exponentially decaying electrostatic potential between particles and modify Onsager's expression of the free energy accordingly. They find out that Onsager's theory can be extended to charged rods suspensions with two modifications:

- the first one is the definition of an effective diameter  $D_{\text{eff}} = D + \delta$  in line with Onsager's original thoughts.

- the second one is a parameter  $h = \frac{\kappa^{-1}}{D_{\text{eff}}}$  referred by the authors as the twisting factor, that comes from the angular dependence of the electrostatic interaction between charged rods.

They demonstrate an increase of the concentrations at which the liquid crystalline phase sets that is found to be proportional to the value of  $h$ . This effect can be qualitatively understood as follows: because the effective diameter of the rods is increased to  $D_{\text{eff}} = D + \delta$  and the effective length is now  $L_{\text{eff}} = L + \delta$ , the new aspect ratio of the particle  $\frac{L_{\text{eff}}}{D_{\text{eff}}} = \frac{L + \delta}{D + \delta}$  is lower than the former aspect ratio. As particles have rod-like shapes, we have  $L \gg D$  in the limit of long particles compared to their electric double layer  $L \gg \delta$ , meaning that the new aspect ratio verifies  $\frac{L_{\text{eff}}}{D_{\text{eff}}} = \frac{L}{D} \cdot \left( \frac{D}{D + \delta} \right) = \frac{L}{D} \cdot \left( \frac{1}{1 + 2h} \right)$ . Because the concentration thresholds of the anisotropic phase depend linearly on the inverse of the aspect ratio  $\frac{D_{\text{eff}}}{L_{\text{eff}}}$ , they also depend linearly on the value of  $h$ . Using a perturbation theory on the value of  $h$ , the authors retrieve quantitative values for this dependence:

$$\varphi_i - \varphi_{i,0} = 2.37 \cdot h$$

$$\varphi_a - \varphi_{a,0} = 3.01 \cdot h$$

where  $\varphi_i$  and  $\varphi_a$  stand for the threshold concentrations of the biphasic regime while taking electrostatic interactions into account,  $\varphi_{i,0}$  and  $\varphi_{a,0}$  stand for the threshold concentrations of the biphasic regime before taking electrostatic interactions into account.

To summarise, the electrostatic repulsions in a suspension of hard rods increase the concentration threshold for the onset of the anisotropic phase for two reasons: the decrease of the effective aspect ratio of the particle – the electric double layer being evenly thick in all directions although hard rods are anisotropic – and the directionality of electrostatic interactions in between rods favouring a perpendicular orientation of rods relative to one another. This twisting factor  $h$  is not chiral, it favours equally clock-wise and counter-clockwise twist of the rods. The prediction of the pitch from the chiral shape of the rods is not a solved problem to date. It is interesting to note that since the phase transition only depends on the aspect ratio of the particles, other colloidal interactions such as Van der Waals attractive forces are expected to have no impact on the phase transition behaviour.

## 1.4. *Optical properties of the cholesteric phase*

In this section, we first develop the classical models of diffraction gratings and multilayer reflectors. We move on to the theoretical description of the optical properties of the cholesteric phase, which is found to be close to a multilayer reflector when illuminated under normal incidence and behaves as a diffraction grating when illuminated perpendicular to the helical axis. Differences with a standard Bragg multilayer reflector are highlighted. Within the limit in which the cholesteric stack can be approximated as a Bragg reflector, a simple law predicting the main features of the optical response can be derived and compared to experimental results.

### 1.4.1. Diffraction gratings

A diffraction grating is a network of regularly spaced identical scattering elements characterised by a periodicity  $d$ , defined as the distance between two consecutive scattering elements. Similarly to the previous calculation, we look at the possible constructive interference of the scattered rays on each element of the network. The optical path difference between the scattered rays of two consecutive scattering motifs is given by  $\delta = d \cdot (n_1 \cdot \sin(\theta_{\text{in}}) \pm n_2 \cdot \sin(\theta_{\text{out}}))$ , the sign depending on the nature of the grating (reflection or transmission) and  $n_1 = n_2$  for a grating in reflection. The condition for constructive interference immediately yields the diffraction grating formula:

$$n_1 \cdot \sin(\theta_{\text{in}}) \pm n_2 \cdot \sin(\theta_{\text{out}}) = m \cdot \frac{\lambda}{d}$$

This equation means that light going through a diffraction grating will be scattered into different diffraction orders regularly spaced in angle, inside which lower wavelengths will be scattered at smaller angles than higher wavelengths.

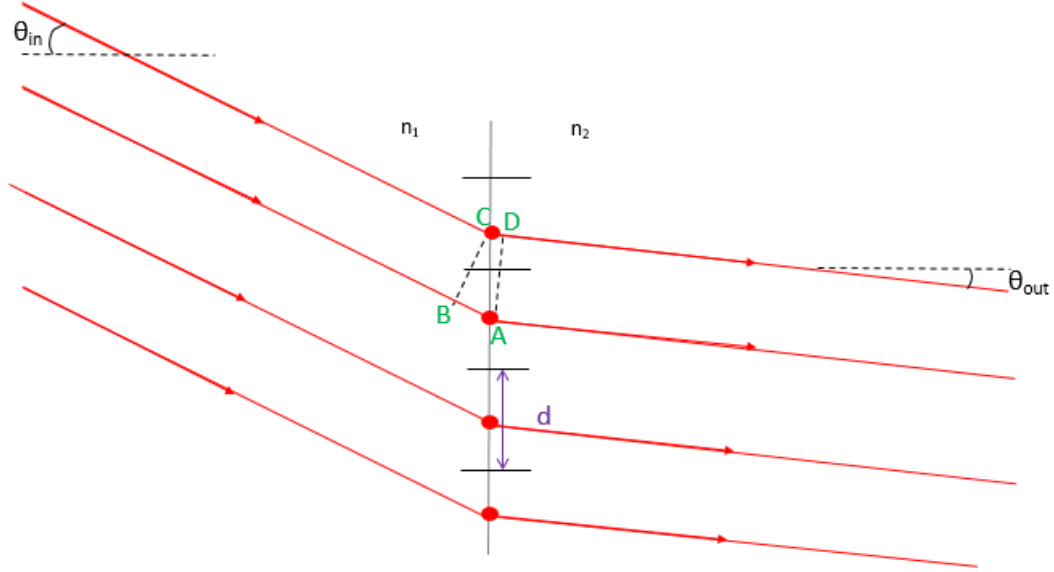


Figure 12 : Schematic of the light path through a diffraction grating (in transmission). Construction lines to retrieve the optical path between two consecutive scattering motifs are drawn. The calculation is very similar for gratings in reflection.

### 1.4.2. Bragg reflection in a multilayer assembly

Whenever a material is made of alternating layers of different refractive indices  $n_1$  and  $n_2$  (e.g.  $n_1 > n_2$ ) and thicknesses  $d_1$  and  $d_2$ , a reflection-transmission event takes place each time light reaches an interface. Reflected light from all interfaces may interfere constructively or destructively when leaving the material. When the optical path difference of reflected light rays is a multiple of the wavelength of the incoming light, they will interfere constructively. The optical path difference of one reflection with the reflection on the next interface can be expressed as a function of the incident light angle and the interlayer distance. It corresponds on the scheme of Figure 13 to two times the optical path  $AC$  minus the optical path  $AB$  in the layer of refractive index  $n_1$ . From geometric considerations, we have  $AC = \frac{d_1 \cdot n_1}{\cos(\theta_1)}$  and  $AB = 2 \cdot d_1 \cdot n_1 \cdot \tan(\theta_1) \cdot \sin(\theta_1)$  which yields the following optical path difference:

$$\delta_1 = 2 \cdot d_1 \cdot n_1 \cdot \cos(\theta_1)$$

The very same calculation can be made in the layer of refractive index  $n_2$ . The condition of constructive interference on the periodic motif (one layer 1 + one layer 2) writes ( $m$  being a relative integer):

$$2 \cdot (d_1 \cdot n_1 \cdot \cos(\theta_1) + d_2 \cdot n_2 \cdot \cos(\theta_2)) = m \cdot \lambda$$

While  $n_1, n_2$  are constants of the materials, the interplay between other parameters contains a rich behaviour. At fixed values of  $d_1, d_2$ , the Bragg condition is fulfilled at different incident angles  $\theta$  if different wavelengths  $\lambda$  are present in the illumination light spectrum. This angular dependence is at the origin of iridescence phenomenon, the spectacular reflection of a given wavelength of incoming light (*i.e.* a colour) at a given angle of observation. The reflected colour blueshifts with increasing angles of observation owing to the  $\cos(\theta)$  dependency in the Bragg condition. The presence of  $m$  implies different orders in reflection as a given wavelength may fulfil the previous condition with several  $\theta$  values if  $m$  varies accordingly. At normal incidence, the reflected wavelength verifies  $m \cdot \lambda = 2 \cdot (d_1 \cdot n_1 + d_2 \cdot n_2)$ . Any increase of the interlayer distances  $d_1, d_2$  result in a redshift of the colour observed at a given angle.

While this law is widely used to describe the scattering of X-rays on a distribution of atoms, it may as well be used to describe the scattering of visible light on nanometric networks. The interlayer distance leading to visible light reflection at normal incidence verifies  $2 \cdot (d_1 \cdot n_1 + d_2 \cdot n_2) \in [400; 800]$  nm, *i.e.*  $d_{1,2} \in [150; 250]$  nm for  $n_1 \sim 1.5$  and  $n_2 = 1$ . This provides an interlayer distance target for photonic materials design.

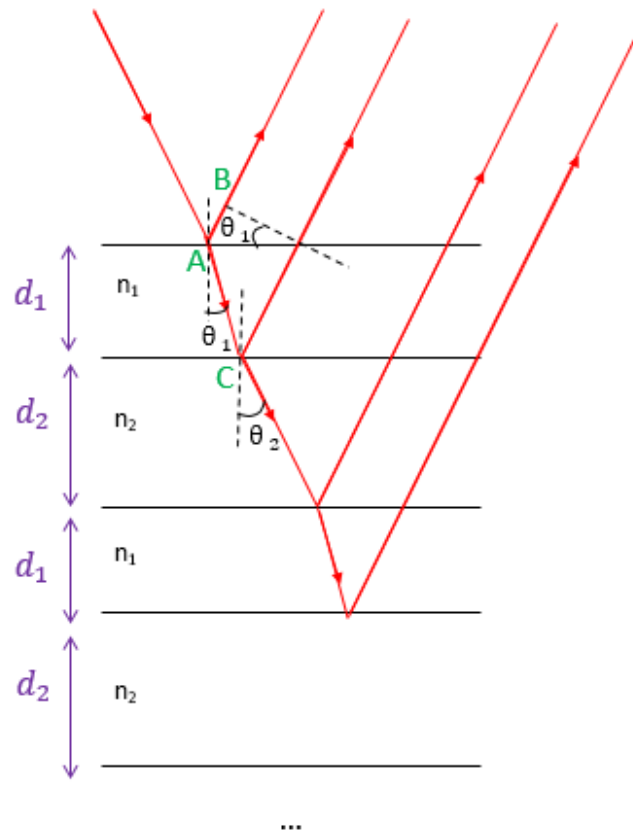


Figure 13 : Schematic of the light path in a multilayer assembly corresponding to regularly spaced interfaces of two different thicknesses  $d_1, d_2$  and refractive indices  $n_1, n_2$ . Construction lines and angles to retrieve the optical path between two consecutive reflections are present on the schematic.

### 1.4.3. Theoretical description of the optics of cholesteric phases

Oseen and de Vries first described the propagation of light through cholesteric phases with a theoretical model (De Vries 1951; Oseen 1929) that has been later reused and developed by other authors (Belyakov, Dmitrienko, and Orlov 1979; Ferguson 1966; Dreher and Meier 1973; Berreman and Scheffer 1970). While de Vries gives an exact solution for normal incidence, Oseen and Belyakov also tackled oblique incidence with approximated solutions allowing for the description of the physics of the problem. The starting point consists in describing the medium as a dielectric tensor undergoing a continuous helical revolution of angle  $\varphi$  around the helix axis  $z$  (with  $\varepsilon_1$  and  $\varepsilon_2$  the principal values of the dielectric tensor) (Belyakov, Dmitrienko, and Orlov 1979):

$$\varphi = 2 \cdot \pi \cdot \frac{z}{p}$$

$$\bar{\varepsilon} = \begin{pmatrix} (\varepsilon_1 + \varepsilon_2) + (\varepsilon_1 - \varepsilon_2) \cdot \cos(2 \cdot \varphi) & \pm(\varepsilon_1 - \varepsilon_2) \cdot \sin(2 \cdot \varphi) & 0 \\ \pm(\varepsilon_1 - \varepsilon_2) \cdot \sin(2 \cdot \varphi) & (\varepsilon_1 + \varepsilon_2) - (\varepsilon_1 - \varepsilon_2) \cdot \cos(2 \cdot \varphi) & 0 \\ 0 & 0 & \varepsilon_3 \end{pmatrix}$$

By constructing a wave solution to Maxwell's equations for such a medium and applying boundary conditions, these authors find four possible waves solutions. Among these solutions, those which are polarised inversely to the helicity of the helical stack are found to interact very weakly with the cholesteric structure and are thus mostly transmitted, whereas the two solutions that have the same polarisation as the helicity of the stack interact strongly and are mostly reflected. This indicates that light interaction with cholesteric assemblies is selective in circular polarisation, in good agreement with experimental observations (De Vries 1951).

Notably, total reflection is predicted in a bandwidth verifying  $\sqrt{\varepsilon_1} \cdot p < \lambda < \sqrt{\varepsilon_2} \cdot p$ . While this looks very much like a Bragg multilayer reflection behaviour (reflection for  $\lambda = n \cdot p$  at normal incidence), the bandwidth feature is specific to cholesteric assemblies and originates from the birefringence of the mesogens. Its physical meaning is that light propagating at any speed in between  $\frac{c}{\sqrt{\varepsilon_1}}$  and  $\frac{c}{\sqrt{\varepsilon_2}}$  will travel through regularly spaced assemblies of matter of the corresponding refractive index, leading to constructive interference of the reflected waves. Another specificity of cholesteric assemblies is the absence of additional orders of reflection at normal incidence.

Finally, an expression of the rotary power – how much the polarisation of an incoming wave is rotated by the medium – can be derived from the model. The real strength of the model is

that all interesting optical features can be simply expressed as a function of three experimentally accessible parameters: the pitch of the helix, the birefringence of the mesogens and the refractive index of the medium. In many cases, it is a good approximation to neglect the aforementioned differences between a cholesteric assembly and a multilayer stack and approximate the optical response of the cholesteric phase to a 1-dimensional Bragg reflection. In this case, the optical response of a thin enough cholesteric stack essentially consists in a single Bragg scattering event on the stack along with two refractive events when light enters and exits the material. This is what describes the Fergason law (Fergason 1966) sketched in Figure 14.

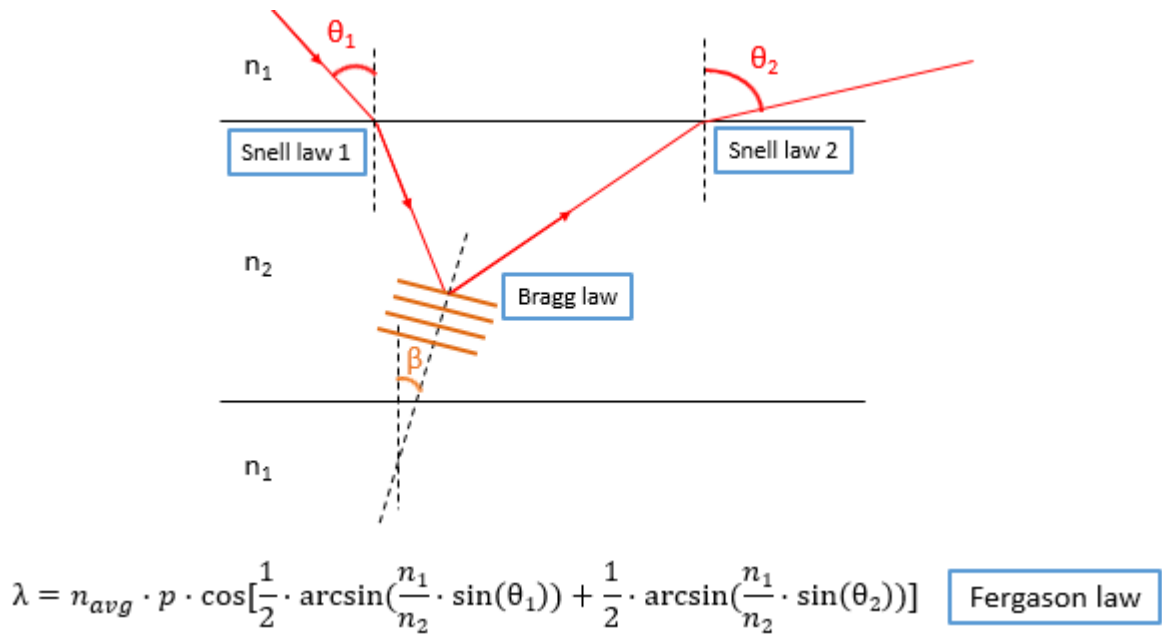


Figure 14 : Scheme of a light path undergoing refractive events at interfaces and Bragg scattering on cholesteric assemblies, described by the Fergason law (bottom).

In the specific case of light illumination perpendicular to the helical axis, the cholesteric assembly behaves like a diffraction grating of spacing equal to half the pitch value for symmetrical mesogens. Laws detailed in the previous section apply.

At oblique incidence, the approximation of a small value for the birefringence is made to provide a solution to the problem. Additional orders of reflection at frequencies multiple of the Bragg frequency are observed. Another important feature is the loss of selectivity in polarisation as the incident angle increases: reflected light becomes elliptically polarised. Numerical methods are useful to solve especially the oblique incidence problem. Approaches involve iterations on a transfer matrix (T-matrix) (Berreman and Scheffer 1970). It is interesting to note that the optical behaviour of a cholesteric assembly varies continuously from a multilayer-like



behaviour at normal incidence to a diffraction grating-like behaviour perpendicular to the helical axis. A simplified view of oblique incidence is an intermediary state between the two, holding features from both a Bragg reflector and a diffraction grating.

## 1.5. Cellulose

### 1.5.1. Cellulose in nature

Cellulose is the major component of the primary and secondary plant cell walls and is therefore the most abundant polymer on Earth with an overall annual production of  $7.5 \cdot 10^{10}$  tons of material (Habibi, Lucia, and Rojas 2010). It is therefore a low-cost, bio-sourced and renewable raw material. However, separating cellulose from the other components of the plant cell wall typically require acidic or basic and/or mechanical treatments that have a significant environmental impact and energy cost (Rol et al. 2019). Throughout this work, cotton cellulose has been used because the size and shape of the colloidal objects resulting from the acid hydrolysis of the cotton cellulose fibres and their self-assembling properties have been thoroughly characterised in previous studies (Elazzouzi-Hafraoui et al. 2008).

### 1.5.2. Chemical structure

Cellulose is a polysaccharide made of a sequence of glucose units bound by  $\beta$ -1,4 links named  $\beta$ -1,4 anhydro-D-glucose with degrees of polymerization (DP) of *ca.* 10,000. In the sequence, each glucose unit is flipped of  $180^\circ$  about the polymer chain axis, making the dimer of glucose – cellobiose – the unit of repetition of the chain as shown in Figure 15. One end-chain is a reactive hemiacetal, called the reducing end, and the other end-chain has only non-reactive alcohol groups and is called the non-reducing end. The most stable equatorial conformation of the –OH groups of glucose along the chain allows for the creation of a dense hydrogen bonds network – both intra and intermolecular – which is of tremendous importance when speaking of the supramolecular architecture of cellulose.

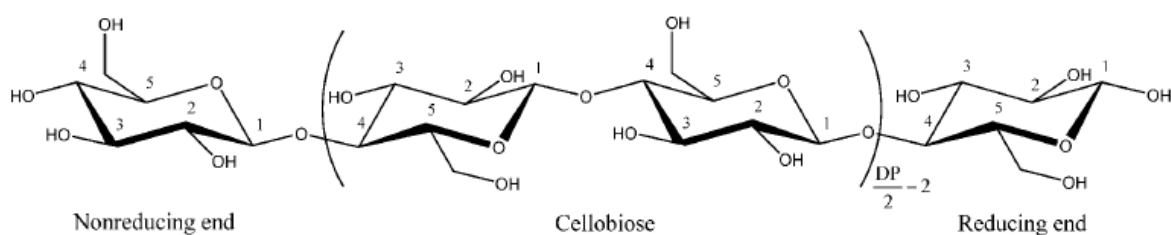


Figure 15 : Chemical structure of cellulose. The unit of repetition of the polymer chain, cellobiose, consists of two glucose units flipped at  $180^\circ$  from one another. The reducing end of the chain is made

of a hemiacetal group whereas the non-reducing end is a simple hydroxyl group. Adapted from Habibi et al, Chem. Rev. 2010.

### 1.5.3. Supramolecular assemblies of cellulose

Cellulose chains naturally form hierarchical fibrous structures ranging from the nanometre to the macroscopic scale, as described in Figure 16. Fibre packing is easily achieved and resilient to solubilisation in water thanks to stabilizing Van der Waals interactions and a dense hydrogen bond network. This fibre packing is remarkable because the conformation of individual cellulose chains is highly strained in this supramolecular assembly, far from the usual statistical knot. This chain conformation is highly unfavourable entropically and is only made possible by powerful enthalpic chain-to-chain interactions. Right after being polymerised by the terminal complex enzymes (Kimura et al. 1999), cellulose readily assembles into protofibrils of 20-30 chains packed laterally (Brown Jr 1996). These protofibrils pack themselves into microfibrils, the cellulosic micrometric building block (Preston, Wardrop, and Nicolai 1948). Numerous microfibrils are brought together to form the macroscopic cellulose fibres of *e.g.* cotton.

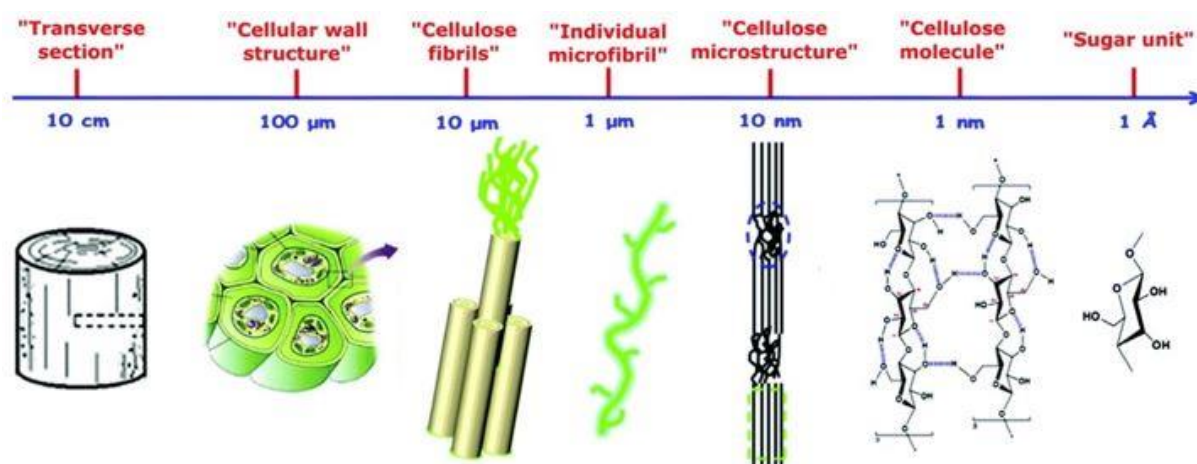
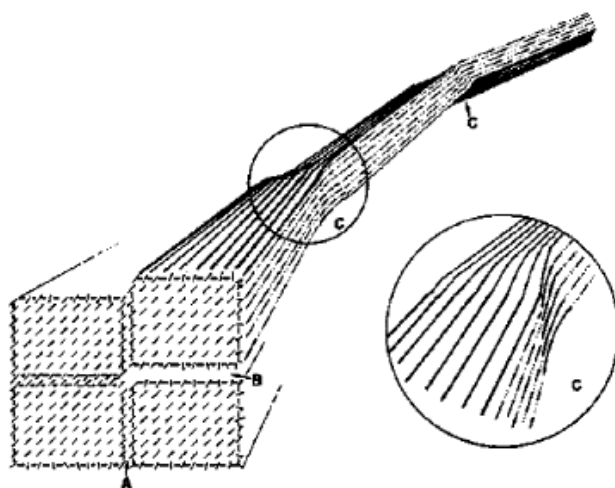


Figure 16 : Hierarchical structures of cellulose ranging from the atomic to the macroscopic scale; glucose monomer, cellulose macromolecule, protofibril, microfibril, cell wall and wood. Adapted from Trache et al, Nanoscale 2017.

The characteristic dimensions of these fibres are highly variable, depending on the cellulose source and hierarchical assembly (Elazzouzi 2006; Chanzy 1990). Microfibrils consist of crystalline parts that are hundreds of nanometres to microns long and separated by intermediate less organised regions, evidenced by  $^{13}\text{C}$  CP/MAS (Earl and VanderHart 1980) and X-ray scattering (Fink et al. 1987). These “defect” regions have been found to be intermediate between a crystalline and an amorphous state, sometimes referred to as pseudo-amorphous. Cellulose

microfibrils from the *Valonia* algae have a cross-section of 15-25 nm and show only a few % of non-crystalline regions (Sassi and Chanzy 1995), cellulose from cotton have a fibre cross-section of 5 to 10 nm and around 30% non-crystalline regions, and cellulose from primary plant cell walls whose cross-sections are about 1.5-3 nm have 65-70% non-crystalline regions (Elazzouzi 2006). The fibre topology summarised in Figure 17 is essential in the process for making cellulose nanocrystals, as discussed in the following section From fibrous materials to colloids.



*Figure 17 : Fibre-packing supramolecular assembly typically observed for cellulose, made of several microfibrils packed laterally to form a macro-fibre owing to the strong chain-to-chain Van der Waals interactions and hydrogen bond network. The fibre is typically crystalline, but presents less organised pseudo-amorphous regions highlighted in the inset of the figure. Adapted from Rowland and Roberts, J. Pol. Sci. 1972.*

#### 1.5.4. Crystallinity and allomorphs

The polymer is semi-crystalline, its crystallinity varying notably with the origin of cellulose and processes. Native cellulose is found in the two allomorphs  $I_\alpha$  and  $I_\beta$ , which differ in their crystalline lattice and the associated hydrogen bonding network.  $I_\alpha$  is a metastable phase that can be converted into the thermodynamically stable  $I_\beta$  for example by temperature treatment or chain dislocation via mechanical treatment (Sugiyama et al. 1990; Yamamoto and Horii 1993; Chen et al. 2018). Cellulose II, also called regenerated cellulose, is obtained from cellulose I by fully dissolving and re-precipitating cellulose chains or by the bottom-up polymerisation of glucose units. The cellulose I to cellulose II modification is considered irreversible (Habibi, Lucia, and Rojas 2010) and the fibrillary structure is generally destroyed in the process (Dinand et al. 2002). This irreversibility is explained by the rotation of the hydroxyl group in C6, enabling a change in the hydrogen bond network and chain packing from a parallel arrangement

to the more stable antiparallel arrangement sketched in Figure 18. Interestingly, this difference in chain arrangement has a big consequence on the molecular dipole of the cellulose chain. Glucose is a polar molecule ( $\mu_D = 8.68 D$ ) that may transfer or not its polarity to the macromolecular chain. In cellulose I, cellulose chains always have the same orientation along the c-axis (the chain direction), resulting in a supposedly big macromolecular permanent dipole. Cellulose II chains alternate between opposite orientations along the c-axis just like their a-axis and b-axis, therefore compensating their macromolecular dipole by their neighbours. Allomorphs can be distinguished for example by NMR or X-ray scattering techniques.

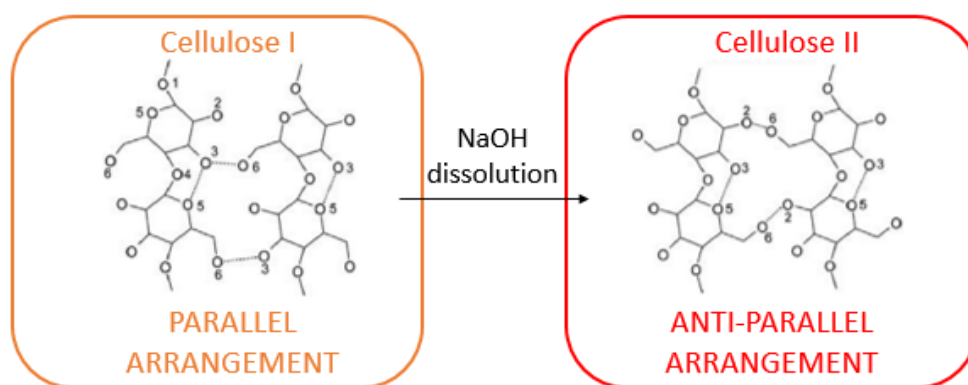


Figure 18 : Schematic of two allomorphs of cellulose, I and II. Chemical structures illustrate the modification of the hydrogen bonding network.

## 1.6. Cellulose nanocrystals

### 1.6.1. From fibrous materials to colloids

Whenever cellulose fibres of any dimension are subjected to a strong acid hydrolysis, one can isolate colloidal nano-rods if the hydrolysis conditions are controlled. This phenomenon has been first discovered by Rånby et al (Ranby 1949). What happens exactly during this chemical reaction?

In a strongly acidic reaction medium (typically 60-65 wt.% acid),  $H^+$  ions are capable of catalysing the breakage of the glycosidic bond in between glucose units, leading to the depolymerisation of the chain at random locations along the cellulose chain following the mechanism of Figure 19 (Philipp et al. 1979). If the reaction is uncontrolled, the DP of the chain decreases rapidly to reach an equilibrium value called level-off degree of polymerisation (LODP) (Nickerson and Habrle 1947; Battista et al. 1956; Habibi, Lucia, and Rojas 2010). The depolymerised cellulose oligomers are largely solubilised in the reaction medium during this process. Because  $H^+$  ions catalyse this reaction, the amount of bond breakages is determined

by the ability of  $H^+$  to diffuse onto cellulose chains. This feature determines what areas of the fibre will be depolymerised, and is at the origin of a remarkable selectivity; remembering from Figure 17 that cellulose fibres are made of highly crystalline regions linked with lesser organised pseudo-amorphous regions,  $H^+$  ions will not be able to diffuse inside the core of the highly crystalline regions. The pseudo-amorphous regions of the fibre have enough space for  $H^+$  ions to diffuse in, and will thus be largely depolymerised during the process. As a result, the hydrolysis of the cellulose fibre by a strong acid behaves as if the least organised parts of the fibre were cut while the highly crystalline part remain essentially untouched and is yielded in the form of nanocrystals as schematically summarised in Figure 20 (Nishiyama, Langan, and Chanzy 2002). From this figure, it is easy to see the direct connection between the fibrous shape of the starting material and the final rod-like shape of the colloidal particles formed. An excessive hydrolysis time can solubilise more and more the crystalline region, until there is no more insoluble cellulose remaining in the medium. This is why the reaction medium is typically quenched by the addition of a large amount of ice, which both dilutes the acid and lowers the temperature, stopping the hydrolysis reaction.

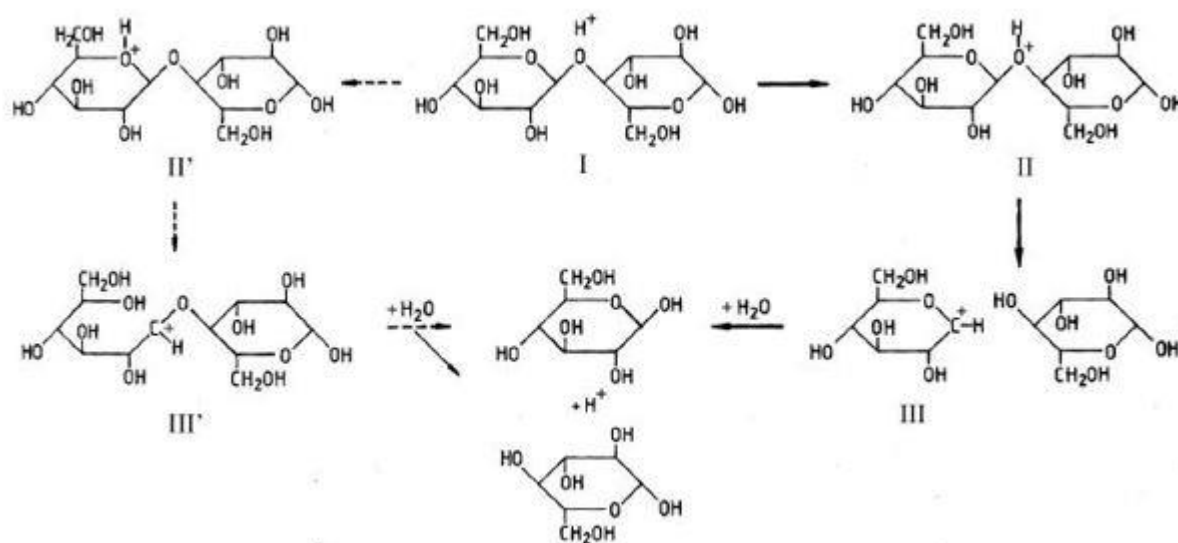


Figure 19: Mechanism of the acid hydrolysis of cellulose.  $H^+$  catalysis leads to the breakage of the glycosidic bond and the formation of a carbocation intermediate that is further hydrated. Adapted from S. Elazzouzi's PhD manuscript.

Another peculiar feature of cotton CNCs Elazzouzi's work (Elazzouzi-Hafraoui et al. 2008) highlighted through cryo-TEM, SAXS and WAXS joint characterisation is that the colloidal objects resulting from the CNC hydrolysis are typically made of several laterally packed individual crystallites as shown in Figure 20. Elazzouzi observed a characteristic size she interpreted as the one of the total crystallites in cryo-TEM and SAXS, but another size in

WAXS on average two times lower, that she interpreted as the size of the individual crystals forming CNCs by lateral packing. TEM characterisation of CNCs typically shows objects that seem to have been stuck together laterally, strongly supporting Elazzouzi's observations. The mechanism by which these objects acquire this final shape remains unclear to date. It could be a reminiscence of the former assembly of cellulose microfibrils into macrofibrils in which the links between neighbour microfibrils have not been completely cut by the hydrolysis, or due to the abrupt solubility change cellulose oligomers encounter as the reaction medium is quenched by cold water.

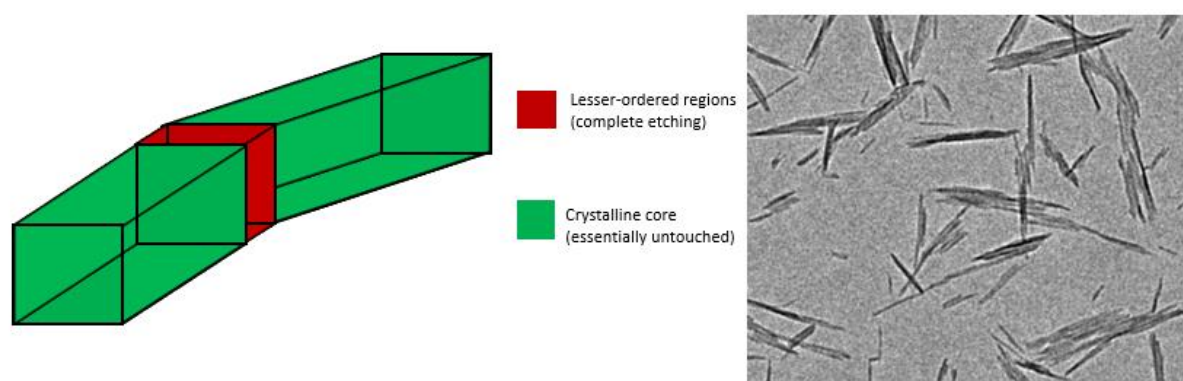


Figure 20 : (left) Schematic summary of the etching observed when cellulose fibres are subjected to a strong acid hydrolysis. Green labelling corresponds to the crystalline core that is left untouched and yield the cellulose nanocrystals at the end of the hydrolysis. Red corresponds to the complete etching of the lesser organised pseudo-amorphous regions of the fibre. (right) Transmission electron microscopy picture of a cellulose nanocrystals suspension dispersed in toluene without negative staining, highlighting that cellulose nanocrystals are formed of several laterally packed individual crystallites.

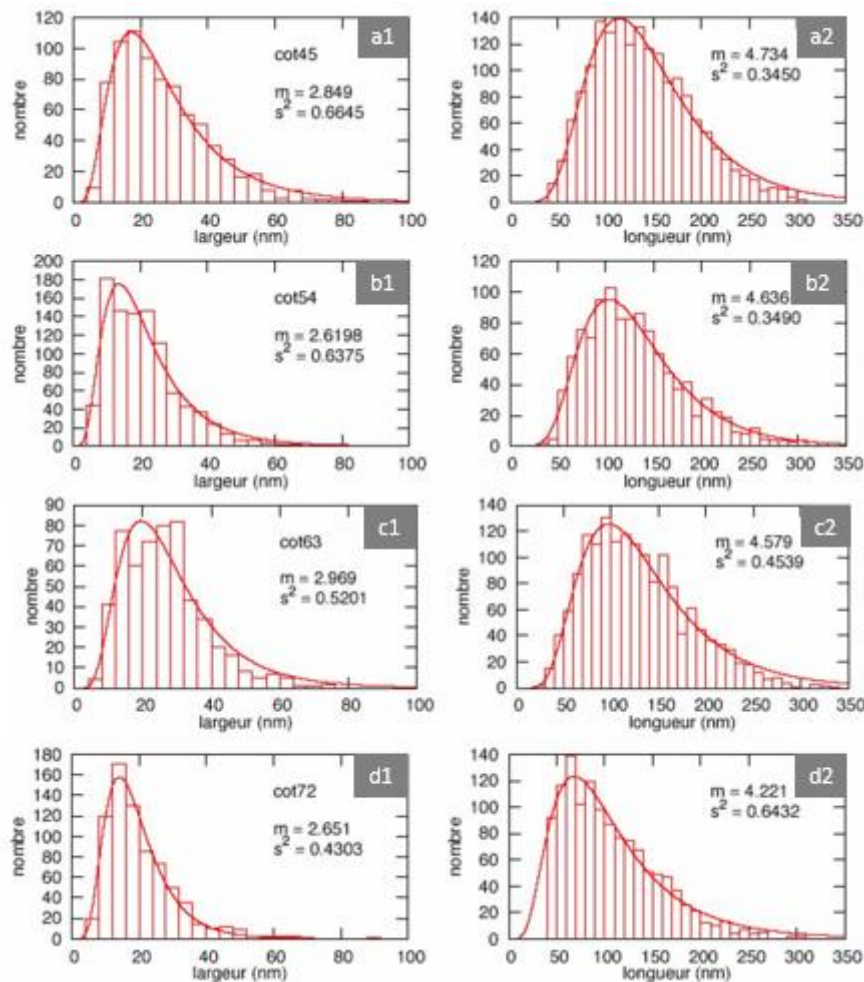
### 1.6.2. Parameters influencing the shape and size of CNCs

Several parameters have a direct influence on the pace at which the hydrolysis takes place. We already underlined the reaction time as one of them. Temperature also plays a major role, as it both influences the diffusion coefficient of  $H^+$  ions through the Stokes-Einstein equation and the kinetics of the glycosidic bond breakage (Elazzouzi-Hafraoui et al. 2008). Elazzouzi et al. led a systematic study on cotton CNCs in which they only varied the hydrolysis temperature (45, 54, 63 and 72 °C) while fixing all other parameters. They report rods shortening and thinning with increasing temperature from 141 to 105 nm in length and from 27 to 21 nm in width. Experimental histograms and log-normal distributions fittings are given in Figure 21.

Another obvious parameter is the amount of acid per gram of cellulose in the medium. The more  $H^+$  ions in the medium, the more likely it is for one to diffuse to a given glycosidic bond (Elazzouzi 2006). As a general rule, the longer the hydrolysis, the hotter the medium, or the more concentrated the acid and the shorter and thinner the resulting colloidal rods.



The initial source of cellulose also has a direct influence on the resulting colloidal objects. Different cellulose sources correspond to different fibre morphologies, and the previous section on supramolecular assemblies of cellulose already highlighted the relationship between the shape of cellulose fibres and CNCs. Elazzouzi et al. (Elazzouzi-Hafraoui et al. 2008) explored the influence of the cellulose source in between cotton, wood, beetroot and tunicate while keeping all other hydrolysis parameters fixed. Results presented in Figure 21 show really different resulting colloidal objects: tunicate cellulose that presents fibres with a very small amount of defects, leads to splinter-shape colloids with big aspect ratios, whose length is on the order of a micron and its width of tens of nanometres (Elazzouzi 2006). Cellulose fibres from cotton and wood are typically less regular, leading to shorter nano-rods whose lengths range approximately at 100 nm and whose widths vary from 10 to 20 nm.



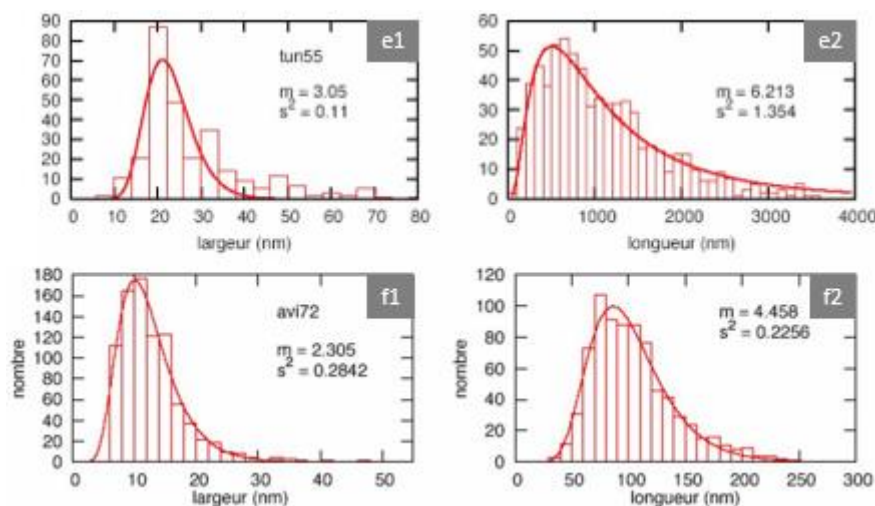


Figure 21 : Histograms and log-normal fitting of the width and length distributions of CNCs from different sources and hydrolysis temperature established from TEM measurements. #1 corresponds to width measurements and #2 corresponds to length measurements. a-b-c-d) Cotton CNCs hydrolysed respectively at 45, 54, 63 and 72 °C. e) Tunicate CNCs hydrolysed at 55 °C. f) Avicel™ wood CNCs hydrolysed at 72 °C.  $m$  and  $s^2$  are respectively the mean and standard deviation of the log-normal fitting. Adapted from Elazzouzi's PhD manuscript, p.90.

### 1.6.3. Polydispersity of CNCs and its statistical description

The polydispersity in CNCs size is high, cotton being more polydisperse than tunicate. On the example of cotton CNCs, while the average length at  $T = 63$  °C is 128 nm, objects typically range from 50 to 300 nm in length and from 5 to 50 nm in width. This property is intrinsically due to the hydrolysis mechanism that takes place at varying positions along the fibre. People typically choose lognormal distributions to describe the polydispersity of CNCs in both length and width. A mathematical explanation for this lognormal distribution has been proposed by Epstein, explaining that particle size distributions resulting from independent and random breakages asymptotically converge to log-normal distributions according to the central limit theorem (Epstein 1947).

### 1.6.4. Colloidal stability of CNCs – influence of the type of acid

This section is deeply related to the introduction made on colloidal systems. We invite the reader to refer to this section for colloidal considerations. The type of acid used during the acid hydrolysis of the fibres is the key parameter that determines the stability of the colloids formed, depending on its ability to create surface charges. While weak acids are not strong enough to depolymerise significantly cellulose macromolecules (Habibi, Lucia, and Rojas 2010), numerous strong acids such as HCl (Araki et al. 1998), HBr (Sadeghifar et al. 2011),  $H_3PO_4$  (Camarero Espinosa et al. 2013),  $H_2SO_4$  (Revol et al. 1992; Elazzouzi-Hafraoui et al. 2008),



citric acid (Yu et al. 2019), maleic acid (Wang et al. 2017) and oxalic acid (Chen et al. 2016) have been successfully used to yield colloidal objects.

In this work we use  $\text{H}_2\text{SO}_4$ , one of the most widely used acid for CNC making.  $\text{H}^+$  ions are capable of depolymerising the glycosidic bond as discussed in previous sections, but sulphuric acid also replaces some -OH groups by half ester sulphate groups  $-\text{OSO}_3\text{H}$  on the surface of cellulose. These groups are largely deprotonated in water, leading to a spontaneous electrostatic stabilisation of the colloids formed. To yield fully deprotonated half ester sulphate groups, it is possible to perform an ion exchange with *e.g.* NaOH to yield  $-\text{OSO}_3\text{Na}$  groups, Na being more likely to be a free counter-ion in suspension. There are two main methods to measure the grafting density of half ester sulphate groups onto cellulose: elemental analysis of the sulphur content of the dry mass of the suspension, sulphur being only present in the form of  $-\text{OSO}_3\text{H}$  functional groups, and conductometric titration of the  $\text{H}^+$  ions in suspension. The proportion of grafted glucose units is found to be around 4% in classical hydrolysis conditions (63 °C, 65 wt.%  $\text{H}_2\text{SO}_4$ , 30 min). Alternatively, measuring the zeta potential of the suspension provides qualitative information on the density of charged groups on the surface of CNCs. An important feature of half ester sulphate groups on CNCs is their partial or total removal occurring upon heat treatment, catalysed by the presence of  $\text{H}^+$  ions and thermally activated above *ca.* 60 °C (Camarero Espinosa et al. 2013; Beck and Bouchard 2014; Vanderfleet et al. 2019).

While we have chosen to work with  $\text{H}_2\text{SO}_4$ -hydrolysed CNCs because the size and shape of the resulting objects have been extensively characterised (Elazzouzi-Hafraoui et al. 2008), results are likely transposable to other acid-hydrolysed CNCs.

### 1.6.5. Order of magnitude of colloidal interactions in CNC suspensions

$\text{H}_2\text{SO}_4$ -hydrolysed and TEMPO-oxidised CNCs do not immediately flocculate thanks to the presence of respectively half-ester sulphate groups and carboxylate groups that are negatively charged on the surface of CNCs and induce a strong electrostatic repulsion between CNCs. This is the only repulsive interaction in the system, and when an excess of electrolyte is added in the suspension (typically above 30 to 50 mM for monovalent ions), CNCs flocculate and either gel or sediment at the bottom of the vial (Araki, Wada, and Kuga 2001).

In the absence of added salt, Israelachvili's simplification  $\kappa^{-1} = \frac{0.304}{\sqrt{I}}$  cannot be used and one needs to use the SLO model to assess the characteristic range of electrostatic repulsion in water. Dong et al. found  $\kappa^{-1} \sim 6$  to 9 nm, depending on CNC concentration (Dong and Gray

1997). This value may be underestimated as Elazzouzi (Elazzouzi-Hafraoui et al. 2008), reasoning on the volume fraction at kinetic arrest in a Wigner-glass type gel, deduces a CNC interparticle distance of 33 nm. Assuming close contact between CNCs at kinetic arrest of Wigner glass-type, that would correspond to an electric double layer of  $\kappa^{-1} \sim 16.5$  nm in absence of added salt.

An interesting experiment to assess how repulsive electrostatic interactions compare with attractive Van der Waals forces is to add increasing amounts of salt to the suspension and observe when the type of kinetic arrest is modified from a Wigner glass jamming to a percolation-like behaviour. This transition in the kinetic arrest mechanism has been observed both by Capron's group (Peddireddy et al. 2016), and indirectly by Frka-Petesic et al. (Private\_communication) at  $[\text{NaCl}]_{\text{threshold}} \sim 25 - 30$  mM. At the threshold value, the range of the electrostatic interactions compares with the range of attractive interactions. Using Israelachvili's simplified expression of  $\kappa^{-1}$  for monovalent ions suspensions, we have:

$$\kappa^{-1} = \frac{0.304}{\sqrt{25 \cdot 10^{-3}}} \text{ nm} = 6.1 \text{ nm}$$

By comparing this value with the range of the electrostatic repulsion of neat CNCs, one can conclude that neat CNC suspensions are colloidal systems dominated by repulsive interactions. The large effective volume taken by CNCs owing to their electrostatic double-layer can therefore be a problem to reach concentrations compatible with the self-assembly. Several groups are working with partially desulphated CNCs or salted CNC suspensions (Parker et al. 2016; Zhao et al. 2019; Vanderfleet et al. 2019) to be closer to a balance between repulsive and attractive interactions, lower the width of the electrical double-layer and thus expand the accessible working domain of aqueous CNC suspensions.

Different colloidal systems involving the steric stabilisation of CNCs have also been prepared in the literature, bound to the objective of dispersing CNCs in non-aqueous solvents. These systems are presented in the state of the art of chapter 3.

#### **1.6.6. Self-assembling properties of CNCs in water**

Cotton CNCs are chiral rod-like nanoparticles of aspect ratios  $\frac{L}{D}$  on the order of 10 to 20. According to Onsager's theory, they are expected to self-assemble into cholesteric liquid crystalline phases above a threshold concentration that depends on the aspect ratio. Dong et al. (Dong et al. 1996) described their self-assembly behaviour in pure water and in the presence of

ions, reproduced in Figure 22. In pure water, the isotropic phase starts self-assembling into a cholesteric phase at approximately 5 wt.%. In between 4.6 and 13.1 wt.%, the cholesteric phase and the isotropic phase are in equilibrium in the biphasic domain. Throughout the biphasic domain, both the isotropic and the anisotropic phase have fixed compositions, respectively the volume fractions  $\varphi_i$  and  $\varphi_a$  from the SLO model. The higher the overall concentration of CNCs in the biphasic domain, the lower the fraction of isotropic phase and the bigger the fraction of anisotropic phase in suspension following a quasi-linear trend. The slight deviation to linearity at higher CNC concentrations is due to the contribution of the counter-ion release from the charged groups on the surface of CNCs to the ionic strength of the medium (see the influence of ions on the phase diagram below). Above 13 wt.%, the suspension is fully cholesteric. Because the anisotropic phase is slightly more concentrated than the isotropic phase, it is also slightly denser, leading to a natural phase-separation mechanism by gravity means with the isotropic phase located at the top and the anisotropic phase at the bottom of the vial. The separation between the two phases is clear by eye from the optical activity of the anisotropic phase. This phase-separation process can take weeks or months in aqueous suspensions. Elazzouzi reports mild centrifugation at 2000 g and heating at 60 °C to speed up the phase separation (Elazzouzi 2006).

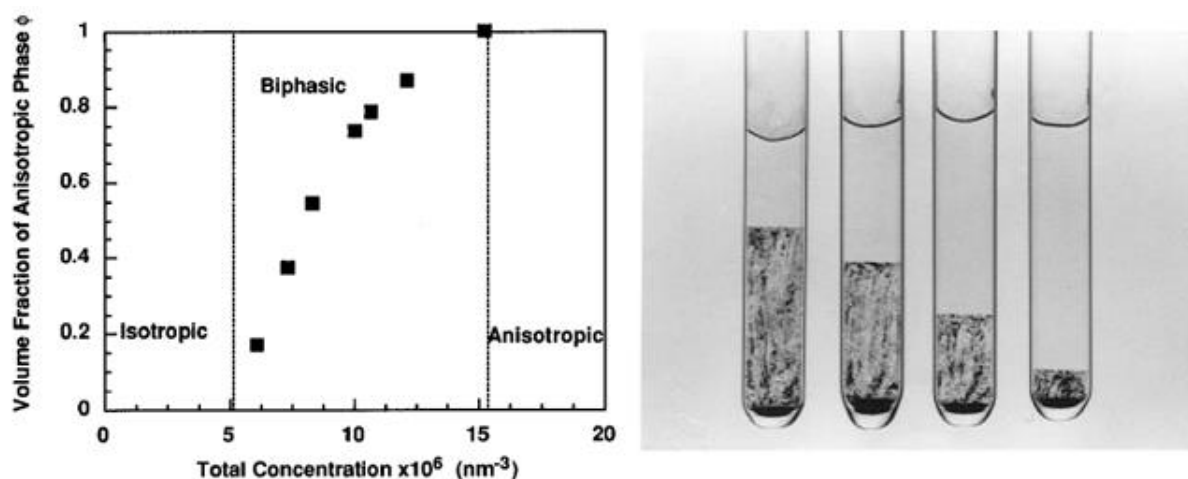


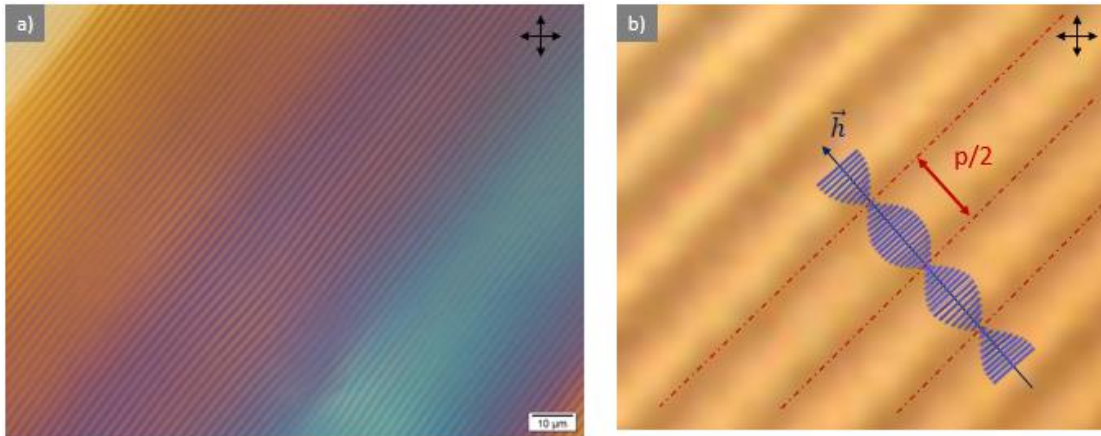
Figure 22 : (left) Phase diagram of a CNC suspension in pure water. The uncommon x-axis unit corresponds exactly to the classical volume fraction unit. (right) Optical appearance of biphasic suspensions of CNCs in pure water at 8.8, 7.8, 6.9 and 5.9 wt.% in concentration from left to right. Reproduced from Dong et al, Langmuir 1996, 12, 2076-2082.

#### 1.6.6.1. Characterising the presence of the cholesteric phase

While a characteristic texture of the cholesteric phase is already observable by eye, the presence of a cholesteric phase is also revealed by polarised optical microscopy in the form of

a “fingerprint pattern” reproduced in Figure 23. This pattern comes from the regular helical arrangement of cellulose nanocrystals within the cholesteric phase. When the helical axis is parallel to the observation plane, the helical assembly of CNCs causes along the helical axis a modulation of the local optical indices perceived by the light propagating through. The regions where the CNCs point out of the plane have the same optical index  $n_o$  in any direction within the plane. The projected birefringent is null and they appear dark between cross-polarisers. In contrast, the region of the helical assembly where the CNCs are within the observation plane present two optical indices,  $n_o$  in the helix direction and  $n_e$  perpendicular to it. The observation of these structures between cross polarisers causes a phase shift between the two polarisations, resulting most of the time in an elliptically polarised light that is partially transmitted between cross-polarisers, unless the helix axis is aligned with the polarisers optical axis.

While the distance between two dark (or light) stripes equals to half the pitch when the helix axis is perpendicular to incoming light, it is not accurate anymore if the helix axis is oblique to incoming light due to a projection bias. Polarised optical microscopy is therefore the easiest characterisation tool to assess the pitch value of a CNC suspension, but is an unreliable one unless the helix axis lays strictly in the plane of observation. Using objectives with long working distances helps reducing this projection bias in measurements as helices whose axes make a large angle with respect to the plane of observation will be blurred compared to the well-aligned ones. Also the displacement of the focal plane by a quantity  $z$  can be used to estimate the tilt  $\theta$  of a domain, as it results in the lateral displacement of the fingerprint pattern.



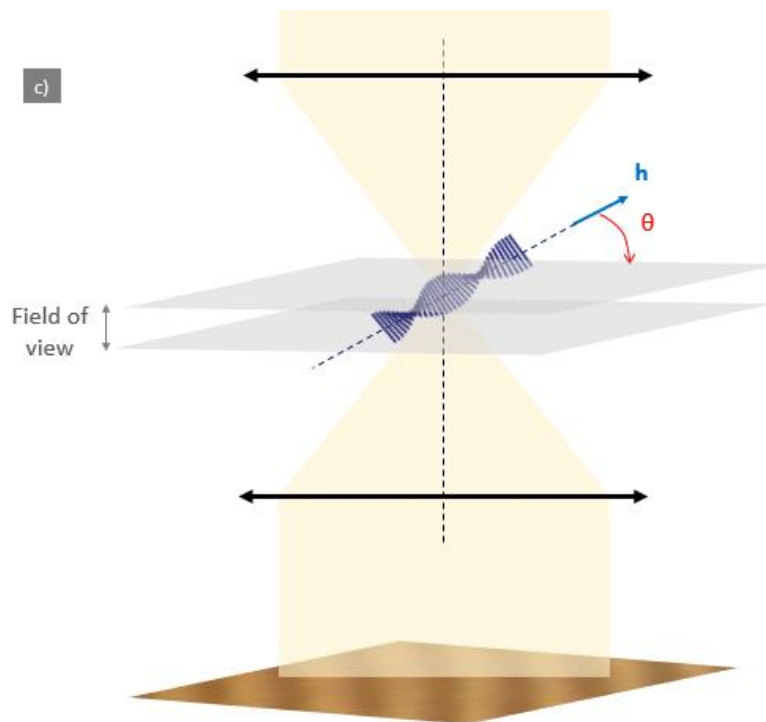


Figure 23 : a) Fingerprint pattern texture characteristic of a cholesteric phase observed by polarised optical microscopy on a suspension of cotton CNCs. b) Schematic superimposition of the helical configuration on a fingerprint pattern. c) Schematic view of the origin of the projection bias in polarised optical microscopy: a helix oriented obliquely still yields a fingerprint pattern.

#### 1.6.6.2. Parameters influencing the phase diagram of CNCs

Any parameter influencing the electrostatic interactions or the aspect ratio of the particles will in turn influence the phase diagram.

Adding an electrolyte to the suspension screens the electrostatic interaction, leading to the decrease of both the effective diameter and the excluded volume of the nano-rods. Dong et al report an electrolyte addition of 2 mM to strongly increase the onset concentration for the anisotropic phase from 4.5 to 9 wt.% and find good agreement with the SLO theory reproduced in Figure 24. The nature of the electrolyte has no influence on that effect. They also measure a strong decrease of the pitch value in suspension following electrolyte addition. This trend indicates stronger chiral interactions when the effective diameter of CNCs decreases. The current interpretation suggested by Araki and Kuga (Araki and Kuga 2001) to explain this experimental fact is to consider that the electrostatic repulsion screens partially the chiral interaction between CNCs, leading to an apparently less chiral object when the Debye layer is big enough. It is difficult to conclude on this question because the origin of chirality in cellulose nanocrystals itself remains an opened question to date. Two models have been suggested, one involving a helical distribution of the surface charges of CNCs (Revol et al. 1992) and the other

one based on an intrinsic geometrical twist in the CNC structure (Revol et al. 1992; Orts et al. 1998). Finally, exchanging the counter-ion of the surface groups of CNCs has an influence on the phase diagram: the bigger the counter-ion, the higher the onset concentration of the cholesteric phase.

The phase diagram is also modified by the morphology of the crystals, *i.e.* is dependent on the source of cellulose and the hydrolysis conditions used. Elazzouzi has compared the phase diagram of cotton, tunicate and wood CNCs at different hydrolysis temperatures and the result is reproduced in Figure 24e) (Elazzouzi 2006). Comparing cotton and tunicate CNCs under the light of their morphologies given in Figure 21, one observes that the higher aspect ratio of tunicate CNCs triggers their auto-organisation at much lower concentrations than cotton CNCs. Hydrolysing at higher temperatures also contributes to lower the aspect ratio of the particles, leading to their self-assembly at higher concentrations.

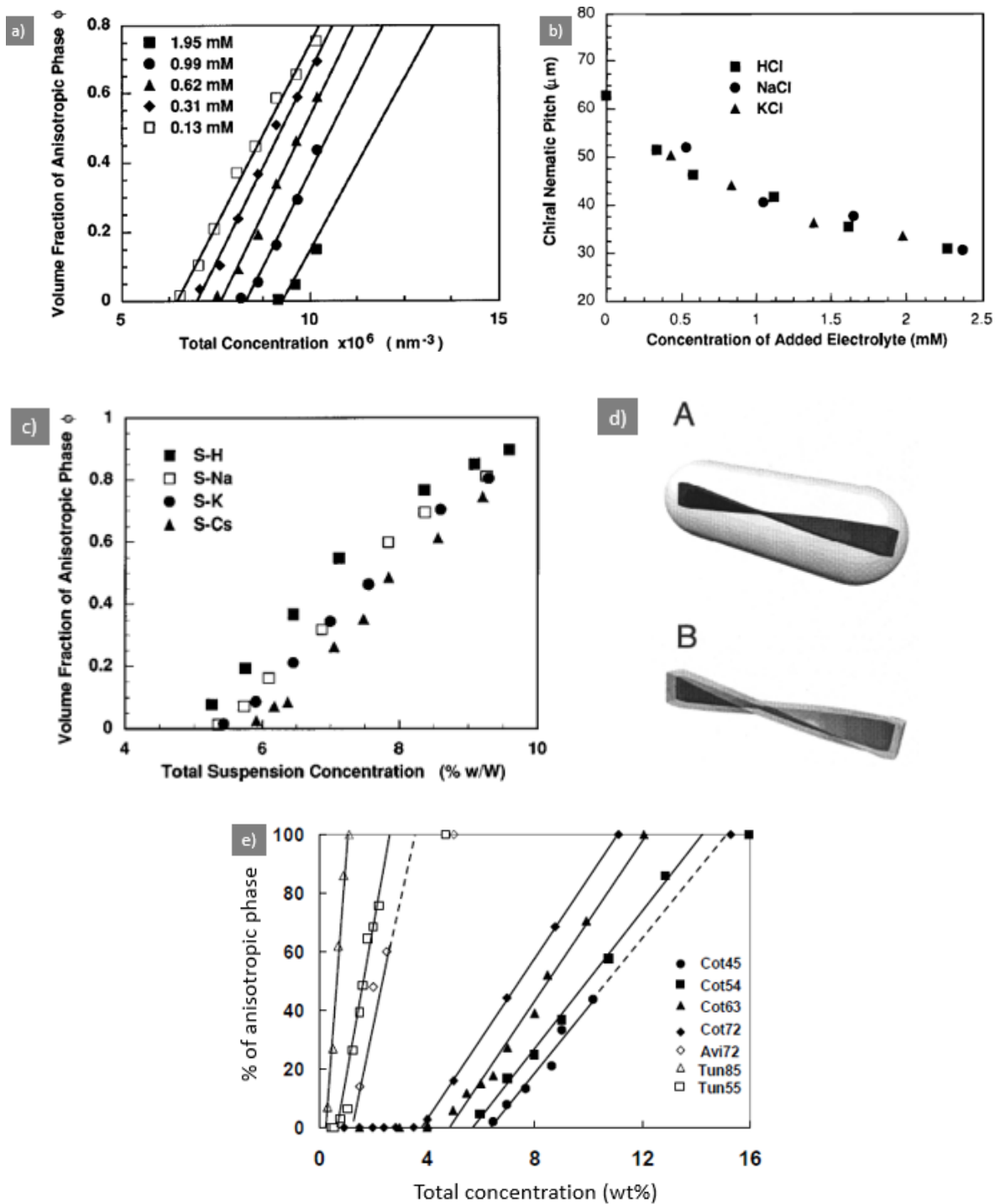


Figure 24 : a) Influence of monovalent electrolyte addition (NaCl) addition on the phase diagram of CNC suspensions. b) Influence of monovalent electrolyte addition on the chiral nematic pitch value of a CNC suspension at 8.5 wt.% concentration. Adapted from Dong et al, *Langmuir* 1996, 12, 2076-2082. c) Influence of the size of CNC counter-ion on the phase diagram of CNC suspensions. Adapted from Dong et al, *Langmuir* 1997, 13, 2404-2409. d) Influence of the screening of the electrostatic interaction on the apparent shape of cellulose nanocrystals. Adapted from Araki and Kuga, *Langmuir* 2001, 17, 4493-4496. e) Influence of the source of cellulose and hydrolysis conditions on the phase diagram of CNCs. Reproduced from Elazzouzi's PhD manuscript, p.150.

### ***1.6.6.3. Phase-separation mechanism: Nucleation/growth versus spinodal decomposition***

How does the anisotropic phase separate from the isotropic phase once super-saturation is observed in suspension? Two main mechanisms can generally take place in this case, namely nucleation-and-growth or spinodal decomposition. In a nucleation-and-growth mechanism, germs of the anisotropic phase spontaneously nucleate at random locations of the isotropic phase owing to super-saturation. These germs try to grow in size because of the volume energy gain of being anisotropic rather than isotropic at this concentration, but they also have an interface energy cost. Whether growth will be observed depends on the balance between the surface energy cost and the volume energy gain, which ultimately depends on the size of the nuclei. In a spinodal decomposition mechanism, the anisotropic phase separates from the isotropic phase due to thermodynamical fluctuations of concentration to form a bi-continuous phase. The longer the phase separation, the bigger the relative size of the isotropic and anisotropic domains of the bi-continuous phase.

Van Bruggen et al (Van Bruggen, Dhont, and Lekkerkerker 1999) evidenced that both mechanisms take place in colloidal suspensions of hard rods, on the example of suspensions of sterically stabilised boehmite rods of aspect ratio 14 similar to CNCs by static light scattering and polarised optical microscopy. Nucleation and growth takes place at lower concentrations whereas spinodal decomposition takes place at higher concentrations. The crossover volume fraction is measured around 20%. Different phase separation mechanisms may take place when suspensions are super-saturated nematic phases (*e.g.* shear-aligned) (Lettinga et al. 2006; Lettinga et al. 2005).

In CNC suspensions, Elazzouzi (Elazzouzi 2006) also observed nucleation and growth to take place at lower concentrations whereas spinodal decomposition is observed at higher concentrations. A recent work from Bonan et al (Zhu et al. 2020) suggests that the same scenario takes place during the evaporation induced self-assembly of a CNC suspension. The authors use hyperspectral imaging to locate defects in the final film, which they interpret as residual tactoids from the early nucleation-and-growth process before spinodal decomposition takes place at higher concentration. Tactoids have not fully reoriented in the anchoring direction of the film whereas helices grown by spinodal decomposition reorient completely, leading, after complete solvent evaporation, to the presence of distorted tactoids embedded in a continuous cholesteric matrix.



## 1.7. Materials

Recent years have shown a renewed interest for bio-sourced materials, and materials made of cellulosic derivatives are no exception to it. Two different approaches have been considered: top-down approaches in which existing materials are transformed to gain new properties and bottom-up approaches in which ultra-structures are rebuilt for targeted applications. Before we develop bottom-up approaches similar to our work, let us mention a few top-down results. Among the most remarkable works on cellulosic materials, Li et al (Li et al. 2016) obtained a transparent wood-like material by delignification and impregnation of wood with a monomer mixture whose refractive index matches wood before polymerising. Huang et al (Huang et al. 2019) proved possible to imprint the transparent wood surface with complex motifs. The relatively simple process forecast great applications in the building sector. Li et al (Li et al. 2019) delignified and compressed mechanically wood to yield a complex mesoporosity inducing a strong mid-infrared light emission to produce a radiative cooling material of Figure 25b) for the building sector.

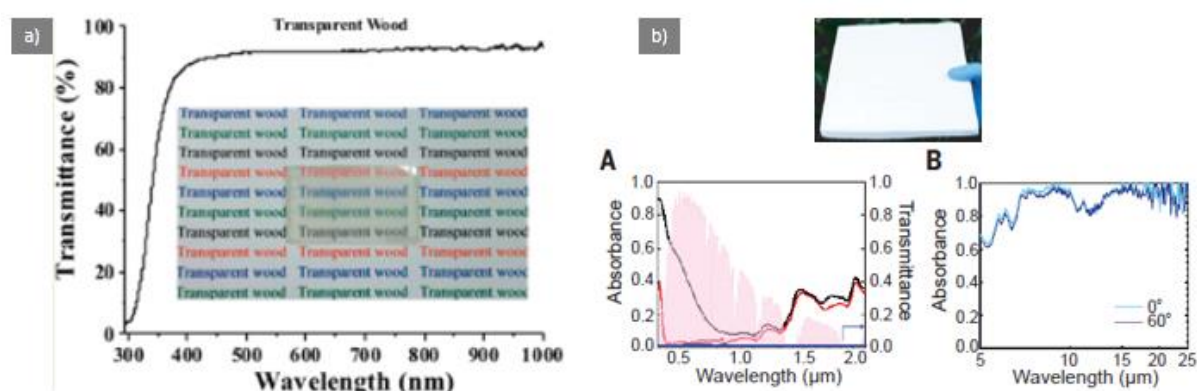


Figure 25 : a) Transparent delignified wood material filled with an index-matching polymer. Adapted from Li et al, *Biomacromolecules* 2016. c) A radiative cooling wood-based material with its visible and infrared absorption spectra, compared to normal wood. Adapted from Li et al, *Science* 2019, 364, 760-763.

Many works have been published on making materials out of CNCs. This section does not aim at reviewing extensively the literature but rather present the main strategies imagined to yield photonic materials using CNCs as building blocks. Major contributions to the field will be presented, along with several limitations in composite materials making out of cellulose nanocrystals building blocks. Some non-photonic materials whose elaboration strategies are relevant in the scope of this work will also be presented.

## 1.7.1. Photonic materials made of cholesteric CNCs

### 1.7.1.1. *Controlled dryings*

Cholesteric CNCs are able to produce an iridescent optical response when their pitch is on the order of the wavelength of visible light, making them interesting building blocks for photonic materials design, *e.g.* diffraction gratings and wavelength-selective reflectors (Almeida et al. 2018). However, the cholesteric pitch of non-salted aqueous CNC suspensions is on the order of tens of microns, decreased by electrolyte addition but still bigger than the wavelength of visible light. For this reason, literature's most pursued strategy to yield photonic materials out of cholesteric CNCs consists in the controlled drying of an aqueous CNC suspension to yield a near-100% cellulose dried film. The evaporation of water induces a mechanical compression on cholesteric domains that may lead to a pitch value in the 150-250 nm range, matching Bragg conditions at normal incidence. The efficiency of water evaporation on the compression of the cholesteric pitch is non-trivial, most efficient when cholesteric domains have planar anchoring for reasons developed in more details in the State of the art: Dryings of CNC suspensions of chapter 6.

#### 1.7.1.1.1. *Dried films with uniform tunable reflected colours*

In this section, we aim to present some results summarised in Figure 26 that have been obtained using a controlled drying of aqueous CNC suspensions strategy. Saha et al., Yao et al., Zhao et al and Frka-Petesic et al. (Zhao et al. 2019; Yao et al. 2017; Frka-Petesic, Guidetti, et al. 2017; Saha and Davis 2018) all obtained uniform reflectance of the dried CNC films by reorienting CNC cholesteric domains in planar anchoring prior to drying, as highlighted by the SEM cross-section characterisation presented in their articles (the data from Yao et al. is reproduced in Figure 26). Additionally, Frka-Petesic et al. used a magnet to tilt the favoured orientation of cholesteric helices, inducing in turn an angular shift in the optical response of the dried films.

Tuning the pitch values of the final films to choose in turn the iridescent colour reflected uniformly by the dried film has been performed by different means. Yao et al. added varying amounts of a non-volatile compound (polyethyleneglycol in their study, PEG) that intercalate in between CNCs to inducing a pitch increase, corresponding to reflectance in the blue, green or red. Zhao et al. adjusted the salt concentration of their starting suspension to induce pitch control in the final films and reflectance in the blue, green and red, taking advantage of pitch reduction following electrolyte addition already shown by Dong et al. (Dong et al. 1996).

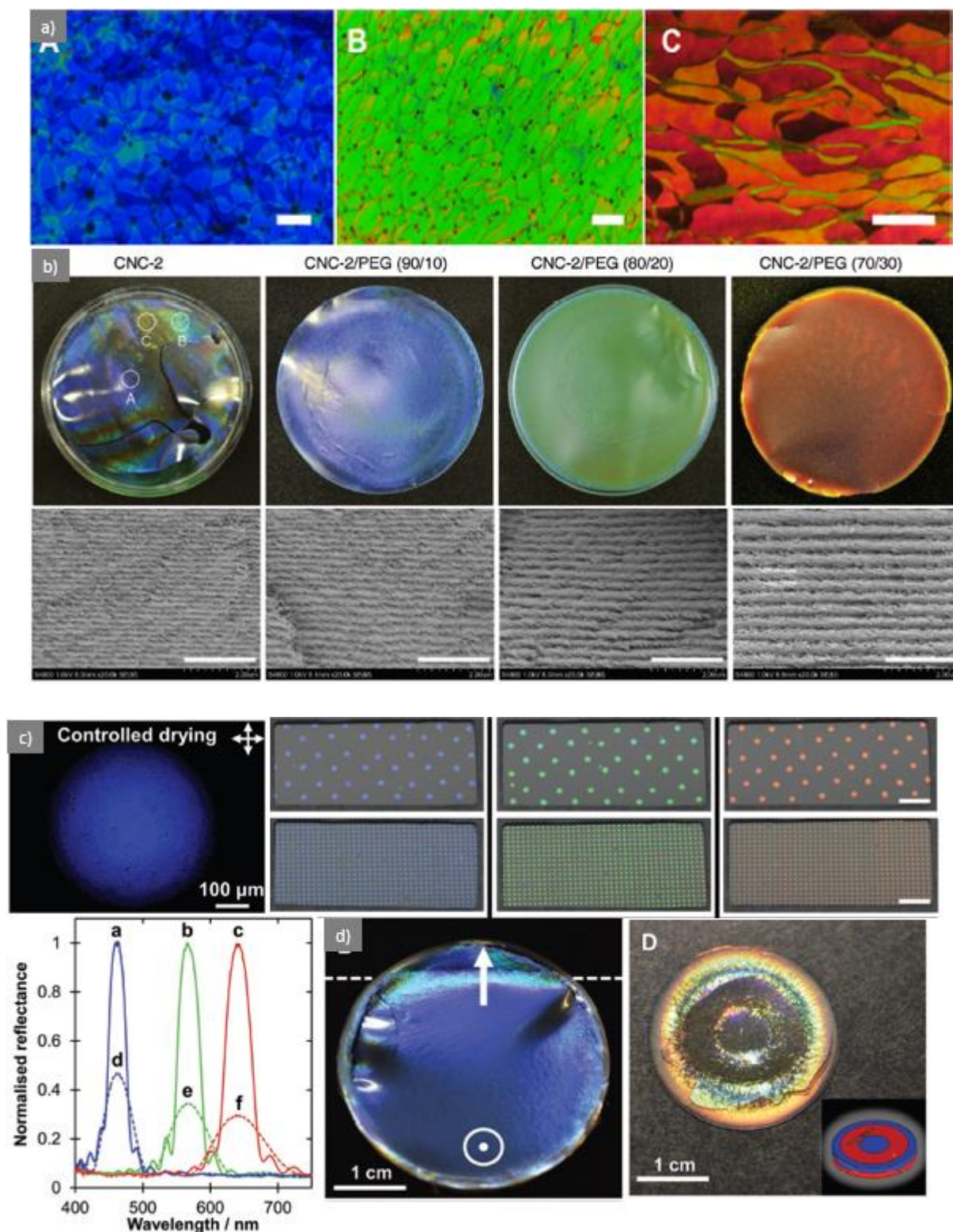


Figure 26 : Examples of uniform photonic CNC dried films from the literature. a) Blue, green and red textures obtained in polarised optical microscopy from drying CNC films with planar anchoring. Adapted from Saha et al ACS Appl. Nano Mater. 2018, 5, 2175-2183. Scales bars are 50  $\mu\text{m}$ . b) Neat CNC and CNC-PEG composite dried films showing the increase in colour uniformity and redshifting provided by PEG addition in SEM cross-section. Scale bars are 2  $\mu\text{m}$ . Adapted from Yao et al, Adv. Mater. 2017, 1701323. c) Slowly-dried CNC dried sessile droplets showing a uniform structural colour. Unlabelled scale bar is 5 mm. LCP reflectance spectra of 10  $\mu\text{m}$  (plain lines) and 6  $\mu\text{m}$  (dashed lines)

*thickness films. Adapted from Zhao et al Adv. Funct. Mater. 2018, 1804531. d) Uniform and patterned CNC films dried respectively under a uniform and patterned magnetic field alignment. Adapted from Frka-Petesic et al Adv. Mater. 2017, 1701469.*

#### 1.7.1.1.2. *On the maximum reflectance of CNC films*

Zhao et al show that a film thickness of 10 microns with a pitch value in the visible range is sufficient to yield 100% reflectance of the left circular polarisation of light whereas 6  $\mu\text{m}$  thickness only leads to *ca.* 50% reflectance (Figure 26c). The thickness required to yield 100% reflectance corresponds to a given number of layers in the cholesteric assembly, which explains why this thickness increases with the pitch value.

An interesting work of Wu et al. (Wu et al. 2016) showed that the selective reflection of the left circular polarisation of light by cholesteric CNCs, which corresponds to 50% of total light reflection, can be circumvented by smart material design. The authors sandwiched a layer of aligned polyamide-6 of controlled thickness in between two dried CNC films. The PA-6 layer acts as a half-wave retarder layer that changes the polarisation of light exiting the first CNC layer from RCP to LCP before it enters the second CNC film. As a result, LCP is massively reflected by the first CNC film and “RCP” is reflected by the second CNC film, yielding a cholesteric CNC-based material whose reflectivity is higher than 50%.

#### 1.7.1.1.3. *Swelling properties in humid environments*

These photonic dried films show interesting sensing properties because of their ability to swell in humid environments evidenced by an early work of Zhang et al. (Zhang et al. 2013). When exposed to increasing relative humidity, the films swell due to water adsorption. Swelling takes place not only at the surface but also in the volume of the film, indicating accessible film porosity for water molecules and yielding a homogeneous increase of the pitch value throughout the film thickness. The pitch increase results in a redshift of the reflected colour presented in Figure 27, studied in particular by Zhao et al. (Zhao et al. 2019) and Yao et al. (Yao et al. 2017). Swelling is reversible and yield no visible difference in the reflectance of the films upon cycling respectively 5 and 10 times. Water adsorption and desorption occurs over the course of 5-15 seconds, corresponding to a quite responsive system. Yao et al. additionally show that CNC dried film containing PEG have increased water adsorption compared to neat CNC films, indicating that the PEG surface is accessible to water adsorption in the dried films as well. In a CNC film containing 30 wt.% PEG, water uptake up to 70 wt.% is observed in a 100% relative humidity environment, which is an important effect.



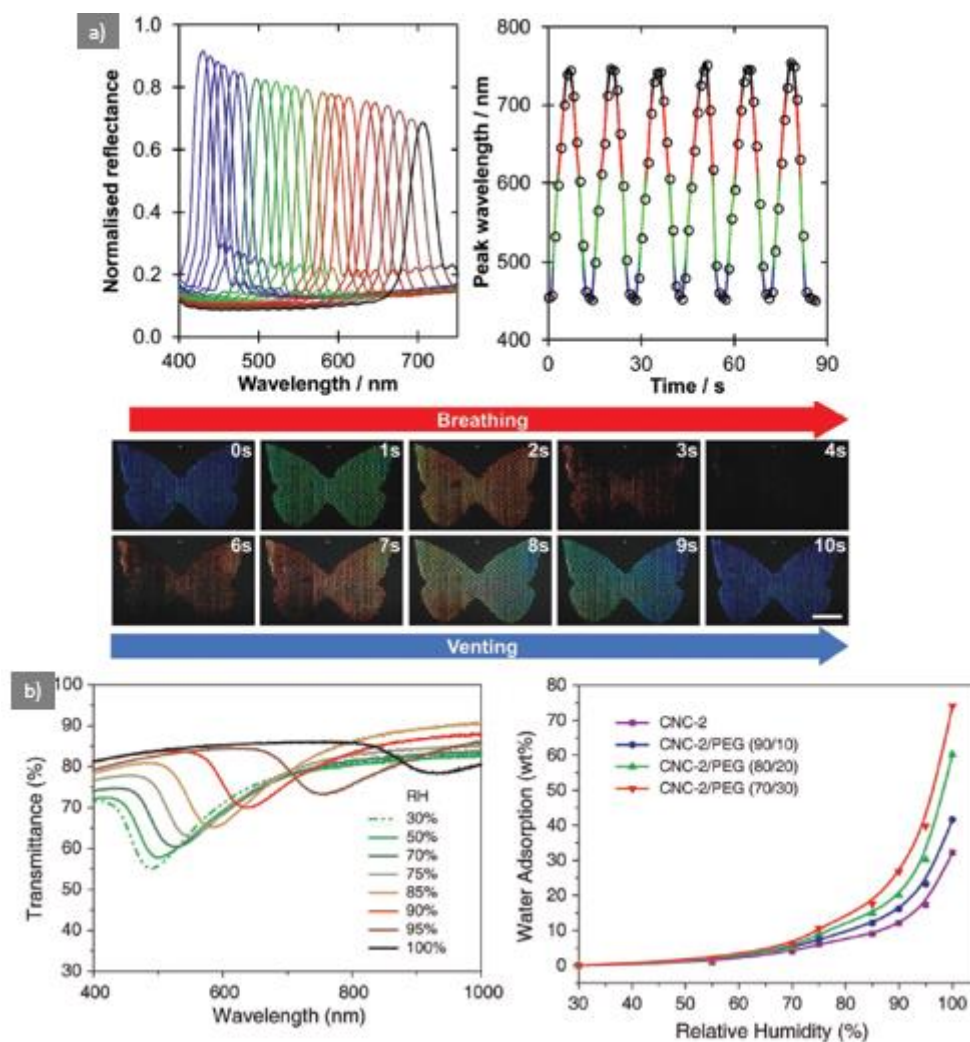


Figure 27 : Swelling properties of dried CNC films when exposed to a humid environment. a) (top left) Reflectance of a CNC dried film 10  $\mu\text{m}$  thick when exposed to relative humidity ranging from 0 to 95%. (top right) Reflectance peak shift of a dried CNC film subjected to rapid relative humidity change (between 0 and 100%). (bottom) Reversible redshift of a CNC dried film pattern exposed to the moisture of exhaled breath. Adapted from Zhao et al Adv. Funct. Mater. 2018, 1804531. b) (left) Evolution of the transmissivity of a dried CNC/PEG film 80/20 exposed to relative humidity changes. (right) Evolution of water absorption as a function of the PEG content of the CNC film. Adapted from Yao et al, Adv. Mater. 2017, 1701323.

#### 1.7.1.1.4. Mechanical properties of the dried films

If we consider the dried CNC films from a mechanical point of view, these are essentially made of stiff rods that have been brought at close contact by drying. Just like in paper, the percolation of the rods makes the network very stiff, but also very brittle upon deformation. While this is one of the main drawbacks of such materials, some authors have tried to improve the mechanical properties of the dried films by different means. Yao et al. (Yao et al. 2017) show that PEG addition brings flexibility to the film, diminishing the stress exerted on the film by mechanical strain. The authors however limited the amount of PEG they added to the

material, as PEG simultaneously redshifts the iridescent optical response of the film. Adding more than 30 wt.% of PEG corresponds to an optical response in the infrared region. Guidetti et al. (Guidetti et al. 2016) added a zwitterionic surfactant dimethylmyristylammoniopropyl sulphate (DMAPS) in a CNC suspension to yield flexible dried films. Zhao et al. (Zhao et al. 2019) and Espinha et al. (Espinha et al. 2016) chose to use polymer supportive layers to improve the mechanical properties of dried CNC films. Zhao et al. deposited dried CNC films on both polydimethylsiloxane (PDMS) and adhesive tape, providing flexibility to the final materials while maintaining photonic properties. Espinha et al. sandwiched a dried CNC film in between two cross-linked elastomer layers to reinforce mechanically the dried CNC film. The flexibility provided by these layers naturally releases the deformations exerted on the CNC layer, therefore providing shape-memory effects to the final material. The photonic properties are mostly maintained with a slight redshift from dried film to sandwich material that is interpreted as the effect of the hydrophilic polymer impregnation of the film.

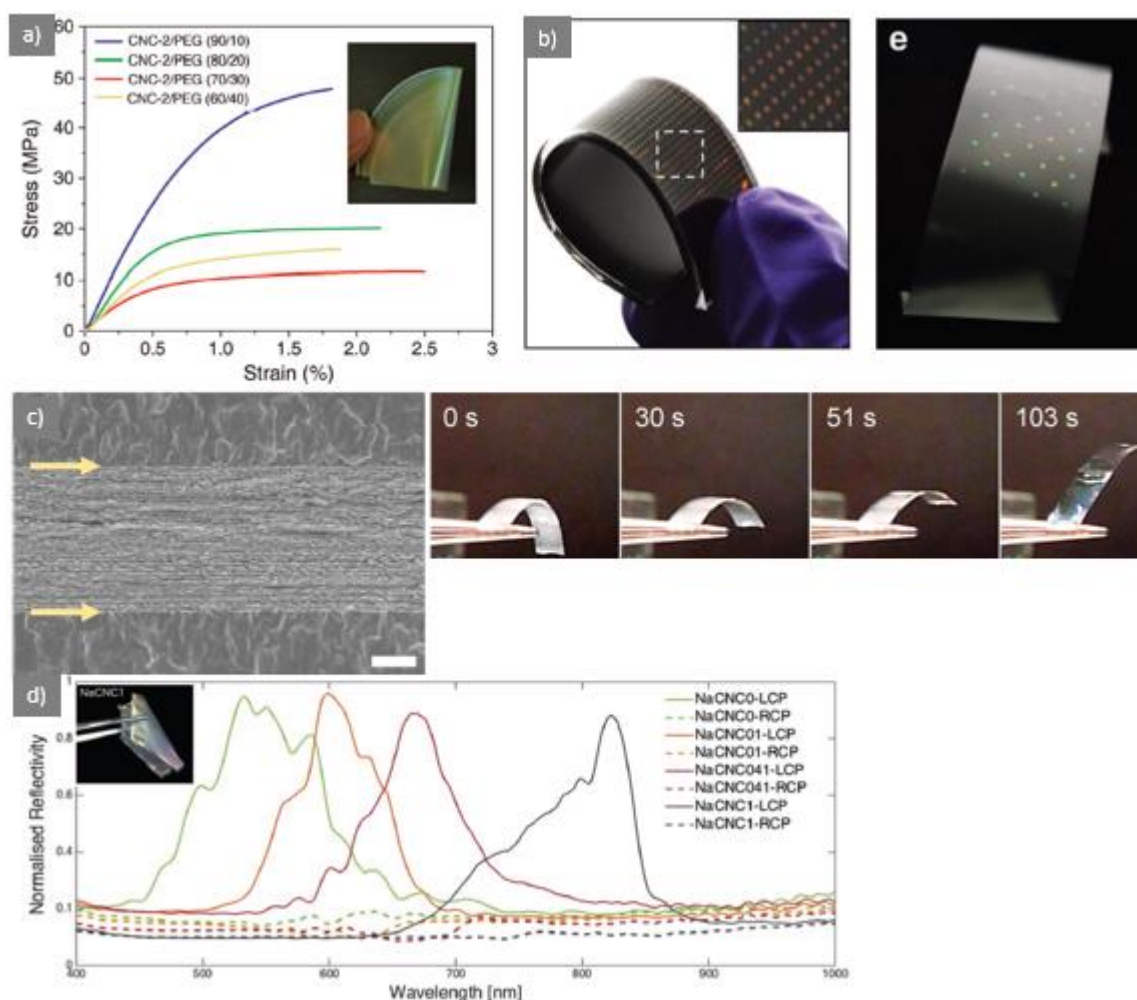


Figure 28 : a) Influence of PEG content on the mechanical properties of dried CNC films. Inset: flexibility of the PEG film. Adapted from Yao et al, *Adv. Mater.* 2017, 1701323. b) Deposition of

photonic dried CNC films on a supportive PDMS layer and adhesive tape. Adapted from Zhao et al *Adv. Funct. Mater.* 2018, 1804531. c) SEM characterisation of dried CNC film sandwiched by two polymer layers of poly(dodecanediol-co-citrate) and associated shape-memory properties. Adapted from Espinha et al, *ACS. Appl. Mat. Interfaces* 2016, 8, 31935-31940. d) Reflectance spectra in LCP and RCP light of flexible CNC photonic films containing DMAPS. Inset: flexibility of the dried film. Adapted from Guidetti et al. *Adv. Mat.* 2016, 26, 10042-10047.

#### 1.7.1.1.5. Drying time

Several authors chose to slow down the drying to improve film uniformity, using a humid environment in the case of Saha et al. (Saha and Davis 2018) and using an intermediate layer of immiscible solvent in the case of Zhao et al. (Zhao et al. 2019). This has the drawback of lengthening the processing time for film making, which is a main limitation for the scale-up of these materials. By contrast, Feng et al. (Feng et al. 2019) showed that a surfactant-assisted self-assembly of cholesteric CNCs in dimethylsulphoxide (DMSO) could yield near-uniform photonic films in two to four hours drying time, reproduced in Figure 29.

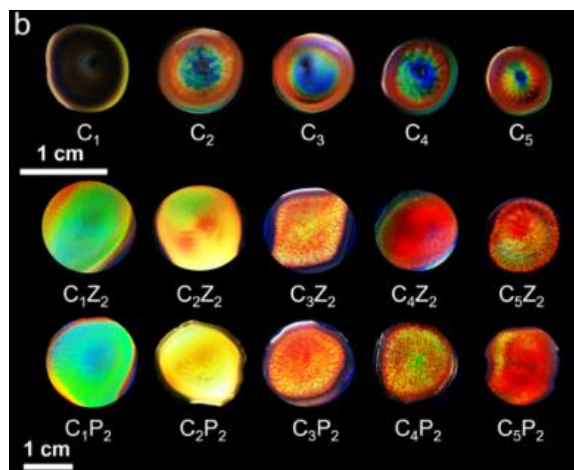


Figure 29 : Optical appearance of CNC films obtained by dryings of CNC suspensions in DMSO containing either a zonyl surfactant (Z) or a block copolymer surfactant (P). Increasing indices indicate increasing concentration either in CNCs (C) or in surfactant (Z, P). Reproduced from Feng et al, *ACS Sus. Chem. and Eng.* 2019, 7, 19062-19071.

#### 1.7.1.2. CNCs as template materials

A seminal contribution in photonic materials made out of cholesteric CNCs is the work of Maclachlan's group (Shopsowitz et al. 2010) on a photonic mesoporous silica material templated by cholesteric CNCs presented in Figure 30. The authors conducted a sol-gel reaction (the inorganic polymerisation of tetraethylorthosilicate, TEOS) in a suspension of cholesteric CNCs to yield a composite material made of a silica matrix and cholesteric CNC fillers. This material was then heat-treated at 540 °C, leading to the decomposition of its organic content, namely CNCs. This treatment yields a mesoporous material with a porous structure inherited

from the cholesteric arrangement of the degraded CNCs, whose aspect ratio and chirality are maintained. As a consequence, the material exhibits an iridescent photonic response whose intensity is strengthened by the high refractive index contrast between silica and air. It is quite remarkable that the end material scatters light in the visible range since the pitch of the starting CNC suspension is above the visible. The authors report the sintering process to lower the pitch value by approximately 300 nm. The end materials reflect approximately 20 % of unpolarised light, which corresponds to a lower optical quality than films obtained by controlled dryings.

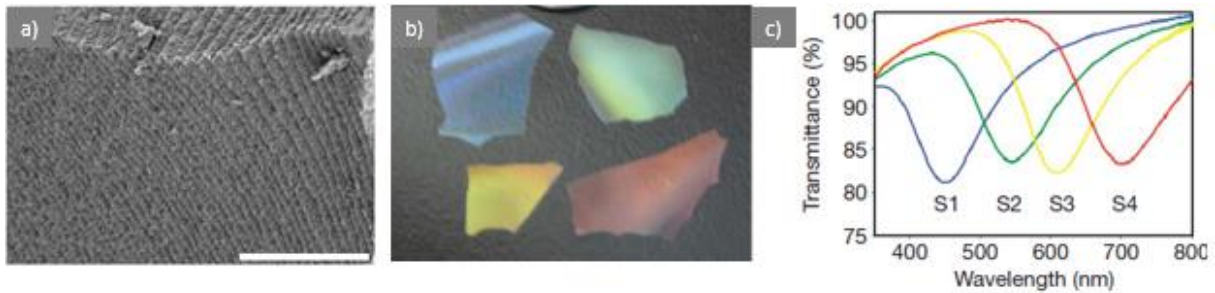


Figure 30 : Mesoporous photonic silica obtained by the inorganic polymerisation of TEOS templated by cholesteric CNCs followed by sintering at 540 °C. a) SEM characterisation of the material, scale bar is 3  $\mu$ m. b) Optical appearance of the materials, whose size is on the order of a coin. c) Absorption spectra of the materials. Shopsowitz et al, Nature 2010, 468, 422-425.

### 1.7.1.3. Elastomer composites

A recent hot topic aims at making photonic elastomer composites to take advantage of the flexibility of the elastomer matrix to yield mechanochromic effects. Maclachlan's group recently published in that scope (Boott et al. 2020; Kose, Tran, et al. 2019; Kose, Boott, et al. 2019; Cao et al. 2019): Kose et al show a conserved chiral-nematic CNC filler assembly with mechanochromic *birefringent* colours and suggest a CNC unwinding scenario upon mechanical stretching. However, their polarised optical microscopy images of the stretched materials display preserved fingerprint patterns. Boott et al present a slight iridescent colour response that is shifted by mechanical stretching as in Figure 31b), *i.e.* the first experimental evidence of possible mechanochromic effects with CNC elastomers. Qu et al (Qu et al. 2019) suggest the same cholesteric CNC unwinding scenario than Kose et al in CNC-polyurethane composites. Their experimental evidence shows some anisotropy induced by mechanical stretching in X-ray scattering along with an extinction in polarised optical microscopy compatible with cholesteric unwinding. Their SEM characterisation displays layered structures similar to Bouligand arches in the stretched materials, which is unexpected as their theoretical scenario envisions a pseudo-nematic assembly of charges.



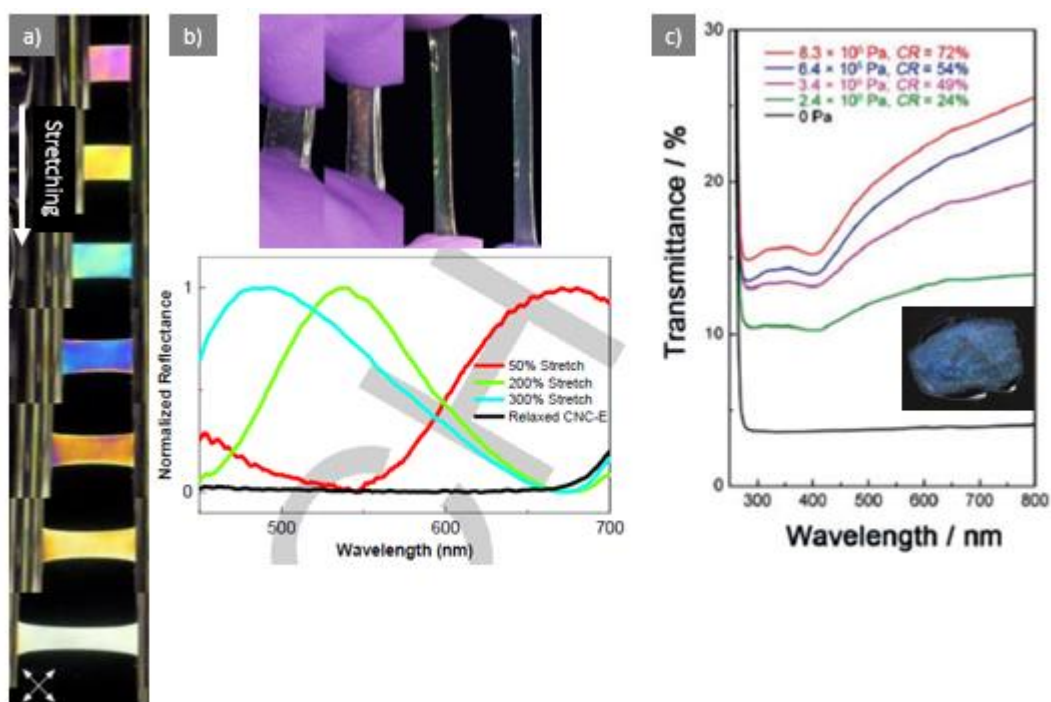


Figure 31 :Elastomer composites obtained by monomer impregnation of dried CNC films and aerogels. a) poly(ethylacrylate)-CNC elastomer displaying birefringence colours under cross polarisers upon mechanical stretching. Reproduced from Kose et al, *Macromolecules* 2019, 52, 5317-5324. b) Iridescent CNC-elastomer composite displaying mechanochromic effects upon stretching. Reproduced from Boott et al, *Angewandte* 2019. c) CNC-PDMS composite obtained by impregnation of a cholesteric CNC aerogel. The material exhibits photonic properties upon water immersion and mechanical compression. Adapted from Cao et al., *Adv. Mat.* 2019, 31, 1808186.

Finally, Cao et al. (Cao et al. 2019) recently made an aerogel material that exhibits photonic properties under mechanical compression when immersed in a solvent. The authors heat-treated a biphasic suspension of aqueous CNCs to induce the gelation of the suspension following CNC desulphation and freeze-dried the resulting hydrogel. The pitch of the aerogel is found to be above the visible, but can reach [300;500 nm] by mechanical compression. Immersion in a solvent is also required to exhibit a photonic response, possibly to increase the index matching between the two media of the aerogel. These aerogels can be impregnated by a PDMS monomer mixture and cured to form an elastomer composite, whose pitch is still above the visible. Under mechanical compression, the material exhibits photonic properties.

### 1.7.2. Chiral plasmonic materials

Kumacheva's group (Rofouie et al. 2019; Querejeta-Fernández et al. 2015; Querejeta-Fernández et al. 2014) has studied in detail the incorporation of gold nanoparticles in CNCs and chitin nanocrystals (Ch-NCs) materials. The specificity of Au nanoparticles is their plasmonic properties, *i.e.* the resonant oscillation of their electronic cloud when excited at a particular

frequency. Combined with the photonic properties of cholesteric CNCs, the composite materials of Figure 32 exhibit novel chiroptical properties capable of precisely controlling light extinction at certain wavelengths. The authors also show the versatility of light control through nanoparticles concentration, shape, and salt addition. In a similar scope, Lin et al (Lin et al. 2019) recently developed a specific grafting of gold nanoparticles on the reducing end of CNCs. The chiroptical properties of the objects have not been studied.

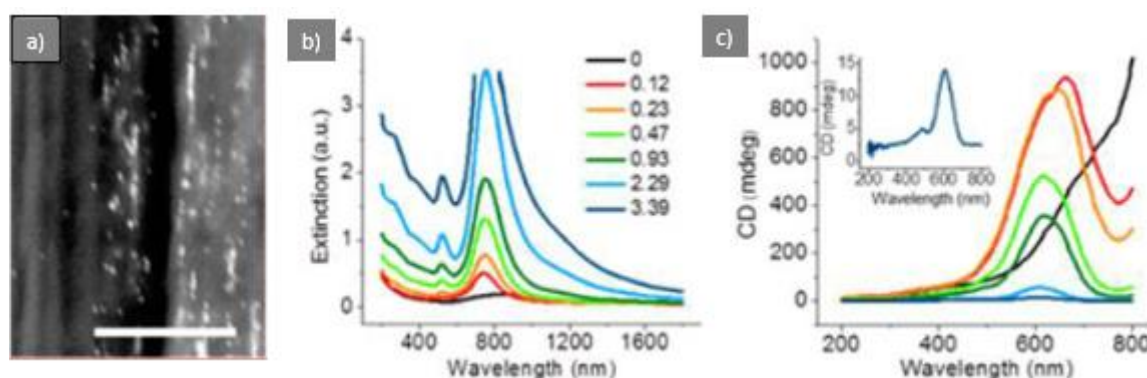


Figure 32 : a) SEM characterisation of a CNC-gold nanorods (AuNR) composite film using a backscattered electron detector. Gold nanorods appear as bright spots. Scale bar is 1  $\mu\text{m}$ . b) Extinction spectra of CNC-AuNR composite films at varying AuNR concentrations (labels in wt.%). c) CD spectra of the composite CNC-AuNR films using the same labels as b). Adapted from Querejeta-Fernandez et al., *J. Am. Chem. Soc.*, 2014, 136, 4788-4793.

### 1.7.3. Mechanical reinforcement in composites

An early and widely explored application of CNCs and cellulose nanofibres is the mechanical reinforcement as fillers of polymer composite materials (Favier, Chanzy, and Cavaillé 1995; Tatsumi et al. 2014), taking advantage of the high Young modulus of the cellulose fibre –  $E \sim 140$  GPa, comparable to steel – along its long axis (Habibi, Lucia, and Rojas 2010). Incorporating CNCs in composite polymer materials has led to big increases of the stiffness of the materials, notably due to the percolation of the cellulose network inside the composites. However cellulosic materials have not been observed to have significant interfacial adhesion with the matrix (Ljungberg et al. 2005), leading to the development of several compatibilisation strategies between the hydrophilic fillers and the mostly hydrophobic polymer matrix that are of interest in the scope of this work and further developed in the State of the art of chapter 3. While the main objective of this work is to yield photonic materials, we briefly discuss the potential of our materials for mechanical reinforcement in the Perspectives on the mechanical reinforcement properties of the composites of chapter 5.

## Chapter 2. Materials and methods

*« Ne soyez rien. Devenez sans cesse. [...]   
Soyez toujours pour vous-mêmes votre dehors,   
le dehors de toute chose. »   
A. Damasio, La Zone du Dehors*

In this second chapter, the protocols used to perform the experiments of the next chapters are presented. The first part describes the experimental protocols relative to the preparation of CNC suspensions, field-alignment experimental setups, polymerisation experiments and drying experiments. The second part develops the characterisation techniques that have been used throughout this work. This chapter aims at providing the reader with all necessary details to reproduce the results of this study.

## 2.1. *Preparation of the CNC suspensions*

### 2.1.1. Aqueous CNC suspensions

Cellulose nanocrystals are obtained by the sulphuric acid hydrolysis (65 wt.%, 63 °C, 30 min) of Whatman n°1 filter paper. The 65 wt.% solution of H<sub>2</sub>SO<sub>4</sub> in water is prepared by drop-by-drop addition of pure H<sub>2</sub>SO<sub>4</sub> (97%, Sigma-Aldrich) in water dipped in an ice bath to maintain a temperature below 60 °C throughout the addition. 60 g of mixer-grinded cotton linters are added under 400 rpm mechanical agitation and left to react for 30 min before being quenched by *ca.* 500 g of ice to *ca.* 40 °C and cooled down to ambient temperature. The initially white suspension turns ivory over the course of the reaction. An initial fraction of sulphuric acid is separated by several centrifugation-redispersion steps (18000 g) before being dialysed (14000 kDa dialysis membrane) against distilled water until stable conductivity as described elsewhere (Elazzouzi-Hafraoui et al. 2008; Revol et al. 1992). Suspensions are sonicated (Branson Digital Sonifier 450, 200 mL, 30%, 4 min), filtered (8 and 1 µm nitrocellulose, Sartorius) and characterised in dynamic light scattering and transmission electron microscopy before use.

Sulphur content is measured by conductometric titration: NaCl is added in excess to quantitatively exchange H<sup>+</sup> counter-ions of half ester sulphate groups and titration is performed with a 10<sup>-2</sup> M NaOH solution to yield the curve corrected for dilution effects presented in Figure 33. At equivalent point, we have:

$$V_{eq} \cdot C_{NaOH} = n_{cellulose} \cdot d_s$$

where  $d_s$  is the degree of substitution, defined as the molar fraction of glucose units functionalised with half-ester sulphate groups.  $n_{cellulose}$  is given by:

$$n_{cellulose} = \frac{m_{cellulose}}{M_{glucose} \cdot (1 - d_s) + M_{glucose-OSO_3^-} \cdot d_s}$$

Extracting  $d_s$ , we have:

$$d_s = \frac{162 \text{ g/mol}}{\frac{m_{\text{cellulose}}}{V_{\text{eq}} \cdot C_{\text{NaOH}}} - 80 \text{ g/mol}}$$

which allows to determine  $d_s$  directly from the conductometric titration, found to be typically 4%.

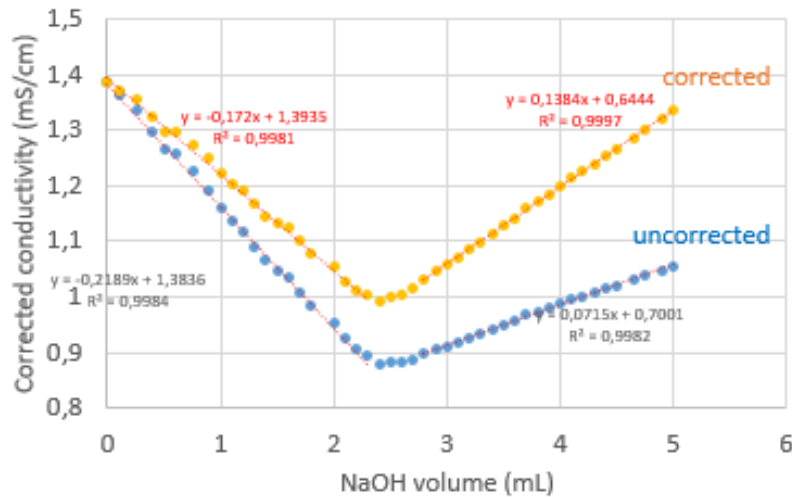


Figure 33 : Conductometric titration of an aqueous CNC suspension with an excess of NaCl against NaOH  $10^{-2}$  M. Blue curve corresponds to raw data, orange curve corrects dilution effects. The intersection of the trend curves gives the equivalent volume.

### 2.1.2. Dispersions in organic apolar solvents

A cellulose nanocrystals suspension at 1-2 wt.% is mixed with a 10 wt.% solution of Surfaline (for styrene, toluene) or Beycostat NA (for acrylates) in a 1 to 4 CNC/surfactant ratio in mass and pH is adjusted to 8 by NaOH addition to allow for  $\text{Na}^+$  counter-ion exchange as previously reported (Elazzouzi-Hafraoui, Putaux, and Heux 2009; Heux, Chauve, and Bonini 2000). Suspensions are freeze-dried in liquid nitrogen ( $-196^\circ\text{C}$ , 3 days) and redispersed in a similar amount of different organic solvents (toluene, styrene, methylmethacrylate) using a disperser (Ultraturrax T25 IKA, 12 000 rpm, 10 min) followed by sonication and filtration in the same conditions as aqueous suspensions. Notably, nitrocellulose membranes dissolve in acrylates, and PTFE membranes need to be used instead. Excess of surfactant is removed in the supernatant of a first centrifugation (18 000 g, 2 hours,  $4^\circ\text{C}$ ) redispersion step (disperser, tip sonication, filtration in the same conditions as before). The suspensions are then concentrated into the anisotropic domain by centrifugation (same conditions) and sonication of the centrifuge pellets (dry mass 55-60 wt.%) in small quantities of solvent to yield mother suspensions in the

fully anisotropic domain stored at 4 °C in the dark and regularly shaken to counteract the viscosity rise over time. The concentration of free surfactant in the first supernatant is measured at approximately 4.5 wt.%, whereas it is at 0.2 wt.% in the second supernatant. Quality of the dispersions are typically characterised by dynamic light scattering, transmission electron microscopy and polarised optical microscopy.

### **2.1.3. Phase diagrams**

Borosilicate capillaries (0.4x4x50 mm<sup>3</sup> Vitrocom, CMSscientific) are flame-sealed on one-side using Miniflam, filled with suspensions at various concentrations by capillary rise followed by mild centrifugation (2000 g, 30 s) and flame-sealed on the other side. Capillaries are left to stand at room temperature until phase separation completes before polarised optical microscopy observation. Capillaries prepared in this manner are stable over years, however helices tend to reorient in the homeotropic configuration over time.

## **2.2. *Field experiments***

### **2.2.1. Magnetic field setups**

In chapter 4, different magnetic field setups are used to generate respectively 0.25 T, 0.5 T, 0.65 T and 9 T magnetic fields. This section describes in more details what setups have been used in which geometries to generate those fields. All magnetic field intensity measurements have been carried out with a Hall effect Gaussmetre LMM GN106 in transverse geometry. The apparatus is calibrated with a 0.5 T magnetic field intensity before use. The measurement is sensitive to angular error on the transverse geometry, therefore numerous measurements are made and the maximum reproducible values are kept.

The first setup generating a 0.25 T magnetic field is made of two 0.5 T NdFeB magnets put in close contact of one another, followed by polar pieces guiding the magnetic field lines in a toric geometry to the sample as schematically described in Figure 34. Additionally, a special polar piece with trapezoidal geometry is used to further narrow the magnetic field lines in one direction (the depth in Figure 34a). This setup was able to generate a 0.25 T magnetic field intensity, probably due to significant magnetic field intensity losses in the polar pieces. This first setup has proved not to be able to align CNC helices as discussed in chapter 4.

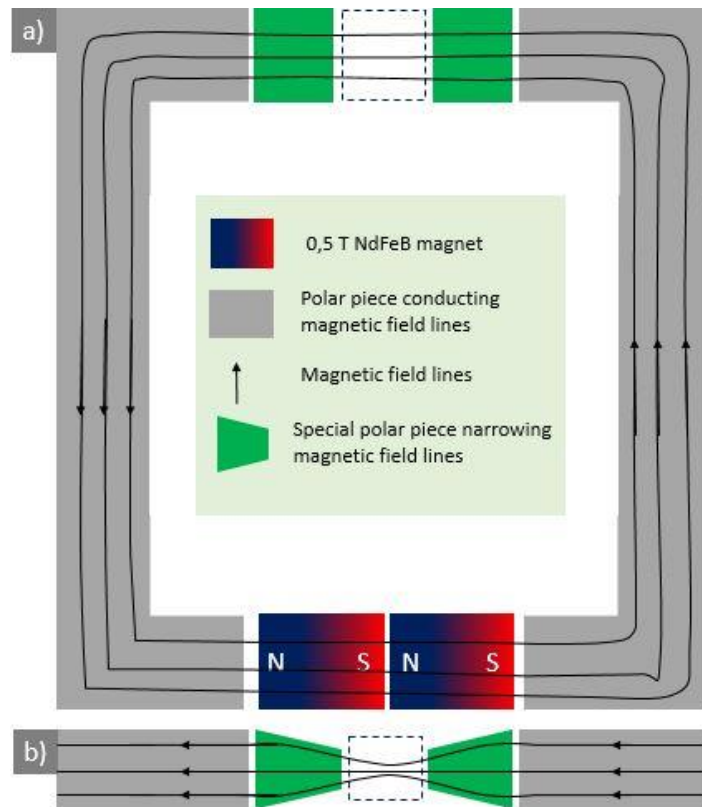


Figure 34 : Schematic (a) side view and (b) top view of the experimental setup used to generate a homogeneous 0.25 T magnetic field. Two 0.5 T magnets are put in close contact, and the magnetic lines they produce are guided and narrowed by polar pieces towards the top of the setup where the sample is to be placed (dashed blue area).

The second setup that has been used in this work is the calibration magnet of the gaussmetre. It is designed to provide a precise magnetic field intensity of 0.5 T; it has thus been used without further characterisation. Because of the geometry of the magnet, it was not possible to carry out direct under-field characterisation. Samples are typically characterised within the next 5-10 minutes after field application.

The third experimental setup is made of two 0.5 T NdFeB magnets in “sandwich” configuration, separated by a 3D-printed interlayer of adjustable thickness as described in Figure 35. This work has been carried out with a 17 mm interlayer leading to a homogeneous magnetic field of  $0.65 \pm 0.02$  T in the inter-magnet space. Edge effects have been measured to take place over 4 mm from the edge of the magnet, corresponding typically to a lower magnetic field intensity averaging around 0.5 T. The magnets are squares of 4 cm, which leaves a large area of homogeneous field intensity available for experiments. Most experimental work has been carried out with this setup as it allows for direct under-field characterisation using the windows made in the interlayer. Samples were typically left to align under magnetic field directly in the UV chamber until the desired state of alignment was reached and polymerised

under field by shining UVs through the windows of the 3D-printed interlayer. White light diffraction has been mostly used as it is easier to perform outside of an optical bench, and provides a global information on the state of alignment of the sample.

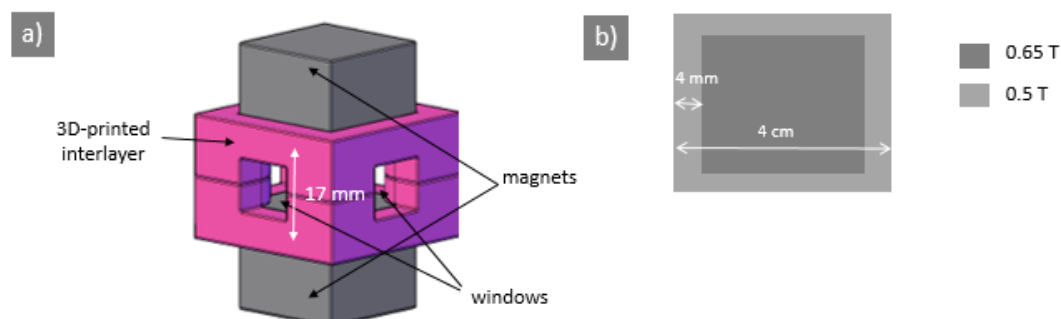


Figure 35 : a) Schematic view of the experimental setup generating a near-homogeneous  $0.65 \pm 0.02$  T magnetic field in the magnet interlayer. The interlayer is 3D printed and can be modified to generate various inter-magnet distances corresponding to different field intensities. b) Top view mapping of the magnetic field intensity in the inter-magnet space (plane of cut perpendicular to magnet surface). From the centre to the near-edge of the magnets, the magnetic field can be considered homogeneous at 0.65 T. Edges effects are measurable within 4 mm on the inner side of the magnet edge, where the magnetic field is averaging around 0.5 T.

The fourth experimental setup is taking advantage from the solid state NMR apparatus from CERMAV, that has a removable external probe to insert samples for NMR analysis. Once removed, it leaves an open funnel of  $\sim 1.5$  m whose end is dipped in the 9 T vertical magnetic field of the apparatus as schematically described in Figure 36. Typically, experiments consisted in suspending samples with long ropes inside the funnel, positioning the sample 1-2 cm higher than the bottom of the funnel. Characterisation were carried out off-field, within 5-10 minutes after the end of the experiments. A white light diffraction setup has been rebuilt in the NMR room to minimise sample rearrangement before characterisation.

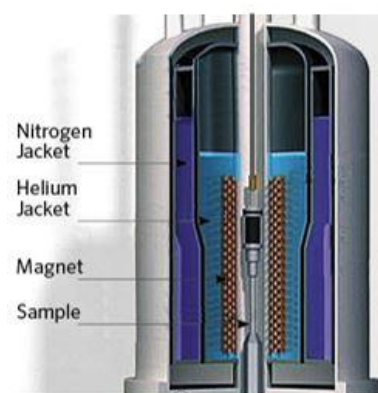


Figure 36 : Schematic inner view of a NMR apparatus. In the solid state NMR apparatus of CERMAV, the probe coming from the top funnel is removable, allowing the experimenter to suspend samples from the top of the apparatus inside the NMR magnet. Magnetic field orientation is vertical.



### 2.2.2. Electric field setups

In order to generate an electric field in our samples, a standard GBF has been used to create an AC sinusoidal signal at 1 kHz that is further strengthened a thousand times by a voltage amplifier to yield voltages ranging from 20 to 5000 V. This particular frequency has been chosen based on the previous work of D. Bordel (Bordel, Putaux, and Heux 2006), who screened the response of CNC suspensions to different field frequencies and intensities and found an “optimum” around this frequency. Arcing currents in between the two electrodes resulting in sample damage has typically been observed one order of magnitude above the biggest electric field values used in this study, corresponding to *ca.* 10 kV/cm.

The phase and the ground wires of the GBF and amplifier setup are then connected to electrodes of two types: brass wires or indium tin oxide (ITO) blades. Taking  $z$  as the direction of propagation of the laser for diffraction, brass wires have been used to generate  $E_x$  and  $E_y$  fields in borosilicate capillaries and composite FEP moulds whereas ITO blades have been used to generate  $E_z$  fields in home-made glass capillaries sealed by Fomblin, a fluorinated grease impermeable to organic solvents, and to generate electric fields in all directions in cuvettes for centimetre scale experiments. Brass wires have been typically locked in the capillaries by trapping them in melted glass at the bottom of the capillary, and sealed on the top of the capillary around the electrodes with Fomblin, an additional layer of PTFE tape and epoxy glue on the outside for mechanical robustness. Electrical connections have been made with standard domestic dominos. ITO blades and home-made capillaries have been made by gluing the different diamond-cut pieces of glass together with a very small amount of fluorinated grease, taking advantage of the strong adhesive capillary forces involved in the lubrication layer of grease in between two solid slides. Connections have been made with a conductive silver glue rather than melted tin because of the very poor wettability of melted tin on the ITO surface. Connection quality is checked with a standard multimeter in the case of brass wires, but requires a specific electric circuit for ITO blades to account for the semi-conducting nature of ITO. The different electrode geometries as well as a connection checking electric circuit are detailed in Figure 37. For centimetre scale experiments, an ITO blade setup similar to  $E_z$  has been built in a UV-visible spectroscopy glass cuvette.

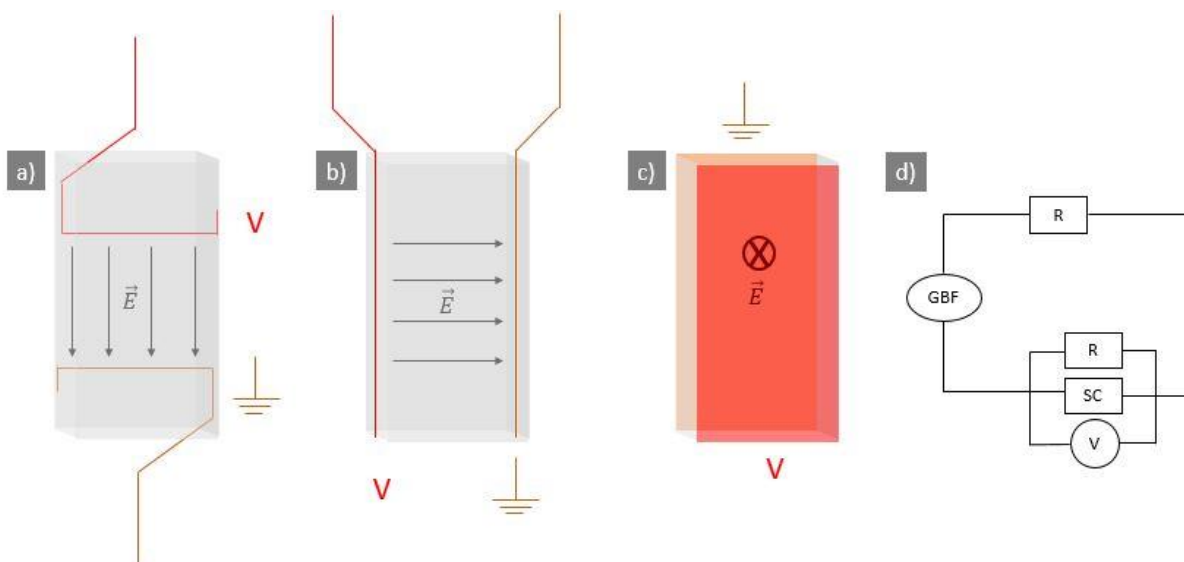


Figure 37 : Schematics of experimental setups generating a)  $E_x$ , b)  $E_y$  and c)  $E_z$  electric fields. a) and b) use brass wires, whereas c) uses ITO blades. Phase and ground electrodes are respectively labelled in red and orange. d) Electric circuit used for semiconductor (SC) connections checking. Whenever SC conducts, the voltmeter (V) measures 0. Otherwise it measures half of the input tension (the circuit is then a voltage divider bridge).

Sealing defects have definitely been an issue using this particular methodology, especially because of the required manipulation to bind the sample electrodes to the rest of the electrical circuit. The slightest movement of the electrode is capable of breaking the sealing around the electrode, resulting in solvent evaporation before or during experiments. This is the major drawback of placing the electrodes directly into the sample. Another possibility would have been to place the electrodes outside the capillary, the major drawback of doing this being that there is no direct link anymore between the input electric field and the effective electric field “felt” by the sample due to a significant charge loss inside borosilicate. The electric circuit equivalent to this situation is two condensers in series, one made of glass and the other one made of the sample. The capacity of these condensers is written as  $C = \epsilon_0 \cdot \epsilon \cdot \frac{A}{d}$ , where  $\epsilon_0$  is the void dielectric permittivity,  $\epsilon$  the dielectric permittivity of glass or of the solvent and  $\frac{A}{d}$  the geometrical ratio between the area and the thickness of the material, that has the same value for both condensers. Given that  $\epsilon_{\text{glass}} \sim 5 - 10$  and  $\epsilon_{\text{toluene}} \sim 2$ , the charge loss will take place mainly in glass, resulting in effective electric fields inside the sample 3 to 5 times lower than the input electric field, and found to vary with the solvent used. Due to this sealing issue coupled with viscosity rise over time, sample lifetimes were typically on the order of one to two days.

For polymerisation experiments involving the electric field, samples directly in the UV chamber were manipulated as normal CNC suspensions until the desired state of alignment was

reached before being UV-polymerised under field. White light diffraction has been mostly used to characterise the state of alignment for the same reasons as in experiments with the magnetic field.

### 2.2.3. Order parameters determination

To retrieve the order parameter of suspensions aligned under electric and magnetic fields, intensity as a function of an in-plane angle  $\varphi$  has been measured either by laser diffraction experiments or angular-resolved optical spectroscopy experiments. From laser diffraction experiments, intensity values are extracted from 1D profiles at fixed  $\varphi$  values using the image analysis software Fiji. Background noise is subtracted and peak intensity and width are averaged on the two intensity peaks at  $180^\circ$  from each other. The master plot of the intensity as a function of the in-plane angle is fitted by the theoretical Boltzmann distribution describing a competition between the magnetic field alignment and thermal energy used in chapter 4:

$$f = \frac{1}{2\pi \cdot \sqrt{\frac{\pi}{4\gamma}} \cdot \operatorname{erfi}(\sqrt{\gamma})} e^{\gamma(h \cdot H)^2}$$

The quadrupolar order parameter associated to this distribution is given by (Frka-Petesic 2010):

$$S_{2,th} = \frac{3}{4\gamma} \cdot \left( \sqrt{\frac{4\gamma}{\pi}} \cdot \frac{e^\gamma}{\operatorname{erfi}(\sqrt{\gamma})} - 1 \right) - 1/2$$

Fitting the experimental data points is performed by varying the value of  $\gamma$ , which yields the values for the order parameters in magnetic fields presented in chapter 4.

Another calculation involving only the experimental data points can also be conducted. If we define  $z$  as the direction of the field and  $\alpha = \theta_z$  as the angle between the helix axis and the field, we have:

$$S_{2,\alpha} = \left\langle \frac{3 \cdot \cos^2 \theta - 1}{2} \right\rangle = \frac{3 \cdot \langle \cos^2(\alpha) \rangle - 1}{2} = \frac{3 \cdot \frac{\int_{\alpha=0}^{\pi} I(\alpha) \cdot \cos^2(\alpha) \cdot \sin(\alpha) \cdot d\alpha}{\int_{\alpha=0}^{\pi} I(\alpha) \cdot \sin(\alpha) \cdot d\alpha} - 1}{2}$$

Knowing  $I(\alpha)$  using a characterisation method, we deduce the value of  $S_2$ . If the distribution of intensity measured by characterisation is  $I(\varphi)$  where  $\varphi = \frac{\pi}{2} - \theta_x$ , one can consider a cylindrical symmetry argument on the field orientation (Yoshiharu et al. 1997) to express the order parameter as a function of  $\varphi$ . This simplification is referred to as the Hermans order parameter.

It consists in assuming that magnetic field orientation of helices takes place evenly in directions having the same angle  $\theta$  with respect to the magnetic field because the energy incentive of helices to align is given by:

$$E_m = \frac{\mu_0 \cdot \Delta\chi \cdot V \cdot H^2 \cdot \cos^2(\theta)}{2}$$

One retrieves in this case the following expression for the order parameter as a function of the angle  $\varphi$ :

$$S_{2,\varphi} = \left\langle \frac{3 \cdot \cos^2\theta - 1}{2} \right\rangle = 1 - 3 \cdot \langle \sin^2(\varphi) \rangle = 1 - 3 \cdot \frac{\int_{\varphi=0}^{2\pi} I(\varphi) \cdot \sin^2(\varphi) \cdot d\varphi}{\int_{\varphi=0}^{2\pi} I(\varphi) \cdot d\varphi}$$

Optical spectroscopy measures the number of helices in only one direction making an angle  $\theta$  with the magnetic field and the hypothesis consists in extrapolating its value to all directions of angle  $\theta$ . This is only valid away from the skin layer close to the interface. Under this hypothesis, an experimental value of the order parameter is directly deduced from the intensity values as a function of the sample tilt.

For laser diffraction experiments, fitting to the Boltzmann distribution has been used for magnetic field experiments wherever the distribution of experimental points was regular enough. Otherwise,  $S_2$  was directly calculated. For angular-resolved optical spectroscopy experiments, two values of the order parameter are calculated.

## 2.3. *Polymerisation experiments*

### 2.3.1. Experimental setups

The polymerisation chambers used over the course of this work are presented in Figure 38. Most of the results have been obtained using a home-made polymerisation box with an industrial UV-lamp delivering 400 W at a distance from the samples. The illumination spectrum of the lamp is given in the appendix of chapter 2 and compared with the absorption spectra of the initiators. A smaller Luzchem UV-reactor delivering a total power of 64 W centered at 313 nm has been used during the last part of the study. Despite the big difference in delivered power, polymerisation behaviours have been found to be very similar in both experimental setups. It could be due to the efficiency of the H1 filter or the travelling distance of the first setup, given the power decreases as the inverse square of the distance.

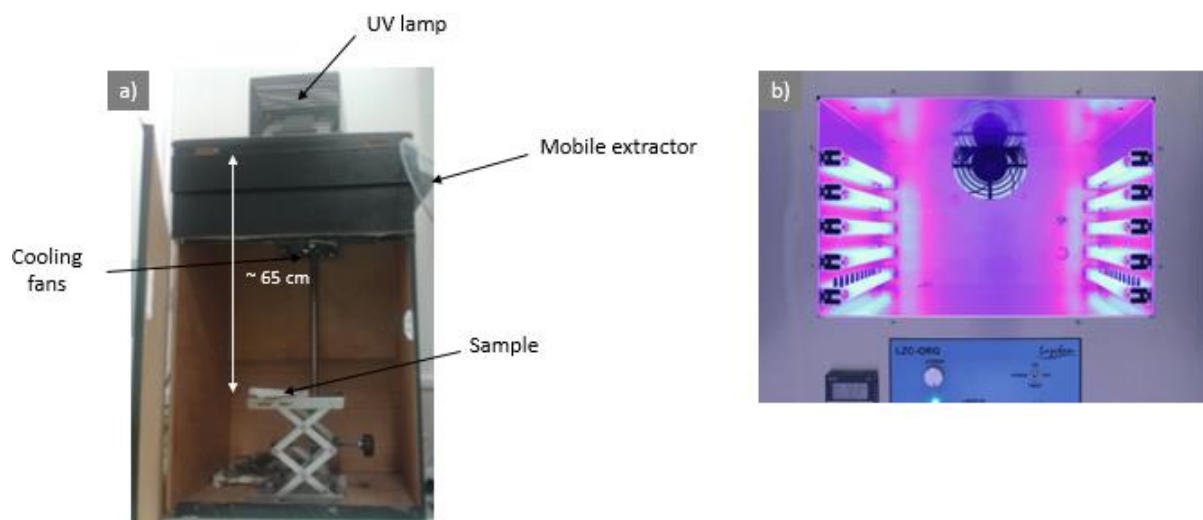


Figure 38 : Polymerisation chambers used over the course of this study. a) Home-made wooden box sealed with black duct tape in which a UVASPOT 400/T F-lamp of 400 W power filtered above 450 nm with a H1 filter (Hönle, France) shines light at approximately 65 cm from the samples. b) Luzchem polymerisation chamber hosting up to 8 LZC-UVB lamps of 8 W each in the immediate vicinity of the samples.

### 2.3.2. Sample preparation

In a typical polymerisation experiment, a starting mother suspension whose concentration is higher – typically fully anisotropic – than the final targeted concentration is extensively vortexed and tip-sonicated shortly before use. Within a final volume of hundreds of microlitres to a few millilitres, a mixture containing the initiator, a possible cross-linker, the CNC suspension in monomer and pure monomer to adjust the final CNC concentration is prepared and vortexed prior to use. Moulds are filled with this mixture, sealed by flame or by a fluorinated grease and possibly aligned under fields prior to polymerisation. Samples of small volumes are made because CNC suspensions in organic solvents are long to make and involve surfactants whose amounts are limited. It is also pointless to make a material several millimetres thick when a cholesteric assembly of 10-20  $\mu\text{m}$  is already able to reflect 100% of the incoming light. This however leads to a higher error on the relative concentrations of the reagents due to evaporation during sample preparation.

In the second part of the study, FEP moulds are used to make transparent films. These moulds consist of two FEP sheets *ca.* 3 cm x 4 cm in a “sandwich” configuration, with the sample in between and sealed with Fomblin grease as in Figure 39. This experimental setup typically yields thicknesses ranging from 200 to 600  $\mu\text{m}$  depending on the thickness of the grease interlayer. The fluorinated grease has the drawback of slightly impacting the transparency of the samples when unmoulding is not carefully performed, and is extremely

difficult to remove from the sample surface. For electric fields alignment, brass wires have been first placed in the grease as in Figure 39, later directly dipped into the suspension corresponding to lower field values for the orientation and unwinding of CNC helices.

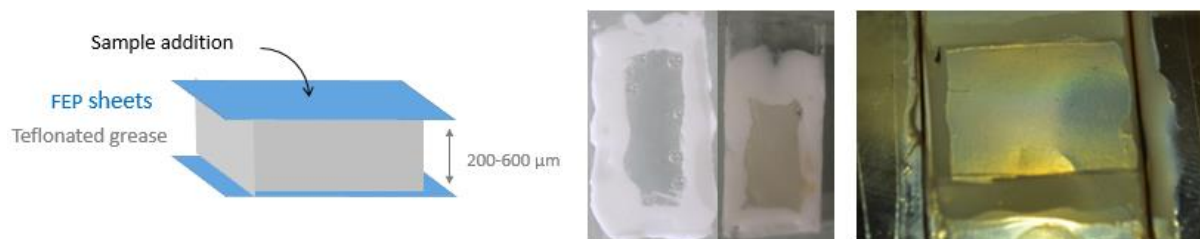


Figure 39 : (left) Schematic of the experimental polymerisation setup yielding transparent polymer films. (right) Pictures of several samples prepared in FEP moulds.

### 2.3.3. Inhibitor removal experiments

As commercial inhibitors of PS and PMMA are phenolic compounds, washing with a 5 wt.% NaOH solution is expected to yield phenolates ( $pK_a \sim 10$ ) that are water-soluble. Upon washing styrene with NaOH, the basic aqueous phase turned red instantaneously which is likely a signature of the above-mentioned phenomenon, since the medium is expected to contain only styrene, water, NaOH and 4-tertbutylcatechol. Aqueous and organic phases have been separated and styrene has been dried with  $\text{Na}_2\text{SO}_4$ . Separation columns filled with either basic or neutral aluminium oxide beads are reported to allow for the separation of 4-tertbutylcatechol (Chen et al. 1998). Home-made aluminium oxide separation columns have been prepared by filling *ca.* 25 cm of basic or neutral  $\text{Al}_2\text{O}_3$  millimetre size beads on top of sand and cotton, and the commercial Sigma-Aldrich “Inhibitor Remover” column (Inhibitor\_remove) has been used as received. Styrene has been poured through the columns with ease several times before use. Standard  $^1\text{H}$  NMR characterisation has been conducted unsuccessfully on styrene before and after inhibitor removal because the proton signal characteristic of 4-tertbutylcatechol could not be observed.

Controlled atmosphere experiments have been conducted by sealing the vials with a septum and bubbling  $\text{N}_2$  directly into the suspension using a needle for 15 min, with another needle allowing  $\text{O}_2$  to exit the vial.

### 2.3.4. Surface treatment of borosilicate capillaries

Hydrophobic surface treatment of borosilicate capillaries has been performed by dipping the surfaces in a 7 wt.% KOH suspension for 15 min followed by rinsing in a water bath for

15 min and drying at 80 °C overnight. This first step aims at cleaning the capillary surfaces. Capillaries are then dipped in a 0.1 wt.% suspension of  $C_{18}H_{37}-SiCl_3$  in toluene two times for 10 minutes, followed by rinsing in pure toluene for 10 min and drying at 80 °C overnight. The grafting reaction occurs at room temperature during the first two bathes, and the last one aims at removing the non-grafted molecules. Capillaries have been sealed using Fomblin grease and PTFE tape as flame-sealing irreversibly degrades the coating. Fluorinated surface treatment has been performed likewise, replacing  $C_{18}H_{37}-SiCl_3$  by  $C_{18}F_{37}-SiCl_3$  and toluene by FC-40, a fluorinated solvent. Contact angle characterisation has been performed with a home-made setup built for the occasion.

## 2.4. *Drying experiments*

While most experimental details of drying experiments are directly discussed in chapter 6 given how closely they relate to the results, we give hereafter a comprehensive summary of typical drying experiments.

A standard glass vial is filled with 2 to 5 mL FC-40 (Santa Cruz Biotechnology) and 5 to 10 mL of pure toluene (Sigma-Aldrich) is carefully deposited on top of it. The vial is closed and vortexed at low speed during *ca.* 10 seconds, or left to stand for at least 30 min to allow for the solvents to diffuse in one another. CNC suspensions in toluene and MMA are adjusted in chemical composition (concentration and initiator, cross-linker for MMA), vortexed and tip-sonicated before use. In uncontrolled volume experiments, suspensions are deposited on the bottom surface of the vial using a 1 mL volume capacity pipette and a 1 mL volume capacity pipette tip. Deposition continues until the suspension volume cannot be pinned on the bottom surface anymore and is observed to migrate at the FC-40/toluene interface. 5-6 droplets are typically deposited in the same vial, spaced enough from one another to prevent coalescence. Samples are closed immediately after droplet pinning with microscope slides coated with Fomblin grease. MMA samples are covered with aluminium foil to prevent their polymerisation. Samples are left to stand at room temperature during the annealing/reorientation step, and characterised in polarised optical microscopy after the annealing. Dried and wet droplets are discriminated by gentle shaking under the microscope. Final drying is performed by opening the samples to open air under a fume cupboard. Full dryings are left for at least 24 hours under fume cupboard before characterisation. Polymerisation at fixed drying times is performed by sealing the samples again at fixed times

and polymerising them immediately after. One should note that drying continues for a time after sealing back the sample, until saturation of the vial atmosphere is complete again.

## **2.5. *Characterisation techniques***

### **2.5.1. $^1\text{H}$ Nuclear magnetic resonance (NMR)**

Commercial styrene samples and styrene washed by NaOH or separated on an aluminium oxide column have been dispersed in  $\text{CDCl}_3$  and analysed using a Bruker Advance III HD apparatus operating at 400 MHz.

### **2.5.2. Mass spectroscopy**

Mass spectroscopy characterisation has been performed using the Molecular Institute of Grenoble (ICMG) platform. Spectra have been recorded on surfactants dispersed in acetonitrile in positive and negative electrospray ionisation (ESI) mode, which is used for sub-1 kg/mol molar mass compounds.

### **2.5.3. Dynamic light scattering (DLS)**

DLS measurements have been carried out with a Nanosizer apparatus (Malvern Instruments) in default configuration. DLS deduces the hydrodynamic radius of an object hypothesized to be spherical by measuring the exponential decrease of the temporal auto-correlation function of the intensity speckle of light scattered by the object to retrieve its diffusion coefficient. The Stokes-Einstein relationship links the hydrodynamic radius  $R_h$  and the diffusion coefficient  $D$ :

$$R_h = \frac{k_B \cdot T}{6\pi \cdot \eta \cdot D}$$

The same apparatus allows for measuring the zeta potential of the suspension, defined as the surface potential outside the Stern layer of ions on the surface of the particle, by measuring the electrophoretic mobility  $\mu_e$ :

$$\mu_e = \frac{2 \cdot \varepsilon \cdot \zeta \cdot f(\kappa a)}{3 \cdot \eta}$$

where  $f(\kappa a)$  is the Henry function, commonly approximated at  $f(\kappa a) = 1.5$  although the Smoluchovski approximation is technically valid for sizes above 200 nm and an electrolyte



concentration above 1 mM. 10 mM NaCl is typically added to suspensions to stay as close as possible to the range of validity of the approximation.

#### **2.5.4. Differential scanning calorimetry (DSC)**

Samples have been analysed in sealed aluminium pans using a Q200 apparatus (TA Instruments) cooled by liquid nitrogen using heat/cool/heat ramps in between -60 °C and 200 °C at 10 °C/min.

#### **2.5.5. Transmission electron microscopy (TEM)**

CNC suspensions were typically diluted to the point where the scattering of a pocket laser was hardly visible. Carbon-coated copper grids were cleaned and made hydrophilic by a short plasma treatment in a glow-discharge unit (easiGlow from Pelco). A droplet of suspension was deposited and the excess liquid is absorbed with a blotting paper two minutes after deposition. Negative stains such as uranyl acetate are generally useful to record high-contrast images of radiation-sensitive nanoparticles like CNCs. However, salts precipitate in organic solvents media. All TEM observations have therefore been performed on unstained specimens to allow for a direct comparison of the objects suspended in water and organic solvents. The preparations have been observed with a Thermo Scientific Philips CM200 electron microscope operating at 200 kV, under low-dose illumination to prevent extensive damage of the CNCs under the electron beam and maintain a sufficient contrast. Images have been recorded with a TVIPS F216 digital camera (2048 x 2048 pixels).

Ultrathin cryo-cuts sections were prepared by cryo-ultramicrotomy, using a Leica UC6 FC7 cryo-ultramicrotome operated at -100 °C. First, a 100x200 mm<sup>2</sup> trapeze-like surface was trimmed with a 45° cryotrim Diatome knife. Ultrathin sections with thicknesses between 20 and 90 nm were then cut with a cryo 35° Diatome knife and collected on 200 mesh carbon coated copper grids. TEM observation has been realised in low dose conditions using a JEOL JEM-2100-Plus microscope operating at 200 kV. Images have been recorded with a Gatan Rio 16 camera (4096 x 4096 pixels).

#### **2.5.6. Scanning electron microscopy (SEM)**

Scanning electron microscopy (SEM) observation is the simplest and most powerful mean to directly observe the distribution of charges inside cholesteric composite materials. Bouligand and coworkers (Leforestier and Livolant 1993) and more recently Frka-Petesic et al. (Frka-

Petesic et al. 2019) have described in detail the relationship between the SEM patterns and the corresponding helical arrangement present in cholesteric materials, reproduced in Figure 40. Given a cholesteric stack of helical axis respectively  $\mathbf{c}$  or  $\mathbf{m}'$ , three different kinds of SEM patterns may be observed from its cut. The most common case is to cut the helical stack obliquely with respect to the helical axis, yielding a SEM pattern made of arches commonly referred to as Bouligand arches (case 3 of Figure 40a, orange cut of Figure 40b). The width of an arch is related to the original pitch value of the helical stack and the angle between the direction of the cut and the helical axis as follows:

$$\frac{p_{\text{app}}}{2} = \frac{p}{2} \cdot \frac{1}{\cos(\theta_{\text{cut}})}$$

While pitch measurements are close to accurate when  $\theta_{\text{cut}}$  is close to  $0^\circ$ , they are completely wrong when  $\theta_{\text{cut}}$  is close to  $90^\circ$  due to a projection bias similar to the one observed in polarised optical microscopy. The second case corresponds to a cut perpendicular to the helical axis (case 1 of Figure 40a, purple cut of Figure 40b), in which the SEM cut contains individual CNCs pointing in the same direction, and the SEM pattern displays close to nothing because its resolution is too low to observe individual CNCs. The third case corresponds to a cut in a plane containing the helical axis (case 2 of Figure 40). The SEM cut contains in one direction lines of individual CNCs having the same orientation while in the other direction, individual CNC orientation varies continuously from perpendicular to parallel to the cut. As a result, the SEM pattern shows no arches, but lines separated by half a pitch one from another corresponding to the CNCs pointing perpendicularly to the cut.

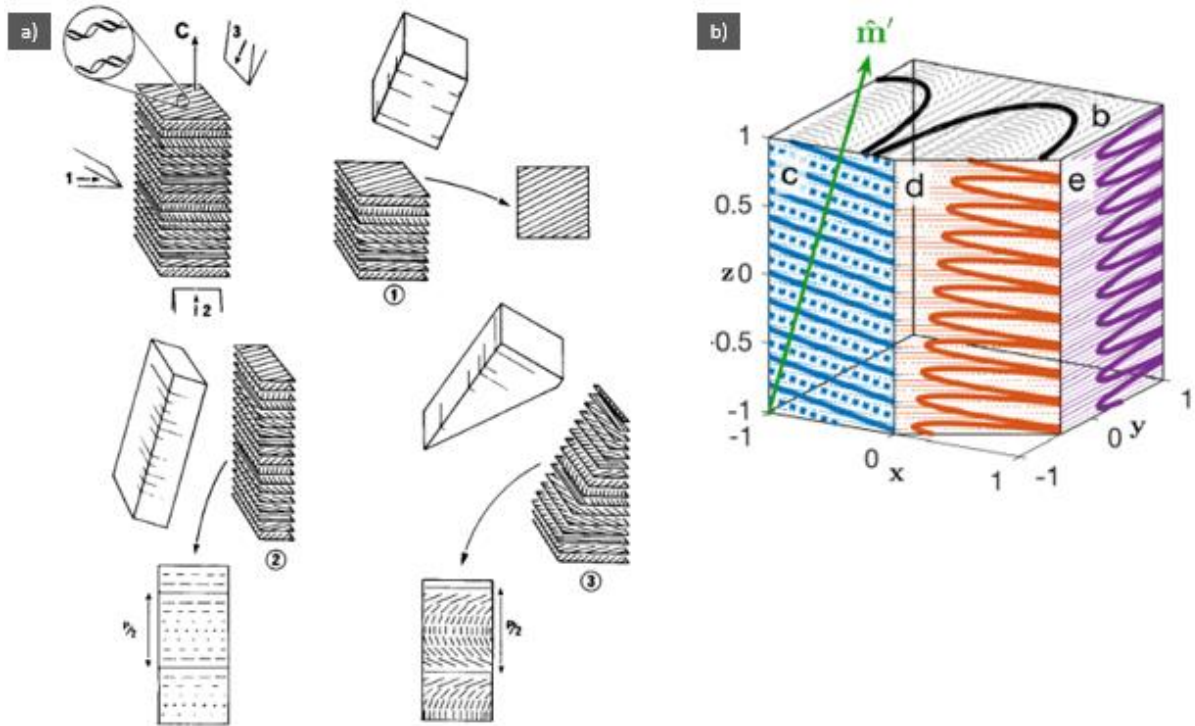


Figure 40 : Schematics of the scanning electron microscopy (SEM) patterns obtained from the cut of a helical stack (1, purple) perpendicular to the helical axis (2, blue) in a plane containing the helical axis and (3, orange) obliquely to the helical axis. a) and b) are two schematics representing the same phenomena. a) Reproduced from Leforestier et Livolant, *Biophysical Journal* 1993. b) Reproduced from Frka-Petesic et al, *Phys. Rev. Mater.* 3, 045601.

In the standard sample preparation protocol for this study, materials have been fractured by hand at room temperature to expose the surface of interest. Fractures have been preferred to cuts because they do not modify the sample surface microstructure, whereas cuts typically crush it. This surface is metallised with Au/Pd using a JEOL JFC-1000 apparatus prior to observations with a FEI Quanta 250 scanning electron microscope of the ICMG platform equipped with a field emission gun operating at 2 kV.

Microtome cuts have been made with a histo diamond knife (Diatome) 45° that is able to cut slices whose thickness is between 200 nm and 5  $\mu\text{m}$  at room temperature for polarised optical microscopy observation and scanning electron microscopy characterisation. The sample surface has been trimmed in trapezoidal shape before the cut is made.

### 2.5.7. Optical characterisation

Laser diffraction and white light diffraction characterisation are relatively simple optical characterisation techniques, yet powerful when applied to suspensions of CNC helices. Angular-resolved spectroscopy is more complex to set up, but rewarding in the quality of the measurements.

### 2.5.7.1. Laser diffraction

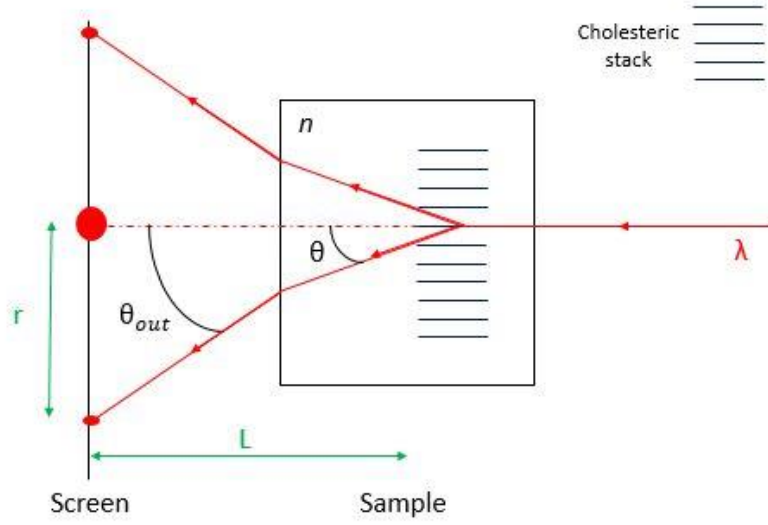


Figure 41 : Schematic of the laser diffraction pattern created by a sample containing a cholesteric suspension of CNCs. The size of the cholesteric stack is exaggerated to emphasise the laser beam pathways.

Laser diffraction has been used to study the changes in orientation and pitch of cholesteric domains under external fields. This method consists in shining a laser beam perpendicular to the sample and looking at the light scattered by the sample at a known distance. The information retrieved is local because the area scanned is a cylinder of *ca.* 1 mm in diameter and whose length is the thickness of the sample, on the pathway of the laser beam. To be in the far field diffraction regime, one must verify  $d \gg \frac{a^2}{\lambda}$  where  $d$  is the screen-sample distance,  $a$  is the size of the diffracting element and  $\lambda$  is the wavelength. Orders of magnitude give  $\frac{a^2}{\lambda} \sim 10 \mu\text{m}$ , so the diffraction patterns observed in this work will always be considered in far field. Within this limit, the plane containing the sample and the plane containing the screen are linked by a Fourier transform relationship. The most important consequences of this relationship are that the intensity scattered in a given direction is directly proportional to the number of helices pointing in this direction in the sample, and the radial position of the intensity peak relative to ballistic light scales as the inverse of the pitch value, allowing for quantitative determination of order parameters and pitch measurements as described hereafter. Laser diffraction allows to scan the orientation of helices in the plane (Oxy) perpendicular to the laser beam direction  $z$ ; helices with a  $z$  component will not scatter light to the screen. This is an important limitation to bear in mind.

We use a standard He-Ne laser of wavelength  $\lambda = 632.8 \text{ nm}$  to illuminate a sample containing cholesteric assemblies of CNCs at normal incidence as described in Figure 41. Whenever the helical axis is perpendicular to the laser beam, the cholesteric stack behaves as a diffraction grating of pitch  $p/2$  described in chapter 1:

$$n \cdot \sin \theta = \frac{\lambda}{p/2}$$

The outgoing ray encounters a refractive event at the sample/air interface:

$$n \cdot \sin \theta = \sin(\theta_{\text{out}})$$

And  $\theta_{\text{out}}$  is also function of the position of the points on the screen according to:

$$\theta_{\text{out}} = \arctan\left(\frac{r}{L}\right)$$

Putting all together, we have:

$$p = \frac{2\lambda}{\sin(\arctan(r/L))}$$

This formula provides a measurement of the pitch of the cholesteric stack by shining a laser on the sample and measuring the position of the diffraction points. For the qualitative analyses of diffraction patterns presented in chapter 4, one must bear in mind that the diffraction points of a given cholesteric stack are observed in the same direction as its helical axis and the implications of the inverse scaling of the diffraction points position with the pitch; whenever the points move closer to the centre of the pattern, the pitch value increases and whenever the points move further one from another, the pitch value decreases. With the intention of giving the reader more familiarity with this technique, Figure 42 displays several experimental diffraction patterns with attached schematics of the helices configuration associated to each pattern.

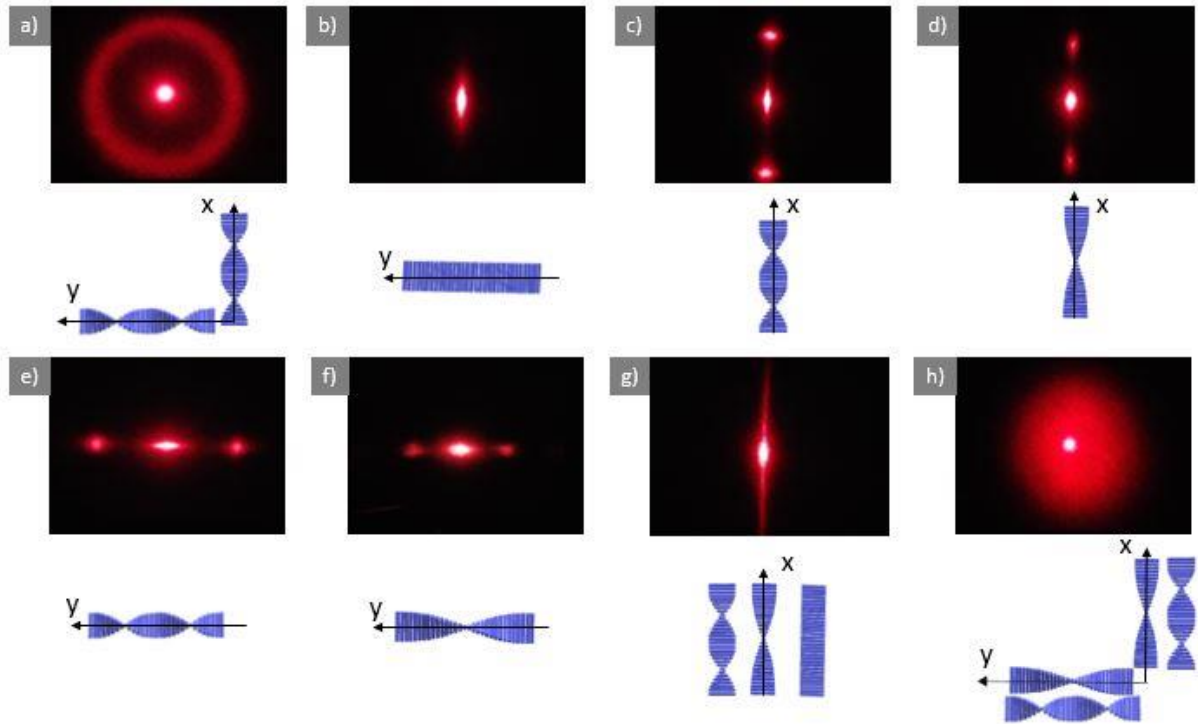
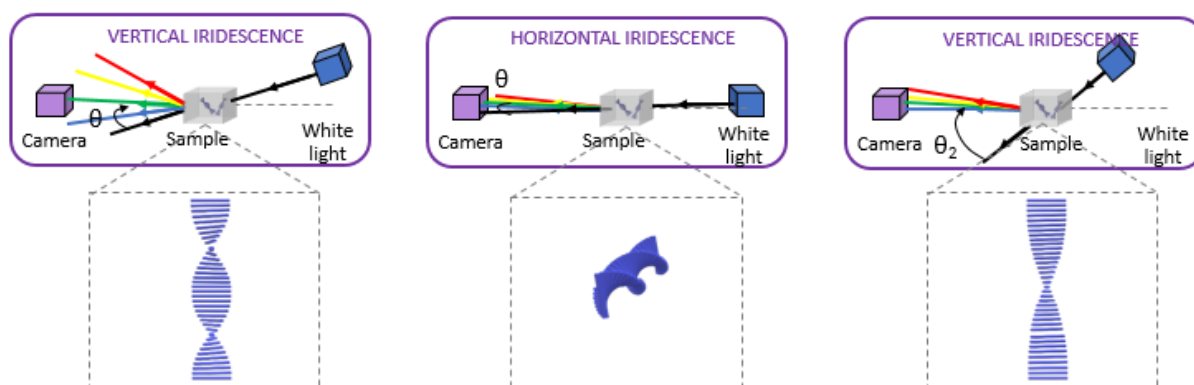


Figure 42 : Examples of experimental diffraction patterns and schematics of the associated helices configurations. a) Helices in random  $xy$  configuration. b) Fully unwound helices in the nematic state. c) Vertical helices of low pitch value. d) Vertical helices of higher pitch value than in c). e) Horizontal helices of low pitch value. f) Horizontal helices of higher pitch value than in e). g) Linear pattern corresponding to vertical helices with different pitches. h) Disk pattern corresponding to helices of random orientations and a range of pitches.

### 2.5.7.2. White light diffraction

This technique refers to the qualitative characterisation of the colours transmitted or reflected by the sample captured by a camera under white light illumination. This technique provides the experimenter with a sample-wide qualitative information on the state of alignment and pitch values of cholesteric helices inside the sample. It is based on the fact that, in a particular geometry of illumination, only the helices of a particular orientation and pitch value will match Bragg conditions and scatter visible light to the camera. By varying the position of the camera relatively to the sample, it is possible to determine the orientation of helices in almost any region of the sample. As a reminder, the pitch range of the samples is typically 2 to 5 microns, yielding Bragg reflection at relatively high angles of incidence. Different characterisation geometries and their corresponding helical configurations are exemplified in Figure 43. Similar to laser diffraction, helices that have an orientation component towards the thickness of the sample will not be observed in white light diffraction as their Bragg scattering will not be oriented towards the detector. One can consider only the scattering from helices whose axes are in the  $(Oxy)$  plane within a few degrees in the  $z$  direction. Bragg scattering is

typically observed when the white light source is 15 to 20° off-centered in the direction of the helices axes with respect to normal incidence. As described in Figure 43, the scattering of vertical helices will be observed if the light source is off-centered vertically and the scattering of horizontal helices will be observed with an horizontally off-centered light source.



*Figure 43 : Examples of optical configuration for the characterisation of the iridescent optical response in CNC helices suspensions. (left) When light is off-centered vertically, helices whose axes are vertical scatter light at an angle  $\theta$  towards the camera. (centre) When light is off-centered horizontally, helices whose axes are horizontal scatter light at an angle  $\theta$  towards the camera. (right) When vertical helices have higher pitch value, the incident and scattering angles have bigger values. Same trend is observed for horizontal helices.*

Several examples of iridescent white light diffraction responses are shown in Figure 44. In Figure 44a), the majority of helices inside the suspension are oriented in such a way that they scatter white light towards the detector, resulting in a homogeneous colour appearance. Increasing the angle of observation leads to a redshift in colour. In Figure 44b), the suspension contains helices that take any in-plane orientation observed with a horizontally off-centered light source. As a result, the sample appears divided into colourful and non-colourful domains. The colourful domains correspond to helices oriented horizontally, whereas the non-colourful domains correspond to helices with other orientations. In Figure 44c), helices having the same orientation as in b) and a wide polydispersity in pitch are viewed under horizontally off-centered illumination. Different colours match the Bragg conditions on helical domains of different pitches and orientations, leading to a scattering white (the sum of a sufficient amount of visible wavelengths so that it ends up appearing white). Illumination in Figure 44d) is off-centered vertically to observe the optical response of vertically oriented helices, yielding therefore a 100% colourful sample. The colour variation from top to bottom is due to a parallax effect, in which the top is viewed at lower angle of incidence than the bottom by the detector. Figure 44e) is a peculiar example, in which helices have random 3D orientation. The reason why the sample is fully coloured similar to d) is because the cholesteric domains are so tiny that there is at least



one vertical domain that is scattering light to the eye per unit of area visible by the eye. Figure 44f) presents the optical response of a suspension of helices oriented in a plane perpendicular to the horizontal direction under horizontal and vertical light illumination. Horizontal illumination leads to absolutely no colour, in good agreement with the absence of horizontally oriented helices. Vertical illumination displays a mix of colourful and non-colourful domains, for the same reason as in b); helices oriented vertically scatter light to the detector whereas other orientations do not. Through these examples, we can see how powerful this method is to retrieve a mental map of the orientation of CNC helices, an order of magnitude of their pitch and a qualitative idea of the size of the cholesteric domains in the sample.

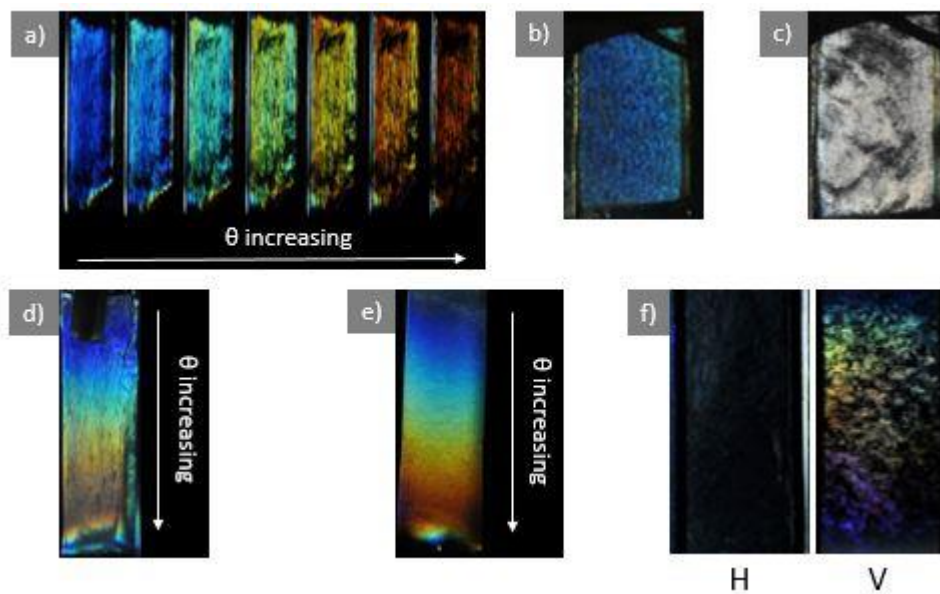


*Figure 44 : Iridescent white light diffraction of CNC suspensions with different helices orientations observed in different characterisation geometries. a) Horizontal helices with increasing angles of illumination from left to right. b) Horizontal white light diffraction from in-plane (horizontal and vertical) helices. c) Horizontal white light diffraction from in-plane helices having a broad range of pitch values, leading to a scattering white. d) Vertical illumination on vertical helices, with changing colour due to a parallax effect. e) Vertical illumination of tiny cholesteric domains of random 3D orientation, with the same parallax effect as d). f) Horizontal (left) and vertical (right) illumination of helices oriented within a plane perpendicular to the horizontal direction.*

There is an intrinsic bias limiting the precision of this method for colour characterisation. The observed colour does depend on three components of the experimental setup: the spectral distribution of the illumination source, the scattering properties of the sample (what we care about) and the sensitivity of the detector as a function of wavelength. Said another way, if the illumination source is for example an LED lamp with three peaks in the blue, green and red, the scattering material scatters all wavelength evenly and the detector is more sensitive in the green, you will be tempted to say that your material scatters only blue, green and red colours, with



more scattering efficiency in the green which is completely wrong. This bias is visible on the iridescent colour series of Figure 46, in which green light is absent, lost to the profit of cyan and yellow although cholesteric CNC helices scatter evenly green and other colours (confirmed using angular-resolved spectroscopy). This is why the quantitative characterisation is performed with another experimental setup and methodology called goniometry, or angular-resolved spectroscopy.

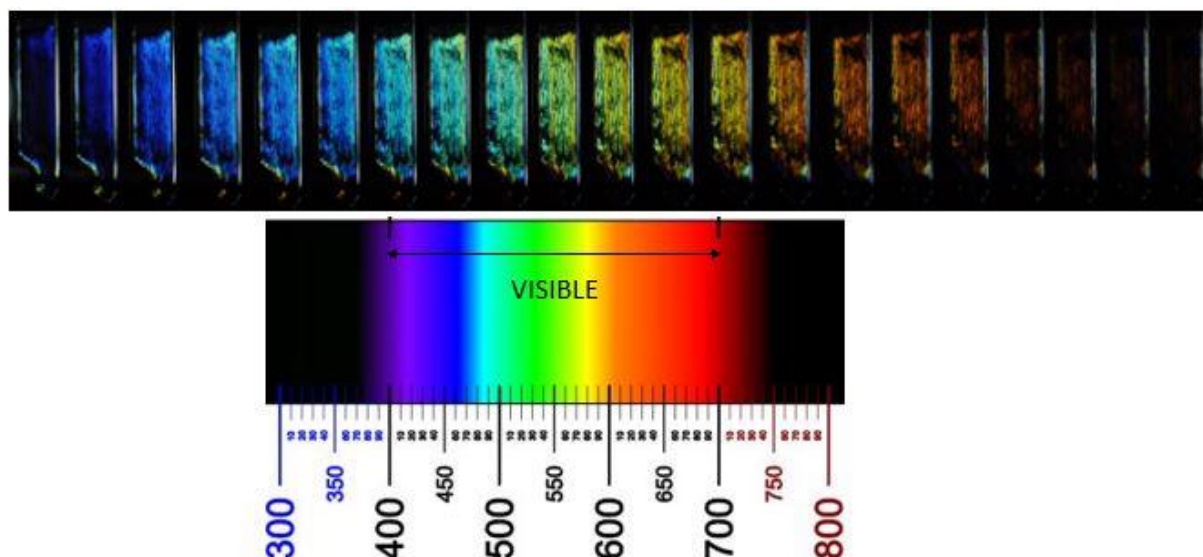


Figure 45 : White light diffraction of a CNC suspension aligned under magnetic fields recorded at a broad range of angles compared to the visible colour spectrum (source: Fulvio on wikimedia – “Light spectrum (precise colours)”)

### 2.5.7.3. Angular-resolved spectroscopy – Goniometry

Angular-resolved optical spectroscopy enables the spectral analysis of the light reflected, transmitted or scattered by a sample while controlling exactly the incident light direction as well as its outgoing direction. It is experimentally implemented by shining a collimated white beam on a sample and collecting the light coming back from the sample, with the possibility to control independently the angle of light illumination and the angle of light collection. In the framework of the laboratory, the incident light is kept fixed and both the sample and the detector are able to rotate co-axially about a vertical axis. This implies that only the light scattered in the horizontal plane is collected. The important features of the experimental setup are a measurement that is relative to the light source emission spectrum and referenced against an evenly scattering material. The background noise is subtracted from measurements and the spectral distribution of the lamp is referenced against a white diffuser or a silver mirror, materials that are considered to scatter all wavelengths evenly. Any measurement consists of a signal  $S$ :

$$S = \frac{I_{\text{raw}} - I_{\text{background}}}{I_{\text{reference}} - I_{\text{background}}}$$

where  $I_{\text{raw}}$  is the intensity directly collected by the detector at all wavelengths (similar to what is collected by a camera),  $I_{\text{background}}$  is the intensity of the background noise and  $I_{\text{reference}}$  is the intensity of the light source, referenced against either a white diffuser or a silver mirror. Silver mirror reflects near 100% of the incident light and allow for quantitative measurements of the reflectivity of strongly scattering samples as in chapter 6. White diffuser only allows for qualitative measurements but its weaker signal provides good signal over reference ratios for weakly scattering samples. The illumination light source consists of a HPX-2000 xenon lamp, that has several peaks over the visible range. The detector consists of a spectrophotometer (AvaSpec-HS2048, Avantes). On this setup, exposure time can be adjusted automatically by a high dynamic range (HDR) method in which the software records data at different exposure times and automatically selects the one that provides the best signal over noise ratio.

In order to collect light scattered at any angle, the experimental setup schematically described in Figure 46 consists of a fixed illumination source and a mobile detector mounted on a rotary arm controlled by a Newport motion controller at the same height than the source. Sample are mounted on a rotating stage, situation that is fully equivalent to having a fixed sample and a source mounted on a rotary arm. This setup allows to collect the scattered light of a sample in the plane containing the source, the sample and the detector. The sample needs precise positioning to scatter light within this plane that is adjusted with the help of a number of micrometre screws (colour labels of Figure 46).

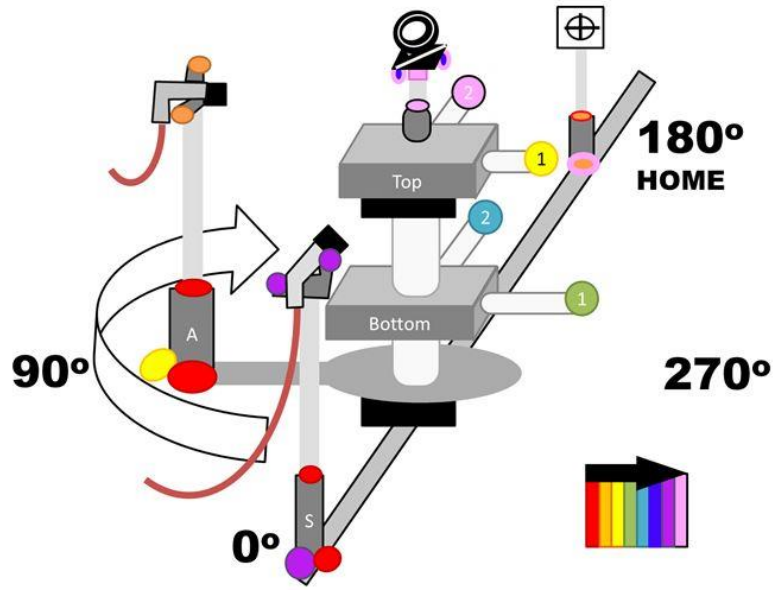


Figure 46 : Schematic view of the goniometer setup. The fixed source is labelled in purple and red. The detector mounted on its rotary arm is labelled in orange, red and yellow. The central pole holds the sample at its top. Colour labels highlight the settings tuning sequence using micrometre screws.

A typical goniometer plot such as in Figure 47 consists of a heat map plot showing the detector angle as a function of the wavelength, the intensity being the third dimension labelled by colours. The large yellow line at 180° detector angle corresponds to the ballistic light from the source that has gone through the sample without encountering any scattering event. The two cyan branches correspond to the iridescent optical response of the sample. One can notice that higher wavelengths scatter at higher angles of incidence, in good agreement with the Bragg law.

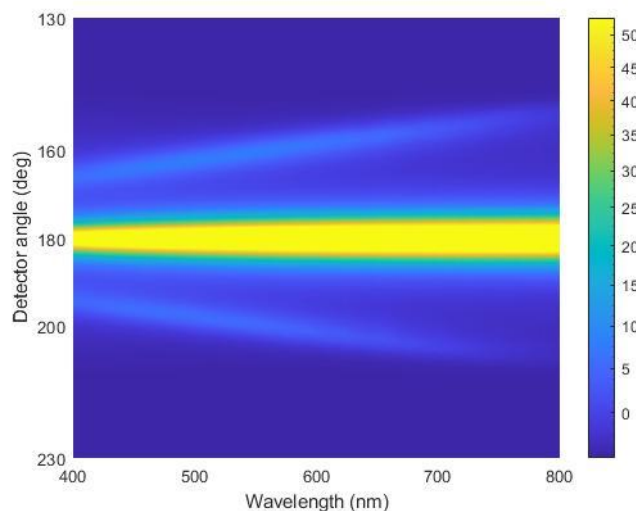


Figure 47 : Goniometer plot of a PMMA-CNC composite material aligned under magnetic fields. Direct light of the source corresponds to the large yellow line saturating the detector at an angle of 180°

(transmission without any scattering event). The two cyan branches correspond to the iridescent optical response of the sample.

The two iridescent peaks are not completely separated from ballistic light peak but they can be isolated in the residues of a gaussian-lorentzian fitting of the ballistic light peak that is re-adjusted for each angle value (Figure 48). Polydispersity in pitch is extracted from the full width at half maximum (FWHM) in angle from the iridescent peaks, further converted into a pitch interval using the Ferguson law.

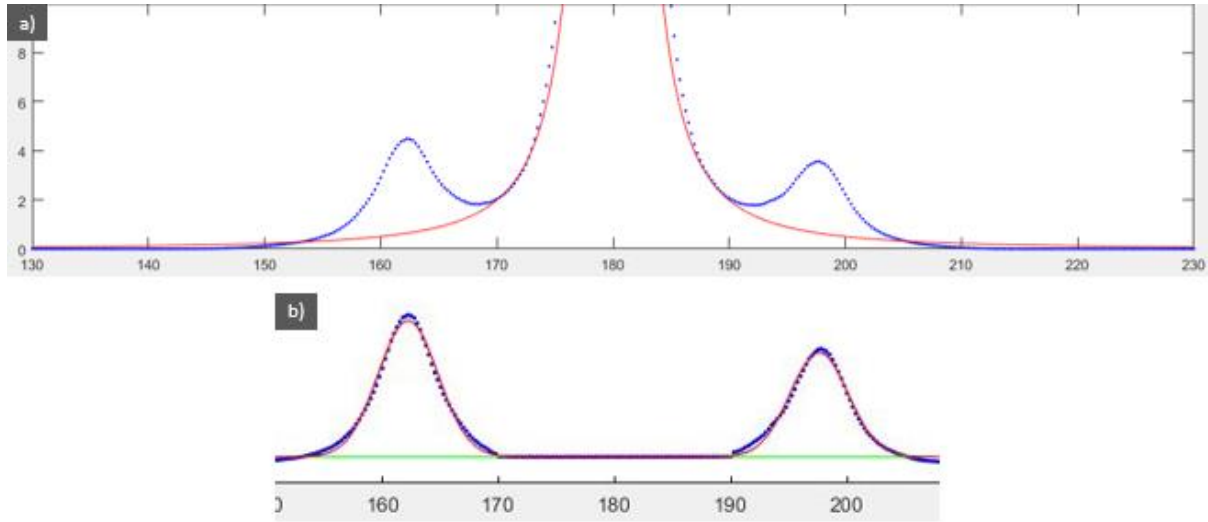


Figure 48 : a) Ballistic light subtraction by a 70% gaussian/30% lorentzian `peakfit.m` function in Matlab (red line) from the experimental data (blue dots) of intensity as a function of the detector angle. b) Iridescent peak signals recovered from the residues of ballistic light subtraction.

To conclude on optical characterisation, laser diffraction allows to scan locally the orientation and pitches of helices located in the plane perpendicular to the laser beam. This technique allows for quantitative determination of the pitch value of CNC helices as well as an order parameter for the planar orientation of helices, intensity scattered being directly proportional to the number of helices pointing in a given direction. White light diffraction allows for a sample-wide qualitative estimate of the size of the helical domains and their orientation. This method is to be seen as the complementary qualitative counterpart of goniometry, which provides a quantitative unbiased measurement of the colour response. While goniometry requires a precisely aligned optical setup and takes time to perform, white light diffraction characterisation can be used on-the-fly for example with the white light source of a cell phone, and allows to record intermediate states of alignment such as under-field suspensions configurations that would not be possible to catch with goniometry.

#### 2.5.7.4. *Optical microscopy*

Samples typically consisted of flat borosilicate capillaries or composite materials, which slightly differs from the usual microscope slides.

Polarised optical microscopy images of chapters 3 to 5 have been taken using an Axioplan (Zeiss) microscope of the ICMG platform either with no polars or in crossed polarisers configuration with an optional quarter wave plate added on the light path. Objectives x2.5, x10 and x40 have been used and complemented by an electronic zoom to approximately x100 maximum zoom.

Polarised optical images of chapter 6 have been collected with a customised ZEISS Axio scope A1 microscope in reflection mode using a Halogen lamp (ZEISS HAL100) as a light source. The reflected light could be filtered with a quarter wave plate as well. A beam splitter directed the filtered light to a CCD camera (UI-3580LE-C-HQ, IDS) and an optical fibre (core diameter 50  $\mu\text{m}$ ) that was mounted in confocal configuration to collect micro-spectroscopic data (AvaSpec-HS2048 spectrometer, Avantes).

Pitch measurements by polarised optical microscopy have been made by measuring the distance corresponding to 10 stripes of the same colour (dark or bright) for each of the 20 to 30 measurements per sample (wherever possible). Non-tilted fingerprint patterns have been privileged, *i.e.* when the dark and white stripes are of equal width and not moving while varying depth of field. In non-field aligned samples, the maximum value measured for the pitch has been kept as it is thought to account for domains laying in the plane of observation of the microscope. In field aligned samples with helices orientation in the plane of observation of the microscope, an average of the measured values has been taken.

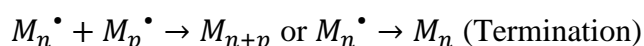
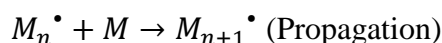
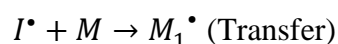
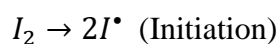
## Appendix to Chapter two: optimisation of the polymerisation of the neat PS and PMMA matrices

This section develops specifically the optimisation of the polymerisation of the neat PS and PMMA matrices that have been used to polymerise CNC-PS and CNC-PMMA composites in chapter 5. The development of such a polymerisation process involved many experimental choices, without cutting-edge characterisation since it was mainly a result-oriented approach, that are detailed hereafter to the interested reader. This appendix is however not needed to understand the results of chapter 5. For these reasons, we thought an appendix format would help not burden the main content of the manuscript unnecessarily.

### 2.6. *Free-radical polymerisation*

A short overview of the process highlighting the most relevant features in regard to this work is given hereafter. The reader is invited to refer *e.g.* to G. Moad and D. H. Solomon's seminal book for further information on this topic (Moad and Solomon 2006).

In free-radical polymerisation, an initiator molecule is likely to break its molecular structure upon UV irradiation to form two radicals. These initiators are often acylphosphine oxides such as the one presented in Figure 51. Radicals are unstable and highly reactive molecules that bind to the surrounding monomer molecules in a so-called transfer reaction. The radical nature is preserved in the product of the reaction, which is likely to undergo further addition of monomer molecules a large number of times in a so-called propagation step. Once in a while, the radical recombines either with another radical of the medium or rearranges itself with a neighbouring hydrogen atom in a so-called termination reaction that has been proved to be diffusion-controlled. This is the end of the growth of the macromolecular chain, and this 'dead' chain will remain in the medium. The reaction cascade can be schematically written as:



Note that initiator end-chain is omitted for clarity in the transfer, propagation and termination steps. The whole process is very fast, typically much faster than the frequency of initiation events. Taking a picture of the medium at moment M, there is a very high chance to

only observe dead macromolecular chains and monomer, waiting for the next initiation event to occur. As the reaction continues, dead chains accumulate, increasing gradually the viscosity of the medium. Whenever a sufficient amount of dead chains has been grown (this amount depends on the average molecular weight of the chains), these chains tend to entangle one with another a lot like in a spaghetti dish. This physical entanglement is at the origin of the gelation of the reaction medium at intermediate monomer conversions of 35-40%. Due to this gelation effect, subsequent growing macromolecular chains are no longer freely moving in suspension during their growth. Because termination reactions are diffusion-controlled, they are less likely to happen in a gelled environment. As a consequence, macromolecular chains grow much longer in length and monomer conversion increases quickly as shown in Figure 49c) and d): this phenomenon is referred to as the Trommsdorff effect, or auto-acceleration of the polymerisation (O'Shaughnessy and Yu 1994a, 1994b). The reaction medium typically has two molecular weight populations as highlighted by the gel permeation chromatography (GPC) presented in Figure 49d). The presence of inhibitors in the reaction medium can be detected by an “induction period” in which monomer conversion increase is delayed at short polymerisation times.

An interesting consequence of the aforementioned macromolecular chain formation process is that the growth and final length of macromolecular chains is independent on the concentration of initiator: growing chains see the same environment regardless of the initiator concentration, conversely to *e.g.* an anionic polymerisation where chains grow simultaneously and chain length scales inversely with the amount of growing chains. Their physical entanglement triggering the auto-acceleration of the reaction takes place evenly at all initiator concentration. Tracking gel time of thermoplastics is therefore believed to be a non-biased indicator of the monomer conversion inside the reaction medium as long as the molecular weights of the chains remain similar, and is much easier to perform experimentally than tracking monomer conversion.

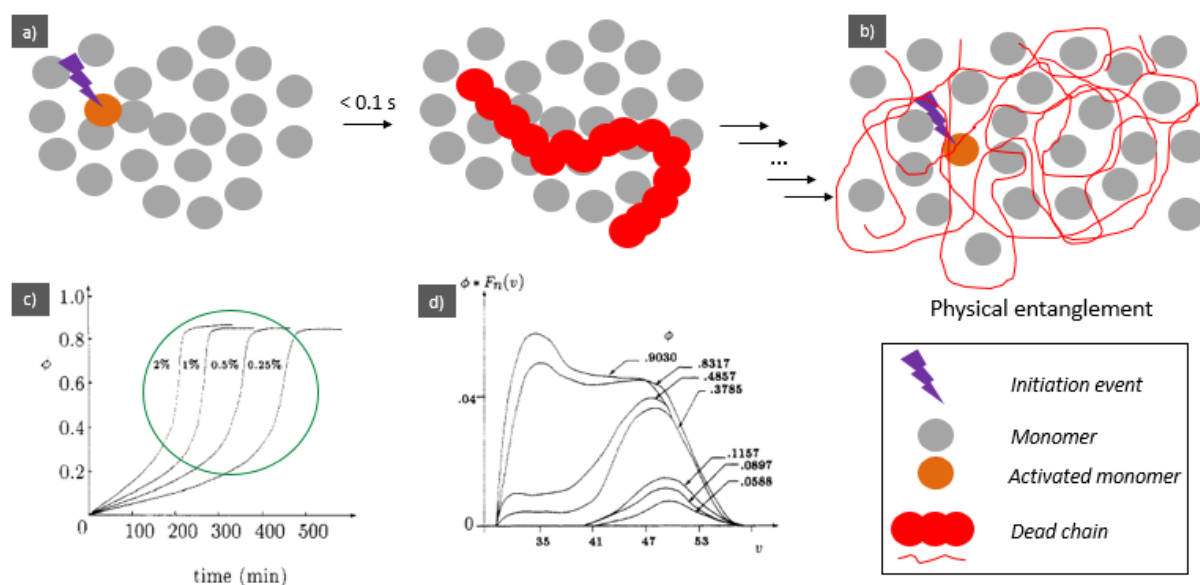


Figure 49 : Schematic highlighting the main steps of a free-radical polymerisation process in a simplified way. a) An initiation-propagation-termination sequence leading to the growth of a macromolecular chain. b) Physical entanglement of the medium at the origin of the auto-acceleration of the reaction (Trommsdorff effect). c) Monomer conversion as a function of the time: the impact of the Trommsdorff effect on polymerisation speed of PMMA is highlighted in green. Adapted from O'Shaughnessy and Yu, *Macromolecules* 1994, 27, 5067-5078. d) GPC results from Balke and Hamielec, *J. Appl. Pol. Sci.*, 1973, 17, 905. Raw chromatogram height is plotted as a function of the retention volume for different monomer conversions in PMMA polymerisation.

## 2.7. Previous works

J. Astruc and N. Montesanti worked partly on the polymerisation of PS and PMMA composites incorporating CNCs during their internships in CERMAV (Astruc 2014; Montesanti). J. Astruc studied the polymerisation of PS matrices using the following chemical composition: [Irgacure] = 1%, [Divinylbenzene] = 10% and 30%, [CNCs+surfactant] = 20% to 31% (anisotropic domain). He reports regions with no cellulose nanocrystals in his composite materials, indicating an inhomogeneous distribution of charges. He mainly performed mechanical characterisation using dynamical mechanical analysis (DMA) on the composite materials with contradictory results observed. N. Montesanti studied the polymerisation of PMMA matrices containing 1% Initiator (detailed in the next section) and 1% azobisisobutyronitrile (AIBN) which is a thermal initiator, 10% polyethyleneglycoldimethylacrylate (PEGDMA) which is a macromolecular di-functional cross-linker, CNC+surfactant from 0 to 30 wt.% and MMA. Her polymerisation process consisted of a 15 minutes UV-polymerisation followed by a thermal post-polymerisation at 80 °C and 150 °C (explaining the presence of AIBN in the medium). She reports on transparent neat polymer matrices obtained in 36x8x2 mm<sup>3</sup> Teflon moulds that become increasingly opaque as CNC content is increased. Thermal annealing at 80 °C yields slightly better mechanical



properties. Mechanical analysis of the materials in DMA presented in Figure 50 is consistent with a cross-linked material as a drop of Young modulus of 2.5 decades before reaching a rubbery plateau at high temperature is observed. Increasing CNC content induces an increase of the Young modulus at the rubbery plateau which is a classical observation in composite materials. Overall her materials seem more advanced than J. Astruc's PS composites.

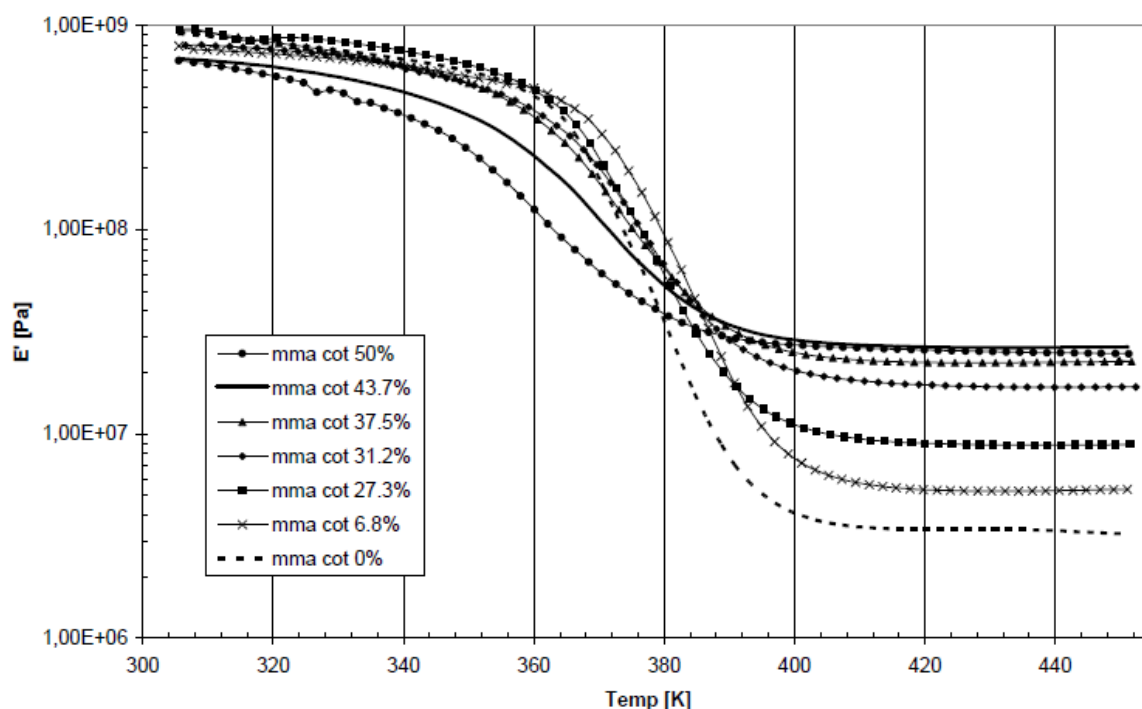


Figure 50 : Young modulus of PMMA-CNC composites of varying charge content as a function of temperature from dynamic mechanical analysis (DMA) characterisation. Reproduced from N. Montesanti, Master internship report.

## 2.8. Fixing the chemical composition of the neat polymer matrices

In this first part, a range of experimental parameters are set for the polymerisation of neat PS and PMMA matrices. Consequences on the microstructure of the polymer networks and alternative choices are discussed. Because a lot of these parameters are common to both PS and PMMA matrices, the optimisation of both systems are presented together and differences are highlighted.

### 2.8.1. Choice of the initiator

In a previous internship in CERMAV, N. Montesanti used Darocure 1173, Irgacure 819 and Irgacure 2022 as initiators of the photopolymerisation of PMMA (Montesanti). The chemical structure of the active molecule of Irgacure 819, phenylbis(2,4,6-trimethylbenzoyl) phosphine

oxide, and its absorption spectrum are presented in Figure 51. Both the UVASPOT F-lamp in CERMAV and the LZY-UVB lamps of Cambridge have an illumination peak around 300 nm that matches well the absorption peak of Irgacure 819 (Irgacure\_supplier\_data ; Lamps\_details), explaining the efficiency in initiation of these molecules. N. Montesanti reported Darocure 1173 and Irgacure 2022 to favour surface polymerisation of the samples whereas Irgacure 819 favours polymerisation in the volume. In a short comparison study, Darocure 1173, Irgacure 2022 and phenylbis(2,4,6-trimethylbenzoyl) phosphine oxide have been used at 1 wt.% to polymerise MMA. Darocure 1173 induced surface polymerisation of the samples, whereas Irgacure 2022 and phenylbis(2,4,6-trimethylbenzoyl) phosphine oxide polymerised very similarly in the volume. In the following study, both initiators have been used likewise without noticing any difference. Both probably contain the same active molecule displayed in Figure 51.

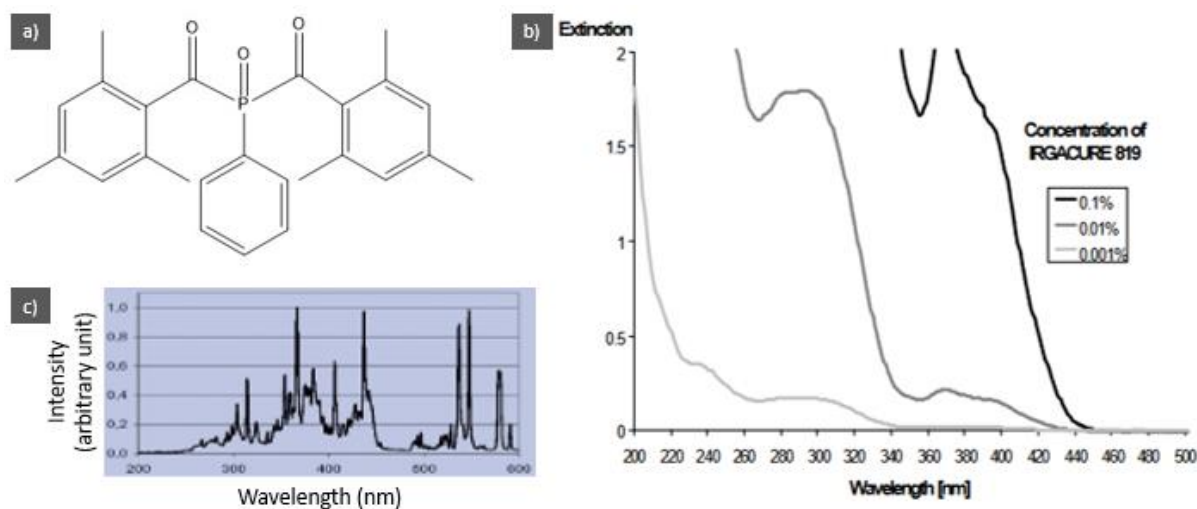


Figure 51 : a) Chemical structure of phenylbis(2,4,6-trimethylbenzoyl) phosphine oxide, the active molecule of Irgacure 819. b) Absorption spectrum of Irgacure 819 at different concentrations in acetonitrile from a general supplier website. c) Emission spectrum of the UVASPOT F-lamp.

### 2.8.2. Influence of the initiator concentration

We first studied the influence of the initiator concentration on the polymerisation of thermoplastic PMMA and PS. Gel time of MMA samples containing Irgacure 2022 at 0.02, 0.25, 0.5, 1 and 2 wt.%, presented in Figure 52, decrease as the amount of initiator is increased, especially at low initiator concentration. The initiator concentration has another visible impact on the Trommsdorff effect: the more concentrated the initiator, the more abrupt the auto-acceleration of the polymerisation reaction. This is typically noticeable on the final appearance of the samples of Figure 52. All samples are fully transparent, indicating both that the polymer

is completely amorphous and that the initiator is fully consumed at all concentrations (*i.e.* no residual yellow colour observed).

Gel time of styrene samples presented in Figure 52 is much longer than MMA samples at the same initiator concentration. The optical appearance of the samples also shows a residual yellow colour at  $[I] > 0.5$  wt.%, indicating the presence of remaining initiator in these samples. The Trommsdorff effect has no visible effect on the appearance of the samples. These observations are in good agreement with the expected lesser reactivity of styrene to radicals created by UV irradiation compared to PMMA (Kruger et al. 2011; Salami-Kalajahi, Haddadi-Asl, and Roghani-Mamaqani 2012). While most of the literature polymerise PS using thermal initiators like azobisisobutyronitrile (AIBN) (Davankov and Tsyurupa 1990), this is hardly compatible with the use of electric and magnetic fields during polymerisation, which is the reason why PS has been polymerised with free radicals in this work. Next sections are dedicated to exploring means to reduce the polymerisation reaction time, particularly for PS but also for PMMA.

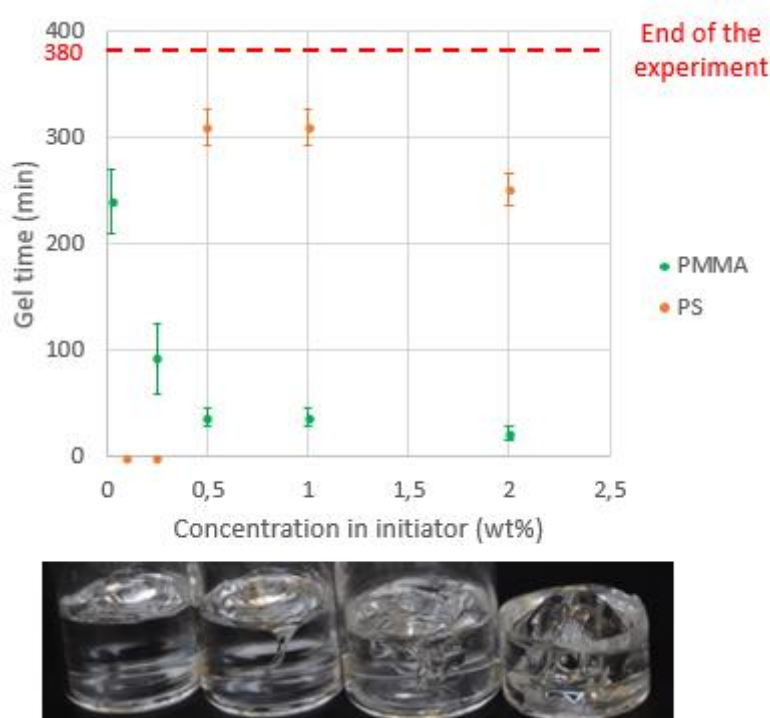


Figure 52 : (top) Gel time as a function of the initiator concentration for neat MMA (green) and styrene (orange) polymerisation over 380 min. At 0.1 and 0.25 wt.% in initiator, styrene does not gel over the course of the experiment. (bottom) Sample series showing the impact of the Trommsdorff effect on the optical appearance of PMMA samples: from left to right, 0.25%, 0.5%, 1% and 2% initiator concentration.

### 2.8.3. Influence of the cross-linking

Whenever a monomer of functionality  $f \geq 2$  is introduced in the reaction medium, it acts as a cross-linker between macromolecular chains, leading to the formation of a macromolecular network referred to as thermoset. In previous internships in CERMAV (Montesanti ; Astruc 2014), N. Montesanti used polyethylene glycol dimethylacrylate (PEGDMA) as a macromolecular di-functional cross-linker for the polymerisation of PMMA and J. Astruc used the di-functional cross-linker divinylbenzene for the polymerisation of styrene. However, using PEGDMA as a cross-linker of PMMA in this work resulted in no significant reduction of the gel time and aggregated macromolecular chains visible by eye that do not dissolve in the reaction medium, probably due to ageing of PEGDMA given the clean mechanical characterisation results of N. Montesanti. PEGDMA being also a readily-formed macromolecule, adding PEGDMA as a cross-linker in suspension does increase the overall viscosity of the medium compared to a molecular cross-linker such as divinylbenzene.

For all these reasons, the tri-functional molecular cross-linker trimethylolpropanetriacrylate (TMPTA) has been preferred to PEGDMA for the polymerisation of PMMA whereas divinylbenzene has been used to cross-link polystyrene. Corresponding chemical structures are presented in Figure 53. Network formation improves the mechanical properties of the material by reducing creeping, increasing the Young modulus and preventing material collapse at high deformations. It also triggers gelation and the associated Tremmsdorff effect earlier in the polymerisation process on account of both physical and chemical crosslinking as presented in Figure 53: gel time is divided by two at 5 wt.% and divided by three at 10 wt.% compared to the corresponding thermoplastic matrix, which is interesting for locking in cholesteric structures earlier and accelerating the overall polymerisation reaction. In the early part of this work, cross-linkers at typically 2 wt.% have been added to the monomers in polymerisation reactions. The amount of cross-linker used has been later increased to 10 wt.% in both systems for other reasons that are developed in the section Syneresis in CNC-PS composites.

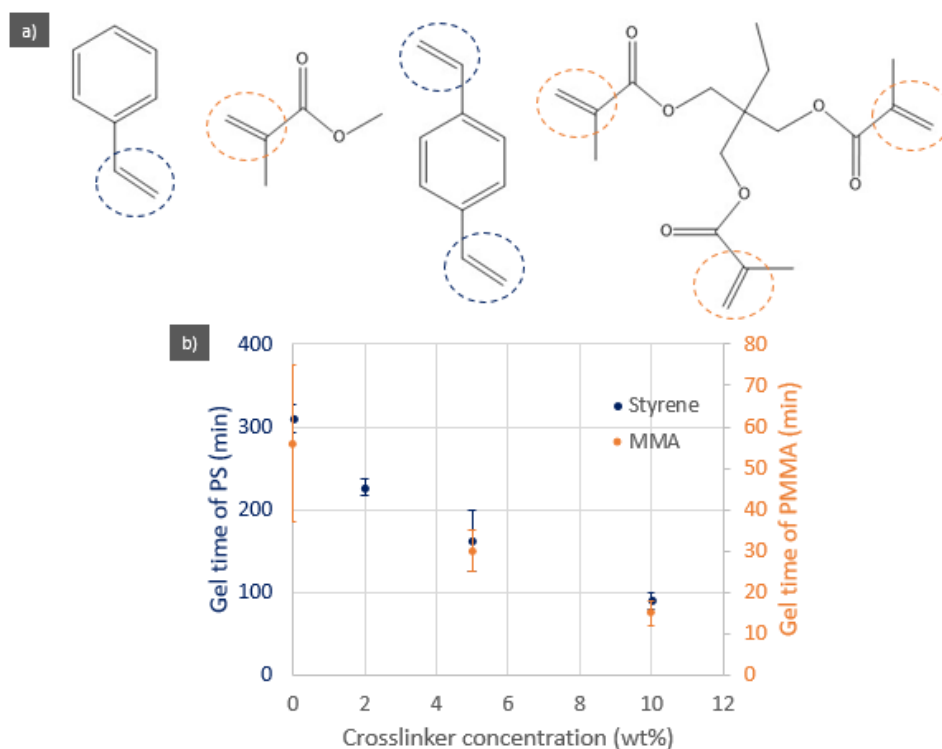


Figure 53 : a) Chemical structures of (from left to right) styrene, MMA, divinylbenzene, TMPTA. Their respective reactive groups are highlighted in dashed circles. b) Gel time of PS and PMMA as a function of the crosslinker concentration (DVB for styrene, TMPTA for MMA). The amount of initiator is 0.5 wt.% in all samples.

#### 2.8.4. Influence of polymerisation inhibitors

Polymerisation inhibitors may be responsible for the long polymerisation times observed in PS systems. In this section, inhibitors added to commercial monomers – less than 30 ppm of 4-methoxyphenol in the case of PMMA, and less than 1000 ppm of 4-tertbutylcatechol in the case of styrene according to the manufacturer – and the inhibiting properties of dissolved O<sub>2</sub> are studied.

It has been tried to remove commercial inhibitors with two methods recommended by the literature (Woon, Dicken, and Bruice 1986; Collman, Kodadeck, and Brauman 1986) and detailed in chapter 2: NaOH-washing and separation columns filled with aluminium oxide. Upon washing styrene with NaOH, the aqueous phase turned red instantaneously upon mixing, which is likely a signature of phenolate formation. However, the precise amount of inhibitor removed could not be assessed by <sup>1</sup>H NMR. Inhibitor removal led to a reduced gel time during the polymerisation of polystyrene presented in Figure 54, however the effect is not that important. Separation has been performed with three different columns: two lab-made columns filled respectively with basic and neutral aluminium oxide and a commercial column from

Sigma-Aldrich (Inhibitor\_remover). Styrene flushed through these columns had a similar gel time to neat styrene as observed in Figure 54.

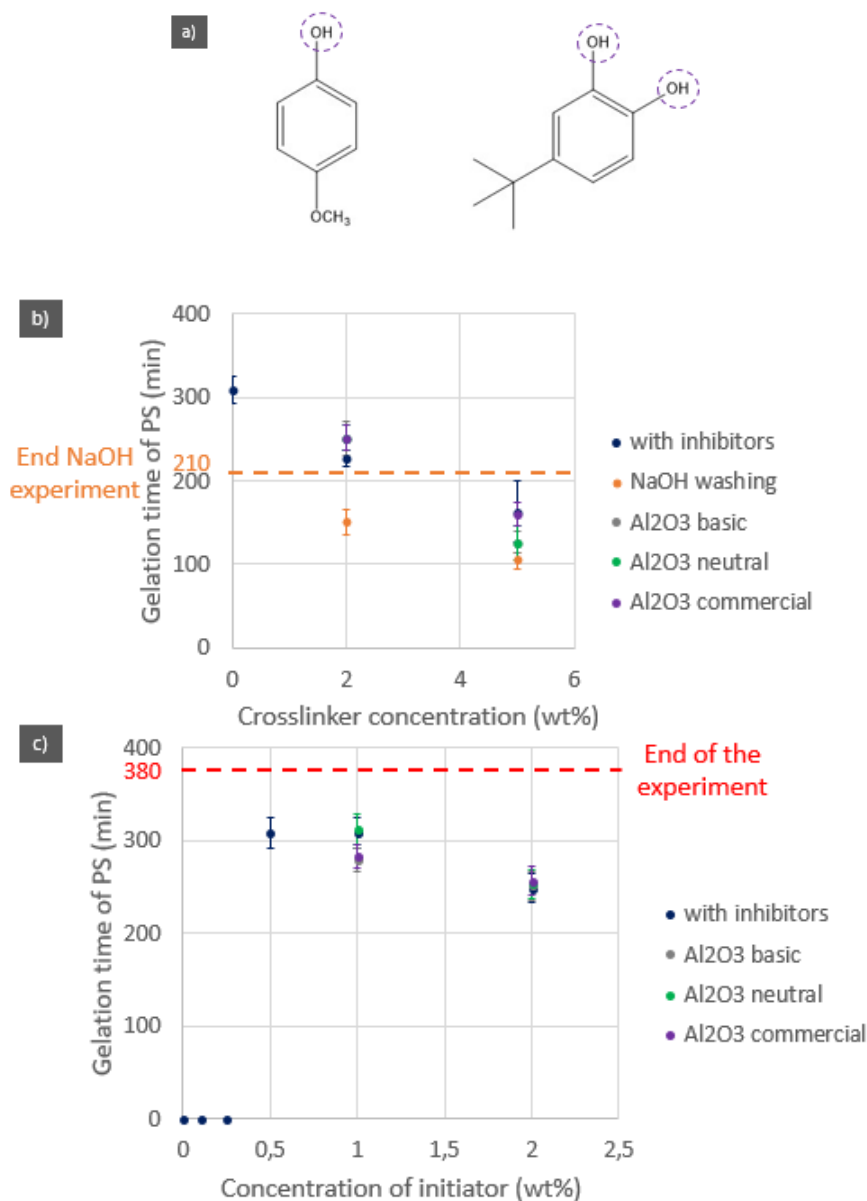


Figure 54 : a) Chemical structures of the polymerisation inhibitors present respectively in MMA (4-methoxyphenol, left) and styrene (4-tertbutylcatechol, right). b) Gel time of polystyrene samples containing 0.5 wt.% of Irgacure 2022 after NaOH washing, separation on neutral, basic and a commercial neutral aluminium oxide column of styrene. c) Gel time of polystyrene from neat and column-separated styrene at varying initiator concentration. A gel time of 0 min indicates no gelation over the course of the experiment. In c), points are slightly offset one from another for readability.

The influence of dissolved O<sub>2</sub> on the gel time has been investigated by bubbling N<sub>2</sub> into the medium prior to polymerisation and compared to control samples at different initiator concentrations. Results presented in Figure 55 only show an influence of dissolved O<sub>2</sub> at low initiator concentration below 0.1 wt.%, for which it importantly reduces gel time. At low

initiator concentration, it is likely that a significant fraction of growing chains are quenched by  $O_2$  dissolved in the reaction medium following early chain termination events and yield shorter dead chains. This participates in reducing monomer conversion inside the medium and delay gelation. At higher initiator concentration, the amount of initiator in the medium seems to vastly overwhelm the amount of  $O_2$  dissolved in the reaction medium. The proportion of growing chains quenched by  $O_2$  remains small, corresponding to no noticeable effect on gel time.

In the end, NaOH-washing has not been considered beneficial enough with respect to the additional constraints added in the process to be implemented. A rather high amount of initiator of 0.5 wt.% has been kept in the medium to compensate for the influence of polymerisation inhibitors. While these two polymerisation conditions lead to similar monomer conversion and polymerisation times, one must bear in mind that the final materials are fundamentally different. When inhibitors are removed, a lower amount of chains grow, which are typically longer in length due to rare termination events. When inhibitors are kept, a bigger amount of chains grow, which undergo more frequent termination events leading to shorter chains and lower mechanical properties.

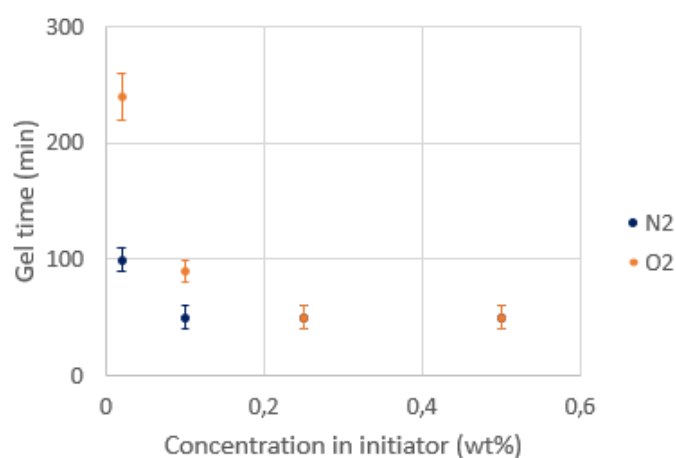


Figure 55 : Influence of the quenching by atmospheric  $O_2$  on the gel time of styrene polymerisation at different initiator concentrations. There is no cross-linker in these samples.

### 2.8.5. Thermal analysis

Thermal analysis of the polymer matrices by differential scanning calorimetry (DSC) has been performed since it is a fast characterisation informative on crystallinity, residual monomer content and chain length.

For PS matrices, DSC is performed 2 hours after capillary opening on a sample containing 2 wt.% DVB and 0.5 wt.% Irgacure polymerised for 8 hours and reproduced in Figure 56. The

broad peak between 135 °C and 165 °C is attributed either to the boiling of residual styrene monomer (approximately 2 wt.% monomer) or a post-polymerisation thermal curing. This value is likely underestimated because of the fade time between capillary opening and the DSC measurement, leading to an expected monomer conversion between 90 and 98%. This result is suggested by O'Shaughnessy and Yu's study (O'Shaughnessy and Yu 1994a, 1994b): our systems do not reach 100% monomer conversion because it is increasingly difficult for monomers to react together to form new macromolecular chains as the reaction medium becomes less and less concentrated in monomer.

A hardly but reproducibly visible slope change is observed at 66 °C, attributed to the glass transition temperature  $T_g$  of PS. Literature reproduced in Figure 57 confirms the small heat flow involved during the transition. This lower  $T_g$  value compared to the expected value  $T_{g,\infty} = 95\text{ °C}$  is both due to the presence of residual monomer and short macromolecular chains, whose experimental impact on the glass transition temperature is given in Figure 57 and described by the Flory-Fox equation:

$$T_g = T_{g,\infty} - \frac{K}{M_n}$$

where  $M_n$  is the molecular weight in number and K an empirical coefficient. The value of the glass transition temperature suggests the presence of relatively short polymer chains, whose molecular weight would be around 3000 g/mol if monomer conversion would have been 100%. While it is difficult to take accurately into account the impact of the incomplete monomer conversion on the glass transition temperature, molecular weights of the chains are thought to be in the 5 to 10 kg/mol range. This result is consistent with the relatively low reactivity of PS in free-radical polymerisation, lowering the amount of propagation events before a termination event takes place. The temperature range of the analysis does not allow for assessing crystallinity ( $T_{\text{melt}}(\text{sty}) = 240\text{ °C}$ ).



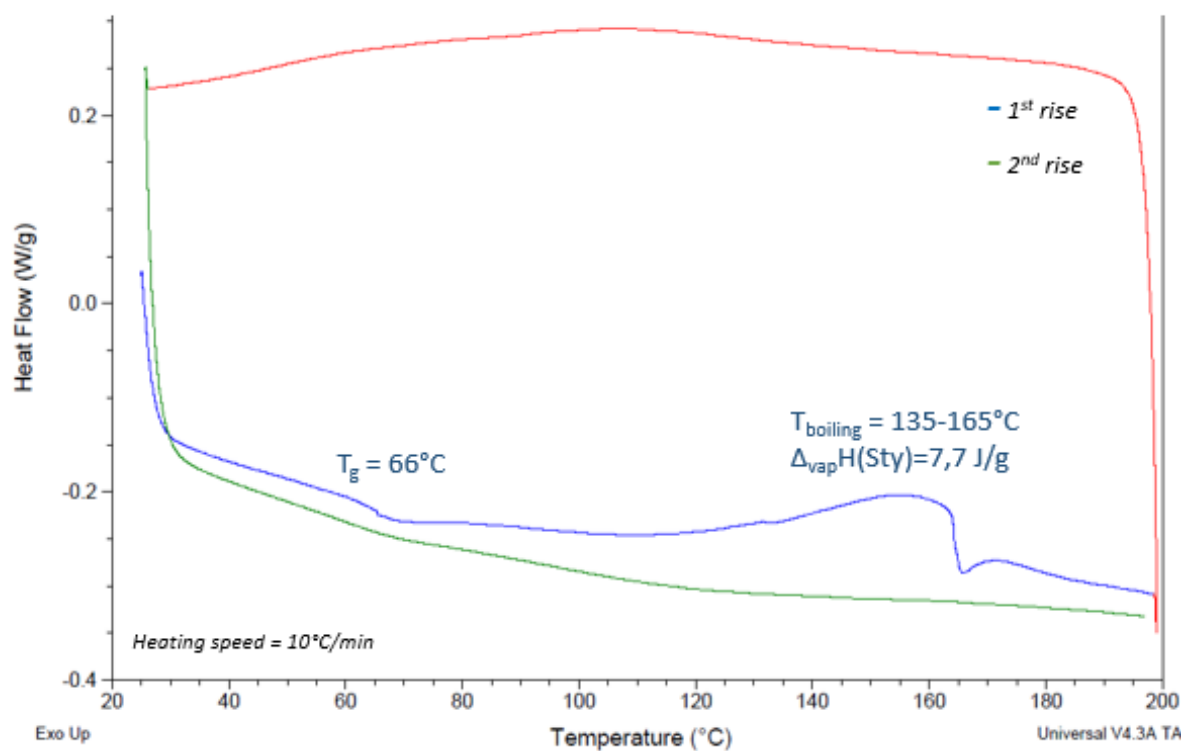


Figure 56 : Differential scanning calorimetry (DSC) analysis of a polystyrene sample containing 0.5 wt.% Irgacure, 2 wt.% DVB and styrene polymerised for 8 hours undergoing a heat/cool/heat cycle between 20 °C and 200 °C at 10 °C/min.

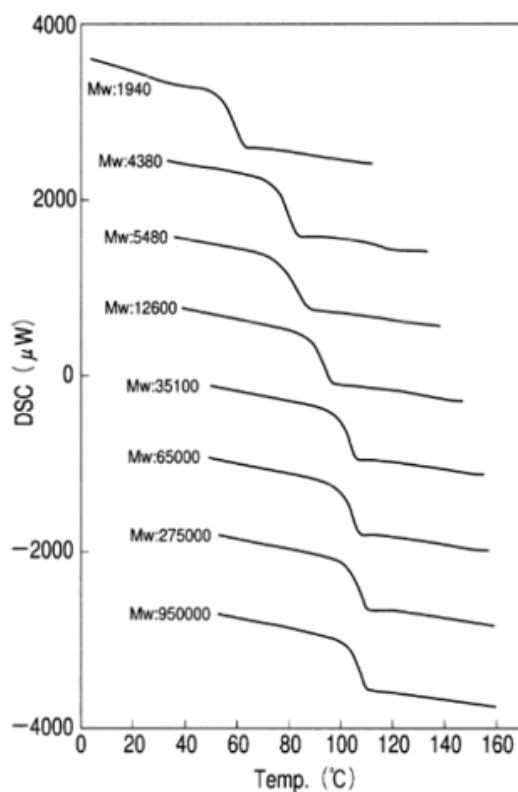
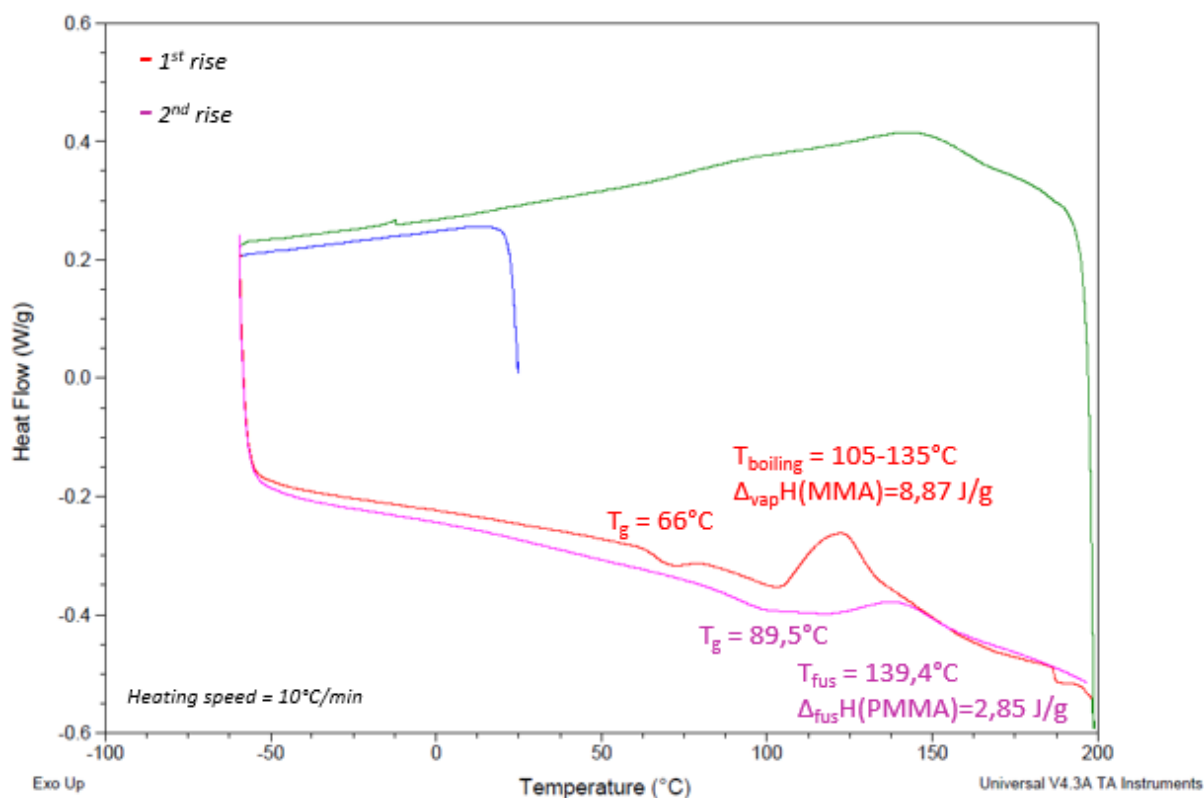


Figure 57 : Differential scanning micro-calorimetry of PS standards of different molecular weights  $M_w$  show the evolution of the glass transition temperature  $T_g$  as a function of the  $M_w$  (source: Hitachi)

For PMMA matrices, DSC results on thermoplastic PMMA show a broad peak in first rise between 105 °C and 135 °C corresponding to 2.5 wt.% residual monomer or a post-polymerisation thermal curing process and a second peak at 139 °C in second rise corresponding to approximately 3% crystallinity in the material that both disappear upon cross-linking the matrix. Residual monomer evaporation shifts the glass transition temperature value from  $T_g = 66\text{ °C}$  to  $T_g = 89.5\text{ °C}$ , closer to the theoretical value  $T_{g,\infty}(\text{PMMA}) = 105\text{ °C}$ .



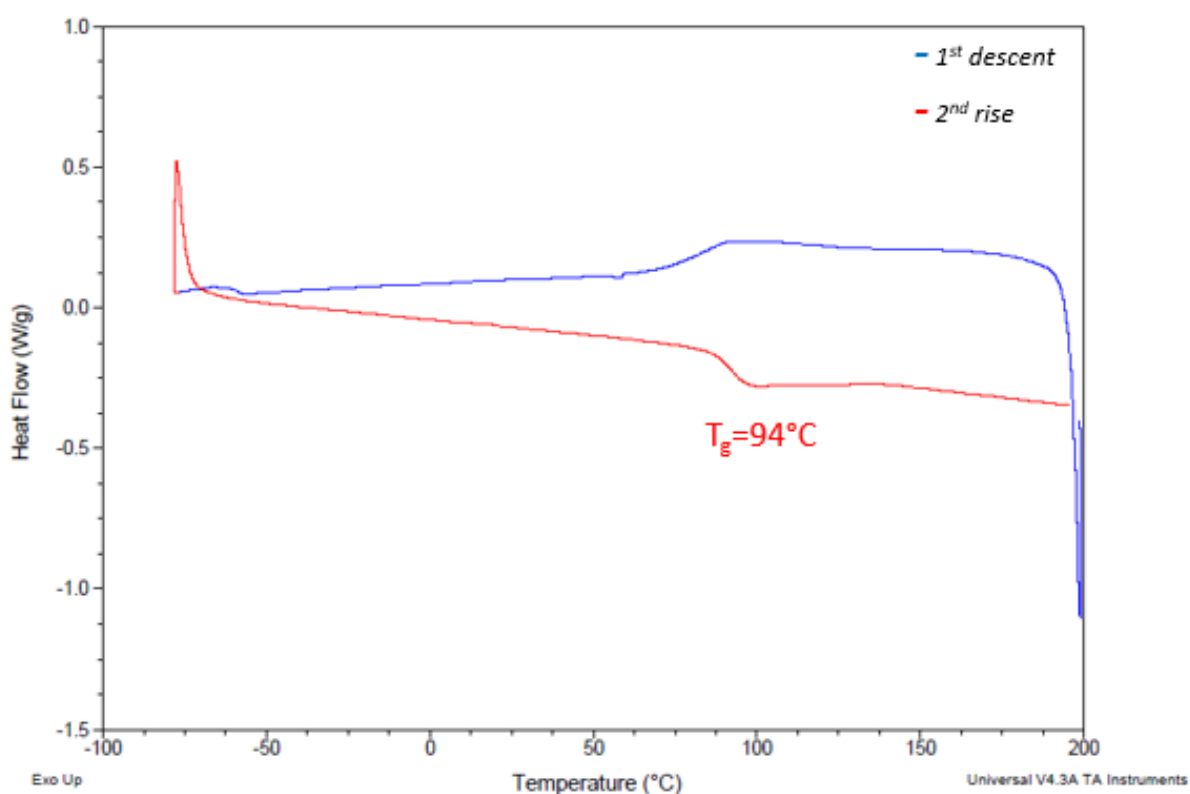


Figure 58 : Differential scanning calorimetry of a PMMA sample containing 0.25% Irgacure and MMA polymerised for 2h30 (top) and a sample containing 0.25 wt.% Irgacure, 10 wt.% TMPTA and MMA polymerised for 2 hours (bottom) and undergoing a heat/cool/heat cycle between 20 °C and 200 °C at 10 °C/min.

To summarise this first section on fixing the chemical composition of the polymer matrices, a single initiator phenylbis(2,4,6-trimethylbenzoyl) phosphine oxide (Irgacure 2022) has been used throughout this work based on former and present studies. DVB and TMPTA have been used as respectively di and tri-functional cross-linkers of the PS and PMMA matrices. Chemical compositions have been set following gel time studies at 0.25 wt.% Irgacure and 2 wt.% TMPTA for the PMMA matrix and 0.5 wt.% Irgacure and 2 wt.% DVB for the PS matrix. Cross-linker concentrations have been later increased to 10 wt.%. A gel time study on the influence of polymerisation inhibitors has been conducted as well. While they do impact the polymerisation reaction, their effect has not been considered important enough to add another removal step in the process. Thermal analysis of PS and PMMA matrices proved incomplete monomer conversion by a few percent in thermoplastic systems. Cross-linked PMMA is fully amorphous, in good agreement with its visual transparency. Glass transition temperatures of both PS and PMMA indicate chains of short to medium length, expected as a consequence of the experimental choices made on inhibitors and initiators. PS has been found to be less

sensitive to UV-induced polymerisation than PMMA, in good agreement with the existing literature (O'Shaughnessy and Yu 1994a, 1994b; Louie, Carratt, and Soong 1985; Kruger et al. 2011).

## **2.9. *Optical properties of the neat matrices***

This work aims at making composite films. For optical applications, a film of CNC helices as thin as 10-20  $\mu\text{m}$  (Zhao et al. 2019; Schütz et al. 2020) is enough to yield a saturating reflectivity of 100% of left circularly polarised (LCP) light (*i.e.* 50% of non-polarised light). In the following, we discuss issues arising when trying to polymerise films in borosilicate capillaries. These capillaries 100  $\mu\text{m}$  to 1 mm thick were selected because they are already suited for field alignment experiments of chapter 4.

### **2.9.1. Transparency in “bulk” and glass capillaries**

Surprisingly, the transparency of both PS and PMMA materials is modified when polymerised in a glass capillary compared to in a vial. After 15 minutes of the polymerisation of PMMA and after 1 hour of the polymerisation of PS, samples in capillaries display a pale blue colour characteristic of Rayleigh scattering, whereas samples in vials remain completely transparent. Optical microscopy shows the nucleation of numerous bubbles or droplets around a micron in size as in Figure 59 at early steps of the polymerisation. Light scattering keeps increasing as polymerisation is pursued, yielding translucent films.

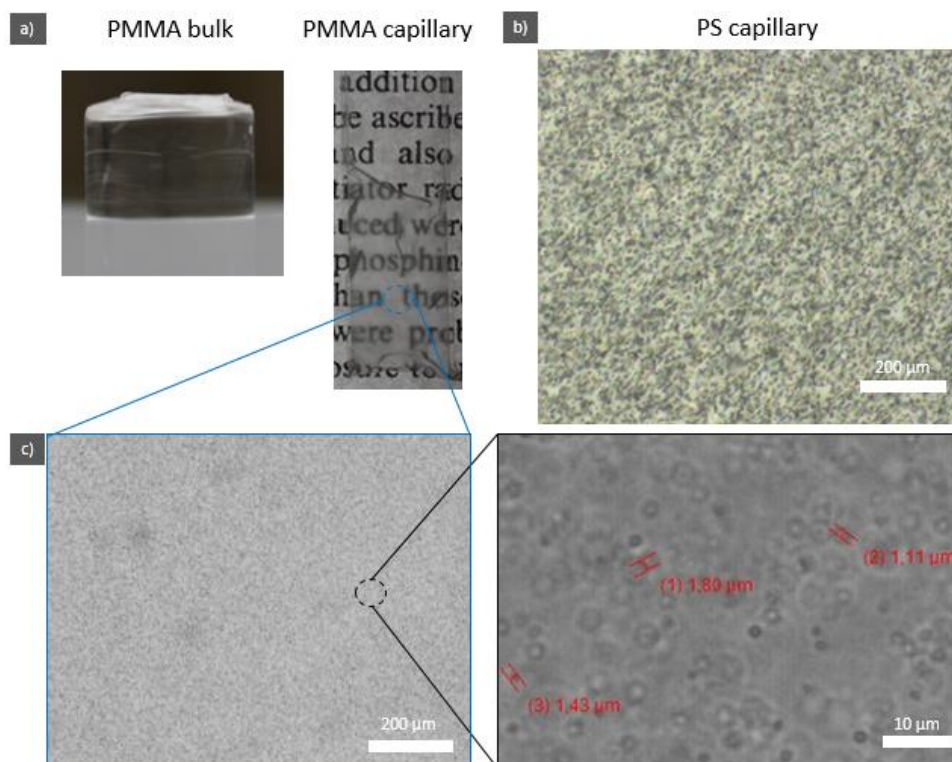


Figure 59 : a) Visible appearance of bulk and capillary PMMA, showing differences in transparency. Optical microscopy of b) a PS capillary and c) a PMMA capillary displaying micron-sized bubbles or droplets that have nucleated at early steps of the polymerisation.

Numerous experiments have been carried out to understand better the origin of these bubbles, what they were made of and most importantly how to remove them. Polymerisation at constant sample temperature has been performed by dipping the capillary in a water bath during polymerisation with no impact on bubble formation, therefore excluding monomer boiling ( $T_b = 106\text{ }^{\circ}\text{C}$ ) as a possible origin. Leaving the capillary open or closed did not change anything to bubble nucleation, indicating that this is not the result of an overpressure inside the sealed capillary. Hydrophobic treatment of the capillary by  $\text{C}_{18}\text{H}_{37}\text{-SiCl}_3$  surface-grafting detailed in chapter 2 followed by PMMA polymerisation did not improve the transparency. Contact angle characterisation before and after hydrophobic treatment presented in Figure 60 pointed out a real loss of the wetting capability of water from  $\theta \sim 40^{\circ}$  to  $\theta \sim 120^{\circ}$ , whereas MMA was still relatively wetting the treated surface. This is why fluorinated surface treatment has been tried as well using  $\text{C}_{18}\text{F}_{37}\text{-SiCl}_3$  surface-grafting, with no impact on the transparency nor bubble formation in the material however. Contact angle characterisation was not possible in this case because only the inner surfaces of the capillary were treated, however phenomenological changes in the wetting properties of MMA in the treated capillaries have been observed. It is worth noting that flame-sealing capillaries does destroy both surface treatments, rendering surfaces very hydrophilic again. Polymerising in rigid Teflon™ moulds

also yielded non-transparent materials. Degassing samples before and after bubble nucleation has been tried as well with no effect on the nucleation or removal of bubbles.

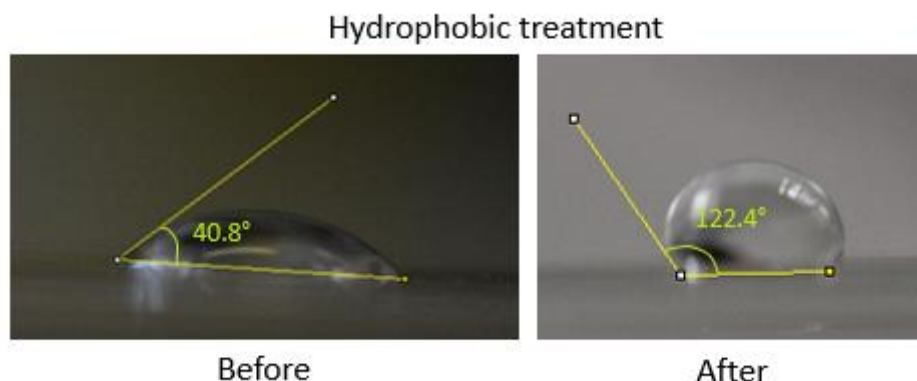


Figure 60 : Contact angle characterisation of a water droplet deposited on the outer surface of a borosilicate capillary treated with  $C_{18}F_{37}-SiCl_3$  to expose hydrophobic  $C_{18}$  pending chains.

### 2.9.2. Bulk pre-polymerisation

A successful approach to recover transparency in capillaries consisted in starting polymerisation in “bulk”, *i.e.* non surface-constrained vials and inject the reaction medium into capillaries shortly before the gelation of the polymer. This process has successfully led to a drastic reduction of bubbles in PMMA and PS polymers yielding near-transparent materials shown in Figure 61. Moreover, the pre-polymerised mixture is stable over days when kept in a cold and dark environment. This result indicates that the presence of a constrained environment at early steps of the polymerisation (before gelling takes place) causes the nucleation of bubbles. This trick is however incompatible with helical assemblies of fillers as the injection induces shear-alignment of the helices into a pseudo-nematic phase.

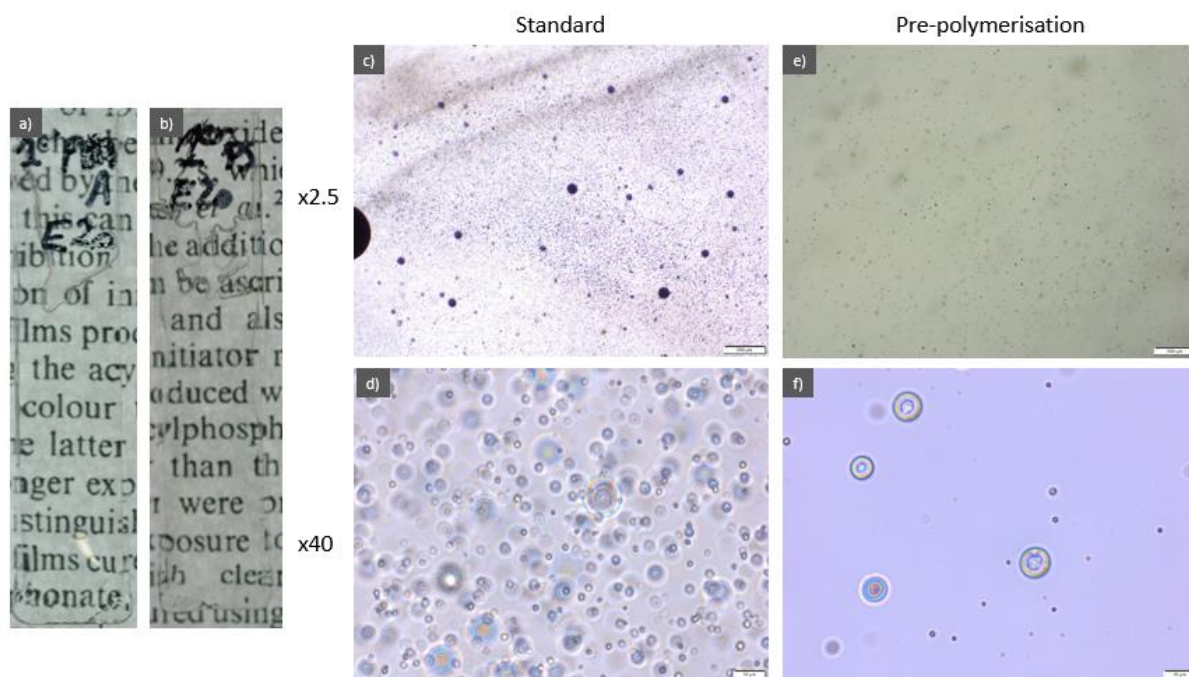


Figure 61 : Optical appearance and transparency from a) PMMA and b) PS pre-polymerised respectively for 40 min and 3h45 in bulk before being injected and polymerised in capillaries (gel time 80 min and 5h). Optical microscopy of a standard (c-d) versus a pre-polymerised (d-e) sample showing a drastic reduction of the number of bubbles trapped inside the material at different magnifications (c-e: x2.5, scale bar 200  $\mu\text{m}$  and d-f: x40, scale bar 10  $\mu\text{m}$ ).

### 2.9.3. Recovering transparency in “capillaries”

The successful approach towards recovering full transparency in capillaries consisted in changing the material capillaries were made of, from borosilicate glass capillaries to a home-made mould made of two pieces of fluoroethylenepropylene (FEP) polymer sheets with a fluorinated grease interlayer. FEP consists of flexible polymer sheets shown in Figure 62a) made of a copolymer of hexafluoropropylene and tetrafluoroethylene. Polymerising PS and PMMA in such a mould immediately yields fully transparent polymer materials shown in Figure 62b). The surface chemistry of such a mould is very similar to fluorinated C18-grafted borosilicate glass capillaries or Teflon™ moulds whereas the main difference comes from the flexibility of the FEP polymer sheets compared to the rigidity of glass. FEP moulds were observed to be impermeable to styrene but not to MMA; typically, 40-50% monomer loss is observed over the course of CNC phase separation. This evaporation is greatly reduced by adding a glass microscope blade on the outer side of each FEP sheet. The location of the air bubbles near the lateral edges of the mould suggests the grease could be responsible for the evaporation.



Based on these observations, we can suggest an interpretation of the nucleation of bubbles in glass capillaries and their absence in FEP moulds. Forming bonds during the polymerisation necessarily leads to a density increase and a corresponding volume shrinkage of the medium. On account of the densities of MMA, styrene, PMMA and PS in Figure 62, the volume shrinkage due to polymerisation is about 19.5% for PMMA and 12.5% for PS. The ability of the medium to accommodate or not the volume shrinkage upon polymerisation seems to dictate the transparency of the final material. In that scope, flexible FEP moulds allow the medium to contract in a cohesive manner, whereas adhesion to surfaces dominates in capillaries. The microscopic expression of this phenomenon is the micro-fragmentation of the suspension into micron-sized bubbles that get trapped by the polymerisation before they can coalesce together to form bigger voids, leading to the observed light scattering.

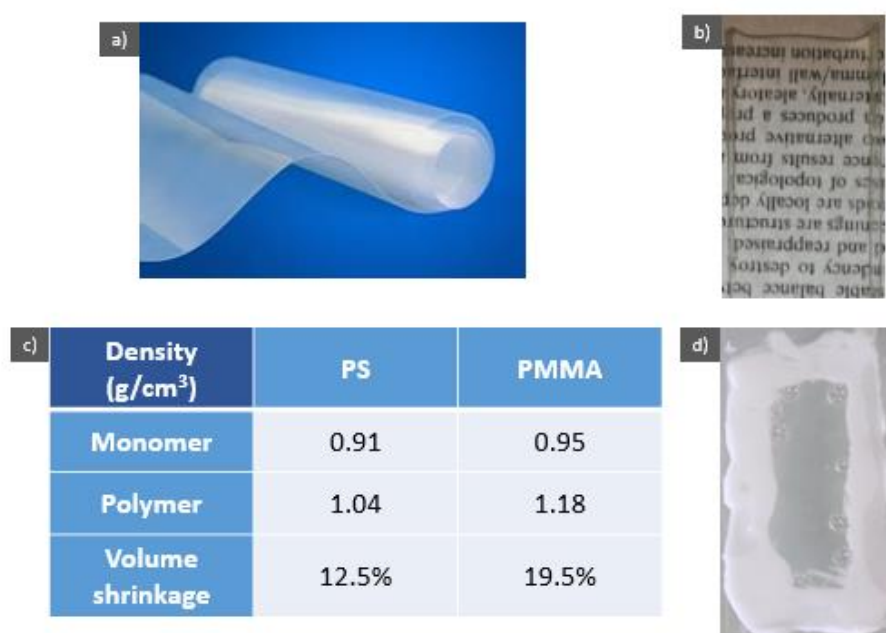


Figure 62: a) FEP polymer sheets used to make a flexible fluorinated mould (source [www.techsling.com](http://www.techsling.com)). b) Transparent PS obtained by simple polymerisation in the FEP mould (89.5 wt.% styrene, 10 wt.% DVB, 0.5 wt.% Irgacure). c) Densities of PS and PMMA monomer and polymers and corresponding volume shrinkage. d) MMA evaporation after 14 hours in the FEP mould.

## 2.10. Conclusions

In this appendix, the free-radical polymerisation of PS and PMMA polymer matrices has been optimised by studying the influence of the initiator, the cross-linker and the polymerisation inhibitors on the gel time of the matrices. The decision of not removing inhibitors from the polymerisation medium led to shorter macromolecular chains evidenced in DSC along with some residual monomer and the absence of crystallinity in PMMA matrices.



Unexpected loss of transparency has been encountered in the neat matrices while downsizing the material from bulk to capillary films due to the nucleation of micron-sized bubbles at early steps of the polymerisation. These bubbles seemed to arise from a micro-fragmentation of the liquid triggered by, on one hand, accumulated contraction stress from volume shrinkage and, on the other hand, strong surface wetting in the confinement of a capillary. Moving to a flexible home-made mould made of FEP polymer sheets allowed to release these internal constraints and recover transparency in the neat matrices.



## Chapter 3. Steric stabilisation of CNCs in organic apolar solvents

*« C'était aussi pour ça qu'il m'avait choisi.  
Parce que j'avais le strerf, le combat intérieur  
de celui qui se sait en-dessous. »  
A. Damasio, La Horde du Contrevent*

This chapter presents a strategy to disperse CNCs in organic apolar solvents and monomers using surfactants, a necessary step before the alignment of the suspensions under external fields in chapter 4, composite materials making in chapter 5 and the drying of CNC films in chapter 6. The first part reviews different strategies of the literature to disperse CNCs in organic solvents and monomers and the modification of their self-assembling properties. The second part presents an experimental study to find a new surfactant capable of dispersing CNCs in organic apolar solvents. In a last part, we discuss the origin of the viscosity increase over time in the suspensions by reasoning on the range of the colloidal interactions in suspension.

### 3.1. *State of the art*

#### 3.1.1. Why is it interesting to try to disperse cellulosic materials in organic solvents?

The appealing mechanical, optical and self-organisation properties of cellulose nanocrystals and cellulose nanofibers make them interesting candidates as fillers of composite materials. However, these very hydrophilic objects contrast with the overwhelming majority of industrial polymer composite materials on the market that are hydrophobic polymers. Figure 63 presents polymer sales in the US in past few years and projections for the future: more than 90% of the market consists of 6 different hydrophobic polymers : polyethylene (PE), polypropylene (PP), polyvinylchloride (PVC), polystyrene (PS), polyurethane (PU) and polyethylene terephthalate (PET). Restraining cellulosic materials to be fillers in hydrophilic polymer matrices would be missing more than 90% of their potential market applications in composite materials.

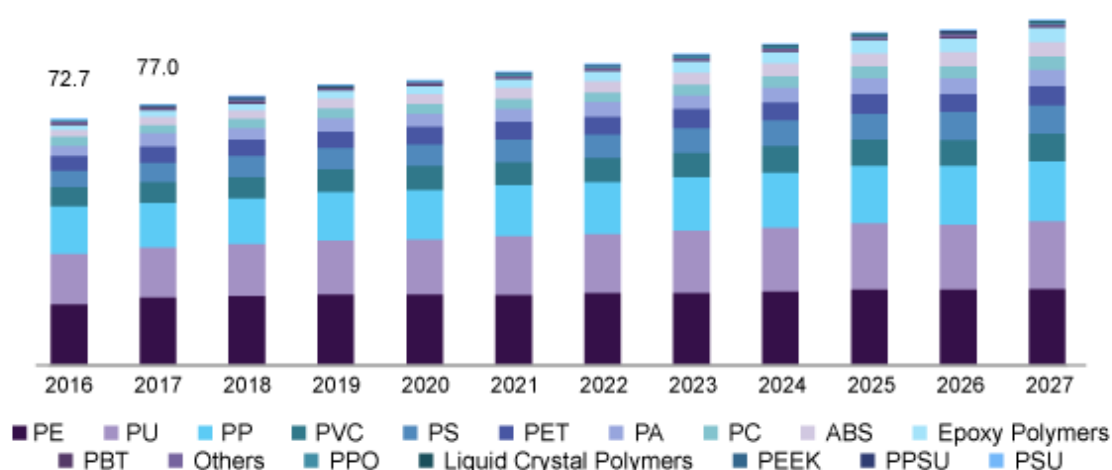


Figure 63 : Actual and projections of market size of plastics in the U.S. between 2016 and 2027 in billion USD. Colour legend indicates the size of the market polymer by polymer within the total. Source: [www.grandviewresearch.com](http://www.grandviewresearch.com).

### 3.1.2. On the colloidal stability of CNCs in organic solvents

While the majority of the community uses electrostatic repulsion to stabilise CNCs in water ( $\epsilon = 80.1$ ), the electrostatic stabilisation is not always efficient in organic solvents. Bruckner et al. (Bruckner et al. 2016) have shown that electrostatic repulsion is efficient to stabilise CNCs in high permittivity and hydrogen bond-forming organic solvents. The authors studied the dispersion and self-assembling properties of CNCs in formamide ( $\epsilon = 111$ ), N-methylformamide (NMF,  $\epsilon = 189$ ) and dimethylformamide (DMF,  $\epsilon = 38$ ). While they prove the dispersion of CNCs in all these solvents by atomic force microscopy (AFM) characterisation, the self-assembling properties of CNCs are only maintained in the highest permittivity solvents formamide and NMF whereas CNCs tend to gel in DMF. Self-assembling typically leads to different onset concentrations for the anisotropic phase, a pitch reduction that is especially significant in NMF and shorter times needed for the self-assembly to take place compared to aqueous suspensions characterised by polarised optical microscopy.

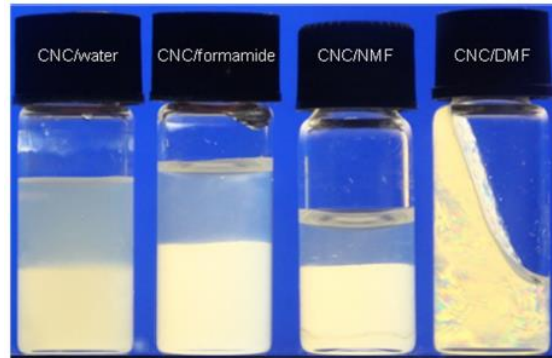


Figure 64 : Phase-separation under cross polars of centrifuged suspensions of CNCs at 6 wt.% in water, formamide, NMF and DMF. CNC/DMF is in a kinetically arrested state. Reproduced from Bruckner et al, *Langmuir* 2016, 32, 9854-9862.

By contrast, whenever neat CNCs are dispersed in toluene ( $\epsilon = 2.4$ ), they rapidly flocculate due to an additional hydrophilic attraction between CNCs and the absence of repulsive interactions. The first reason for the absence of repulsive interactions is the low dissociating power of toluene compared to water allowing few charges to exist in solution. The Bjerrum length, defined as the length at which the electrostatic interaction between two elementary charges is on the order of thermal energy, quantifies this low dissociating power:

$$\lambda_B = \frac{e^2}{4\pi \cdot \epsilon_0 \cdot \epsilon \cdot k_B \cdot T}$$

As the dielectric permittivity changes from 80.1 to 2.4,  $\lambda_B$  becomes much larger, meaning charges will be more likely to be bound to one another in solution. The dissociation equilibrium

between  $-\text{OSO}_3^-$  and  $-\text{H}^+$  is displaced into the non-ionic form, corresponding to a lower surface charge of CNCs. The second reason is the lowering of the range of the electrostatic repulsion as a direct consequence of the lower electric permittivity, owing to the dependency  $\kappa^{-1} \sim \sqrt{\epsilon}$ . As a consequence, there is obviously a need for another stabilisation mechanism for CNCs in low permittivity organic solvents.

### **3.1.3. Approaches for the compatibilisation of cellulosic materials in organic apolar solvents and materials**

A first approach towards dispersing CNCs in organic apolar solvents consists in grafting chains from the surface of CNCs. These chains typically bear reactive functional groups that will not only help to disperse the fillers in monomers, but also participate in forming the polymer network of the eventual composite material (Fumagalli et al. 2018; Ljungberg et al. 2005; Felix, Gatenholm, and Schreiber 1993; Araki, Wada, and Kuga 2001; Carlmark and Malmström 2002). Examples of the literature involve atom transfer radical polymerisation (ATRP) from the cellulose surface to graft methyl acrylate functional groups and esterification of neat CNCs and TEMPO-CNCs respectively with dithiodipropionic acid chloride, maleic anhydride to graft respectively vulcanisation reactive groups and polypropylene chains and peptidic coupling of PEG-NH<sub>2</sub> chains on TEMPO-CNCs interestingly leading to cholesteric phases in water. The advantage of this approach is that fillers are expected to take an active part in responding to the mechanical stress exerted on the matrix as they are bound to the matrix by covalent chains themselves. The big challenge of this approach relies in the development of a successful chemistry to graft onto the CNC surface. Research efforts are typically long and yield low amounts of material. The grafting also needs to be sufficiently dense to stabilise cellulosic materials sterically in organic solvents.

A more recent approach notably developed by Maclachlan's group (Cheung et al. 2013; Kose, Boott, et al. 2019; Boott et al. 2020) consists in using an intermediate organic polar solvent as a mediator between the hydrophilic fillers and the less hydrophilic polymer matrix. The mediating solvent is typically dimethylformamide (DMF) or dimethylsulfoxide (DMSO) as cellulosic materials are dispersible in both of them. A wide range of polymer matrices are claimed to be compatible with the process, ranging from acrylates such as hydroxyethylmethacrylate (HEMA) and polymethylmethacrylate (PMMA) to purely hydrophobic matrices such as polycarbonate (PC), polyvinylcarbazole (PVK) and PS. The process consists in swelling a dried CNC film in the mediating solvent containing the monomer,

polymerising the medium and finally evaporate the mediating solvent from the organogel. The film obtained by this process is similar to the method of casting dispersions of latex and CNCs, in the sense that only the percolating network of CNCs prevents charges segregation from the polymer matrix when the mediating solvent is removed. With no interfacial adhesion, fillers are not expected to actively contribute to the mechanical reinforcement of the film. The process is also limited to making films.

The last pathway to compatibilise cellulosic materials in organic apolar solvents initiated in CERMAV consists in adding surfactants to mediate the interaction between CNCs and the hydrophobic solvent (Heux, Chauve, and Bonini 2000; Elazzouzi-Hafraoui, Putaux, and Heux 2009; Ljungberg et al. 2005; Zhou, Brumer, and Teeri 2009; Qu and Zussman 2020). The chemical structures of these surfactants are given in Figure 65: a phosphorylated and ethoxylated surfactant (BNA) in the case of Heux et al. and Qu et al. and a xyloglucan-PEG-PS triblock copolymer in the case of Zhou et al.

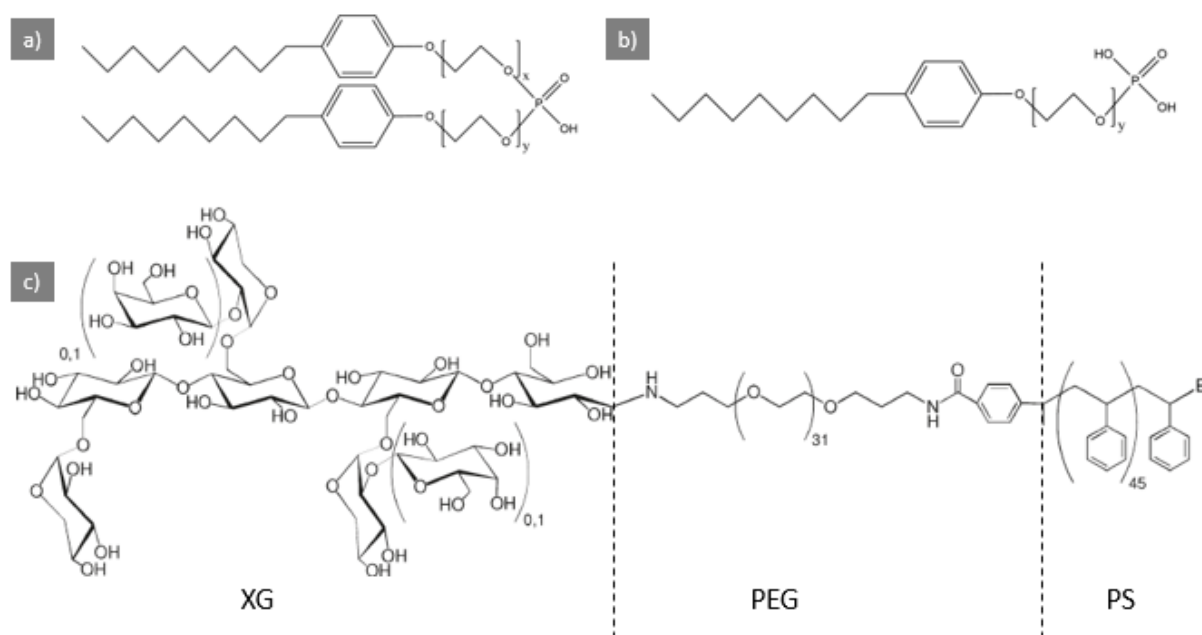


Figure 65 : Chemical structures of the surfactants used in works of the literature. Beycostat NA (BNA) is a mix of phosphate di-ester (a) and mono-ester (b). c) xyloglucan-polyethyleneglycol-polystyrene triblock used by Zhou et al. Adapted from Elazzouzi et al., *J. Phys. Chem. B* 2009, 113, 11069-11075 and Zhou et al, *Macromolecules* 2009, 42, 15.

Xyloglucan is a hemicellulose that binds naturally to cellulose in the plant cell wall. It is counter-intuitive to predict an interaction of the anionic phosphate ester head of BNA with the negatively charged surface of CNCs. Kostritskii et al. (Kostritskii et al. 2017) used molecular modelling to study the interaction between phospholipid bilayers with cellulose, and found two main driving forces for the interaction: the attractive interaction of choline groups and hydrogen

bonding of the phosphate group with the hydroxymethyl and hydroxyl groups of cellulose. While choline is not present in BNA, phosphate group hydrogen bonding on the other hand could likely take place in the system of Heux et al. By contrast with latex polymerisation and organic polar mediating solvent, this process provides colloidal stability of the objects in suspension through steric stabilisation. The process relies on a first mixing of CNCs and surfactant, followed by a freeze-drying process and a redispersion in the desired apolar solvent, in which the polar head of the surfactant is likely to interact with the cellulose surface whereas the apolar head compatibilise the particle with the solvent. In that sense, the adsorption of the surfactant is forced during the drying steps and the redispersion in the apolar solvent results in the spontaneous organisation of the surfactants at the cellulosic surface. As approximately 4-5 wt.% of tightly bound water remains after the freeze-drying step (Foster et al. 2018), CNCs surface is expected to be still hydrated in suspension. Bonini et al (Bonini et al. 2002) reported on a measurement of the thickness of the layer of bound surfactant on the surface of CNCs by small angle neutron scattering (SANS), estimated at 1.5 nm. This is basically an assessment of the range of the steric repulsion induced by the presence of the surfactant. The adsorption is reversible, which means there is a dynamic equilibrium between bound and free surfactant in suspension. This last mean of stabilising CNCs in organic apolar solvents has been used throughout this work. Its main features will be developed in the next sections.

### **3.1.4. Surfactant-stabilised CNCs self-assembly**

In both cases, surfactant stabilisation does not prevent self-assembly to take place; Zhou et al report on obtaining a cholesteric suspension of CNCs in the biphasic domain without providing additional details. Heux and coworkers (Elazzouzi-Hafraoui, Putaux, and Heux 2009; Heux, Chauve, and Bonini 2000) give a detailed analysis of the self-assembling properties of CNCs in organic solvents reproduced in Figure 66. For CNCs “Cot63” whose dimensions are approximately  $8 \cdot 26 \cdot 128 \text{ nm}^3$ , the onset of the anisotropic phase in cyclohexane is observed at 18 wt.% in concentration of CNC+surfactant and the fully anisotropic domain is reached at 34 wt.% in contrast with aqueous suspensions. The boundaries of the biphasic domain are much higher than aqueous solvents. This is attributed to the contribution of the electric double-layer present in aqueous systems to an effective volume fraction of the rods much higher than the real CNC volume fraction; it results in an early phase transition into the anisotropic domain in aqueous systems compared to organic solvent systems. Longer CNCs “Cot54” shift the phase diagram to lower concentrations, whereas shorter CNCs “Cot72” shift the phase diagram to higher concentrations, in good agreement with Onsager’s calculations. The pitch value is



drastically reduced compared to non-salted aqueous CNC suspensions, from tens of microns to the 6 to 2.5  $\mu\text{m}$  range depending on CNC concentration.

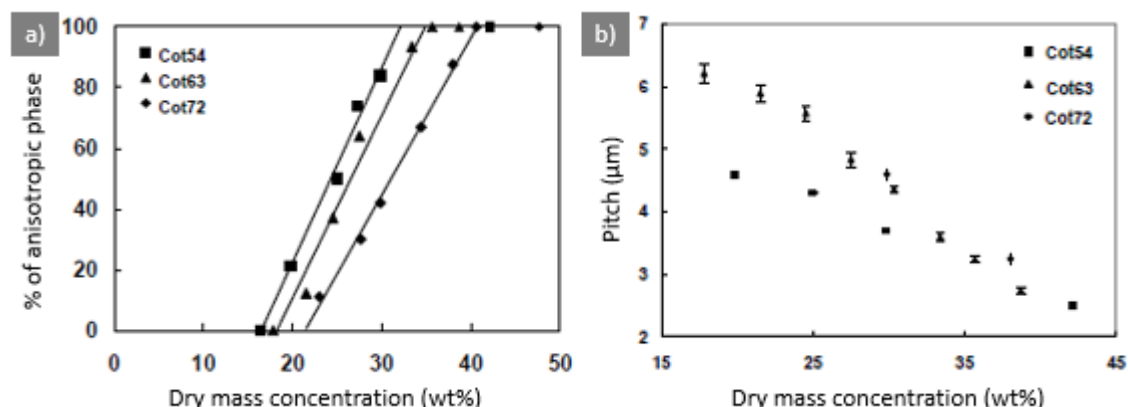


Figure 66 : a) Phase diagram of a cotton CNC suspension in cyclohexane at different hydrolysis temperatures. b) Pitch value in suspension as a function of the total concentration in CNC+surfactant measured by polarised optical microscopy. Reproduced from Elazzouzi PhD manuscript pp. 166-169.

### 3.1.5. Proportion of CNCs and surfactant in suspension

Conversely to aqueous suspensions, dry mass only gives access to the amount of CNC+surfactant in suspension. While the aspect ratio taken into account in Onsager's description of the boundaries of the phase diagram for anisotropic particles consists of CNC+surfactant in the hard core interaction limit, the chirality should be mostly brought by the particles themselves, the surfactant being essentially achiral. Elazzouzi et al. (Elazzouzi-Hafraoui, Putaux, and Heux 2009) provided an assessment of the amount of BNA bound on the surface of CNCs by UV-visible spectroscopy. They measured the proportion of adsorbed and free BNA in CNC suspensions prepared with a single centrifugation step: *e.g.* they assess 55 wt.% of BNA adsorbed on CNCs hydrolysed at 63 °C and 1.3 wt.% free BNA in suspension.

The reduced pitch value in suspension from tens of microns in non-salted CNC suspensions (Dong and Gray 1997) to 6 to 2.5  $\mu\text{m}$  in cyclohexane suspensions (Elazzouzi-Hafraoui, Putaux, and Heux 2009) suggests more intense chiral interactions between CNC rods, similarly to the pitch reduction value observed upon screening the electrostatic repulsion with salt. Kinetic arrest also takes place at higher concentrations of *ca.* 40 wt.% in CNC+surfactant (Elazzouzi 2006) in cyclohexane compared to *ca.* 19 wt.% in partially de-sulphated CNC suspensions (Parker et al. 2016).

### 3.1.6. Previous works in CERMAV on the dispersion and self-assembly in monomers

J. Astruc studied the suspension behaviour of BNA-stabilised CNCs in styrene during his master internship in CERMAV (Astruc 2014). His results reproduced in Figure 67 show that CNCs in styrene behave similarly to CNCs in toluene which is consistent with the very similar chemical structure of toluene and styrene. The only notable difference is a broadening of the biphasic domain by a few % on each side in styrene compared to toluene. Elazzouzi reports on the suspension behaviour of BNA-stabilised CNCs in methylmethacrylate (MMA) compared to toluene and cyclohexane in her manuscript. Her results reproduced in Figure 68 show that dispersing CNCs in MMA leads to a shift of the phase diagram towards lower concentrations by a few %, which she attributes to the higher value of the dielectric permittivity of MMA ( $\epsilon = 6.3$ ) compared to other solvents. The pitch value in MMA is also slightly reduced compared to other solvents.

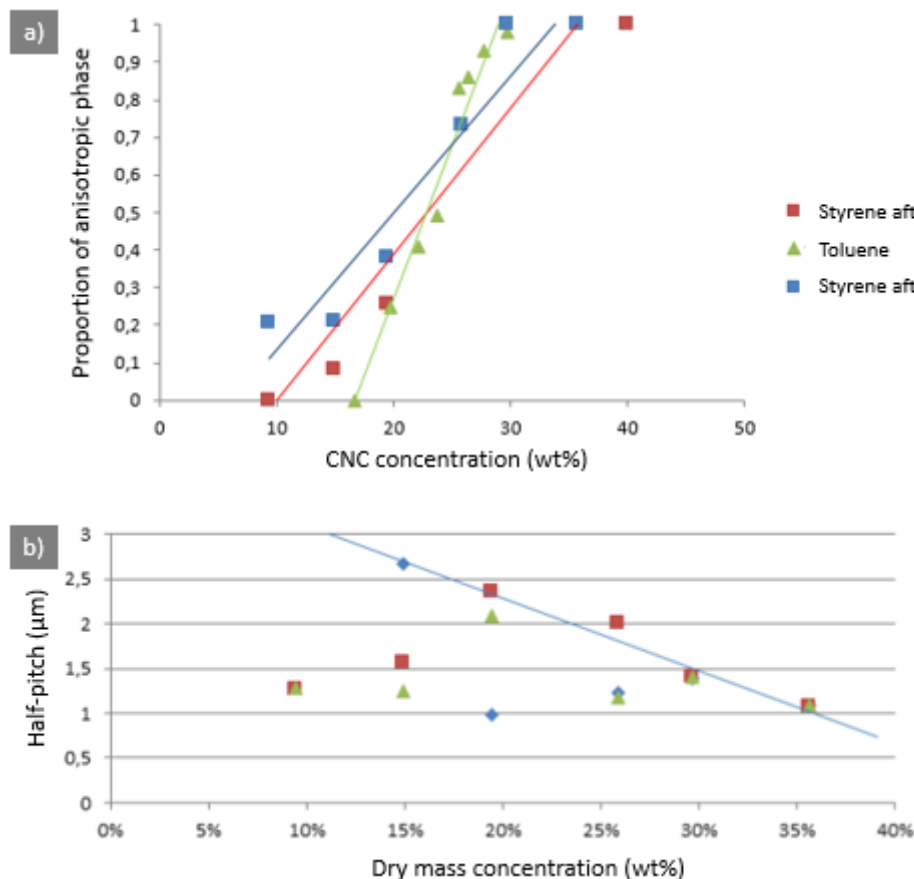


Figure 67 : a) Phase diagram of a CNC suspension in toluene and styrene. b) Half-pitch value of a CNC suspension in styrene as a function of its dry mass concentration (markers correspond to three different samples for each concentration). Reproduced from J. Astruc, master internship report p.19.

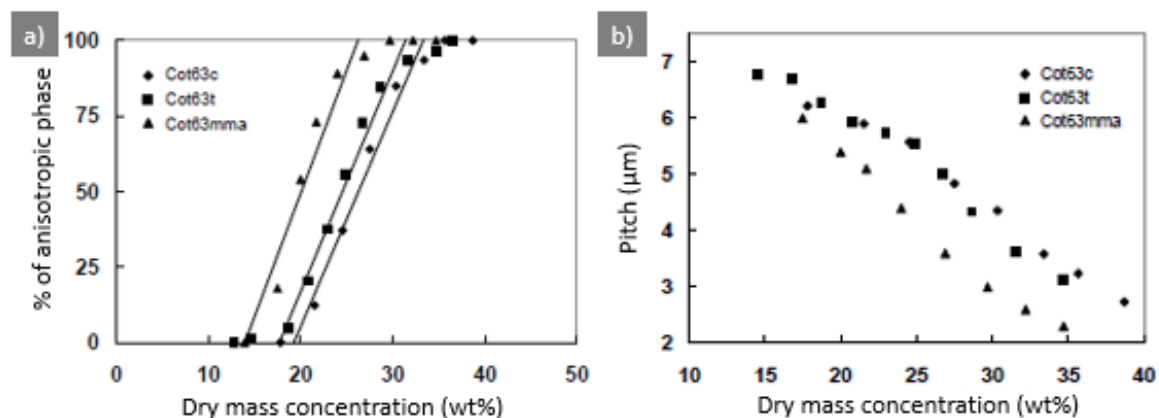


Figure 68 : a) Phase diagram and b) pitch value of CNC suspensions in cyclohexane (c), toluene (t) and MMA (mma) as a function of the dry mass concentration of the suspension. Reproduced from Elazzouzi's PhD manuscript pp. 173-174.

## 3.2. Results

### 3.2.1. Finding a new surfactant for the process

Beycostat NA, the surfactant that has been used in Elazzouzi's work is not produced by CECA Chemicals anymore. While CERMAV still hosts some remaining BNA, there is a need to find a new surfactant with similar properties than BNA to conduct this work. In that scope, Arkema has kindly supplied us with two potential candidates for the replacement of BNA: Surfaline and Melioran. The next sections study their potential to replace BNA as a steric stabiliser of CNCs in organic apolar solvents.

#### 3.2.1.1. Mass spectroscopy characterisation of the surfactants

The chemical structures of the surfactant mixes have been analysed and fully resolved by mass spectroscopy means, detailed hereafter.

BNA is an industrial mix of phosphate mono and di-ester whose pending chains are structured into a hydrophilic polyethyleneoxide (PEO) oligomer close to the phosphor atom followed by a nonylphenol hydrophobic end-chain. While literature gives 9 ethyleneoxide (EO) moieties in the PEO block (Elazzouzi-Hafraoui, Putaux, and Heux 2009), mass spectroscopy characterisation of Figure 69 shows that this is the average of a distribution ranging from 6 to 13 EO moieties. Two populations characteristic of the mix of mono and di-ester are clearly visible in mass spectroscopy, although this characterisation method does not allow for a quantitative assessment of the mono and di-ester ratio. Each peak is doubled with a  $\frac{m}{z} = 22$  spacing, indicating the presence of both  $H^+$  and  $Na^+$  counter-ions.

By carrying out the same mass spectroscopy analysis on Surfaline (Figure 70), one also observes two populations of peaks corresponding to a mix of mono and di-ester phosphates. Peaks are attributed to a C18 hydrophobic tail with a double bound – whose location has been given by the manufacturer – and a PEO hydrophilic block with a phosphate head group. The PEO block varies also between 2 and 13 EO moieties in length in the mono-ester in good agreement with the average of 8 given by the manufacturer. While a lower amount of EO moieties peaks is observed for the di-ester, it is thought to be due to the resolution of the technique.

Mass spectroscopy of Melioran given Figure 71 highlights some differences: there is only one distribution of peaks, indicating the absence of di-ester phosphates in this surfactant mix. Peaks are fully attributed to a hydrophobic saturated C12 tail and a PEO hydrophilic block composed of 5 to 15 EO moieties with a phosphate head group. Notably, the mass spectroscopy signal is a lot messier despite the high peak intensity.

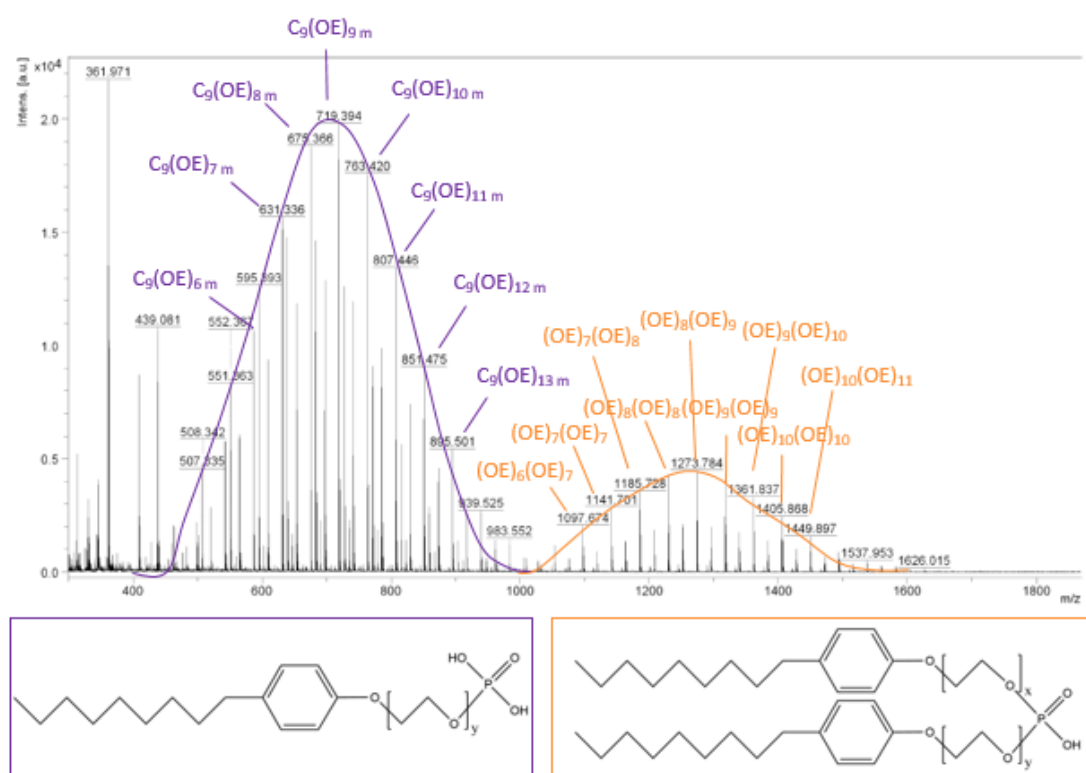


Figure 69 : Mass spectroscopy characterisation and peak attribution of Beycostat NA by electrospray ionisation reflectron positive (ESI-RP) and corresponding chemical structures,  $x$  and  $y$  ranging from 6 to 13.

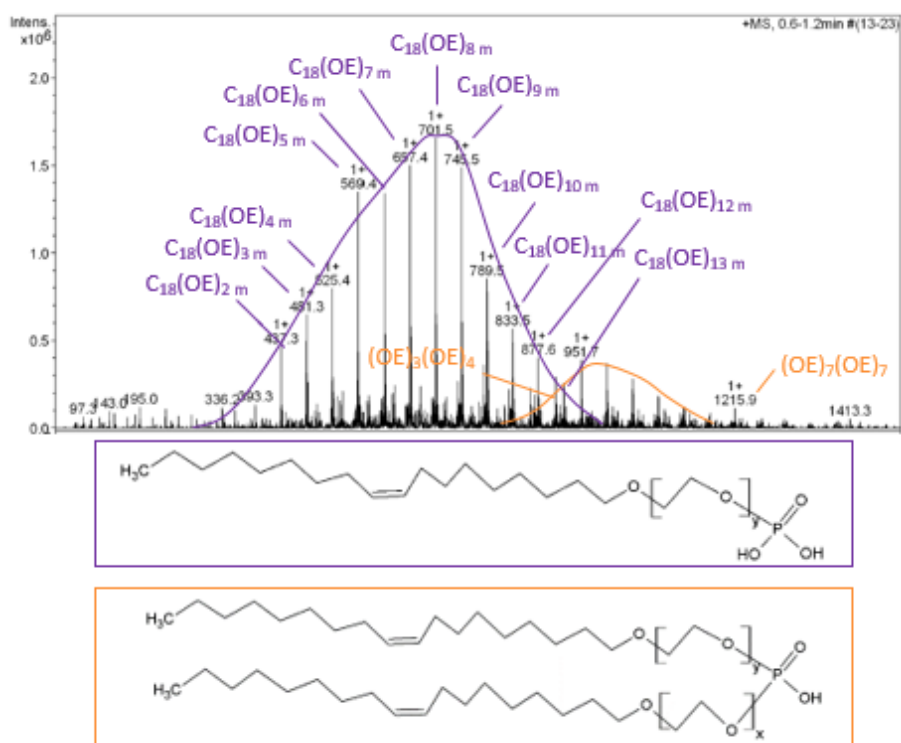


Figure 70 : Mass spectroscopy characterisation and peak attribution of Surfaline PE 683 by positive electrospray ionisation (ESI+) and corresponding chemical structures, x and y ranging from 2 to 13.

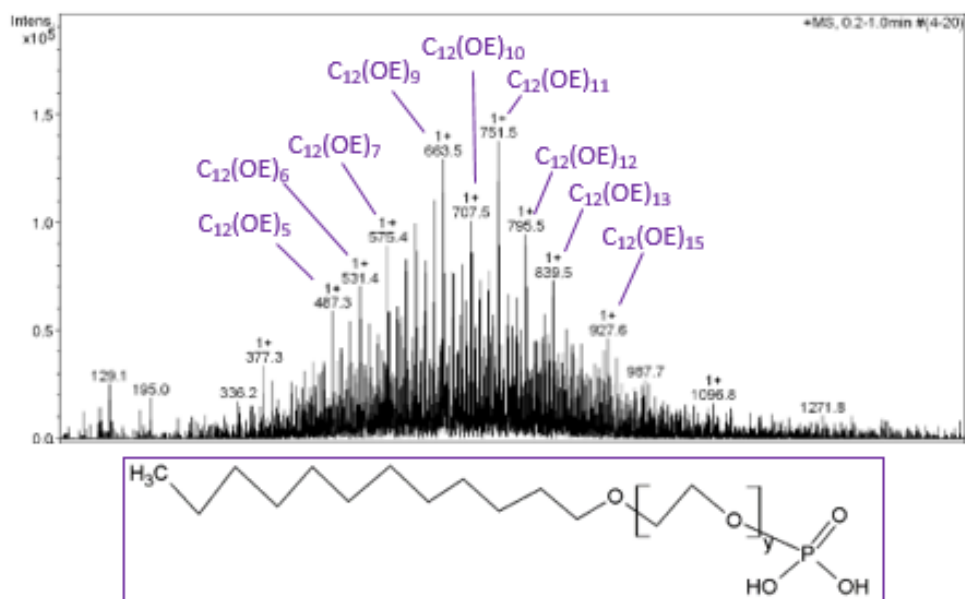


Figure 71 : Mass spectroscopy characterisation and peak attribution of Melioran by positive electrospray ionisation (ESI+) and the corresponding chemical structure, y ranging from 5 to 15.

### 3.2.1.2. On the experimental process

The experimental process used to disperse CNCs in organic solvents in this work described in chapter 2 differs slightly from the process of Elazzouzi et al. Because of the intrinsic viscosity

increase of the suspensions developed in a next section, it has been tried to remove the excess of free surfactant as much as possible. From the initial redispersion of CNCs and surfactant in toluene, repeated centrifugation-redispersion steps have been performed until destabilisation of CNCs has been observed due to surfactant removal. Sedimentation of CNCs has been observed after the third redispersion, which likely corresponds to an amount of surfactant for which the surface of CNCs is not fully covered anymore. Throughout this work, dispersions in organic solvents have been obtained using a double centrifugation-redispersion step – one additional compared to Elazzouzi's work – which likely corresponds to a lower proportion of surfactant in suspension that has not been quantitatively measured.

### ***3.2.1.3. Dispersions in organic apolar solvents***

An identical process to the one used for BNA has been applied to probe the dispersion of CNCs with Surfaline and Melioran in apolar solvents. Upon mixing CNCs with the surfactant in water, Surfaline suspension appears milky white whereas BNA and Melioran are transparent. This suggests there is already an interaction between CNCs and the surfactant in the Surfaline suspension. 24 hours after redispersion of the CNC-surfactant aerogels in toluene, Melioran suspensions sediment indicating a lack of efficient repulsive interactions in suspension. The two dispersions have been cross analysed by dynamic light scattering (DLS), transmission electron microscopy (TEM) and polarised optical microscopy (POM).

The cross analysis of Melioran-stabilised CNC suspensions in toluene is presented in Figure 72. In DLS characterisation, the CNC peak shifts towards bigger sizes and becomes much broader, indicating the presence of objects of bigger sizes. Transmission electron microscopy also shows aggregates with high electronic contrast, corresponding to tens or hundreds of objects piled up together. Finally, polarised optical microscopy in the anisotropic domain displays pastel birefringent colours without identified structures similar to what was already observed by Elazzouzi et al. for concentrated suspensions of CNCs kinetically arrested before their self-assembly takes place (Elazzouzi-Hafraoui, Putaux, and Heux 2009). Altogether, those results confirm the partial aggregation of the particles using this surfactant.

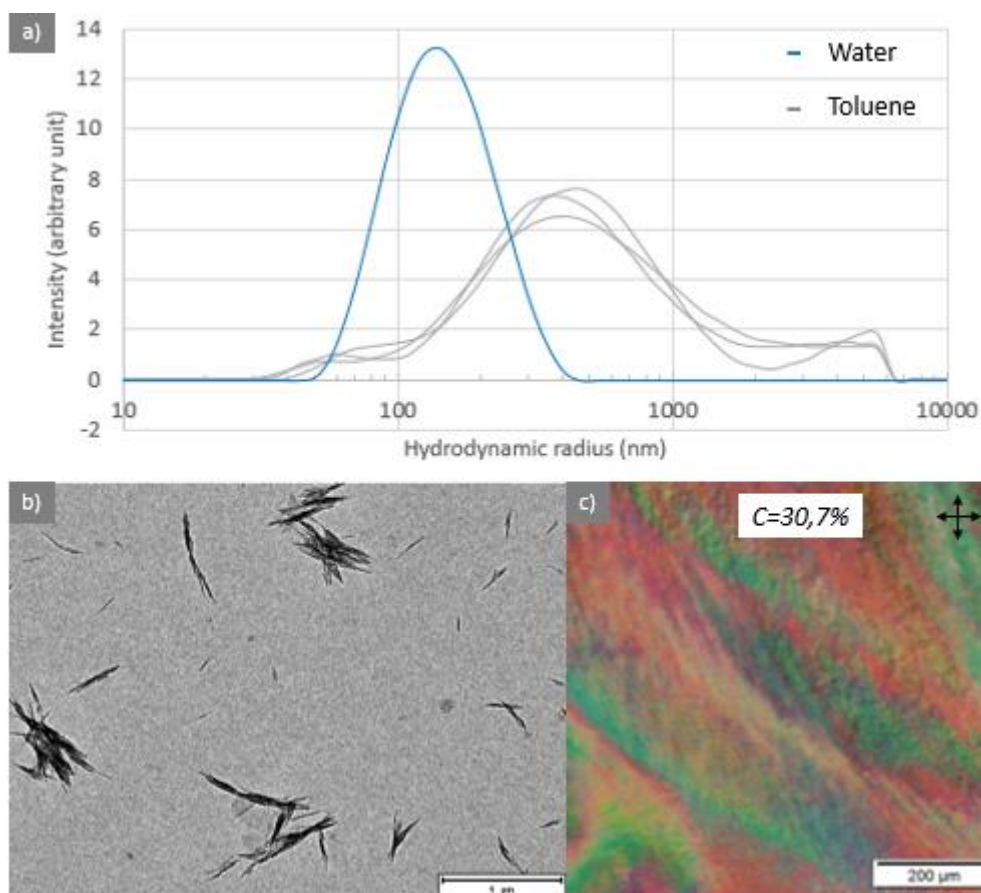


Figure 72 : Cross analysis of CNC suspensions in toluene stabilised by Melioran. a) Dynamic light scattering data plotted in log scale of the starting CNCs in water (blue) and the suspension in toluene (3 measurements, grey). b) Transmission electron microscopy image of CNCs in toluene without negative staining (scale bar is 1  $\mu\text{m}$ ). c) Polarised optical microscopy image in the anisotropic domain. Obj. x2.5. Scale bar is 200  $\mu\text{m}$ .

The cross analysis of Surfaline-stabilised CNC suspensions in toluene is presented in Figure 73. Dynamic light scattering characterisation shows a very similar distribution of sizes compared to the starting aqueous suspension, with possibly a slight broadening in size (Figure 73a). Transmission electron microscopy images shown in Figure 73b) allows to observe mostly individual crystals very similar to aqueous suspensions observed in the very same conditions, without negative staining. A significant polydispersity in size and shape is also observed, which is expected for cotton CNCs (Elazzouzi-Hafraoui et al. 2008). Polarised optical microscopy in the anisotropic domain not only proves the good dispersion of the crystals and their colloidal stability, but also their retained ability of self-assembling into cholesteric phases indicated by the observation of a characteristic fingerprint pattern. Altogether, the cross analysis provides evidence for the steric stabilisation of CNCs by Surfaline in toluene.

Using the same experimental protocol to disperse the nanocrystals in MMA with Surfaline, complete sedimentation of CNCs is observed 3 days after redispersion. The same result is



obtained using Melioran. These two surfactants do not yield stable CNC suspensions in MMA, whereas BNA led to stable dispersions in this monomer. Conversely, Surfaline achieves dispersing CNCs in styrene with a very similar self-assembly behaviour to toluene (data not shown).

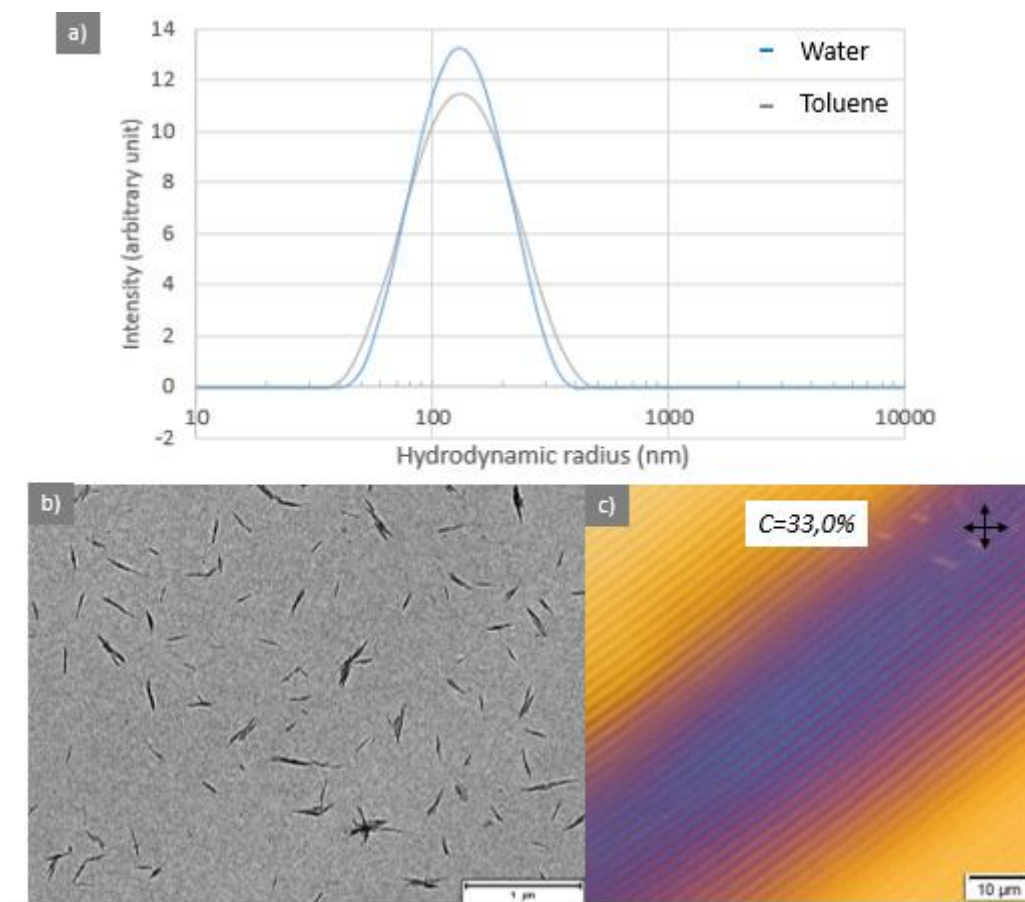


Figure 73 : Cross analysis of CNC suspensions in toluene stabilised by Surfaline. a) Dynamic light scattering data plotted in log scale of the starting CNCs in water (blue) and the suspension in toluene (grey). b) Transmission electron microscopy image of CNCs in toluene without negative staining. Scale bar is 1  $\mu\text{m}$ . c) Polarised optical microscopy image in the anisotropic domain. Obj. x40, scale bar is 10  $\mu\text{m}$ .

#### 3.2.1.4. Self-assembling properties of CNCs stabilised by Surfaline

The self-assembly behaviour of Surfaline-stabilised CNCs in toluene has been investigated in more details by establishing a phase diagram given in Figure 74. One can observe an overall similar phase diagram for CNCs stabilised by Surfaline compared to CNCs stabilised by BNA in toluene. Note that in the superimposition of the data with Elazzouzi's work on BNA of Figure 74b), data has been corrected to account for the evaporation during capillary preparation. The phase diagram of CNCs dispersed with Surfaline is very close to Elazzouzi's data in toluene (Elazzouzi-Hafraoui, Putaux, and Heux 2009). Superimposing the pitch values of Surfaline-



stabilised CNCs obtained by polarised optical microscopy measurements with the data of Elazzouzi on BNA-stabilised CNCs, it can be observed that the pitch value of Surfaline-stabilised CNCs is very close to the pitch of BNA-stabilised CNCs.

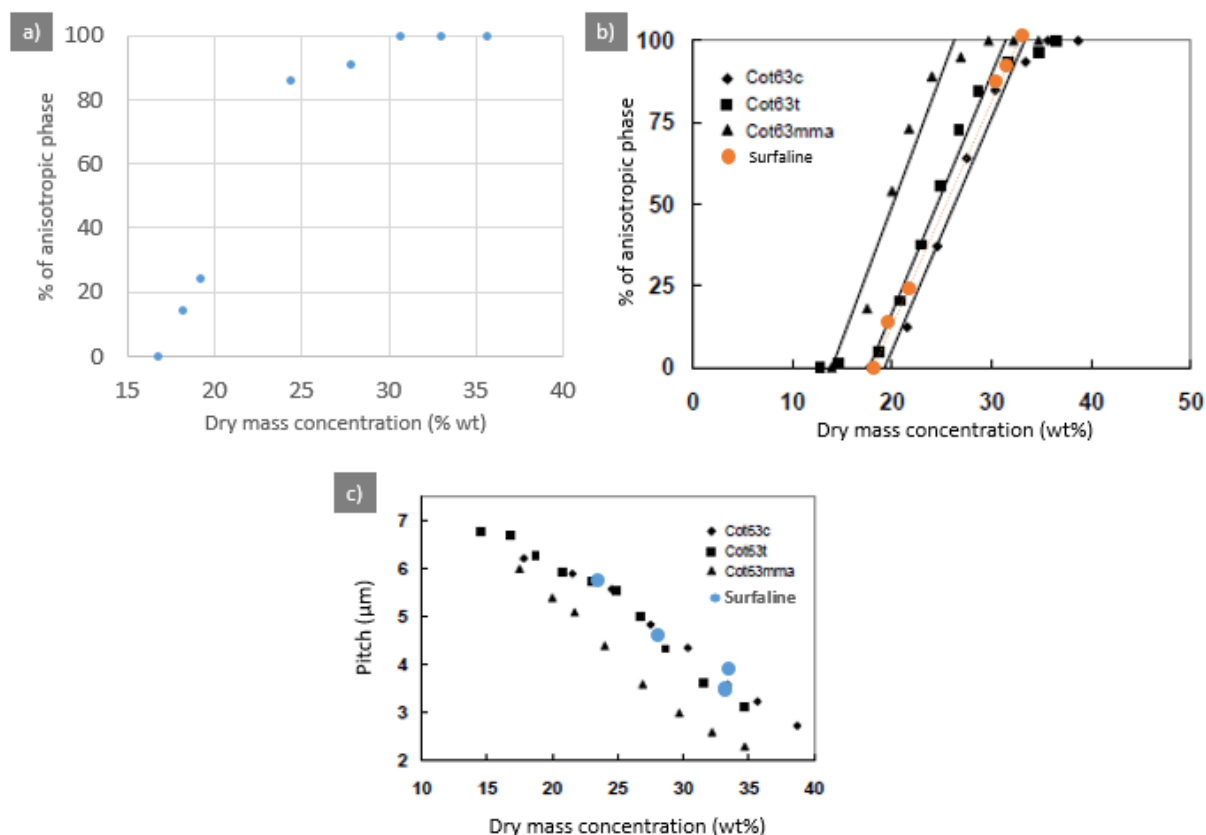


Figure 74 : a) Phase diagram of a Surfaline-stabilised CNC suspension in toluene (raw data) obtained by hydrolysis at 63 °C. b) Superimposition of the phase diagram presented in a) and corrected to account for evaporation on the data of Elazzouzi's manuscript for suspensions stabilised by BNA. c) Superimposition of the pitch value as a function of concentration dry mass concentration for suspensions stabilised by Surfaline (this work) and BNA (data from Elazzouzi's manuscript).

From this study, one can conclude that even though BNA, Surfaline and Melioran have very similar chemical structures, they lead to different colloidal stability and self-assembly behaviours for the dispersion of CNCs in organic apolar solvents. BNA allows to sterically stabilise CNCs in toluene, styrene and MMA. Surfaline stabilises CNCs in toluene and styrene with a very similar self-assembly behaviour compared to BNA, but cannot disperse them in MMA. Melioran does not achieve dispersing CNCs in the organic apolar solvents of this study. Results suggest that surfactants having either a mix of mono and di-ester phosphate matters in the scope of stabilising CNCs sterically. This mix could for example help accommodate the varying curvatures in CNCs object shapes. Another parameter that differs between the three molecules is the nature and rigidity of their aliphatic tail, long and rigid for Surfaline (18 carbons with a double bond, around 1.5 nm), intermediate and rigid for BNA (9 carbons and a

polarisable rigid benzyl ring, around 1.4 nm) and short and flexible for Melioran (12 carbons saturated chain, around 1.2 nm).

### **3.2.2. On the viscosity increase of CNC suspensions in organic apolar solvents over time**

#### **3.2.2.1. *Experimental observations***

Whenever mother suspensions in the fully anisotropic domain in all solvents are kept for storage (sealed, 4 °C, dark), their viscosity increases regularly over time until gelation is observed. This behaviour is unexpected to take place in these systems and also very difficult to characterise quantitatively due to the difficulty to perform accurate rheological measurements on cholesteric CNC suspensions.

The timescale within which the suspensions gel depends on many parameters. Notably, the viscosity rise depends strongly on solvent characteristics: gelation typically occurs over weeks to months in toluene and styrene, whereas it can be as fast as 24 to 48 hours in acrylate monomers. The CNC content is also a key parameter determining the gel time of suspensions: while gelation of biphasic suspensions in toluene at approximately 25 wt.% in dry mass concentration occurs over months, gelation of a fully anisotropic suspension in toluene (35-40 wt.%) occurs over several days only. The quality of the dispersion, *i.e.* the way it is prepared, could also influence the gel time.

Interestingly, gelation can be counteracted by shaking and mixing means. Vortex treatment during several minutes has a shear thinning effect on the suspension capable of bringing it back from gel to fluid liquid state. This shear thinning effect is only transient and the suspensions gel again within several hours. By contrast, if the vortex treatment is followed by tip sonication, its gel time is observed to be very similar to its original state. This result suggests that the suspension goes back to its original dispersion state in this case.

This viscosity increase over time brought additional experimental difficulties like the need to rejuvenate the samples before performing experiments: samples have had limited lifetime, and could lose their sensitivity to external fields on short notice during the experiments of chapter 4. It is often difficult to assess the influence of viscosity on the phenomenon one is willing to observe in a given experiment. As a standard practice throughout this work, samples have been extensively vortexed and tip-sonicated shortly before being used in experiments to exclude as much as possible the influence of the increasing viscosity of the samples on the

results. Samples have been typically prepared in the biphasic domain to allow for a sufficient sample lifetime to carry out further experiments. However, this experimental constraint may have influenced the optical response of the composites made in chapter 5, especially the quality of the self-organisation of charges.

### ***3.2.2.2. Possible origins of the viscosity increase over time***

In aqueous suspensions, gelation over time have been observed in various situations. Dorris et al (Dorris and Gray 2012) have shown that gelation over time can be obtained by exchanging water with glycerol and enhancing the desulphation of the CNC. While the transparency is a direct proof that the suspensions were still non-aggregated, this work clearly shows that a viscosity increase over time can arise from the change in the properties of the suspending medium, the decrease of the charge density or both of them. This behaviour has been reproduced and used for the design of alcohol-gels further transformed in functional materials (Wang et al. 2020). The systematic rheological investigation of the effect of salinity and concentration of suspensions of sulphonated CNCs has shown a sequence of four phases (liquid, viscoelastic, repulsive glass and attractive glass) that can be finely tuned with physico-chemical parameters (Xu, Atrons, and Stokes 2018). A similar concomitant change of the concentration and salinity of the medium takes place during the drying of a CNC suspension and keeping cholesteric domains mobility during the drying is determinant for the design of the optical properties of the dried films (Frka-Petesic et al. 2019).

There are quite a lot of modifications in the system of CNC-surfactants dispersed in organic solvents compared to aqueous CNC suspensions: the presence of a surfactant that is partly bound on CNCs and partly free in suspension and the modification of colloidal interactions between CNCs from electrostatic to steric repulsion following solvent exchange. The attractive forces that leads to aggregation of the particles still rely on Van der Waals forces that are efficient at short distances. The free surfactant in suspension could be responsible for such a thickening effect whenever it self-assembles into supramolecular assemblies – micelles, lamellae *etc.* – over time. However, these assemblies are expected to have a signature either in DLS or TEM that is not observed and the concentration of free surfactant seems too low to lead to such structuration.

The major change in these suspensions in apolar solvents is the nature of the colloidal interactions. As detailed in the state of the art, electrostatic repulsion is severely decreased in low permittivity organic solvents due to their poor dissociation ability. The experiments with

high voltage electric fields presented in chapter 4 is an indirect proof of the extremely low conductivity of the suspensions in apolar solvents. In our case, the layer of BNA on the surface of CNCs has been measured to be 1.5 nm thick by Bonini et al. (Bonini et al. 2002), corresponding to the size of the apolar tail of the surfactant and providing a steric repulsion of approximately this range. It is often overlooked that attractive Van der Waals interactions are modified as well by the solvent nature. That can be rationalised through the assessment of the Hamaker constant between the solvent and the particles that modulates the extent of the attractive forces. An approximated expression of the Hamaker constant can be calculated from the dielectric properties of the material and the solvent (Findenegg 1986) p.261. While the London contribution to the Hamaker constant is supposed to be an integral expression over all frequencies, this approximation only takes into account a single absorption frequency in the UV ( $\nu = 3 \cdot 10^{15}$  Hz) to yield an expression on the Hamaker constant that only depends on accessible experimental parameters: the dielectric permittivities and refractive indices of the media:

$$A = \left[ 3,1 \cdot 10^{-21} \frac{(\epsilon_{cell} - \epsilon_{sol})^2}{(\epsilon_{cell} + \epsilon_{sol})^2} + 2,6 \cdot 10^{-19} \frac{(n_{cell}^2 - n_{sol}^2)^2}{(n_{cell}^2 + n_{sol}^2)^{1,5}} \right]$$

where the indices *cell* and *sol* respectively refer to cellulose and the solvent. Figure 75 gives the calculated Hamaker constants using the previous expression for the solvents of this study. By comparing the obtained values with water, one notes that the Van der Waals attractive interactions are about 3 times less strong in MMA, about 10 times less strong in toluene and about 20 times less strong in styrene. The influence of the nature of the solvent on the strength of the attractive interactions could have important consequences on the stability of the suspensions.

Solvent	Refractive index (solvent)	Dielectric permittivity (solvent)	Calculated Hamaker constant (J/kB*T units)
Water	1.33	80.1	3.30
Toluene	1.497	2.38	0.28
Styrene	1.547	2.47	0.12
MMA	1.41	6.32	1.1

Figure 75 : Calculated Hamaker constants in J/k<sub>B</sub>T units using the previous expression. The ordinary refractive index  $n = 1.55$  and the dielectric permittivity  $\epsilon = 6.1$  of cellulose have been used for this calculation.

Interestingly, the apolar solvent with the highest Hamaker constant lead to the fastest viscosity increase in suspension as a result of the modification of the colloidal interactions in suspension. More precisely, suspensions of surfactant-stabilised CNCs in organic solvents may be a colloidal system where attractive interactions are slightly stronger than repulsive interactions, leading to a secondary minimum in the total interaction potential whose depth is bigger than  $k_B T$ . Colloids get progressively trapped into the secondary minimum under the action of Brownian motion which results in the formation of loosely bound aggregates that eventually percolate in suspension. The depth of the secondary minimum depends on Van der Waals attraction, *i.e.* on the nature of the solvent.

### 3.2.2.3. *Theoretical modelling of colloidal interactions in suspension*

Modelling presented in Figure 76 has been carried out in the scope of assessing the depth of the secondary minimum for our experimental system with the different solvents of the study. The expression of the Van der Waals potential has been adapted from Israelachvili's expressions (Findenegg 1986) p.254, (Boluk et al. 2011) for two identical cylinders of radius  $R$  and length  $L$  perpendicular or parallel from each other and  $R \gg r$ :

$$\varphi_{VdW,perp} = \frac{-A \cdot R}{6r}; \varphi_{VdW,parallel} = \frac{-A \cdot \sqrt{R} \cdot L}{24 \cdot r^{3/2}}$$

with  $A$  the Hamaker constant in J already calculated in Figure 75 and  $r$  the surface-to-surface distance between the cylinders. Considering a thickness of the surfactant layer of 1.5 nm in the case of the surfactant BNA, the relevant surface-to-surface distance to consider in the system is probably 3 nm – corresponding to close contact between CNCs – or slightly less if the steric repulsion potential is smoother than a hard sphere potential.

Figure 76a) and b) respectively describe the shape of the calculated Van der Waals potentials arising between perpendicular and parallel cylinders in different solvents as a function of the inter-cylinder distance. Parallel cylinders interact more strongly than perpendicular ones, and one will therefore mainly consider the interaction of parallel cylinders in the following, because all geometries should take place in suspension under action of thermal agitation. One can more or less ignore what is happening at  $r < 3$  nm which corresponds to steric repulsion of the surfactant layer, and observe how the attraction potential compares to  $k_B T$  at 3 nm (*i.e.* at close contact between the rods): in toluene and styrene, the depth of the minimum is comparable to  $k_B T$ , corresponding to a balanced situation between aggregation and redispersion of the rods by Brownian motion. In MMA however, the attraction potential at

3 nm is on the order of  $5 \cdot k_B T$ . Once a particle approaches at this distance, its thermal agitation can no longer drive it out of this minimum of potential. Accumulation of such events over time explains the observed viscosity increase of the suspensions. The ability of the system to transiently come back to its original state upon vortexing, but fully come back to its original state upon tip-sonicating is also consistent with the existence of a minimum of several  $k_B T$ : vortexing breaks some links between CNC aggregates, leading to a seemingly well-dispersed suspension that rises quickly in viscosity as those aggregates pack together again whereas tip sonication provides enough energy to the system to individualise CNCs again. The relationship between increased CNC content and reduced suspension gel time seems to be simply due to the closer proximity of the particles.

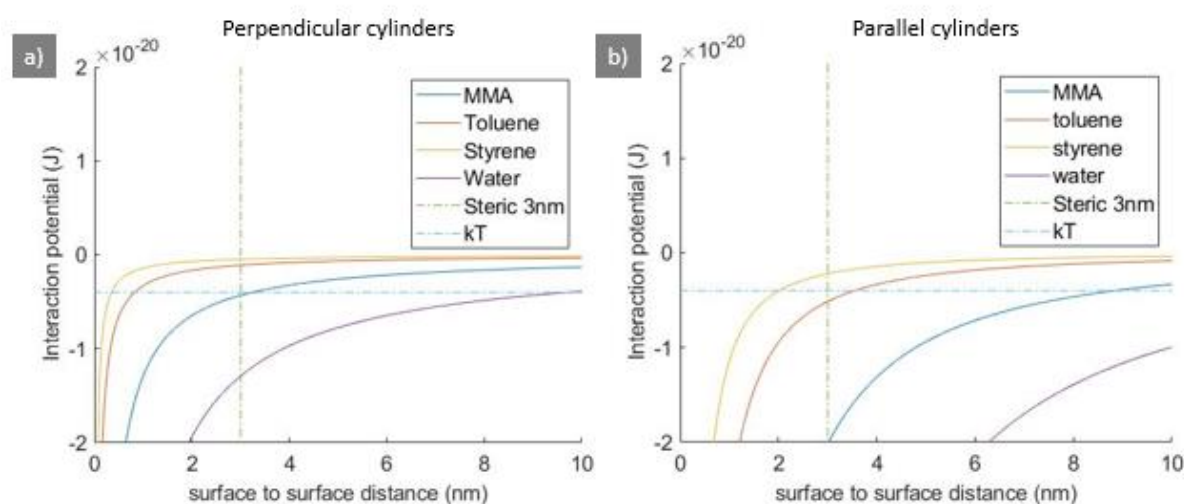


Figure 76 : Modelling of the theoretical attractive potentials corresponding to the experimental system using Matlab. a) Van der Waals attraction potentials of a) perpendicular cylinders and b) parallel cylinders in different solvents given by the expression above and the Hamaker constants of Figure 75. Steric repulsion hard sphere potential at 3 nm and  $k_B T$  value are superimposed to the curves.

The contribution of the surfactant layer itself to the attractive potential is not taken into account in this calculation. Whenever the Hamaker constant of the surfactant layer with respect to the solvent matters, *i.e.* when there is a permittivity and/or refractive index contrast between the surfactant and the solvent, the distances involved are much lower and an additional attractive Van der Waals interaction is expected. Another missing attractive interaction comes from the hydrophobic-hydrophobic attraction of the aliphatic tails of the surfactant at short distances, *i.e.* its incentive to form a “bilayer” in between two crystals. These additional attractive interactions could explain the experimentally observed viscosity increase over time in toluene and styrene, and possibly the aggregation observed with certain surfactants like Melioran.

While this scenario lacks a direct experimental proof, assuming it is true readily suggests means to suppress gelation in CNC dispersions in organic apolar solvents: if this phenomenon arises from the colloidal interactions balance, one needs a longer range repulsive interaction to yield a minimum in the total interaction potential that is higher than  $-k_B T$ . Efforts could therefore be aimed at finding a longer non-flexible surfactant molecule compatible with the process to remove gelation from the suspensions and widen the range of applications of these CNC suspensions in organic solvents.

### 3.2.3. Conclusions

Dispersing CNCs in organic apolar solvents and monomers is a much-needed checkpoint to broaden the possible uses of CNCs as fillers in polymer composites. Different strategies to tackle the problem have emerged in the literature: surface-grafting of CNCs, organic polar mediating solvent and surfactant stabilisation. The latter allows for stable dispersions in solvents and monomers by steric repulsive interactions along with an interesting retention of the self-assembling ability of CNCs with a much reduced pitch value compared to non-salted aqueous suspensions.

However, the surfactant BNA is not produced anymore and research effort has been carried out to find another surfactant compatible with the process: Surfaline and Melioran have been probed within that scope. Mass spectroscopy characterisation shows that these two surfactants have similar chemical structures compared to BNA. Dispersions using Melioran always lead to CNC aggregation, whereas Surfaline is able to disperse CNCs in toluene and styrene, but not in MMA. The self-assembly behaviour of Surfaline-stabilised CNCs is very similar to BNA-stabilised CNCs. These results suggest the need of a mix of mono and di-ester phosphate and/or rigidity in the aliphatic tail for the surfactant and/or long aliphatic tails to efficiently disperse CNCs.

Viscosity increase over time in CNC suspensions is then discussed under the light of empiric observations. A likely origin for the phenomenon accounting for most experimental observations hypothesizes that the colloidal system is made of slightly stronger attractive interactions than repulsive ones. These features lead to a minimum in the total interaction potential whose depth is found to depend importantly on the nature of the solvent in good agreement with experimental results. While this hypothesis remains to be proved, it readily suggests the use of a longer range repulsive force to get rid of gelation effects in CNC suspensions.





# **Chapter 4. Alignment of CNC suspensions in external fields**

*« Neige sur flamme,  
Roseau dans le vent  
Marchombre »  
P. Bottero*

In this chapter, we study the behaviour of CNC suspensions in toluene under external fields. Results can likely be transposed to other solvents and monomers given CNCs can be stabilised in these as well. In the first part, we explain why CNCs are sensitive to external fields. In a second part, we review the literature works on the alignment of CNC suspensions and composites under external fields. Results are then presented starting with the alignment of CNC suspensions in magnetic fields, followed by their alignment in electric fields. A geometrical model is developed to rationalise the main results. Alignment of CNC suspensions under combined electric and magnetic fields are then presented. We finish with the alignment of thick CNC suspensions and detail the consequences on their optical response.

## ***4.1. State of the art: Sensitivity of cellulose nanocrystals to external fields***

In order to understand the effect of external fields in assemblies of objects, let us have a look at the different phenomena that may occur when individual objects in suspension are subjected to external fields.

### **4.1.1. Interaction of single objects with an external field**

#### ***4.1.1.1. Permanent moment of an object***

The objects may have a non-zero permanent moment (dipolar  $\mathbf{p}$  for an electric field  $\mathbf{E}$  and magnetic  $\mathbf{m}$  for a magnetic field  $\mathbf{H}$ ) owing to the distribution of respectively electric charges and magnetic dipoles in their internal structure. The energy of interaction with the field is written  $E_{\text{interaction}} = -\mathbf{p} \cdot \mathbf{E} = -p \cdot E \cdot \cos \theta$  or  $E_{\text{interaction}} = -\mathbf{m} \cdot \mathbf{H} = -m \cdot H \cdot \cos \theta$  where  $\theta$  is defined as the angle between the moment and the field. The energy is minimised when  $\mathbf{p}$  (resp.  $\mathbf{m}$ ) is parallel to  $\mathbf{E}$  (resp.  $\mathbf{H}$ ) and  $\theta = 0^\circ$  while it is maximised when  $\mathbf{p}$  (resp.  $\mathbf{m}$ ) is antiparallel to  $\mathbf{E}$  (resp.  $\mathbf{H}$ ) and  $\theta = 180^\circ$ .

#### ***4.1.1.2. Induced moment of an object***

Additionally, the external field may create an induced moment by deforming the electronic cloud of the atoms composing the object. The induced moment is written  $\mathbf{p}_i = \bar{\alpha} \cdot \mathbf{E}$  where  $\bar{\alpha}$  is the tensor of polarizability of the object or  $\mathbf{m}_i = \bar{\chi} \cdot \mathbf{H}$  where  $\bar{\chi}$  is the tensor of susceptibility of the object. The interaction energy is thus  $E_{\text{interaction}} = -\frac{1}{2} \mathbf{E} \cdot \bar{\alpha} \cdot \mathbf{E}$  or  $E_{\text{interaction}} = -\frac{1}{2} \mathbf{H} \cdot \bar{\chi} \cdot \mathbf{H}$ . These two moments shape the response of an object subjected to a field.

#### **4.1.1.3. Dielectric and diamagnetic anisotropy**

For isotropic objects, the induced dipole is always parallel to the field, and its interaction energy is thus irrelevant as it causes no torque. For anisotropic particles, their permanent moment, polarizability and susceptibility tensors normally have three components. In the case of cellulose nanocrystals, described in good approximation as cylindrical objects, only electric permanent dipoles will be considered since there is no source of permanent magnetic dipoles in this material ( $\mathbf{m} = \mathbf{0}$ ). Two of the three directions are equivalent for symmetry reasons, so the induced interaction of a cylindrical object with an electric or a magnetic field can be summarised in two scalars that contain the contribution from the induced dipolar moments; the polarisation anisotropy  $\Delta\alpha$  and the diamagnetic anisotropy  $\Delta\chi$  defined as follows:

$$\Delta\alpha = \alpha_{zz} - \alpha_{xx} \text{ and } \Delta\chi = \chi_{zz} - \chi_{xx}$$

The energy of interaction of the induced moments with the field therefore simplifies as  $E_{\text{interaction}} = -\frac{1}{2} \cdot \Delta\alpha \cdot E^2 \cdot \cos^2 \theta$  or  $E_{\text{interaction}} = -\frac{1}{2} \cdot \Delta\chi \cdot H^2 \cdot \cos^2 \theta$ .

To summarise,  $p$ ,  $\Delta\alpha$  and  $\Delta\chi$  are the fundamental parameters one is willing to measure to predict the interaction of cellulose nanocrystals with external fields.

### **4.1.2. Experimental alignments of individual cellulose fibres and nanocrystals**

#### **4.1.2.1. Electric fields**

In the following, all studies are conducted on the cellulose I allomorph, which bears a dipolar moment. Experimental results on the alignment of CNCs under electric fields in water should be handled carefully. A strong electric field is required to induce an aligning effect and because of the numerous ions dissolved in water, the field is expected to induce electrophoretic effects that have an unknown effect on the observation reported by the authors. Habibi et al (Habibi, Heim, and Douillard 2008) studied the impact of AC electric fields on aqueous isotropic suspensions of tunicate CNCs, achieving a high orientation in the direction of the field for fields higher than 2 kV/cm and frequencies ranging from 10 kHz to 1 MHz. Kalidindi et al (Kalidindi, Ounaies, and Kaddami 2010) then studied the interaction of CNCs from palm tree with high AC electric fields ranging from 5 kV/cm to 30 kV/cm at frequencies ranging from 1 mHz to 100 kHz. They observed a field-induced chain formation: CNCs align parallel to each other, similarly to paramagnetic colloids in the presence of a magnetic field (Wang, He, and

Yin 2013). Because the electric field is alternating at high frequencies compared to the frequency of rotation of the nanocrystals or fibres, these authors probably measured the ability of individual fibres and nanocrystals to align parallel following an induced dipole interaction with the field.

On the other hand, because of the generally low dissociating power of organic apolar solvents, few charges are present in such solvents and electrophoretic effects are expected to be drastically reduced in contrast with aqueous solvents. Bordel et al (Bordel, Putaux, and Heux 2006) studied first the interaction of cellulose ramie fibres dispersed in chloroform or cyclohexane with an AC electric field. They were able to align the fibres parallel to an electric field ranging from 1.2 kV/cm to 2 kV/cm at 1 kHz by optical and electron microscopy means. These results suggest a positive contribution of either the permanent or the induced dipole moments of cellulose.

#### ***4.1.2.2. Magnetic fields***

Conversely to electric fields, the alignment of aqueous CNC suspensions in magnetic fields do not suffer from electrophoretic side effects. As a result, aqueous medium is a perfectly fine solvent to study the magnetic alignment of CNC suspensions. An early work first noticed using X-ray diffraction that cellulose fibres and cellulose microcrystals tend to align their long axis perpendicular to strong magnetic fields in suspension, suggesting negative anisotropy in the internal structure of cellulose (Sugiyama, Chanzy, and Maret 1992).

### **4.1.3. Assessment of the permanent and induced dipoles of CNCs under electric and magnetic fields**

Frka-Petesic et al have led two experimental studies to determine quantitatively the values of  $p$ ,  $\Delta\alpha$  and  $\Delta\chi$  for cellulose nanocrystals.

In a first study (Frka-Petesic, Jean, and Heux 2014), the authors reversed the sign of the electric field in a Kerr cell containing CNCs dispersed in toluene with surfactants and measured the transient relaxation of the birefringence to its steady state as shown in Figure 77. This experiment allows one to dissociate the permanent dipole contribution to the birefringence from the induced one by taking advantage of their dependency to odd powers or even powers of the field. Eventually, this experiment allows to retrieve estimated values for the dipolar moment  $p = 4400 \pm 400 \text{ D}$  and the polarizability  $\Delta\alpha = 1.75 \pm 0.40 \text{ \AA}^3$ . It means cellulose nanocrystals tend to align in the direction of the electric field. As a consequence, typical electric

fields required to align individual cellulose nanocrystals are stronger than 1-2 kV/cm and therefore have limited interest for applications.

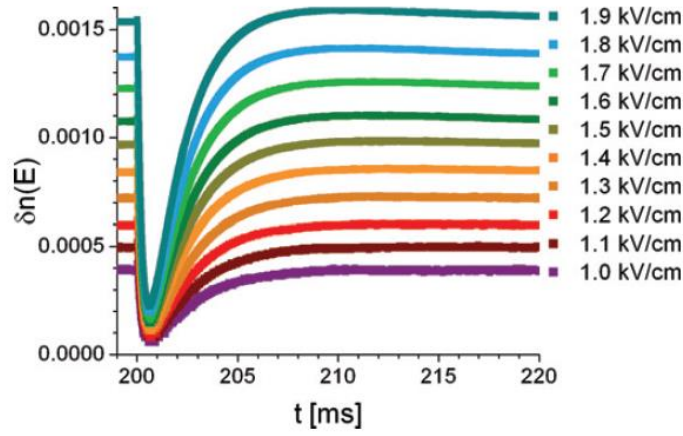


Figure 77 : Recovery of the birefringence of suspensions of CNCs stabilised in toluene with surfactants and subjected to an electric field ranging from 1 to 2 kV/cm during transient electric birefringence measurements. Adapted from Frka-Petesic et al., EPL 2014, 107, 28006.

Under magnetic fields, Frka-Petesic et al (Frka-Petesic et al. 2015) reported a negative diamagnetic anisotropy coming from the induced contribution. They assessed its value by performing a Cotton-Mouton experiment on a dilute aqueous suspension of tunicate CNCs, in which they record the saturation of the induced optical birefringence under increasing magnetic field values, up to 17.5 T. Given the dimensions of the tunicate crystals, their polydispersity, the ordinary and extraordinary refractive index of cellulose crystals, they use a fitting model to retrieve a value of  $\Delta\chi = -9.5 \cdot 10^{-7}$  SI. It means cellulose nanocrystals tend to align their long axis perpendicular to the magnetic field direction. Figure 78 summarises schematically the previous results on the behaviour of individual cellulose nanocrystals under electric and magnetic fields.

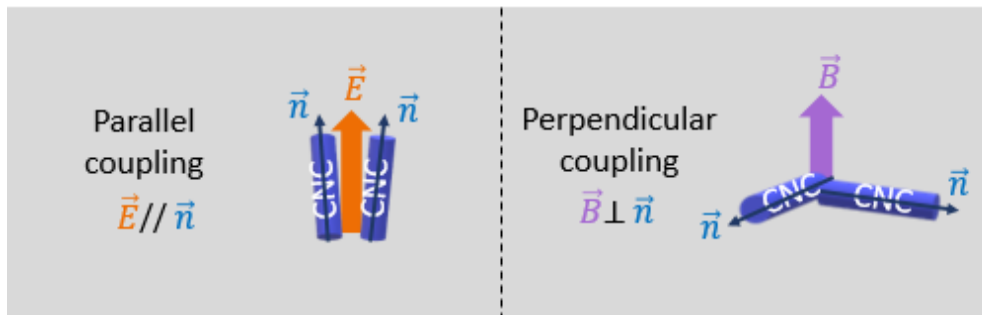


Figure 78 : Parallel and perpendicular coupling of individual cellulose nanocrystals respectively under electric and magnetic fields on account of their permanent and induced moments.

#### **4.1.4. Experimental alignment of cholesteric phases of CNCs under external fields**

##### ***4.1.4.1. Electric fields***

Frka-Petesic et al (Frka-Petesic, Radavidson, et al. 2017) later studied the alignment of cholesteric assemblies of cotton CNCs dispersed in organic solvents. By subjecting concentrated CNC suspensions in toluene to increasing electric fields, the authors unveiled an interesting two steps behaviour using laser and white light diffraction summarised in Figure 79. Additional information on laser diffraction and white light diffraction observation techniques are provided in chapter 2. The same experimental setup has been used for our experiments.

##### *4.1.4.1.1. Low field regime*

At lower field values, up to 300 V/cm, the authors report a progressive change of the laser diffraction pattern, from an initially circular pattern to two symmetrical arches and finally two symmetrical points located in the direction perpendicular to the electric field (Figure 79d). Based on these observations, the authors suggest that the initially randomly oriented CNC helices progressively reorient into a near-perfect alignment in the direction perpendicular to the electric field as the electric field value is increased. This leads to strengthen the iridescent optical response of the sample in this particular direction as the number of helices scattering light in this direction increases (Figure 79c). The pitch value of those helices remain essentially unchanged. This first step will therefore be referred to as the “orientation step” hereafter.

##### *4.1.4.1.2. Moderate field regime*

At “moderate” field values, from 400 to 700 V/cm, the authors report a redshift of the iridescent colour scattered from blue to red and eventually to infrared. Shortly before leaving the visible range, the sample displays a scattering white colour (Figure 79c). In laser diffraction, the two symmetrical points move toward the centre of the diffraction pattern. Shortly before merging in the centre, a continuous line is observed in the direction perpendicular to the electric field. Based on these observations, the authors suggest that the previously oriented helices are unwound by the electric field, ending up with a paranematic phase with no optical properties in which all CNC rods point in the direction of the electric field. The pitch increase over the course of the unwinding lead to match Bragg scattering conditions at higher angles of observation for a given wavelength, explaining the redshift of the iridescent response. We will refer to this second step as the “unwinding step” hereafter.

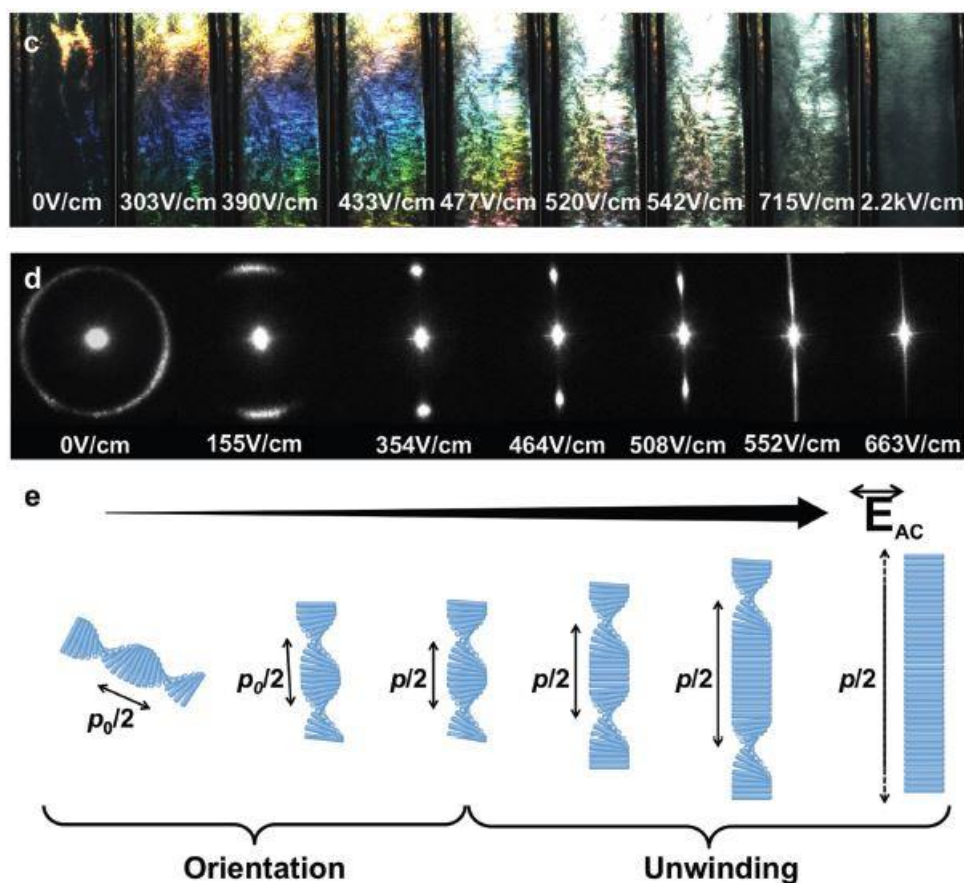


Figure 79 : White light and laser diffraction pattern of a CNC helices suspension in organic apolar solvents under electric fields and schematics of corresponding helical configurations. Adapted from Frka-Petesic et al, *Adv. Mat.* 2017, 29, 1606208.

#### 4.1.4.1.3. Modelling of the unwinding

Following these observations, the authors focused on the quantitative modelling of the unwinding using the theoretical calculations of de Gennes (De Gennes 1968). De Gennes predicts first a scaling of the pitch value with the electric field as  $p \sim E^4$ , and second a divergence in the pitch value – corresponding to the unwinding phenomenon – that occur above a critical field value of  $E_c = \frac{\pi}{2} \cdot \left( \frac{K_{22}}{\Delta\chi} \right)^{1/2}$  where  $K_{22}$  is the twisting elastic constant and  $\Delta\chi$  is the dielectric anisotropy. The fit of de Gennes' model to the experimental data of the authors displayed in Figure 80 is very good, and yields critical field values that increase with the sample concentration, from 250 V/cm to about 550 V/cm. From the value of  $E_c$ , it is possible to derive an estimation of the twist constant  $K_{22}$  on the order of 0.05 pN for CNC helices. This result is a measurement of the strength of chiral interactions within the helical assembly in apolar solvents.

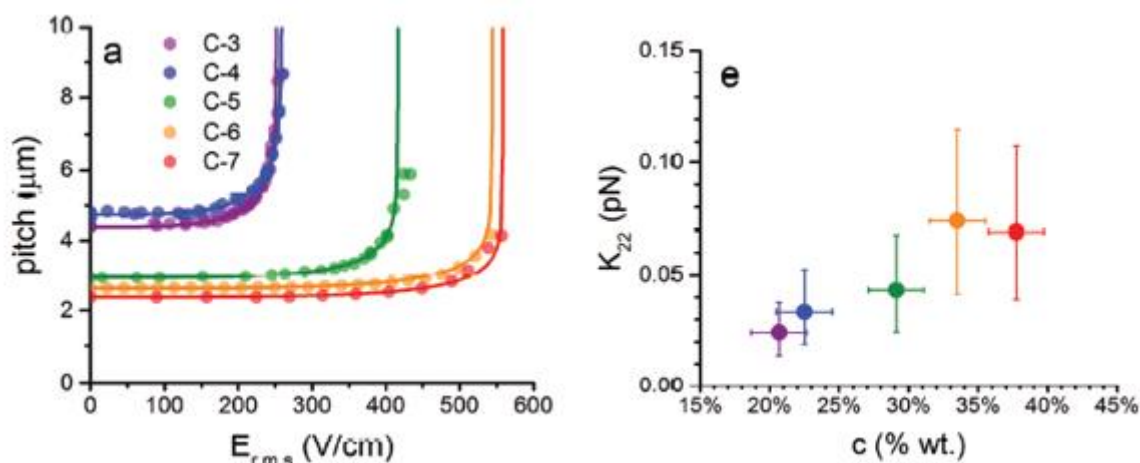


Figure 80 : a) De Gennes model fitting of experimental pitch measurement data of CNC suspensions in organic apolar solvents. e) Calculated  $K_{22}$  values deduced from de Gennes fitting as a function of sample concentration. Adapted from Frka-Petesic et al, Adv. Mat. 2017, 29, 1606208.

#### 4.1.4.1.4. Other features of the alignment

Finally, the authors show that it is possible to keep the alignment of domains perpendicularly to the electric field at zero field using a process referred to as “slow-annealing”. On the other hand, if the field is brutally cut after the unwinding, a uniform iridescent response is observed. Additionally, the authors showed that by switching in between two field values  $E_1$  and  $E_2$  below  $E_c$  it was possible to dynamically tune the iridescent optical response with a response time on the order of seconds. This looks interesting for applications in stimuable optics, or to incorporate into materials: only few photonic systems are able to dynamically tune their scattered colour upon a stimulus (Goerlitzer and Taylor 2018). Highlighted by this work, electric field seems to be a powerful tool to tune their photonic properties in organic apolar suspensions. To date, nobody reported materials containing electric field-aligned CNCs.

#### 4.1.4.2. Strong magnetic fields

Revol et al then observed biphasic and anisotropic capillaries of CNCs under crossed polars after strong field alignment, reproduced in Figure 81 (Revol et al. 1994). They note a fast orientation step in minutes followed by the reorganisation of the texture towards full alignment over several hours in biphasic samples. In the case of fully anisotropic samples, sample state at short times is unclear but also yields good quality alignment overnight. One must also bear in mind that the texture is possibly more aligned than what is shown in the polarised optical microscopy images because these have been taken off the field. They also note the alignment of CNC tactoids under magnetic field that surprisingly do not disalign before they observe them under the microscope.



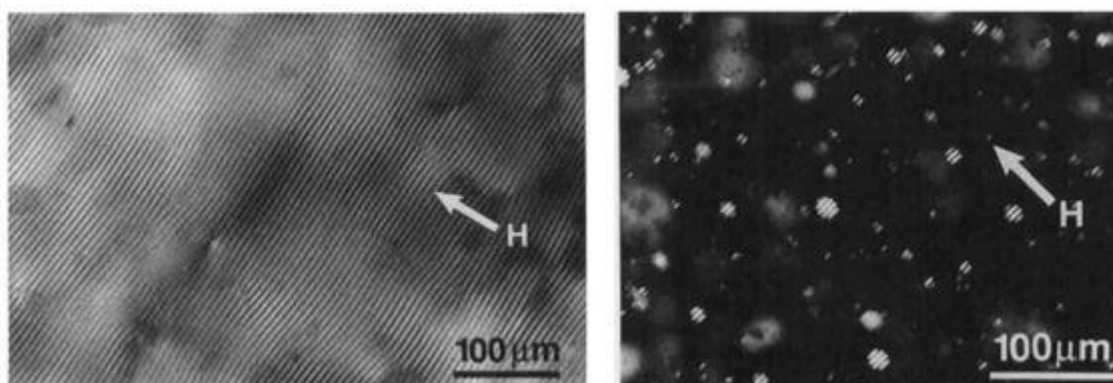


Figure 81 : Polarised optical microscopy images of the 7 T magnetic field alignment of (left) a fully anisotropic CNC suspension after 12h and (right) tactoid droplets inside the isotropic phase. Adapted from Revol et al *Liq. Cryst.* 1994.

Kyoto University's group then explored the alignment of chiral nematic phases of tunicate suspensions of cellulose microfibrils under static magnetic fields ranging from 1 to 28 T and slowly rotating magnetic fields of 5 T at 10 rpm (Kimura et al. 2005). They show using polarised optical microscopy that CNC helices tend to align their helical axis along the magnetic field direction under static magnetic fields, corresponding to an individual cellulose microfibril orientation perpendicular to the magnetic field in good agreement with previous observations. Under slowly rotating magnetic fields, they observed the untwisting of the chiral nematic phase into a nematic phase characterised in polarised optical microscopy. Their experimental observations are summarised in Figure 82. These works show really good quality of alignment for cholesteric CNCs in suspension, but the main drawback is that it typically requires NMR fields to perform the alignment, which is incompatible with applications.

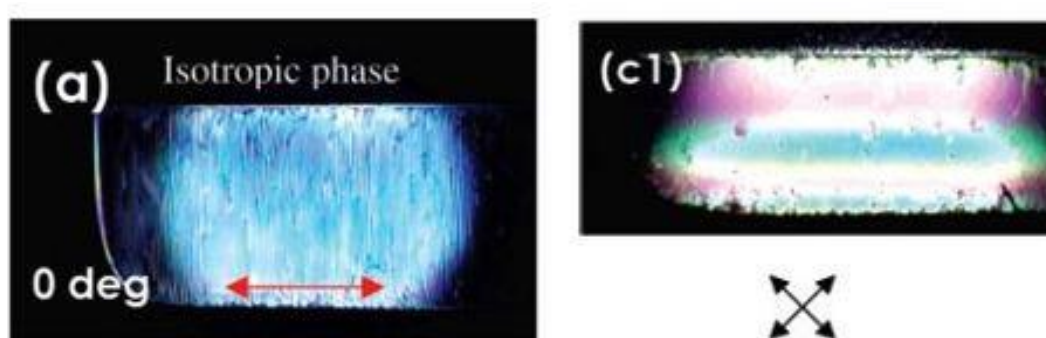


Figure 82 : Polarised optical microscopy of a chiral-nematic CNC suspension under (a) a 28 T static magnetic field showing near-perfect alignment of helices orientation along the field through the observation of “fingerprint patterns” and (c1) a 7 T rotating magnetic field at 10 rpm leading to a typical nematic texture under crossed polars. Adapted from Kimura et al *Langmuir* 2005.

#### 4.1.4.3. Weak magnetic fields

De France and Mao studied the alignment of cholesteric assemblies of CNCs in water under weak magnetic fields (De France et al. 2016; Mao et al. 2018). De France et al studied specifically the kinetics of alignment of an isotropic and a biphasic CNC suspension under 0.56 and 1.2 T magnetic fields using an in-situ SAXS experimental setup and report near-perfect anti-alignment of the individual crystals corresponding to an order parameter of  $S_{2,\text{particles}} = -0.499$  obtained respectively in 4 hours and 3 hours (*i.e.* perfect alignment of the helices axes).

They observed a two-step behaviour composed of a rapid initial alignment in the first two minutes ( $S_{2,\text{particles}} = -0.22$ ) followed by a slow reordering of the cholesteric domains in which  $S_2$  follows a sigmoidal curve over time, similarly to what Revol et al (Revol et al. 1994) observed under strong fields. Noteworthy, the SAXS diffractogram they show is far from a perfect mono-domain of CNC helices aligned along the field and the polarised optical microscopy images display tactoids of several different orientations, although these data are according to the authors both taken in conditions corresponding that would correspond to a perfect alignment. Figure 83 gathers the obtained results.

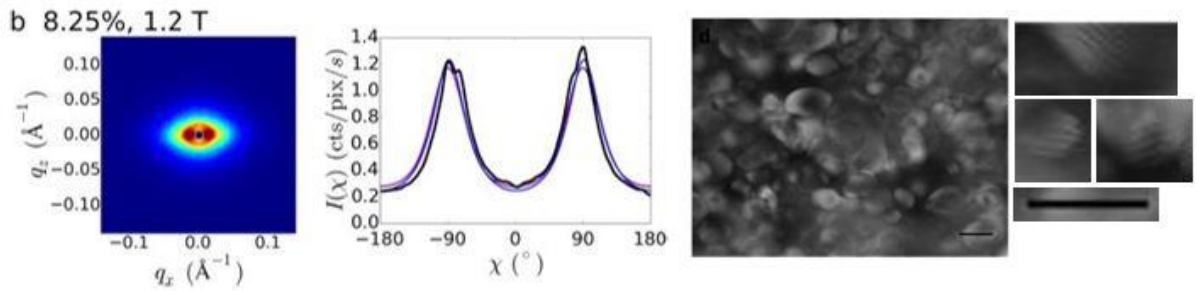


Figure 83 : (left) in-situ SAXS measurements and (middle) polarised optical micrographs of a 8.25 wt.% CNC suspension under a 1.2 T magnetic field after 5 hours. Scale bar is 10  $\mu\text{m}$ . (right) Close-up of (middle) showing different tactoids orientation with corresponding scale bar. These two experimental results do not correspond to a fully aligned chiral nematic phase. Adapted from De France et al Langmuir 2016.

On the other hand, Mao et al performed a similar in-situ SANS study on a 7.4 wt.% CNC suspension using an approximately 0.5 T magnetic field and report partial alignment of CNC helices in the field characterised by a Hermans order parameter of  $P_{2,\text{helices}} \sim +0.5$  consistent with the shown SANS diffractogram, which remains unchanged over the course of 10 hours (refer to Order parameters for definitions).  $P_2$  refers here to the order parameter of the helical axis in this case which explains its positive value compared to the previous work. In contrast with the previous section, these works show that it is typically possible to retain partial or total

alignment of CNC helices under fields in the range of commercial neodymium magnets, that are easily accessible for labs and industries.

#### ***4.1.4.4. CNC-based materials aligned under magnetic fields***

Several works have developed strategies to make materials or composites reinforced by cellulose fillers and benefit from their magnetic field alignment. Kimura and coworkers polymerised respectively a hydrophilic UV-curable resin and hydroxyethyl methacrylate (HEMA) around CNC aligned under strong magnetic fields to yield composites in the scope of unidirectional mechanical reinforcement (Tatsumi et al. 2014; Kimura and Kimura 2009). CNC-PHEMA composites are nicely aligned according to SEM data and polarised optical microscopy data, corresponding to an order parameter for the individual crystals of  $S_{2,\text{particles}} = -0.42$ . The authors also used strong rotating magnetic fields similarly to their previous work in suspension to yield CNC-PHEMA composites with pseudo-nematic CNC fillers, corresponding to an order parameter for the directors of CNCs of  $S_{2,\text{particles}} = -0.30$ .

The authors proved the anisotropic mechanical reinforcement by performing tensile tests in the direction of the magnetic field and in the perpendicular direction, measuring a 2 GPa difference in Young modulus. Compression tests in the direction perpendicular to the field show the highest Young modulus for the nematic phase of fillers, in good agreement with their uniaxial alignment in this direction. Kvien and Osman (Kvien and Oksman 2007) followed a similar strategy by aligning cellulose nanocrystals in polyvinyl alcohol (PVA) under strong magnetic fields. They also report a strong alignment using SEM data and a toughening of 2 GPa of the Young modulus in the transverse direction compared to the field direction. The literature results towards anisotropic mechanical reinforcement of composites aligned under magnetic fields are summarised in Figure 84.

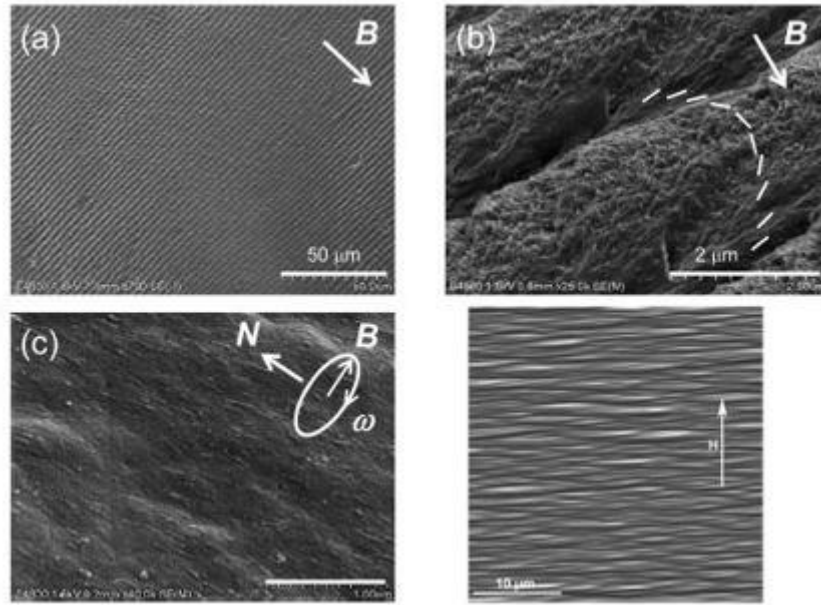


Figure 84 : (a)(b)(c) FE-SEM fracture of a CNC-PHEMA composite aligned under (a)(b) an static 8 T magnetic field and (c) under an 8 T rotating magnetic field at 150 rpm prior to polymerisation. Adapted from Tatsumi et al Biomacromolecules 2014. Bottom right: FE-SEM fracture and etching of a CNC-PVA composite aligned under a 7 T magnetic field showing a very aligned microstructure. Adapted from Kvien et al J. Appl. Phys. 2007.

Finally, Frka-Petesic and coworkers (Frka-Petesic, Guidetti, et al. 2017) have been interested in tuning the photonic properties of CNC films using weak magnetic fields. Their idea consists of evaporating CNC films in the immediate vicinity of commercial magnets with different field geometries, tuning in turn cholesteric domains orientation. By tilting the helical axis orientation by an angle, the authors demonstrate using angular resolved spectroscopy and k-space imaging that the Bragg reflection is also shifted by an angle. Main results are put together in Figure 85. This work is of importance in the scope of this PhD because it is the first one that directly links the magnetic field alignment with the tuning of an optical response for CNC materials.

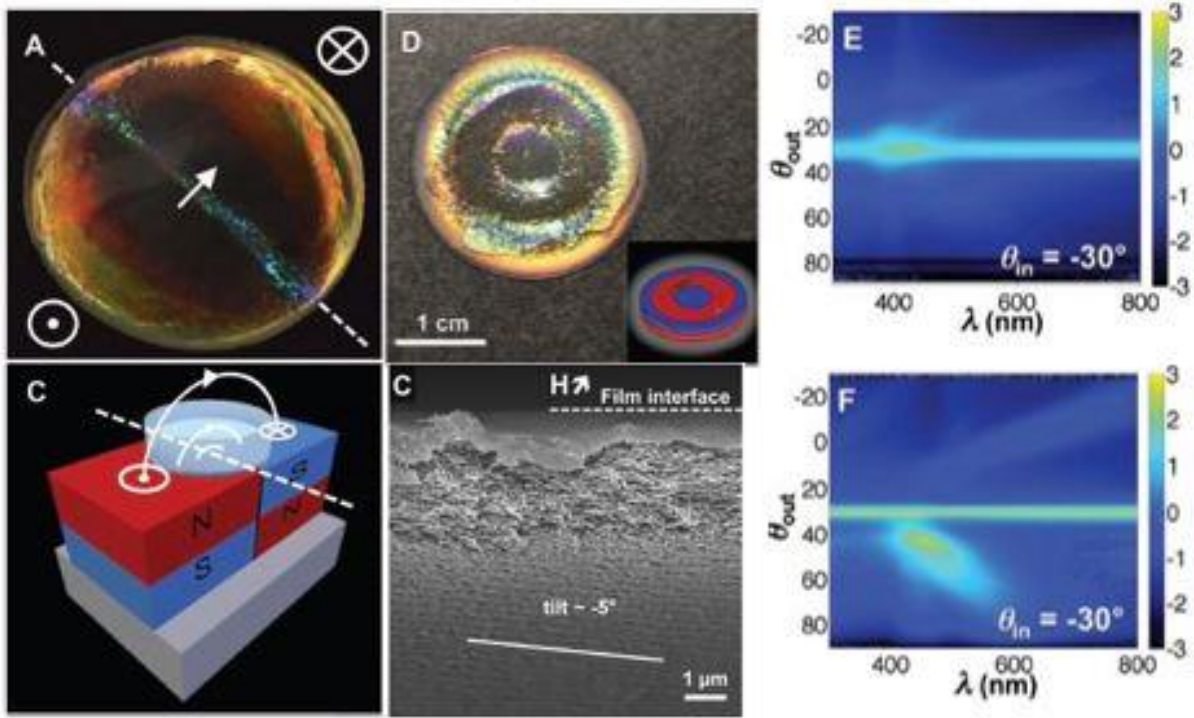


Figure 85 : (left and top middle) Original photonic patterns in CNC films using non-trivial magnet arrangements. (bottom middle) CNC helix orientation tilt with respect to the anchoring direction evidenced by SEM cross-sectional cut. (right) Angular resolved optical spectroscopy data displaying the optical response of CNC films aligned with (top) a magnetic field oriented in the anchoring direction and (bottom) a magnetic field tilted with respect to the anchoring direction. Adapted from Frka-Petesic et al Adv. Mat. 2017, 29, 1701469.

#### 4.1.4.5. Most recent works

Let us finish this literature review by mentioning two very recent works from Ounaies' and Maclachlan's groups (Cao et al. 2020; Meddeb et al. 2020) published after the results of this work have been obtained. Ounaies' group studied the alignment of isotropic and cholesteric CNCs in N-methylformamide under a weak 0.7 T magnetic field by SAXS, similarly to De France's study. They report partial alignment of the crystals, corresponding to a quadrupolar order parameter of orientation of  $S_{2,\text{particles}} = -0.22$ , which is quite low compared to similar works. Y. Cao's strategy is similar to this work: the authors aligned a suspension of aqueous cholesteric CNCs containing polyacrylamide precursors under a strong 7.5 T magnetic field before crosslinking the structure under UV irradiation into a hydrogel that locks in the cholesteric structure. The optical quality of the diffraction grating reproduced in Figure 86 is impressive, showing up to five diffraction orders owing to a near-perfect alignment of the material characterised in polarised optical microscopy and SEM.



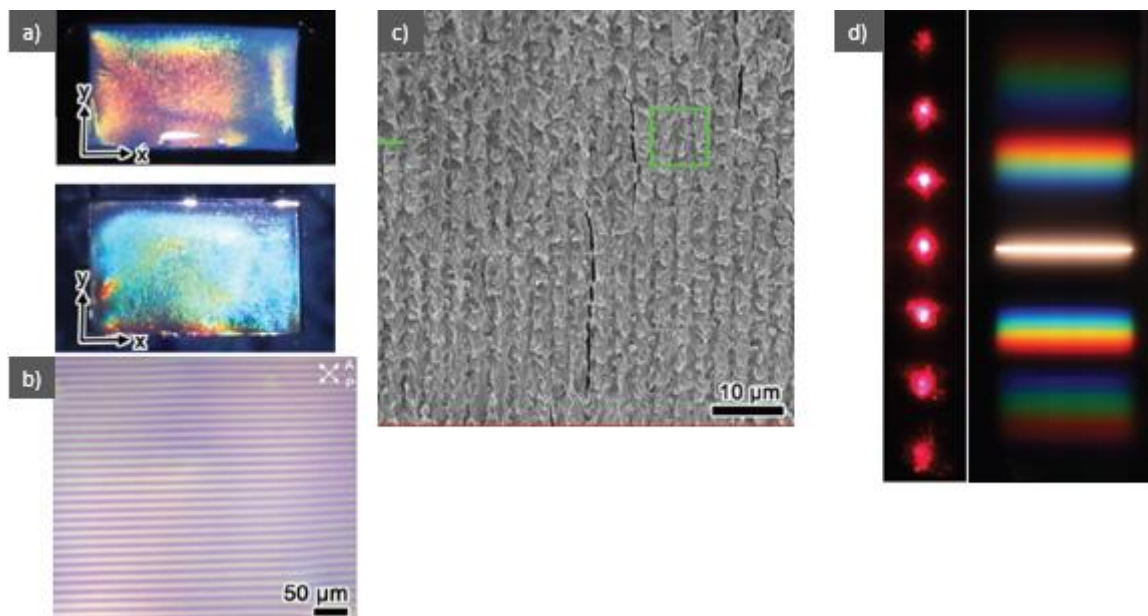


Figure 86 : a) Optical appearance of a polyacrylamide-CNC hydrogel aligned under strong magnetic fields of 7.5 T before being polymerised. b) Polarised optical microscopy of a PAAM-CNC hydrogel at 4 wt.%. c) SEM cross-section of the material presented in a). d) Laser and white light diffraction of the material presented in a). Adapted from Cao et al. *Adv. Mat.* 2020, 1907376.

To conclude on literature results on the alignment of CNC helices under magnetic fields, it seems that the alignment under strong magnetic fields yielded converging and reproducible results whereas the results of an alignment under weak magnetic fields tended to vary from one work to the other. This discussion is pursued with the results of this work in the next sections.

## 4.2. Results

Note that in the following results any polarised optical microscopy characterisation is performed shortly after electric or magnetic field alignment, out of field, whereas laser and white light diffraction experiments are all performed under fields. Suspensions used in the study are anisotropic CNC suspensions dispersed in toluene unless stated, to exclude the possible effect of the polymerisation of monomers. However, no significant difference in the behaviour of suspensions under fields has been noticed while switching from toluene to monomer solvent to synthesize composite materials in chapter 5.

In alignment experiments,  $z$  is labelled as the direction of the thickness of the sample, which also always corresponds to the direction of propagation of the incident laser beam in laser diffraction experiments. The  $x$  axis is defined as the vertical direction, corresponding to the length of the capillary. The  $y$  axis is defined as the horizontal direction, corresponding to the width of the capillary. Coordinates definition are summarised in Figure 87.

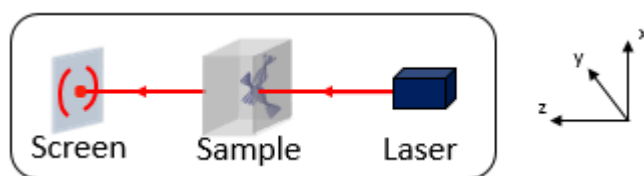


Figure 87 : Definition of the coordinates in the following sections and schematic view of laser diffraction characterisation experiments.

## 4.2.1. Alignment of CNC suspensions under magnetic fields

### 4.2.1.1. Influence of field intensity on cholesteric textures and alignment

Several experimental setups have been used or made to generate 0.25, 0.5, 0.65 and 9 T magnetic field intensities, which are detailed in chapter 2. Samples used in this section are typically extensively shaken before being sealed in capillaries and allowed to phase-separate prior to alignment.

#### 4.2.1.1.1. 0.25 T magnetic field

Under a 0.25 T magnetic field, after 3 days of alignment of a 24 wt.% biphasic suspension of CNC helices, randomly oriented and anchored cholesteric textures are observed as in Figure 88. A close-up in the randomly oriented texture displays well-developed helices fingerprint patterns superimposed with no preferred orientation. In laser diffraction, it is not possible to observe any modification of the orientation of a cholesteric domain even after long field orientation (data not shown). In white light diffraction, only several areas of the sample match the Bragg conditions to scatter light to the detector. These helices have typically some polydispersity in pitch, allowing the Bragg scattering of different wavelengths at a given angle of incidence and leading to colour mixes as the red first order and blue second order in Figure 89. These characterisations suggest no effect of the 0.25 T magnetic field on the alignment of the cholesteric domains of CNCs.

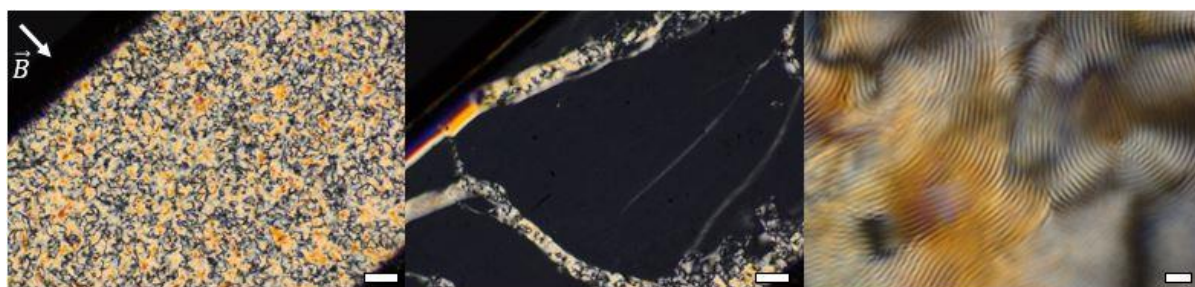


Figure 88 : Polarised optical microscopy images of a glass capillary containing a 24 wt.% CNC suspension under a 0.25 T magnetic field after 3 days. (a) Randomly oriented texture formed of grown

and kinetically trapped tactoid coalescence (x2.5). (b) Anchoring orientation texture corresponding to the helical axis in the depth of the sample (x2.5). (c) Fingerprint patterns in the random region displayed in (a) (x40). Scale bars of (a) and (b) are 200  $\mu\text{m}$ , scale bar of (c) is 10  $\mu\text{m}$ . Magnetic field has the same orientation in all three images.



Figure 89 : Optical appearance of a  $1 \cdot 10 \cdot 50 \text{ mm}^3$  capillary containing a 31.9 wt.% CNC suspension under a 0.25 T magnetic field. The pink colour displayed by the sample is typically the result of the additive scattering of second order blue with first order red domains. Copper wires are in the sample for another experiment and are to be ignored in this section.

#### 4.2.1.1.2. 0.5 T magnetic field

Under a 0.5 T magnetic field, one can observe an effect of the magnetic alignment in polarised optical microscopy. Images of Figure 90 have been taken for a capillary before field alignment and after three weeks of alignment. In area 1 towards the bottom of the capillary, field alignment has increased the amount of helices whose axes are oriented along the field direction although the alignment is far from perfect. In area 2 towards the isotropic-cholesteric boundary, a lesser amount of fingerprint patterns is visible, indicating reorientation in the anchoring direction  $z$  over time. One can conclude that area 1 has been sensitive to field alignment, while area 2 has not. This field value might be close to the threshold value at which magnetic field start to efficiently align CNC helices.



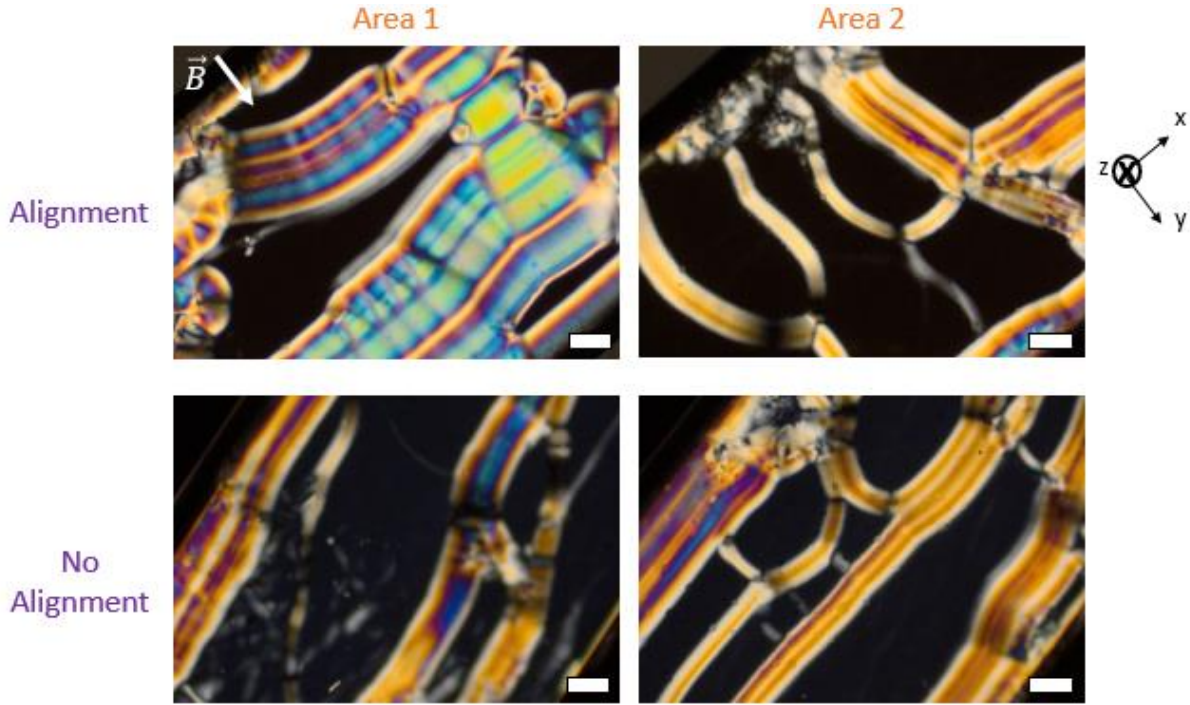


Figure 90 : Polarised optical microscopy images of two capillary areas containing a 24 wt.% CNC suspension before and after three weeks of alignment under a 0.5 T magnetic field. Area 1 shows an increase of the fingerprint area and strengthened alignment following field alignment, while area 2 rather shows a reduction of the amount of visible fingerprints, indicating more helices oriented in the anchoring direction. Part of the remaining helices are also oriented perpendicular to the field.

#### 4.2.1.1.3. 0.65 T magnetic field

Under a 0.65 T horizontal magnetic field, unambiguous alignment of CNC helices axes in the direction of the magnetic field is observed in agreement with what has been previously observed in the literature (De France et al. 2016; Mao et al. 2018). In the laser diffraction experiment reproduced in Figure 91, initially randomly oriented cholesteric domains – not necessarily isotropic – reorient over a couple of hours, yielding a pattern made of two arches in the direction of the magnetic field. Leaving the sample to align under field for one day strengthen significantly the amount of helices oriented parallel to the magnetic field, as evidenced by the increase in the intensity of laser diffraction in this direction. It is possible to assess the strength of the alignment using a quadrupolar order parameter for the helices axes orientation:

$$S_2 = \left\langle \frac{3 \cdot \cos^2 \theta - 1}{2} \right\rangle$$

Laser diffraction measures the intensity scattered in every direction within the diffraction plane, which is directly proportional to the number of helices of the (Oxy) plane scattering in this direction. Intensity weight coefficients can therefore be directly used for order parameter

determination, as shown in Figure 92. The curve obtained is quite irregular compared to the theoretically expected one (Frka-Petesic et al. 2019), which is why we use the Hermans order parameter here to yield a value of  $S_{2,\text{helices}} = +0.85$  for the helices axes orientation after one day of alignment. This value corresponds to a good quality but not perfect alignment.

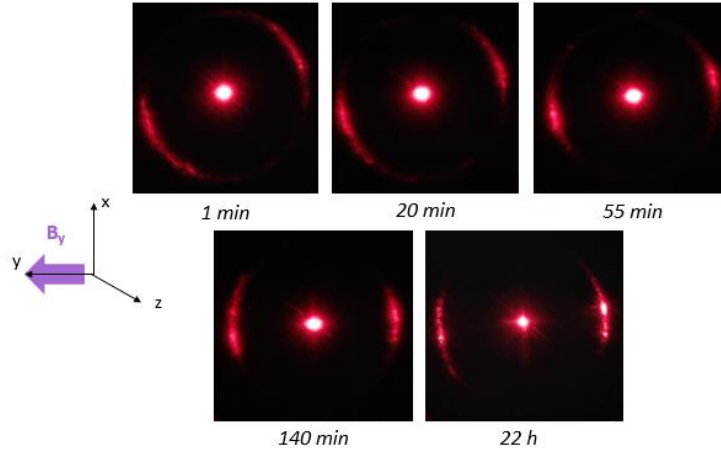


Figure 91 : Following the alignment of a phase-separated biphasic 26 wt.% CNC suspension under a 0.65 T horizontal magnetic field using laser diffraction. The initially randomly oriented cholesteric domain slowly reorients in the direction of the magnetic field. The alignment keeps strengthening in between 2h30 and 22h.

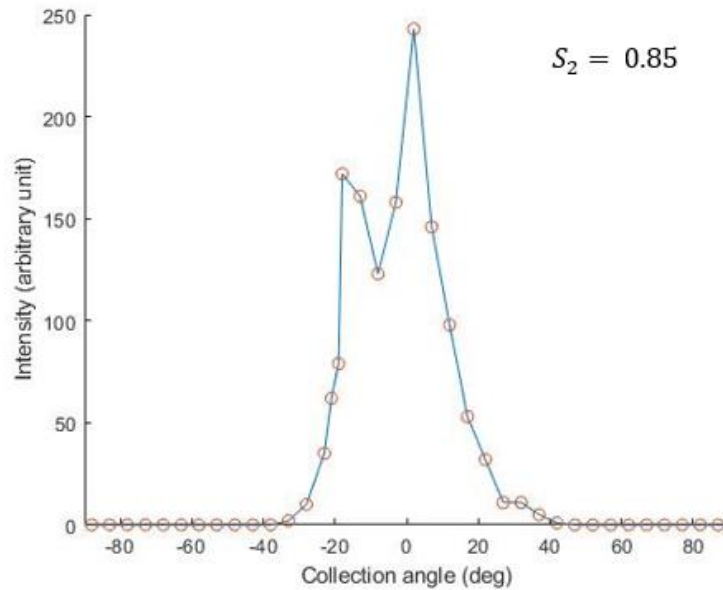


Figure 92 : Intensity scattered in grey values as a function of the direction of observation described by an arbitrary angle (orange points are experimental). The order parameter  $S_2$  is directly deduced from these measurements.

In comparison with the literature, De France et al claim an order parameter of the particles of  $S_{2,\text{particles}} = -0.499$  under both 0.56 and 1.2 T magnetic fields, corresponding to an order parameter for the helices close to 1 although the experimental proofs they give do not directly advocate their claim. Mao et al on the other hand measure similarly to this work partial

alignment of CNC helices at  $P_{2,\text{helices}} = +0.5$ . Results of this work are found to be in between these two works.

#### 4.2.1.1.4. White light diffraction characterisation

While laser diffraction provides local information, iridescent white light diffraction by contrast provides a global information on the orientation of cholesteric domains inside the sample. Over the course of the magnetic field alignment, an increasing fraction of the sample scatters light towards the detector, corresponding to the reorientation of domains in the horizontal direction that matches the Bragg conditions of the horizontally offset illumination source. The scattered colour becomes also more homogeneous, indicating a more homogeneous pitch value throughout the samples. Hydrodynamic flows of suspension are observed, indicating that the reorientation of domains is not a local phenomenon, rather a free energy minimisation taking place simultaneously in the entire sample. In sharp contrast with the non-aligned samples shown in Figure 89, capillaries subjected to a 22 hours magnetic field alignment at 0.65 T appear near-homogeneously iridescent to the eye presented in Figure 93. Comparing the top and bottom samples of Figure 93 which are prepared and aligned in the same conditions but present different alignment qualities, the history of the sample seems to influence the final state of the alignment. This is further discussed by accounting for additional experiments in the next section. This series of experiments show that magnetic field alignment is a very efficient tool to yield homogeneously iridescent samples on account of the reorientation of all helices axes towards a single direction, the one of the magnetic field.

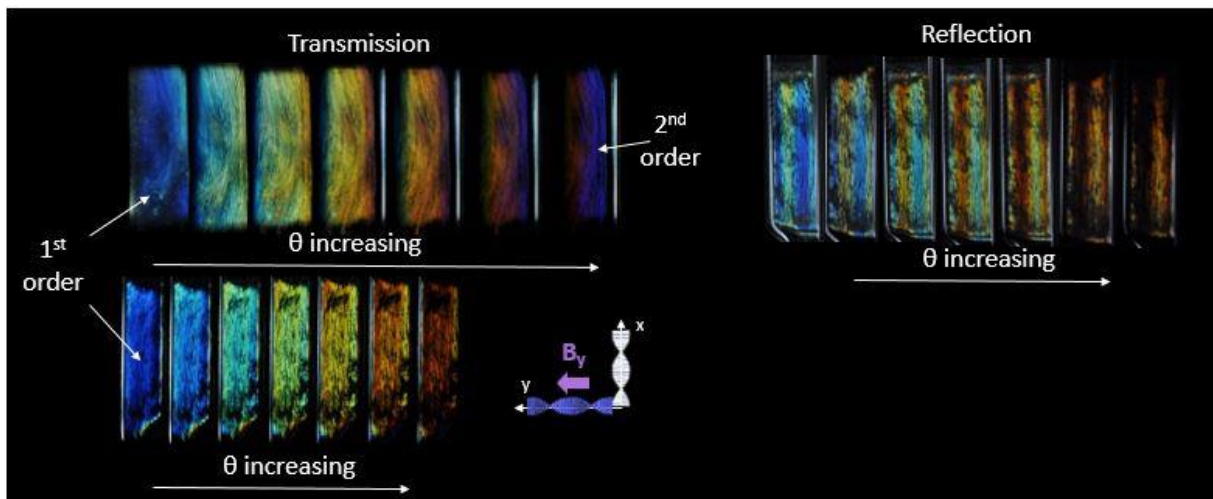


Figure 93 : Optical appearance of CNC suspensions aligned under a 0.65 T horizontal magnetic field. (top left) 26 wt.% aligned overnight in transmission. (bottom left) 26.5 wt.% aligned during 22 hours in transmission. (top right) 26.5 wt.% aligned during 22 hours in reflection. From left to right, the angle of incidence of the white light source increases. Top left sample is larger than bottom left, leading to different iridescent colours due to parallax effect. The loss of the left part of the top left sample colour

*is due to elements of the setup shadowing the optical response, which is also the reason why the rest of the second diffraction order are not shown. Schematics of the helix axis reorientation expected under a horizontal magnetic field.*

Additional optical features are observed following magnetic field alignment, namely higher orders of diffraction and an iridescent optical response in reflection. Higher orders of diffraction are additional iridescence sequences that take place at multiples  $m$  of the first diffraction order following the Bragg equation:

$$m \cdot \lambda = n \cdot p \cdot \sin(\theta)$$

They are predicted by the theory (Berreman and Scheffer 1970), but not always observed depending on the optical quality of the samples and the order of magnitude of the pitch. Observing them following magnetic field alignment is therefore an indication that the sample behaves increasingly like an ideal diffraction grating. Orders higher than +2 and -2 are barely visible, meaning the optical quality of the sample can be improved, as proved by Cao's recent work (Cao et al. 2020). In reflection, a two-colour stripy pattern is observed which was unexpected in this experiment. By looking at the transmission response, it seems like they are due to slight pitch variation of pitches in the horizontal direction of the samples that are magnified in the reflection configuration.

#### 4.2.1.1.5. 9 T magnetic field

Finally, samples have been placed in an NMR magnet in CERMAV to perform alignment experiments under a 9 T vertical magnetic field and white light diffraction characterisation shortly out of field. However, the sensitivity of the samples to shaking prevented laser diffraction characterisation. The optical response of a CNC suspension aligned overnight is displayed in Figure 94. Surprisingly, the intensity of the colour scattered is not strikingly different from a 0.65 T magnetic field alignment. Second order iridescent scattering and scattering in reflection are visible as well, but quite shady in terms of intensity. The texture of the samples is modified as shown by the inset of Figure 94: white light scattering indicates well aligned vertical cholesteric domains, that have however not merged into one giant domain, rather numerous millimetre scale domains.

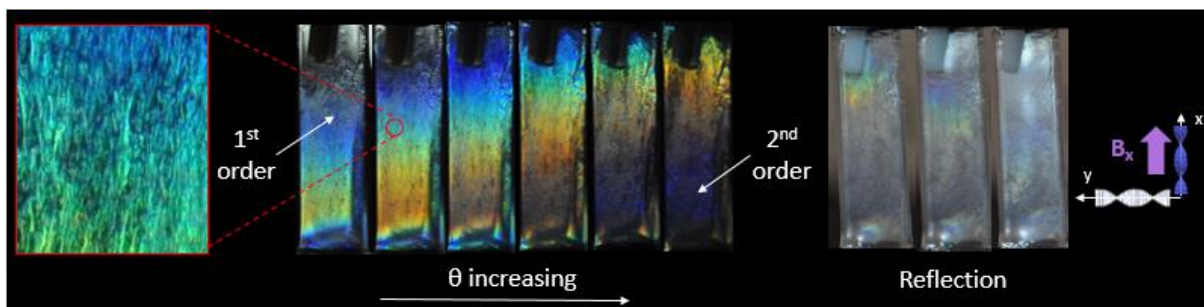


Figure 94 : Optical appearance of a 26 wt.% CNC suspension aligned under a 9 T vertical magnetic field overnight. (middle) Iridescent response in transmission. (right) Iridescent response in reflection. From left to right, the angle of incidence of the white light source increases in each series. (left) Close-up of the iridescent texture in transmission showing a poly-domain texture. The different colours displayed within the sample are due to parallax effects given that the white source is vertically off-centered, in agreement with helices aligned along a vertical magnetic field. Pitch values are still expected to be homogeneous inside the sample.

To conclude on the influence of field intensity on the alignment of CNC helices suspensions, we have seen that a 0.25 T magnetic field is not sufficient to induce any reorientation. A 0.5 T magnetic field has uncertain influence on the alignment of CNC helices, possibly close to the threshold field intensity at which the alignment starts to be observed. A 0.65 T magnetic field already leads to a really good alignment of CNC helices within a couple of hours, that keeps being strengthened over a day to yield an order parameter for the helices axes orientation of  $S_{2,\text{helices}} = +0.85$ . Finally, 9 T magnetic field experiments have proved to yield a fully aligned cholesteric texture. We have observed that a weak magnetic field alignment has major impact on the optical appearance of cholesteric domains, yielding near-homogeneous iridescent texture that is of great interest towards making photonic materials. The observation of higher orders of diffraction and iridescent colours in reflection are additional indications of the good optical quality of the sample after magnetic field alignment. Due to the low value of the pitches of concentrated suspensions in apolar solvents, an iridescent colour response can be observed directly in suspension, which allows for the first time to have a qualitative sample-wide information on the state of alignment of cholesteric domains, complementary to the local characterisation techniques – SANS, SAXS, SEM – previously reported in the literature.

#### 4.2.1.2. Nucleation of cholesteric domains in a magnetic field

##### 4.2.1.2.1. Final state

The preceding paragraphs have emphasized the importance of the initial state of the suspension on the quality of the final alignment. In order to investigate this effect, we performed an experiment where a CNC suspension is extensively vortexed prior to being poured in



capillaries, and aligned under magnetic field immediately after capillary sealing, compared to a four days old phase-separated suspension that was then exposed to the same magnetic field. Both samples come from the same CNC suspension, at 26 wt.%, in the biphasic domain. Laser diffraction characterisation, presented in Figure 95, has been performed on the two samples left to align for 22 h in a 0.65 T magnetic field. The sample that has been left to form helices under fields looks significantly more aligned than the initially phase-separated sample later exposed to the magnetic field. Moreover, the curve displaying the intensity scattered as a function of the angular direction is more regular, close to the theoretically expected Boltzmann distribution. Using the previously mentioned theoretical fits, it is possible to retrieve precise values for the order parameter of orientation of CNC helices axes in regard to the direction of the magnetic field. Sample developing helices under magnetic field reaches an order parameter of  $S_{2,\text{helices}} = +0.96$ , to be compared with  $S_{2,\text{helices}} = +0.85$  of the sample developing helices before magnetic alignment took place.

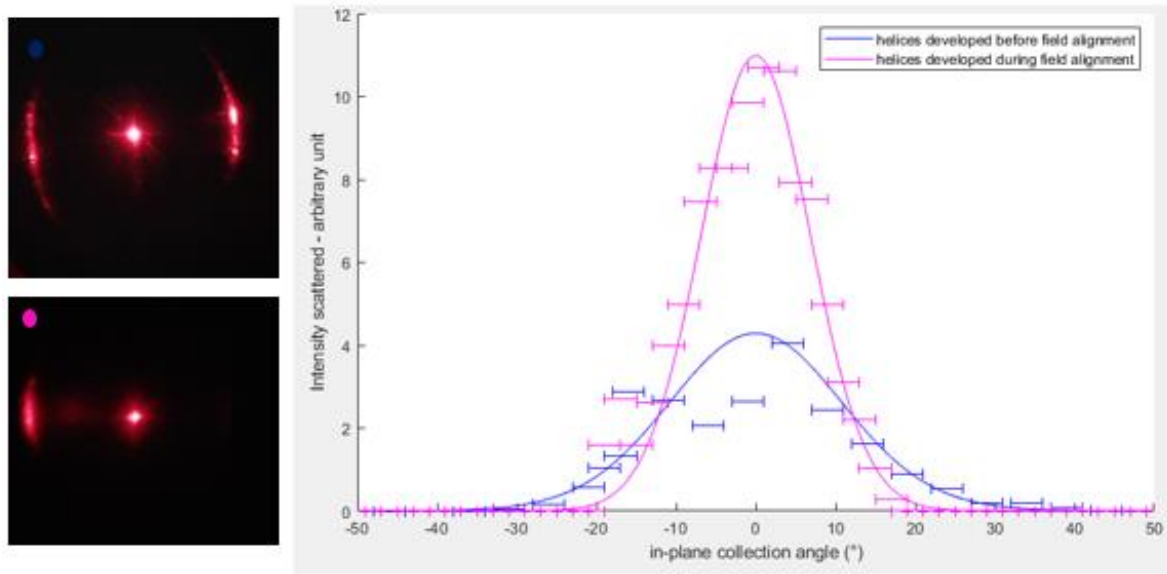


Figure 95 : (left) Laser diffraction patterns of the 4 days old phase-separated CNC suspension subsequently exposed to magnetic fields for 22h in blue and of the vortexed and field-aligned CNC suspension after 18 hours in magenta. Both suspensions are at 26 wt.%. (right) Angular plots and theoretical fits of the two previous laser diffraction patterns, showing intensity as a function of the angular direction. In the laser diffraction pattern of the vortexed CNC suspension (magenta), one of the two diffraction arches is blocked by the experimental setup. See chapter 2 for more details on data processing and fits.

#### 4.2.1.2.2. Alignment kinetics

In order to decipher the mechanism underlying the alignment of the samples, time lapse laser diffraction patterns presented in Figure 96 have been recorded over time for the freshly vortexed sample and compared to the phase-separated sample that has already been presented

in Figure 91. For the phase-separated suspension, we have seen that cholesteric domains were readily formed prior to alignment and slowly reorienting after a few hours in the direction of the field. For the vortexed suspension, the first distinguishable diffraction pattern at short times is made of two diffraction points in the direction of the magnetic field that grow in intensity over time. Between one and two hours of alignment, the scanned domains get slightly misaligned, before reaching a high level of alignment after 18 hours.

These data strongly suggest that the nucleation of fully aligned domains takes place in the suspension within the first hour of experiment. The number of aligned domains increases over time with little change on the quality of their orientation. The misalignment observed after an hour of experiment is attributed to macroscopic flows during sample reorganisation. This scenario is in good agreement with what has been previously described by Revol et al. (Revol et al. 1994) with polarised optical microscopy. As a reminder, they observed that tactoids spontaneously nucleating in an anisotropic aqueous CNC suspension would align under strong magnetic fields leading to extended mono-domains after tactoids coalescence. Our results show that this also takes place under weak magnetic fields, interestingly leading to very good quality alignments.

Figure 97 presents the evolution of the scattered intensity (relative to final intensity obtained after 19 hours) and pitch values over time retrieved from image analysis of Figure 96. Under the hypothesis that the RGB intensity recorded by the camera is linear, the intensity scattered is directly proportional to the number of helices developed in the sample. Helices nucleation is detected as early as 5 min after the beginning of the alignment, 25% of the final amount of helices are developed after 50 min and 50% of the final amount is developed after 3 hours. Interestingly, the pitch value decreases significantly over time, especially in the early stages of the alignment. This could correspond to the observation of a fractionation of the biphasic suspension taking place as cholesteric domains form. Shorter rods are expelled from the growing cholesteric phase into the isotropic phase whereas longer rods form helices of shorter pitches in the anisotropic phase (Honorato-Rios and Lagerwall 2020). Figure 98 sums up experimental results by suggesting schematically a likely scenario for the alignment of readily-formed cholesteric phases, compared to the one of an extensively vortexed CNC suspension based on experimental results.

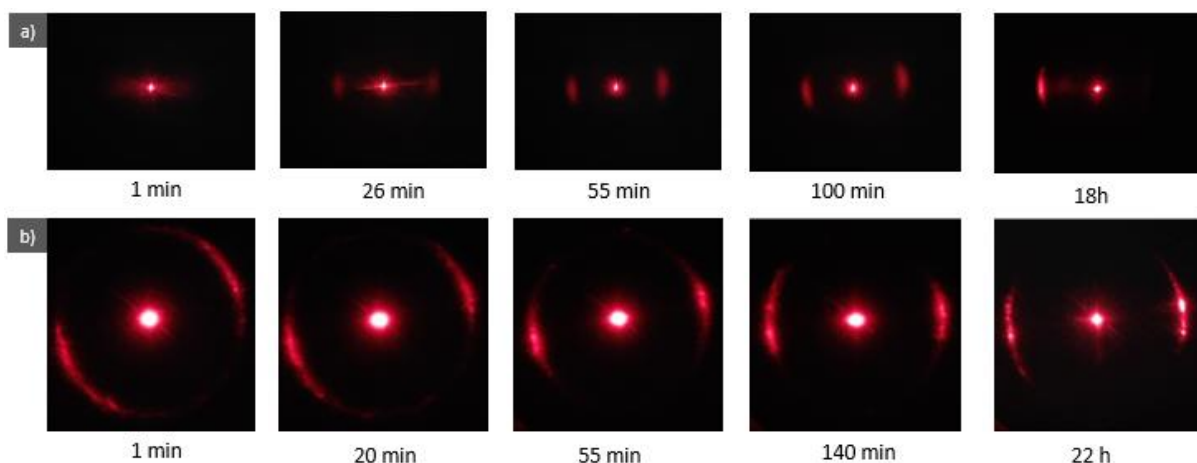


Figure 96 : Laser diffraction patterns time lapses of the magnetic field alignment of a) an extensively vortexed CNC suspension and b) a phase-separated suspension both at 26 wt.%. Second diffraction point is blocked by the experimental setup in the last picture of a).

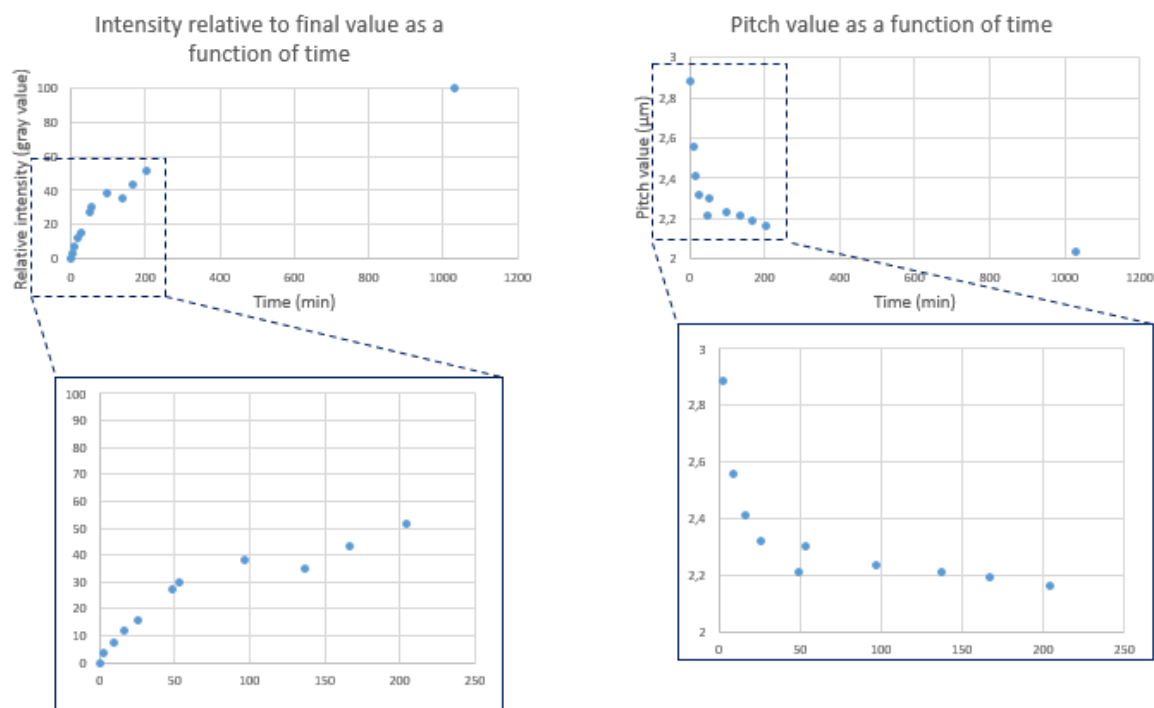


Figure 97 : Evolution of the scattered intensity (left, in relative % to the final scattered intensity) and pitch value (right) of an extensively vortexed CNC suspension at 26 wt.% over time obtained by image analysis of Figure 96. Dark blue insets are close-ups of the previous curves at short times. 25% of the helices are developed after the first 50 min, 50% of the helices are developed after 3 hours. The pitch value as the helices develop, most notably at early stages of the alignment.



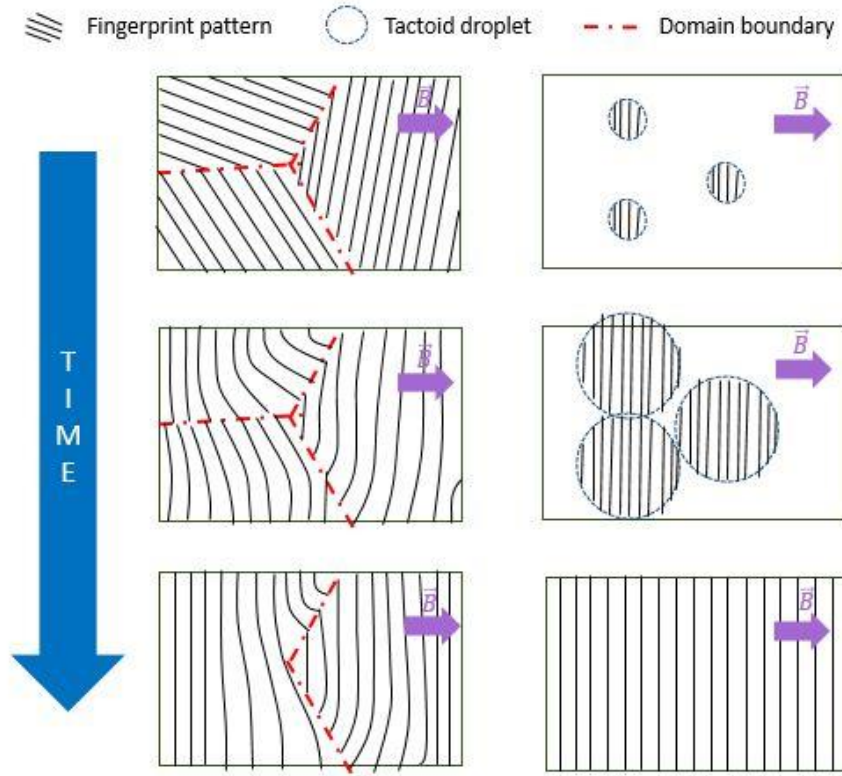


Figure 98 : Schematic of the magnetic field alignment of (left) a readily-formed cholesteric phase and (b) a super-saturated isotropic CNC suspension viewed under polarised optical microscopy. On the left, the cholesteric phase struggles to reorient in the magnetic field direction owing to domain boundaries already present in the microstructure, leading to imperfect alignment. Only some of the defects are melt by the field. On the right, tactoids nucleate and are readily aligned under magnetic field as they grow. Tactoid coalescence yield large aligned domains, corresponding to an overall more aligned sample.

## 4.2.2. Alignment of CNC suspensions under electric fields

### 4.2.2.1. Alignment with different field geometries

While Frka-Petesic et al. (Frka-Petesic, Radavidson, et al. 2017) have demonstrated a complex and potentially promising behaviour for the orientation of concentrated CNC suspensions in toluene under electric fields for applications, they have only explored a configuration in which the electric field is oriented in the horizontal  $y$  direction. We investigate hereafter three possible configurations for the electric field, along  $x$ ,  $y$  and  $z$  as in Figure 99.

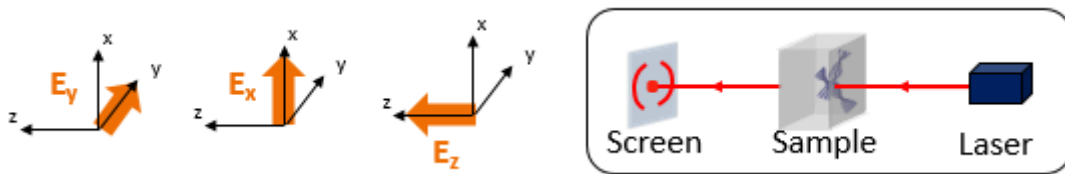


Figure 99 : Schematic view of the configurations for the electric field alignment and laser diffraction characterisation geometry.

#### 4.2.2.1.1. Horizontal electric field in the $y$ direction

We have first tried to reproduce literature results with lab-made CNC suspensions aligned under a horizontal electric field  $E_y$  and the results are presented in Figure 100. Similar laser diffraction and iridescent patterns as Frka-Petesic et al have been observed. In laser diffraction, the initially random configuration reorients around  $E_y \sim 200$  V/cm into a two-point vertical configuration perpendicular to the electric field whose points merge around  $E_y \sim 450 - 500$  V/cm into the centre of the diffraction pattern. By slowly releasing the electric field, it is possible to reform helices that are strictly aligned in the direction perpendicular to the electric field. Looking at white light scattering, the increase in intensity corresponding to the reorientation of cholesteric domains in the scattering direction is hardly noticeable, but the redshift in colour due to the unwinding is clear. When the field is decreased again from an unwound state, the rewinding around 400 V/cm leads to a more homogeneous iridescent response in good agreement with the better alignment state.

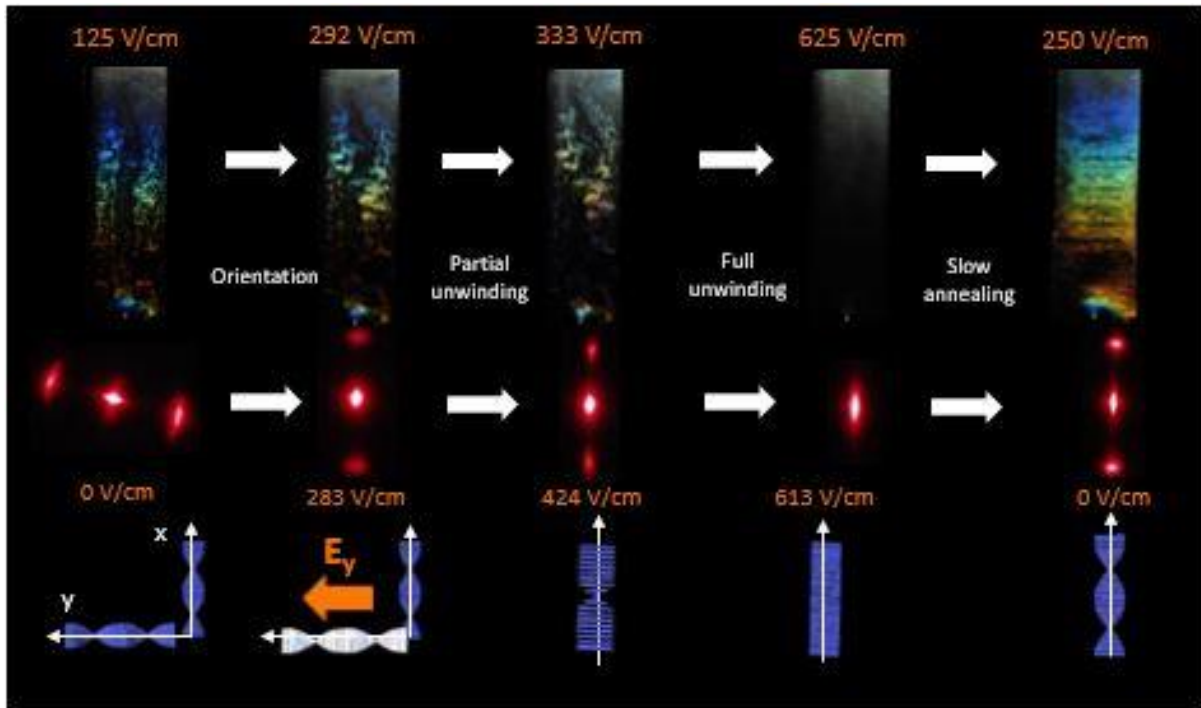


Figure 100 : Characterisation of the behaviour of a 29 wt.% CNC suspension under horizontal electric field  $E_y$ . (top) Iridescent white light scattering displayed by the samples for different electric field values in orange. (middle) Laser diffraction patterns displayed by the sample at different electric field values in orange. (bottom) Schematics of the different helices configurations corresponding to the white light and laser diffraction patterns observed.

#### 4.2.2.1.2. Vertical electric field in the $x$ direction

The white light and laser diffraction of concentrated CNC suspensions under a vertical electric field  $E_x$ , with corresponding schematics of the helices configurations, is shown in

Figure 101. Similarly to the horizontal direction, the laser diffraction pattern is what one expects based on current knowledge: a random initial diffraction pattern reorients into a two-points horizontal pattern around 250 V/cm perpendicular to the applied vertical field whose points further merge into the centre of the diffraction pattern around 400 V/cm due to helices unwinding. Slow-annealing occurs in a similar fashion. Notably shortly before scattering in the infrared, the colour becomes white and the laser diffraction pattern is made of a horizontal line resembling a “moustache”. This configuration is very similar to the one described by Frka-Petesic et al.

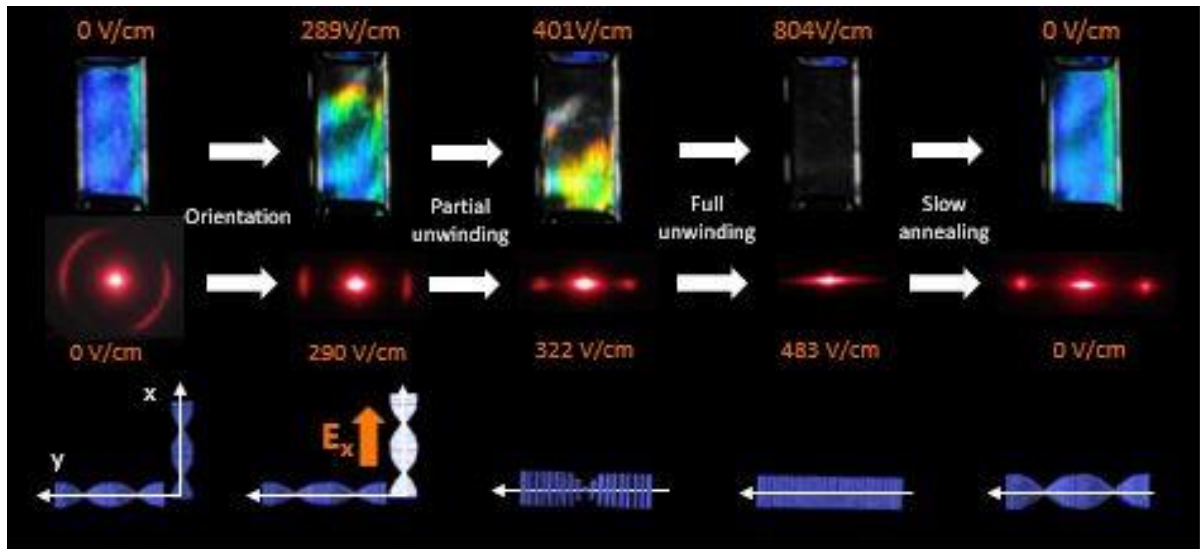


Figure 101 : Characterisation of the behaviour of a 32.8 wt.% CNC suspension under vertical electric field  $E_x$ . (top) White light scattering of the samples for different electric field values in orange (performed just after laser diffraction experiments, explaining the very homogeneous starting state). (middle) Laser diffraction patterns displayed by the sample at different electric field values in orange. (bottom) Schematics of the different helices configurations corresponding to the white light and laser diffraction patterns observed.

#### 4.2.2.1.3. Transverse electric field in the z direction

Finally, alignment of CNC suspensions have been carried out under an electric field  $E_z$ , *i.e.* oriented in the thickness of the sample. A slightly different setup involving transparent electrodes has been used and is detailed in chapter 2, to allow for the electric field and the laser to be in the same direction. While white light scattering data is not very different – increase in sample area scattering light followed by redshift out of the visible –, laser diffraction patterns are completely changed. When applying an  $E_z \sim 200$  V/cm electric field along the direction of propagation of the laser, a transition from a random initial configuration to a circular diffraction pattern is observed. As the electric field intensity is further increased, the circle decreases in radius, becomes a disk short before becoming a point at the centre of the pattern. Slowly releasing the electric field leads again to a circular pattern. The circular pattern observed at

200 V/cm shows that any helix orientation within the plane of diffraction (Oxy) is still possible after the reorientation step has occurred, conversely to the two previous configurations where only one helix direction was favoured by the field. The decrease in radius of the circular pattern as the field increases corresponds to an increasing pitch value for the helices in the (Oxy) plane, consistent with observations made in the two previous configurations. The disk pattern corresponds to different pitch values close to the end of the unwinding, and seem to be the analogue of the previously described “moustache” pattern.

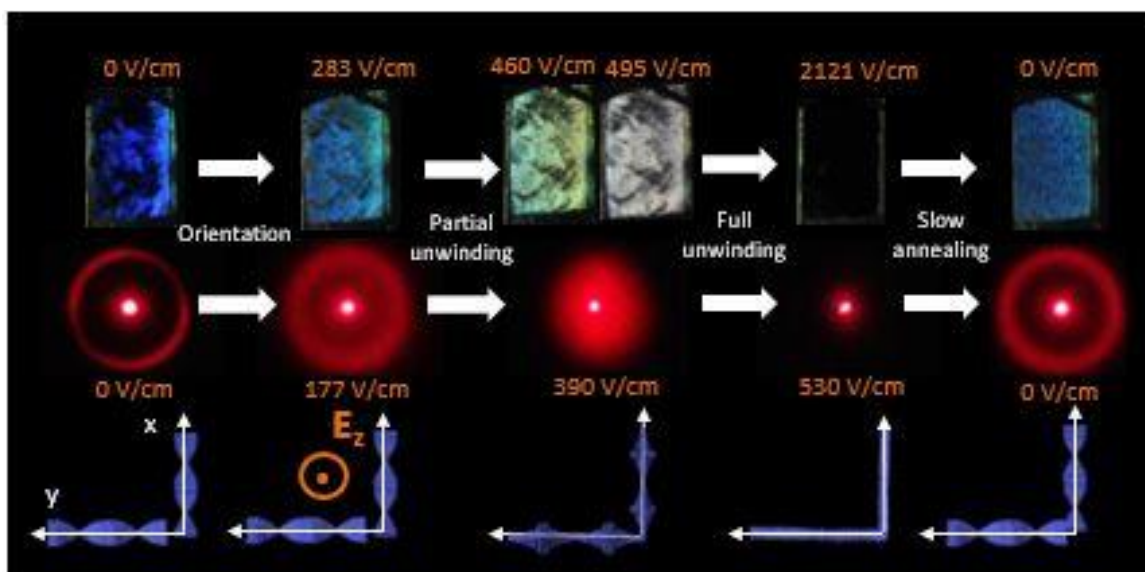
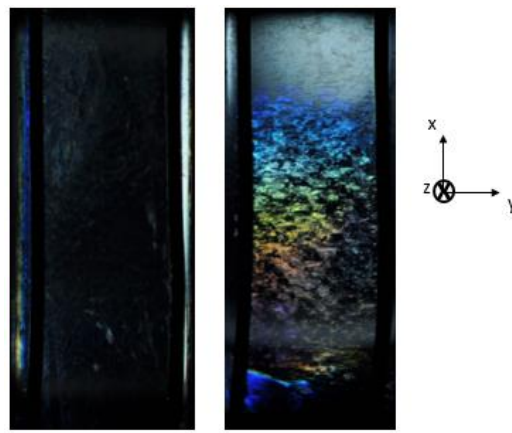


Figure 102 : Characterisation of the behaviour of a 32.8 wt.% CNC suspension under in-depth electric field  $E_z$ . (top) Optical appearance of the samples for different electric field values in orange. (middle) Laser diffraction patterns displayed by the sample at different electric field values in orange. (bottom) Schematics of the different helices configurations corresponding to the white light and laser diffraction patterns observed. Notably, the gap between the two electrodes is only  $1.0 \pm 0.1$  mm in this experiment in contrast with centimetre scale gaps of the two previous experiments.

#### 4.2.2.1.4. Orientation mechanism under electric fields

The key to interpret these data is the fact that laser diffraction only probes the orientation of helices of the (Oxy) plane, whose orientation is perpendicular to the direction of the laser. Helices with a component in the z direction do not contribute to the diffraction patterns. The same phenomenon is occurring in all three cases (the alignment of helices under electric fields), but from different point of views. Results therefore imply that in all three cases the electric field allows for a plane of helices orientation perpendicular to the direction of the electric field rather than a single direction of orientation as suggested by previous works. Whenever the field is oriented in the x or y direction, the planes containing the remaining helices after the reorientation step are respectively the (Oyz) and (Oxz) planes. The intersection of these planes with the plane of diffraction (Oxy) gives the helices visible in laser diffraction, corresponding

to helices oriented respectively along  $y$  and  $x$ . This leads to the observation of respectively a horizontal and vertical two-points pattern. Conversely while applying an  $E_z$  field, the plane containing the remaining helices is the (Oxy) plane, which is also the plane of diffraction: all remaining helices are visible in laser diffraction, leading to a circular pattern as observed. A further convincing proof of this hypothesis is the optical appearance of a sample shortly after electric field slow-annealing in the  $x$  or  $y$  direction. The iridescent texture is not homogeneous like under magnetic fields, rather only parts of the sample are scattering light to the camera as in Figure 103, corresponding to the fraction of cholesteric domains that are oriented to match Bragg conditions.



*Figure 103 : Optical appearance of a 29 wt.% CNC suspension after unwinding and slow-annealing under an  $E_y$  electric field. (left) White light source off-centered horizontally ( $y$  axis) from the sample. Scattering is not observed on account of sample reorientation. (right) White light source off-centered vertically ( $x$  axis) from the sample. White light scattering is observed, but only covers part of the sample on account of the 2D possible orientations for helices under electric field.*

The take-home message of this series of experiments is that, conversely to magnetic fields, an electric field yields a plane of helices orientation perpendicular to the electric field during the previously described reorientation step, followed by the unwinding of the helices. We will see in the next sections that this result has various consequences on the appearance and optical quality of CNC helices aligned under electric fields.

#### **4.2.2.2. *Quality of the electric field alignment***

While the electric field alignment during the reorientation step and after slow-annealing seems qualitatively strong, it is of interest to try to put a quantitative number on it. An order parameter for the helices axes orientation with respect to the electric field direction can be derived from the angular distribution of scattered intensity from laser diffraction data presented in Figure 104 similarly to the magnetic field alignment treatment of Figure 92, and yields a



value of  $S_2 = -0.44$ . Note that we only use the data from the (Oxy) diffraction plane to perform this calculation, which does not take into account helices with a z component but is thought to be representative of the overall state of helices orientation in the sample according to symmetry arguments on the electric field. The validity of this hypothesis is further discussed under the light of additional results in materials in the section Anchored skin layer in field-aligned composites of chapter 5. This value is very close to a perfect anti-alignment with respect to the electric field direction, which confirms the observation that the electric field aligns almost perfectly CNC cholesteric domains during the reorientation step or at the end of slow-annealing. One can summarise the different degree of alignment obtained as such: electric field alignment  $\geq$  extensively vortexed magnetic field alignment  $>$  simple magnetic field alignment.

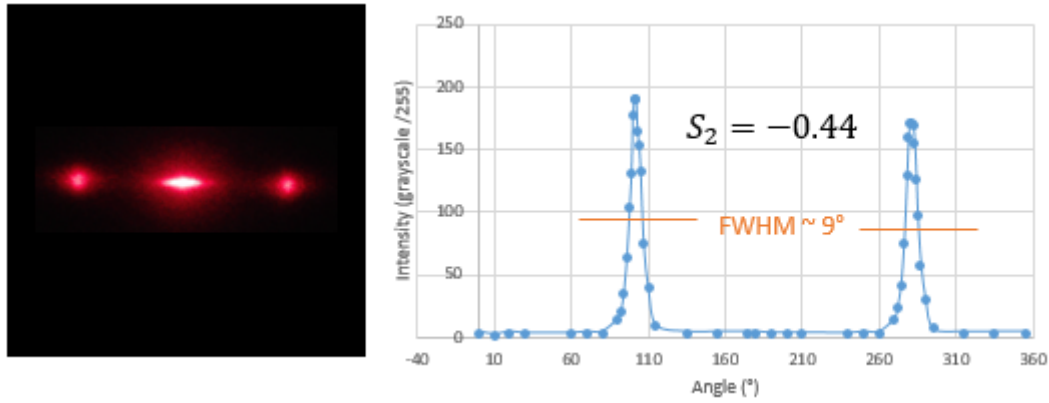


Figure 104 : Angular distribution of the scattered intensity of a 32.8 wt.% CNC suspension after slow-annealing derived from laser diffraction data and corresponding order parameter determination. The full width at half maximum (FWHM) of the distribution is approximately  $9^\circ$ .

#### 4.2.2.3. Description of the critical transition values

Reorientation of helices has been observed at values of typically 100-110 V/cm in the biphasic domain, and slightly higher values of typically 150-200 V/cm in the fully anisotropic domain. This evolution is most likely due to the increased viscosity of the suspension making it more difficult for helices to realign along the field.

We have measured the critical transition value for the unwinding by slowly decreasing the electric field from a fully unwound state and oscillating around the targeted value to help reduce the influence of kinetic barriers on the measurement. At  $E \sim E_c$ , it takes as long as 1h30 to get rid of the scattering white appearance to the profit of an iridescent colour response while maintaining the electric field just below the transition value due to the little thermodynamic incentive of the system to evolve, as presented in Figure 105. This result could indicate that the response time of the system scales as  $(E - E_c)^\alpha$  where  $\alpha$  is an unknown exponent. As a good

practice, fitting data to De Gennes' model (De Gennes 1968; Frka-Petescic, Radavidson, et al. 2017) may be a more reliable way of measuring  $E_c$  because it relies on taking points all over the course of the alignment rather than relying on experimental points at  $E \sim E_c$ .

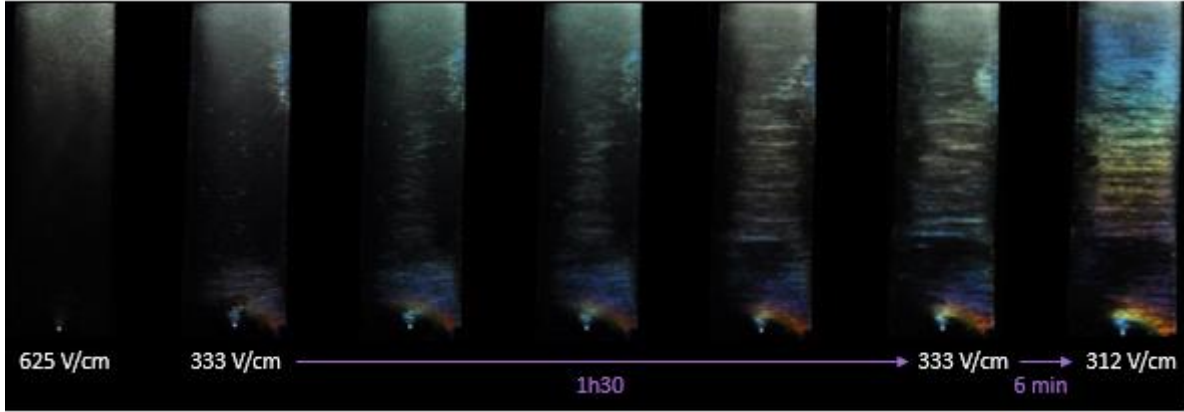


Figure 105 : White light scattering characterization of the careful rewinding of a 28,8 wt.% CNC suspension in toluene. Plenty of time is given to the sample to relax to its equilibrium state after each electric field value modification. At 333 V/cm just below  $E_c$ , sample relaxes to its final state in 1h30 whereas it takes only 6 min at 312 V/cm.

Comparing our data to Frka-Petescic et al (Frka-Petescic, Radavidson, et al. 2017) in Figure 106, the critical electric field value for the unwinding  $E_c$  is very comparable in both cases. Data from this work seem to be 20 to 50 V/cm lower than theirs, increasing with the concentration. This may well be due to the fact that  $E_c$  has only been measured by decreasing electric fields in this work whereas Frka-Petescic et al. took a mean of the increasing and decreasing electric field values for  $E_c$ .

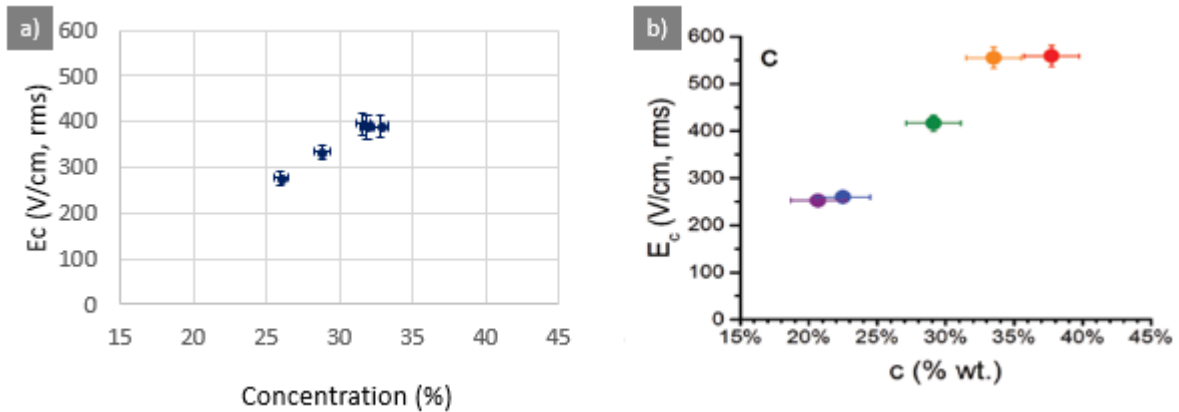


Figure 106 : Critical electric field values for the unwinding derived from De Gennes' model as a function of concentration for (a) experimental data from this work and (b) data from Frka-Petescic et al., Adv. Mat. 2017.

#### 4.2.2.4. Electric field cut-off and dynamic colour switching

While these two experiments described in the state of the art and respectively consisting in cutting off abruptly the electric field from a fully unwound helical state and in cycling the electric field in between two electric field values corresponding to two different visible colours are among the most interesting features of manipulating CNC suspensions with electric fields, the physics of the phenomena have been already described in detail by Frka-Petesic et al (Frka-Petesic, Radavidson, et al. 2017). We have performed these experiments using our systems, and have obtained very similar results which are summed up in Figure 107.

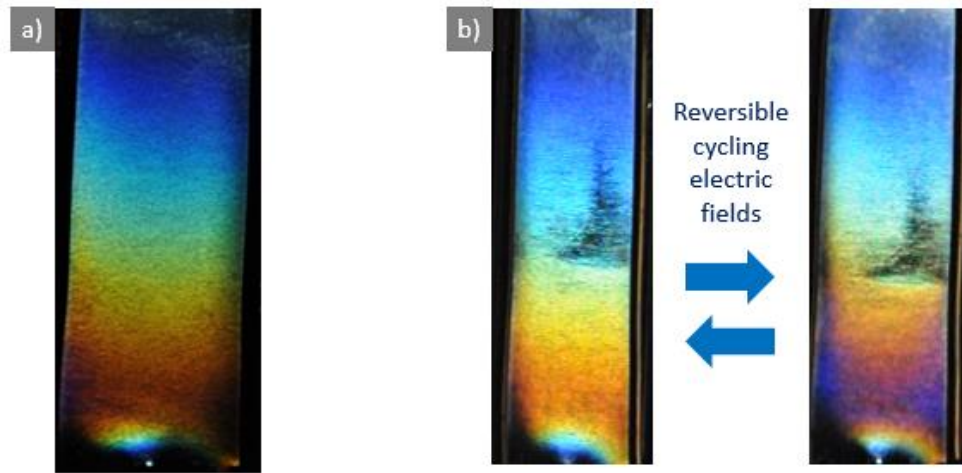


Figure 107 : a) Vertical iridescent texture from a 28.8 wt.% suspension subjected to a 2086 V/cm electric field corresponding to complete unwinding before abruptly cutting off the electric field. Picture is taken after a few minutes. The different colour displayed are due to parallax effects. b) Vertical iridescent texture from a 28.8 wt.% suspension subjected to two different electric field values at 125 V/cm and 312 V/cm cycling every 5 seconds corresponding to the two different colour states displayed. From left to right, colour shifts upwards with increasing electric fields, leading to the observation of the second order blue on the right.

#### 4.2.2.5. Reversibility of the electric field alignment

In order to probe the reversibility of the electric field alignment, cycling experiments have been performed by repeatedly sweeping from zero to high electric field values and the critical transition values are reported in Figure 108. Interestingly, the critical field value measured at  $498 \pm 13$  V/cm while increasing electric field values is reproducibly higher than the values measured  $438 \pm 6$  V/cm while decreasing the electric field values. We interpret the difference in critical field values from rise and descent as a direct consequence of the sample state as the unwinding occurs. While the electric field is increased, the sample is made of multiple cholesteric domains whose orientations are random within a plane of possible domain orientations, corresponding to multiple defects in between domains whose melting is a kinetic



barrier to overcome. Conversely when the field is decreased, the sample is made of fully aligned individual CNCs in the direction of the electric field that rewind at the transition value, corresponding to no real kinetic barrier to overcome in the process. From the average over-voltage  $E_{c,up} - E_{c,down} = 60 \pm 18$  V/cm required to unwind existing cholesteric domains, one can derive a measurement of the energy incentive required to melt domain boundaries in the overall sample:

$$E_{\text{boundaries,sample}} = \frac{1}{2} \cdot \epsilon_0 \cdot \epsilon \cdot V \cdot (E_{up} - E_{down})^2$$

$$E_{\text{boundaries,sample}} \sim 4 \cdot 10^{-11} \text{ J}$$

To give a sense to this result, let us consider a cholesteric domain of volume  $10 \cdot 10 \cdot 10 \mu\text{m}^3$ . The energy required to melt the domain boundaries of this domain writes as:

$$E_{\text{boundaries,1 domain}} = \frac{V_{\text{domain}}}{V_{\text{sample}}} \cdot E_{\text{boundaries,sample}} = 3 \cdot 10^{-19} \text{ J} \sim 100 \cdot k_B T$$

While we have no way to critically assess the validity of this result, its order of magnitude seems to make reasonable sense. Note that the uncertainty on  $E_{up} - E_{down}$  is significant and transfers into the result. The energy of domain boundaries and defects is large because the rearrangements required to modify pitch values in existing domains involve necessarily cooperative movements of individual CNCs in the whole cholesteric domain. Moreover, the sample used in Figure 108 is fully anisotropic, possibly leading to bigger cholesteric defects energy than a biphasic sample.

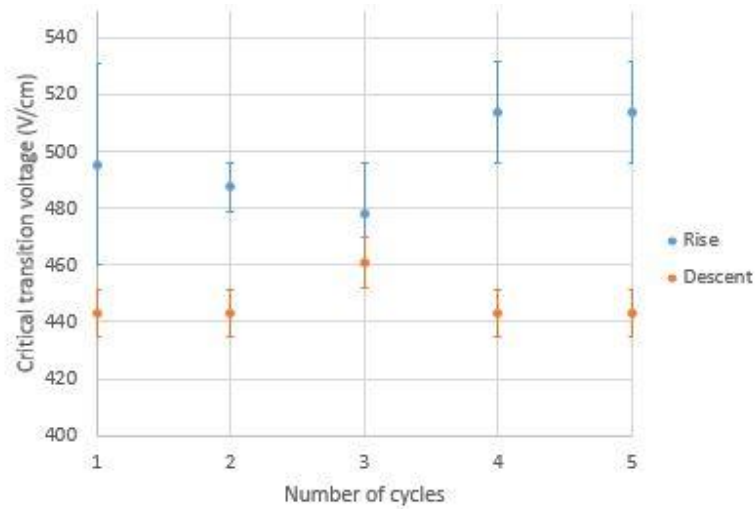


Figure 108 : Plot of the critical electric field transition voltage as a function of the number of cycles during cycling electric fields alignment of a 31.6 wt.% CNC suspension. (blue) Increasing electric fields. (orange) Decreasing electric fields.

#### 4.2.3. Geometric arguments to explain the behaviour of cholesteric CNCs under electric and magnetic fields

The experimentally observed helix selection under external fields alignment can be rationalised by considering the effect of each field on individual particles. In a helix assembly, all individual rods have their long axis oriented perpendicular to the helix axis. We have seen that Frka-Petesic et al (Frka-Petesic, Jean, and Heux 2014; Frka-Petesic et al. 2015) measured a positive dipolar moment for CNCs meaning they are willing to align their long axis along the electric field, and a negative diamagnetic anisotropy meaning CNCs are willing to align their long axis perpendicular to the magnetic field.

Whenever an electric field is set, helices whose axes are along the field are composed of CNC that are all perpendicular to the field. They thus are strongly unfavoured by the sum of all unfavourable CNC interactions with the field. By considering helices that are perpendicular to the field, some rods are along the field therefore maximising their favourable interaction with the field while others are perpendicular to the field, therefore having an unfavourable interaction with the field. So the energy level of these configurations does not vary much. As a result, the electric field will tend to suppress the helix whose axis is along the field while keeping the others untouched. This results in orientation of the helices axes in the plane perpendicular to the field as observed experimentally.

However, there is a remaining frustration in the interaction of helices perpendicular to the field as some of the rods have unfavourable interactions with the field. At stronger field values,

the rods will prefer to maximise their quadrupolar interaction with the field at the cost of their chiral stabilising interaction. This will lead to helices being unwound as observed experimentally.

Applying a magnetic field corresponds to a reverted situation: helices whose axes are along the field are favoured by the sum of all favourable CNC interactions with the field, while helices whose axes lay perpendicular to the field contain both rods with favourable and unfavourable interactions. As a result, the magnetic field will tend to keep the helices whose axes are along the field to the detriment of all other orientations. It is interesting to see that this simple qualitative model involving geometrical considerations and two types of interaction – quadrupolar and chiral – summarised in Figure 109 is enough to describe the experimental behaviour of the system.

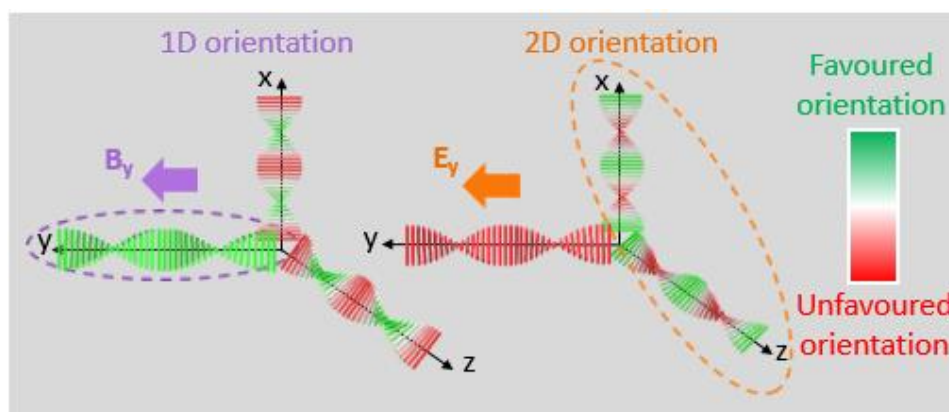


Figure 109 : Qualitative model for the alignment of CNC helices obtained by extrapolating the properties of individual CNCs, predicting the experimental behaviour of CNC helices under fields. Rod orientations in green are favoured by the applied field, rod orientations in red are unfavoured by the field. Final configurations are highlighted in dashed lines: the configuration along the field is favoured under magnetic field and unfavoured under electric field compared to other configurations.

#### 4.2.3.1.1. Distortion of the cholesteric helix at moderate field values

This theoretical model also predicts the distortion of the helices at moderate field values on the model of Figure 110: rods that are close to being aligned along the field wish to be fully aligned, whereas rods that are perpendicular do not want to be twisted more. The distortion of the helix structure within a pitch distance consists of a “core” structure of CNCs near-fully aligned with the field (green regions) separated by “defect regions” where CNCs have higher twisting angles than at equilibrium state (red regions). Direct observation of the distortion is further developed in the section Orientation of cholesteric helices in field-aligned PS composites of chapter 5.

This distortion can be modelled by adding a higher uneven harmonics perturbation to the periodic modulation of the helical director; If we define  $\alpha$  as the angle between the director of individual CNCs and the direction of the field, we have a periodic modulation of  $\cos(\alpha)$  for an undistorted helix that writes:

$$\cos(\alpha) = \cos(qr)$$

where  $q = 2\pi/p$  and  $r$  is the position along the helical axis. In the case of a distorted helix, we can write in first approximation:

$$\cos(\alpha) = A \cdot \cos(qr) + B \cdot \cos(3qr)$$

with  $B$  small compared to  $A$ , so that  $B \cdot \cos(3qr)$  remains a perturbation of the undistorted signal. Additional uneven harmonics ( $5qr, 7qr \dots$ ) can be added to refine the non-periodicity of the modulation. The physical origin of adding uneven harmonics to deform the signal comes from the fact that, at infinite electric field value, one expects a square function to describe the orientation of individual CNCs. The development in Fourier series of the square function is the infinite sum of the uneven harmonics of the signal (Fourier\_square).

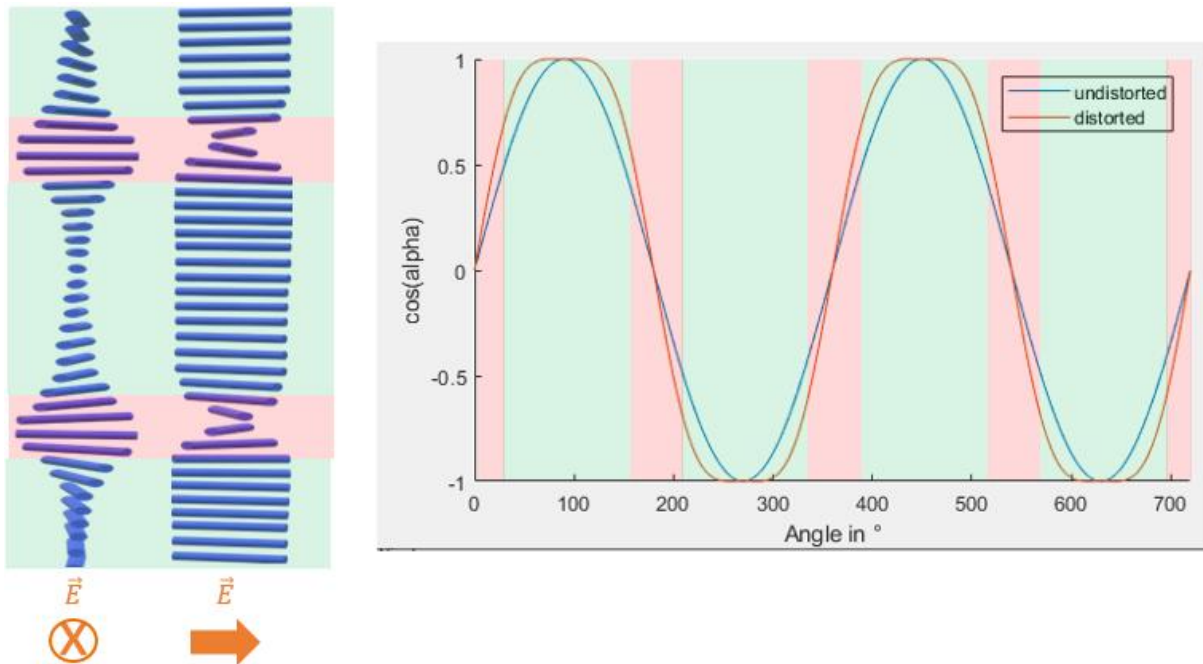
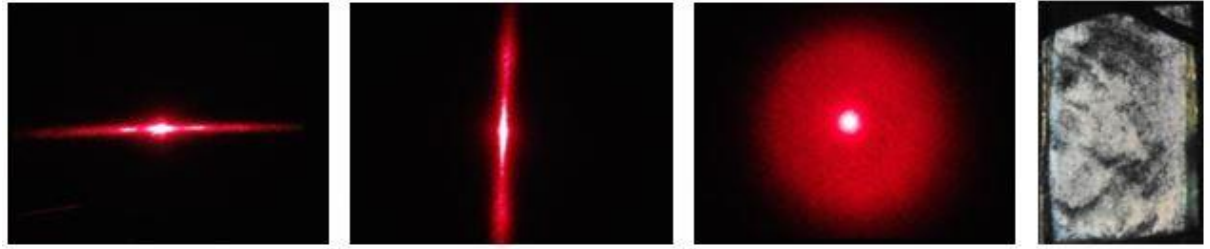


Figure 110 : Distortion of the director of individual CNCs when subjected to a moderate electric field value. (left) Schematic view of a distorted helical stack under two different viewing angles. (right) The periodicity of the angular variation of the director along the helix is broken by the application of the electric field. The angle  $\alpha$  in ordinates is defined here as the angle between the director of individual CNCs and the direction of the electric field. In both subfigures, green regions contain CNCs that have reoriented to maximise their interaction with the field, whereas red regions contain CNCs showing increased twist angles.

Interestingly, there is a physical argument that tells us there is a remaining twist even in the most aligned green regions of Figure 110 as long as the pitch of the helix is well-defined. Giving a proof by contradiction, if there was no remaining twist in the green region, there would be no energy cost for the red regions to move in the direction of what used to be the helical axis (other than at short distance on the order of the initial pitch). There are therefore no reasons why red regions would stay at their initial location along the chain. Red regions would then tend to get randomly distributed in non-periodic positions along what used to be the helical axis, and we would not be able to define a pitch value anymore (half the pitch of the helix being defined as the distance in between two red regions in undistorted helices).

Up to  $E \lesssim E_c$ , the pitch value is precisely defined, *i.e.* there is a small remaining twist in between rods in distorted helices. Conversely at  $E = E_c$ , the laser and white diffraction patterns presented in Figure 111 are observed: a linear diffraction pattern perpendicular to the electric field with  $E_x$ ,  $E_y$  and a disk pattern corresponding to a scattering white with  $E_z$ . This is likely the experimental manifestation of the fact that the pitch value of the helices cannot be defined anymore.



*Figure 111 : Laser diffraction patterns and optical appearance of samples on the edge of helices unwinding at  $E = E_c$ . From left to right,  $E_x$ ,  $E_y$  (“moustache” patterns),  $E_z$  (disk pattern) and  $E_z$  (scattering white).*

#### **4.2.4. Alignment under combined magnetic and electric fields**

A natural question that arises at this point is to observe what happens if magnetic and electric fields are combined within the same sample. Such experiments have been conducted using a 0.65 T magnetic field and an electric field at various intensities. As the characteristic time to align in magnetic fields is long and short in electric fields, it has been chosen to pre-align the samples under magnetic fields until near-final state is attained after 1h15 before applying an increasing electric field in the same direction, therefore favouring the opposite orientations while maintaining the magnetic field.

Laser and white light diffraction data presented in Figure 112 consistently show that a reorientation from the magnetic field-aligned orientation to the electric field-aligned orientation takes place at 111 V/cm. In laser diffraction, the initial pattern with two horizontal points is replaced by a pattern with two vertical points. In white light diffraction, the colour has entirely disappeared after 15 minutes at 111 V/cm, indicating that no helices are oriented along  $y$  anymore. By looking at the vertical scattering, *i.e.* the scattering of helices along  $x$ , approximately half of the sample area scatters light from millimetre scale cholesteric domains and one can therefore conclude that the remaining areas of the sample are made of different helices orientations, some of them having a component along  $z$ . The reorientation seems to take place by nucleating fully electric field-aligned domains out of magnetic field aligned domains (inset of Figure 112).

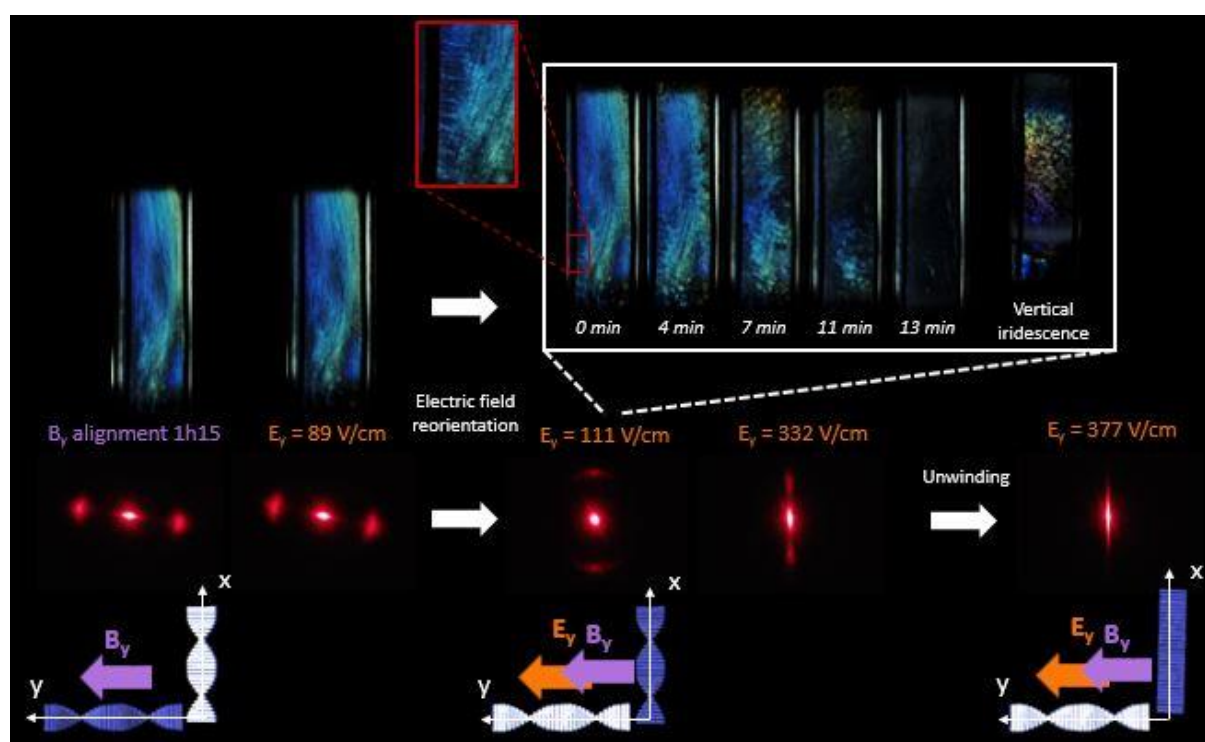


Figure 112 : Laser and white diffraction in the magnetic field-aligned configuration of a 26 wt.% CNC suspension pre-aligned under magnetic fields for 1h15 before being aligned under increasing electric field values favouring opposite orientations. Complete electric field reorientation is observed at 111 V/cm over 15 min followed by unwinding. Close-up of 111 V/cm 0 min in red highlights the nucleation of an electric field aligned phase in the immediate vicinity of the electrodes.

Observing more specifically the critical electric field value for the unwinding, Figure 113 presents the laser diffraction patterns close to the electric field unwinding in the presence and absence of a 0.65 T magnetic field. One observes that the critical field value for the unwinding appears to be the same, within the resolution of approximately  $\pm 10$  V/cm of the experiment. It

is possible to theoretically assess the electric field value needed to compensate the influence of the magnetic field by writing the equality of the energetic stabilisation contributions:

$$N \cdot \mu_0 \cdot \Delta\chi \cdot V_p \cdot H^2 = N \cdot (\mu_p \cdot E + \Delta\alpha \cdot E^2)$$

where  $N$  is the total number of rods and  $V_p$  the volume of the crystals. By solving this second order equation on the electric field value  $E$  and keeping the positive solution, we find:

$$E_+ = \frac{\mu_p}{2\Delta\alpha} \left( \sqrt{1 + \frac{4 \cdot \Delta\alpha \cdot \Delta\chi \cdot B^2 \cdot V_p}{\mu_0 \cdot \mu_p^2}} - 1 \right)$$

From this expression, one can estimate the electric field value equivalent to the magnetic field incentive to align at  $E = 2.75$  V/cm. This calculation explains why the influence of the magnetic field on the unwinding is not observed experimentally. It could be observed with a bigger magnetic field intensity, or with bigger particles.

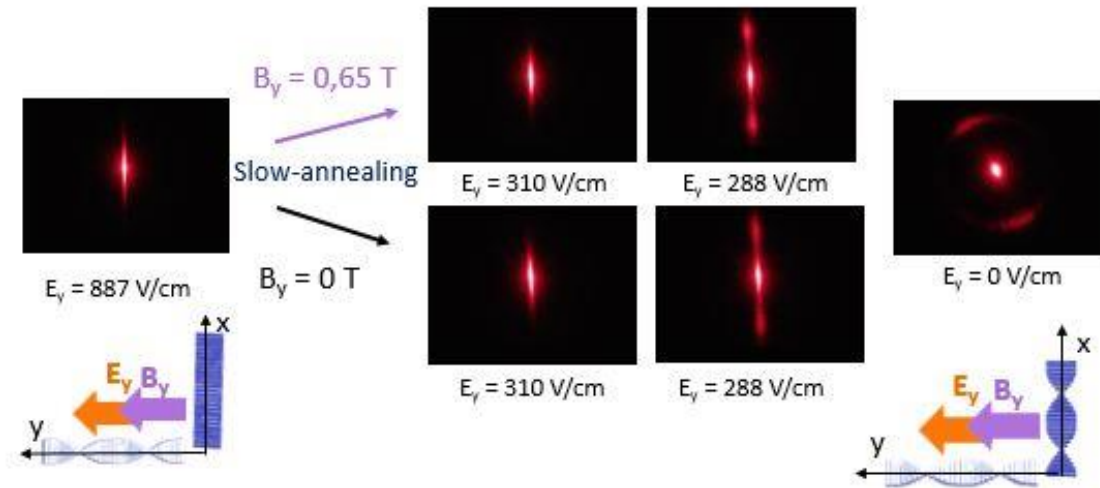


Figure 113 : Electric field slow-annealing experiment followed by laser diffraction in the presence (top) and absence (bottom) of a 0.65 T magnetic field. The rewinding of the helices is observed at the exact same critical electric field within the resolution of  $\sim 20$  V/cm of the experiment, showing little influence of the magnetic field on the electric field rewinding.

To summarise, electric field has been shown to dominate these competition experiments over magnetic field. Magnetic field pre-alignment can be used for a one-time switch of the cholesteric domain orientation.

#### 4.2.5. Centimetre scale thickness experiments

In this section, we study the alignment of cholesteric CNC suspensions of centimetre scale thicknesses. Experiments have been performed in UV-spectroscopy glass cuvettes coated with



ITO electrodes, filled and sealed with CNC suspensions and left to align under magnetic or electric fields.

Starting with magnetic fields alignment, one can observe on Figure 114 that both a 0.65 T and a 9 T magnetic field successfully align cholesteric domains and induce an iridescent response in centimetre scale thickness samples. The laser diffraction pattern under 0.65 T during 2h30 is made of two large points, indicating good quality alignment throughout the thickness of the sample. Points are thought to be enlarged by a small proportion of multiple scattering events taking place in the sample. Results are overall similar to low thickness samples.

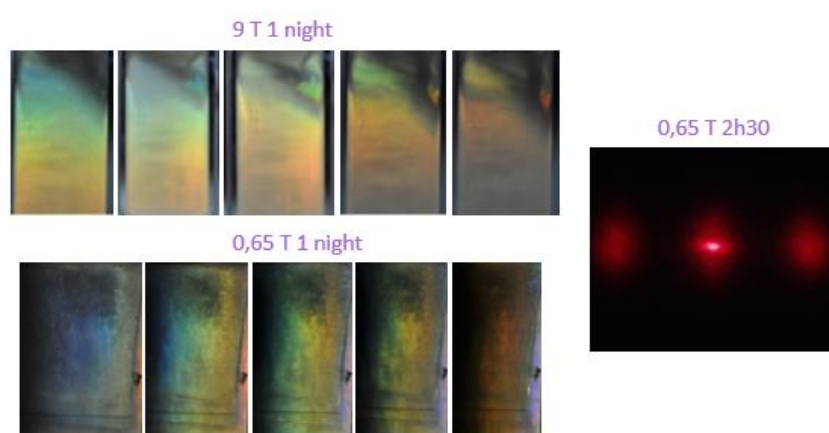


*Figure 114 : White light and laser diffraction of a 26 wt.% CNC suspension under a 0.65 T horizontal or a 9 T vertical magnetic field alignment during 2 hours or 1 night. 9 T pictures are taken within 10 minutes after field removal, whereas 0.65 T pictures are taken under field. From left to right in each series, the angle of incidence of incoming white light is increased.*

Under electric field alignment, a very different optical response is observed at centimetre scale thicknesses. The optical appearance of the samples is either opaque and grey at low and moderate field values, or completely transparent at electric field values inducing unwinding of the helices. The iridescent optical response is completely lost. Laser diffraction characterisation indicates a two-step behaviour made of the reorientation and unwinding of the helices, similar to low thickness experiments. The laser diffraction pattern is largely blurred by multiple scattering. We interpret this observation as a loss of coherence of the laser beam as it travels through a large number of cholesteric domains of different orientations. Light is incoherently scattered at the boundary between the domains, resulting in an opaque, grey appearance.



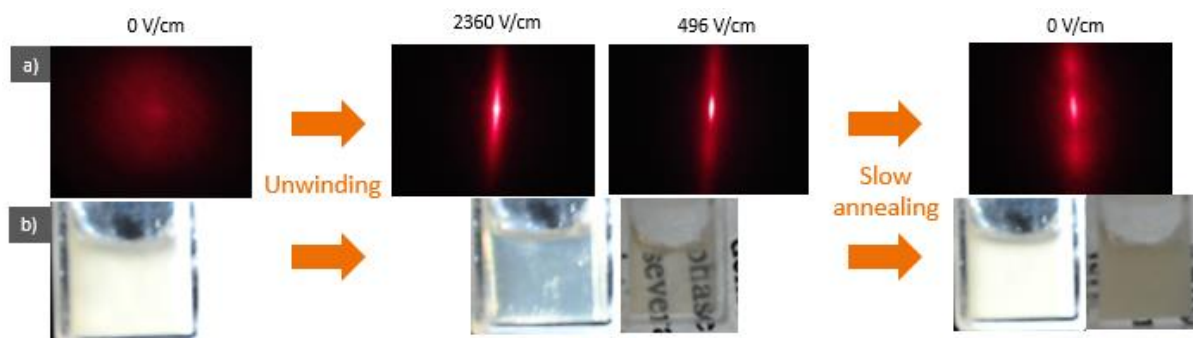


Figure 115 : (a) Laser diffraction and (b) optical appearance of electric field-aligned centimetre thicknesses CNC suspensions at 39.5 wt.%.

Centimetre thickness experiments therefore highlight the importance of favouring a single helix orientation through magnetic field alignment compared to multiple possible orientations through electric field alignment on the optical response of the samples. This is clearly a limitation of the electric field alignment.

### 4.3. Conclusions

#### 4.3.1. Alignment experiments under magnetic fields

This work has focused on the alignment using weak and commercially accessible magnets. It is first shown that 0.25 and 0.5 T magnetic field intensities are too weak to reliably align CNC suspensions, in contrast with a 0.65 T value that showed a very good quality of alignment. Higher fields from NMR magnets add further cholesteric domain homogeneity with however little gain on the optical response of the sample. Characterising further the 0.65 T magnetic alignment, the quality of alignment of phase-separated samples is first assessed by laser diffraction, corresponding to an order parameter for the orientation of helices axes of  $S_{2,\text{helices}} = +0.85$ . This alignment readily leads to near-homogeneous optical appearance of the sample, scattering in reflection and higher orders of diffraction in transmission. The intrinsic variability of the results obtained from weak magnetic field alignment in the literature are rationalised by experimental evidence on the tremendous importance of the initial state of the CNC suspension on the quality of the alignment: rejuvenating the samples by vortexing them before letting the phase separation occur in the magnetic field lead to near-perfect alignment under weak magnetic fields ( $S_{2,\text{helices}} = +0.96$ ). Finally, we show that the iridescent optical response of magnetic field-aligned cholesteric CNC suspensions is conserved over centimetre thicknesses.

### **4.3.2. Alignment experiments under electric fields**

While literature shows that the electric field alignment of CNC suspensions suffers from obvious limitations in aqueous solvents, organic apolar solvents by contrast show promising results: near-perfect reorientation and stimuable optical response through the reversible unwinding of CNC helices. This work tempered literature results by proving that the reorientation observed at moderate field values allows for any helices orientation in the plane perpendicular to the electric field. This feature of the alignment limits the quality of the optical response firstly because only part of the sample is scattering light in the direction of observation, secondly because multiple scattering blurs the optical response as the sample thickness is increased. Performing cycling experiments unwinding and rewinding the helices allowed to assess the energy incentive required to melt cholesteric domain boundaries of the sample. Finally, we establish that cholesteric helices are expected to be deformed under moderate field values, which is further developed in chapter 5.

### **4.3.3. Combining electric and magnetic fields**

For the first time, electric and magnetic field alignments have been performed on the very same colloidal system, allowing to directly compare the strength of each alignment. Competition experiments highlighted that the incentive of CNC helices to align under electric fields is much stronger than under magnetic fields: in the presence of both fields, CNC suspensions behave as if there was only an electric field applied. This is confirmed by theoretical calculations on stabilisation energy induced by each field. Whenever both fields favoured the same helix orientation, no significant increase of the alignment quality has been noticed.

### **4.3.4. Summary**

To summarise, magnetic field alignment yields the best optical quality for the samples owing to the 1D orientation of CNC helices taking place along the field, compatible with both aqueous and organic apolar solvents and robust to increasing sample thicknesses. The major drawbacks are the slow alignment and lack of stimulability in the system using permanent magnets. Electric field alignments have a richer behaviour due to the possible unwinding of helices into a pseudo-nematic phase on top of helices reorientation, forecasting promising applications in stimuable optics. However, the system suffers from several drawbacks: its use is limited to non-aqueous solvents because of electro-osmotic effects, the helices reorient into

a plane of possible configurations perpendicular to the electric field leading to blurring in thicker samples.



## Chapter 5. Iridescent polymer composites

*« J'ai besoin de cette énergie fluante du groupe [...].  
J'ai besoin de me sentir noué dans la pelote de nos fils. »  
A. Damasio, La horde du Contrevent*

This chapter develops a versatile strategy to lock-in cholesteric CNC assemblies into non-aqueous polymer composites, with the aim of making iridescent composite materials. Composites with original charges organisation are made and expected to be useful not only to optical applications, but also potentially for the mechanical reinforcement of polymers. The general idea is to take advantage of the acquired knowledge on the self-organisation of CNC helices in organic apolar solvents of the literature (Heux, Chauve, and Bonini 2000; Elazzouzi-Hafraoui, Putaux, and Heux 2009) and chapter 3 by replacing the solvent with a monomer mixture that can be polymerised. The on-demand polymerisation triggered by UV-irradiation also allows for tuning the self-assembling properties in suspension with external fields in a similar way to chapter 4 in order to create original optical responses. Since neither CERMAV and Cambridge labs are specialists in photopolymerisation techniques, there have been limited polymerisation know-how readily available in the labs for this work. The first part presents the choices and optimisation of the polymerisation of neat matrices. The second part develops the incorporation and retention of organisation of cholesteric CNCs inside the composites with emphasis on the optical properties of the resulting materials. The third part presents the retention of organisation of field-aligned charges in composites and the optical properties of the composites. The fourth part is dedicated to the characterisation of the optical properties of the composites and comparison with existing CNC materials. Throughout this document, CNCs locked in polymer composites will be referred to as “charges” or “fillers”.

### ***5.1. Choice of the polymer matrix***

A broad range of polymer matrices and processes are available for this application. For the sake of time, some polymer matrices have been pre-selected as potential candidates. The required properties for the choice of these matrices are the best possible transparency, a chemical nature compatible with stabilisation of CNCs with surfactants, as developed in chapter 3, and a tuning of the refractive index contrast between the matrix and the charges.

Making transparent matrices requires that the polymers themselves are fully amorphous, as semi-crystalline polymers are opaque due to the presence of micron-sized crystallites scattering light. The tendency to crystallise is favoured by the regularity of the microstructure of the polymer, namely its tacticity. In that sense, radical polymerisation leads most of the time to atactic polymer chains that are fully amorphous. The refractive index contrast between the matrix and the charges definitely plays a major role in the scattering properties of the composite but it is difficult to predict if we should keep it low to lower incoherent scattering and rely on

the intrinsic birefringence of cellulose to scatter light coherently, or keep a sufficient contrast to enhance the iridescent optical response of the materials. Because refractive indices of polymers range from  $n = 1.345$  for PTFE to  $n = 1.675$  for poly(N-vinylcarbazole), the refractive index contrast of the polymer matrix with cellulose is necessarily going to be rather small compared to what is possible to do with air in porous cellulosic materials ( $n = 1$ ) or inorganic composite materials such as titanium dioxide ( $n = 2.2 - 2.4$ ). So while working with dispersions of CNCs in non-aqueous monomers is handy process-wise, making polymer composites is clearly a limitation to the range of refractive contrasts explored in this work.

Polymerisation processes involving the mixing of two chemical species such as a resin and a hardener are avoided because shearing will destroy the helical supramolecular assembly slowly developing inside the sample. Likewise, viscous polymer matrices are also avoided because they slow down or even prevent sample self-organisation, CNC suspensions in organic apolar solvents being already significantly viscous. Due to this viscosity issue, the crosslinking of readily-grown polymer chains is not possible either, although its processing would have been significantly easier. Focus has been set on two glassy polymer matrices obtained by conventional free-radical photopolymerisation: polystyrene (PS) and polymethylmethacrylate (PMMA). UV-induced initiation has been preferred as it can be performed remotely, does not require sample heating, which could lead to convection streams that would destroy the helical assembly.

PS has been selected because styrene has a chemical nature very similar to toluene (Figure 116), in which CNCs are readily dispersible using surfactants. Moreover, a previous internal study showed that CNCs are dispersible and self-assemble in styrene with very similar self-assembling properties compared to toluene (Astruc 2014). Its transparency is however not so good, usually 85-90% depending on the quality of the polymerisation. The refractive index of the polymer ( $n_{\text{PS}} = 1.59$ ) (Lipatov et al. 1971) is close to the one of CNCs ( $n_o = 1.544$ ,  $n_e = 1.618$ ) (Frka-Petesic et al. 2015). Styrene and divinylbenzene, the di-functional cross-linker that can be added to strengthen the styrene matrix, are both completely fluid, which ensures minimal additional viscosity is brought into the CNC suspensions.

PMMA has also been selected because it is known for its near-perfect transparency of 92% that makes it promising for a lot of industrial applications where transparency is the main feature of the material, *e.g.* automotive windows or reading desks. 92% transparency is about the best transparency one can possibly get out of a material, because about 4% of incoming

light is lost on each refractive event at sample interfaces (depending slightly on the refractive index,  $\rho = \frac{(n-1)^2}{(n+1)^2}$ ). With two sample interfaces, that is about 8% of incoming light loss. The refractive index of PMMA ( $n_{PMMA} = 1.49$ ) is inferior to both the ordinary refractive index of CNCs, and the extraordinary refractive index of CNCs, leading to a possibly bigger contrast than PS. The chemical structures of PMMA and toluene presented in Figure 116 are quite different, explaining why all surfactants do not succeed dispersing CNCs successfully in this monomer. Methylmethacrylate (MMA) is very fluid, but the tri-functional cross-linker trimethylolpropanetriacrylate (TMPTA) used in this work is viscous, which has the drawback of adding viscosity to the overall suspension whenever used.

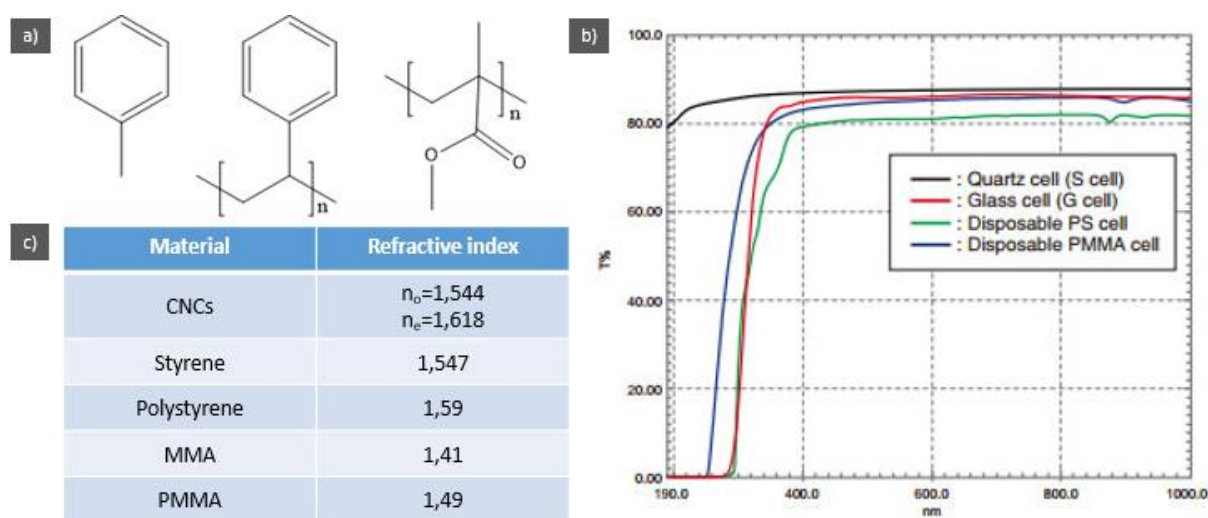


Figure 116 : a) Chemical structure of toluene, PS and PMMA from left to right. b) Transparency as a function of wavelength data from disposable UV-spectroscopy cuvettes, notably showcasing the difference in transparency between PS and PMMA (source: Shimadzu). c) Refractive indices values from different materials relevant to this work, allowing to predict refractive index contrasts between the polymer matrices and the charges.

The optimisation of the polymerisation of the PS and PMMA neat matrices is a process development that has involved many different experimental choices on the initiators, cross-linkers, polymerisation inhibitors *etc.*, that have been required to yield well-polymerised transparent neat matrices. However, in-depth knowledge of the polymer matrices is not required to understand the results obtained in the following sections. For this reason, it has been decided to regroup this process development in an Appendix in chapter 2 in order not to burden the reading unnecessarily. The interested reader is invited to refer to this section for more information.

As a summary, PS matrices are photopolymerised with 0.5 wt.% initiator, 2 wt.% divinylbenzene, a di-functional cross-linker, and styrene over typically 8 hours. PMMA



matrices are polymerised with 0.25 wt.% initiator, 2 wt.% TMPTA, a tri-functional cross-linker, and MMA over typically 1 hour. Neat matrices are fully transparent in the next sections unless stated.

## 5.2. *Polymerisation of CNC-polymer composites*

This section is dedicated to the incorporation of isotropic and cholesteric CNC charges in the previously described polymer matrices and means to observe an iridescent optical response from these materials. Process-wise, it simply consists in replacing the monomer fraction of the reaction mixture by a CNC suspension in monomer whose features have been described in chapter 3. CNC loadings given hereafter always correspond to dry masses (*i.e.* CNC+surfactant content).

### 5.2.1. Isotropic CNC-polymer composites

In this section and the next, materials have been polymerised in matrices containing scattering bubbles, for chronological reasons on solving the transparency of the neat matrices. At 7.5% CNC loading, the initially near-colourless suspension due to the index matching of styrene ( $n = 1.547$ ) with cellulose ( $n_o = 1.544$ ,  $n_e = 1.618$ ) quickly appears pale blue in reflection and yellow-orange in transmission over the course of the polymerisation. The final material displays a grey-white colour reproduced in Figure 117 owing to the numerous scattering objects (CNCs and air bubbles) present in the material. One observes a completely homogeneous distribution of CNC charges inside the composite with no polymerisation-induced aggregation visible by naked eye and by polarised optical microscopy.

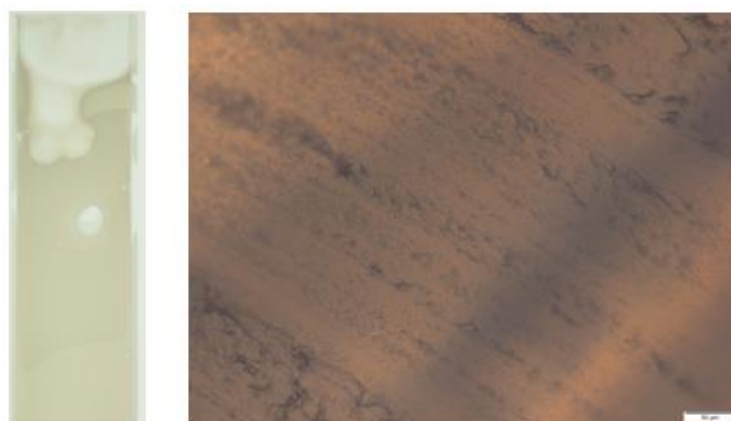


Figure 117 : Visual appearance of a CNC-PS composite with 7.5% CNC loading, 0.5% Irgacure and 2% DVB polymerised in borosilicate capillary without pre-polymerisation a) by naked eye and b) under polarised optical microscopy.

## 5.2.2. Anisotropic CNC-PS composites

### 5.2.2.1.1. Optical appearance

CNC-PS composites have been polymerised from self-assembled and phase-separated biphasic suspensions at 26.7 wt.% CNC loading. The optical appearance of the samples over the course of the polymerisation presented in Figure 118 is quite different in its isotropic (top part of the sample) and anisotropic phase (bottom part of the sample). While the isotropic phase looks like an even more scattering version of Figure 117 consistent with the increased CNC content, the anisotropic phase by contrast shows a partial recovery of transparency although it is supposed to bear a slightly higher CNC content than the isotropic phase. This is unambiguously a signature of the supramolecular organisation of CNC fillers: while isotropic CNCs scatter light individually and incoherently, anisotropic CNCs scatter light coherently much like a multilayer reflector. Assuming the absence of light absorption by the material, the sum of the coherent and incoherent scattering components of the sample (both backward and forward) directly corresponds to incident light which is an invariant. In other terms, the more coherent light an object scatters and the less incoherent light it scatters. This balance is thought to be what leads to the transparency increase of the anisotropic phase observed in Figure 118, although only forward scattering is observed. While the material is in majority too thick to transmit the light of a polarised optical microscope through, it is possible to observe fingerprint patterns on the edges of the material that are reproduced in Figure 118.

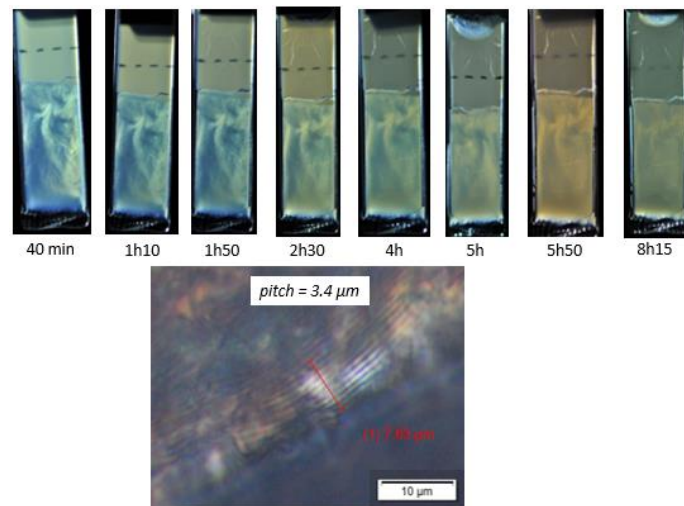
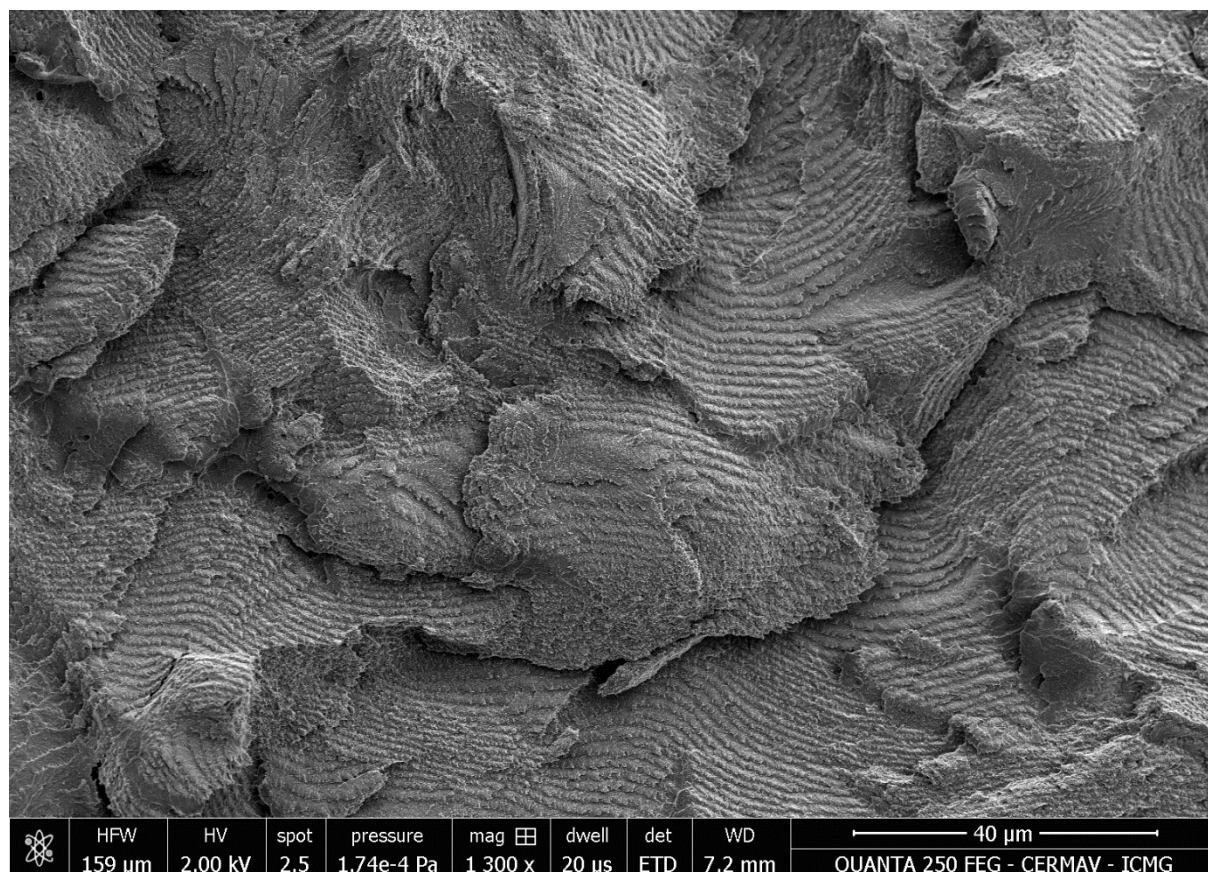


Figure 118 : (top) Optical appearance of a phase-separated CNC-PS composite at 26.5 wt.% CNC loading at different polymerisation times illuminated in transmission offset by an angle. The isotropic-cholesteric boundary is located in the vicinity of the crack. Black dashed lines hold no meaning. Gel time is expected to take place around 5 hours. (bottom) Edge of the anisotropic phase observed in polarised optical microscopy in which a fingerprint pattern is visible. Measuring 9 alternating stripes gives a pitch value of  $1.7 \mu\text{m}$  on the image.

#### 5.2.2.1.2. SEM observations

SEM micrographs taken from fractured samples and presented in Figure 119 allowed to directly observe the distribution and organisation of charges inside cholesteric composite materials. The detail of sample preparation and of the different patterns obtained depending on the helical axis and direction of cut is given in chapter 2. At low magnification, it is remarkable that nearly any visible area in the anisotropic phase displays Bouligand arches characteristic of helical assemblies of charges. At higher magnification, images show that the cholesteric structure has not been visibly distorted by the polymerisation process at this resolution. By contrast, SEM characterisation of the isotropic phase presented in Figure 120 clearly shows no Bouligand arches, as expected from a random distribution of particles. Retention of organisation of cholesteric helices in composites is a strong result in the sense that the cholesteric arrangement needs to be maintained close to its original state for the composites to yield an optical response. Light is thought to be very sensitive to defects in the cholesteric arrangement, quickly leading to loss in coherent scattering intensity to the profit of incoherent scattering from individual CNCs. With such a helical arrangement maintained inside the composite, there are reasons to think that an iridescent optical response may be observed out of these materials.





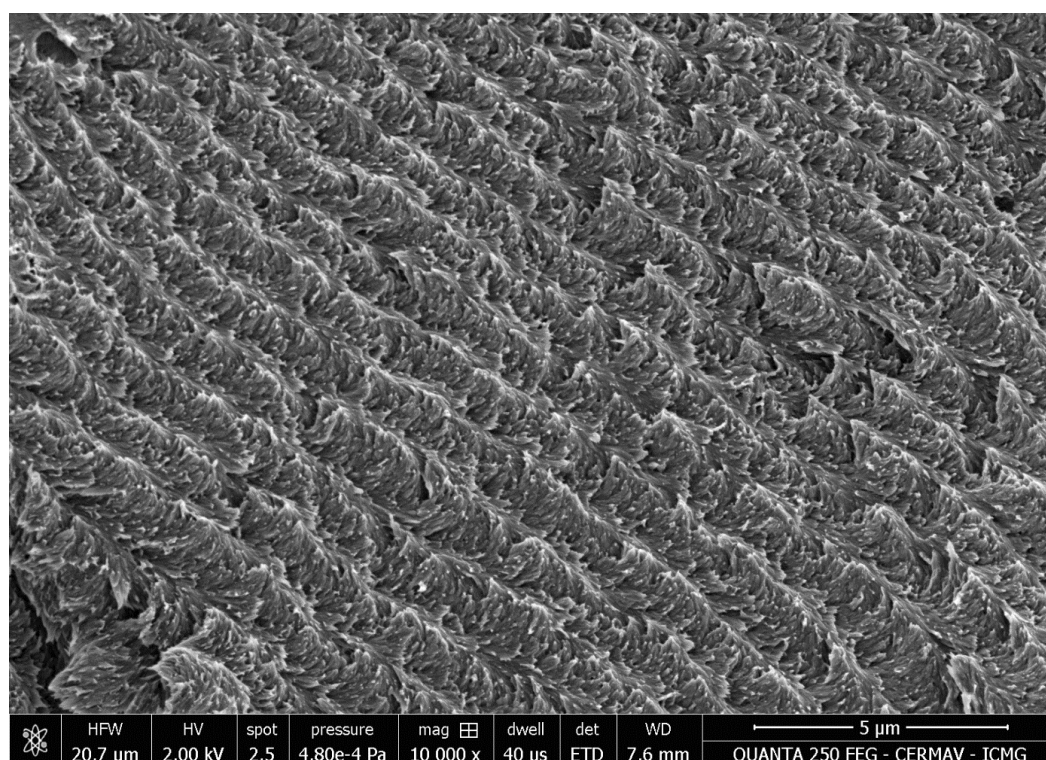
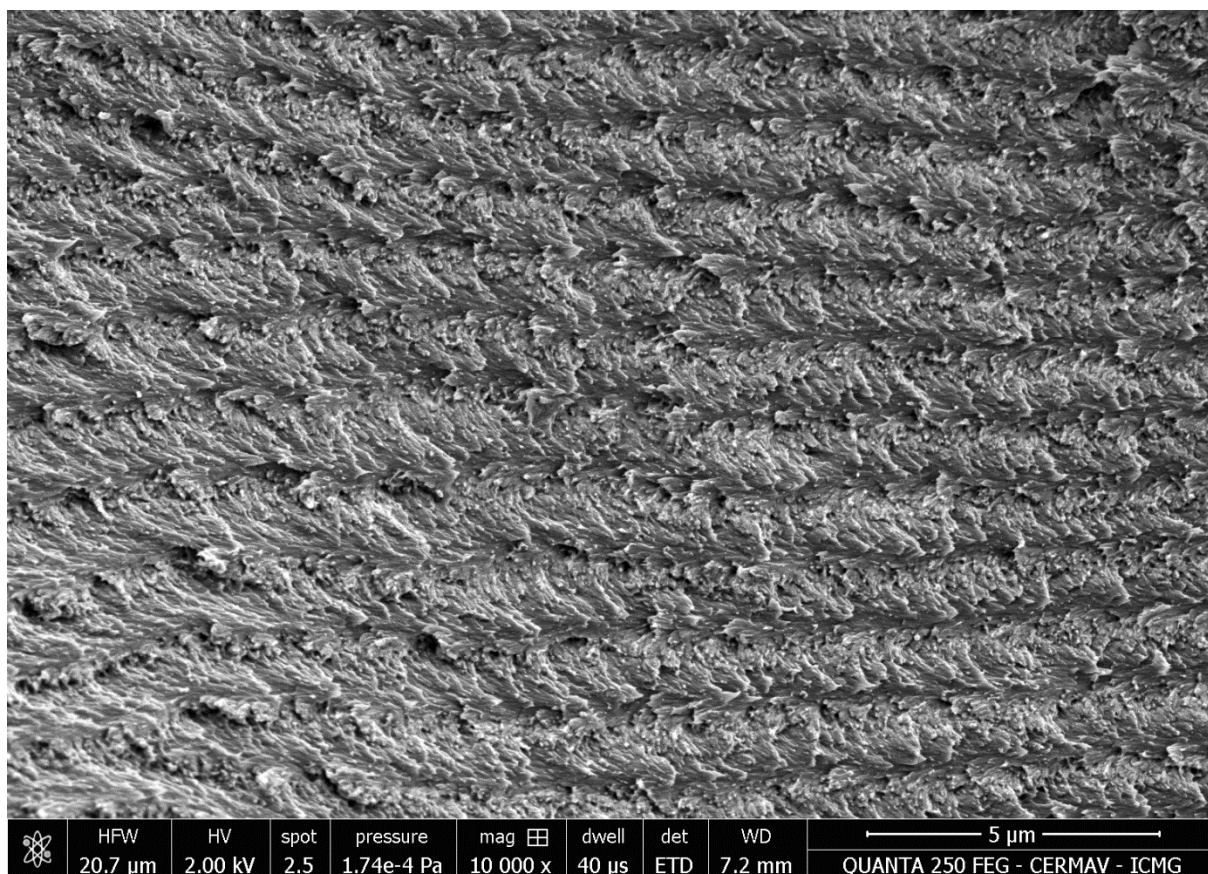
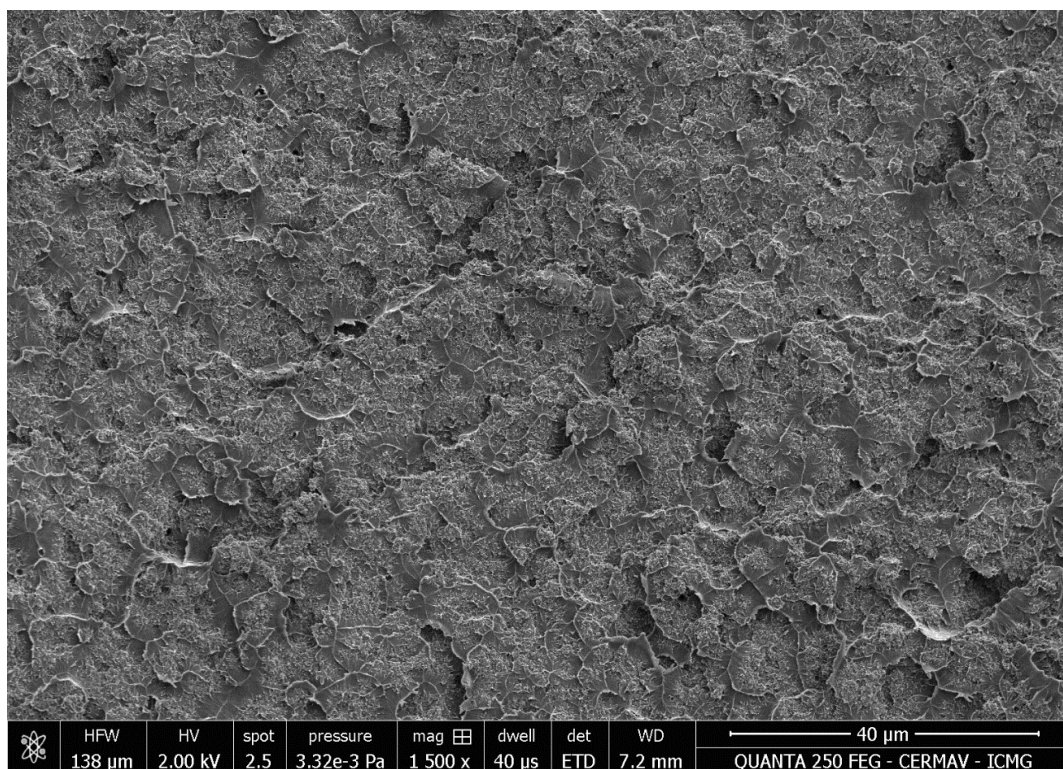


Figure 119 : Scanning electron microscopy images of the CNC-PS composite at 26.5 wt.% CNC loading of Figure 118 fractured by hand at room temperature in the anisotropic region and observed at different magnifications (x1300, x10 000).





*Figure 120 : Scanning electron microscopy image of the CNC-PS composite at 26.5 wt.% loading of Figure 118 fractured by hand and at room temperature in the isotropic region and observed at x1500 magnification.*

To assess whether all of the anisotropic phase is made of helical structures, a microtome cut of approximately 1  $\mu\text{m}$  in thickness has been made on the material and its observation in SEM and polarised optical microscopy is given in Figure 121. Both analyses show a coexistence of two phases, one made of CNCs organised in cholesteric helices as indicated by the fingerprint pattern and Bouligand arches and the other one appearing smooth in SEM, exhibiting no particular feature in optical microscopy. There are a number of possible reasons for this observation, but incomplete phase separation is likely involved, as the nucleation of cholesteric domains is quite fast in organic solvents, while the viscosity of the system slow down the complete phase-separation between isotropic and anisotropic areas. In any case, micron-scale inhomogeneity is likely the reason why the anisotropic phase still scatters incoherent light.

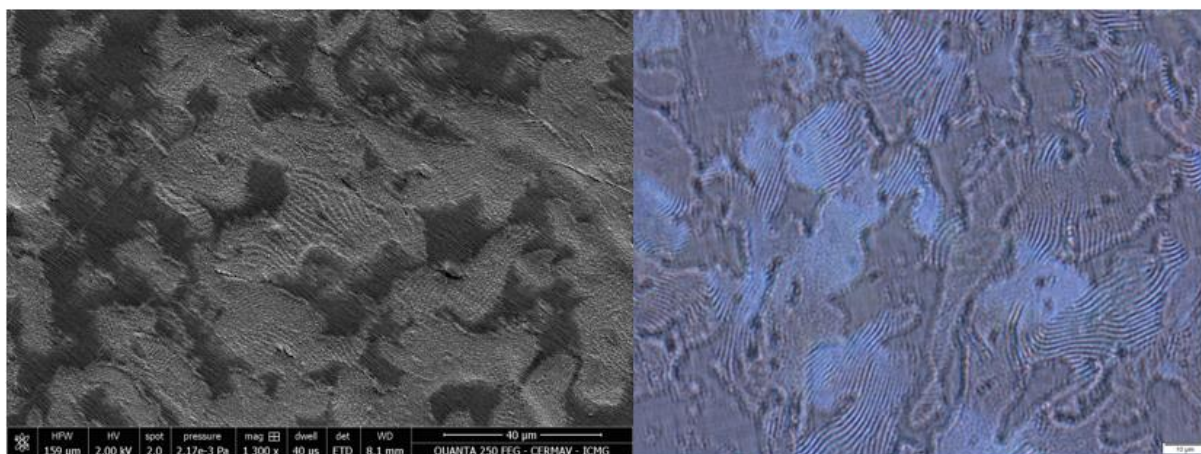


Figure 121 : Scanning electron microscopy of block-face observation and polarised optical microscopy images of a microtome section of the CNC-PS composite at 26.5 wt.% loading of Figure 118. Scale bar of the SEM is 40  $\mu\text{m}$ , scale bar of the POM is 10  $\mu\text{m}$ .

### 5.2.3. Syneresis in CNC-PS composites

When anisotropic CNC-PS composites are polymerised in fully transparent matrices (*i.e.* with no residual bubbles, see Appendix for more details), the result is disappointing. The grey-brown material shown in Figure 122a) displays some kind of “cracks” in its structure. These are not empty cracks and the material still has good mechanical properties. The SEM image of Figure 122 is taken in similar conditions as Figure 120, and yet displays a completely different distribution of charges. While helical assemblies of CNCs are visible throughout the anisotropic phase, forming a sort of continuous phase, two other kind of structures containing no cholesteric structures are visible: cracks and spherical inclusions. Cracks are found to vary between 10  $\mu\text{m}$  and several millimetres in width, explaining the apparent cracks on the materials while maintaining mechanical continuity. Spherical inclusions of approximately 5  $\mu\text{m}$  in size are regularly distributed everywhere inside the cholesteric phase; one can deduce that there is a refractive index contrast between the material in the inclusions and the continuous cholesteric phase given how strongly the material scatters light (it would be expected to be near-transparent otherwise). Taking into account the chemical composition of the material, the only reasonable assumption to do is that the inclusions are made of the neat monomer – or polymer – as all other chemicals are present at less than 2 wt.% in the mixture.



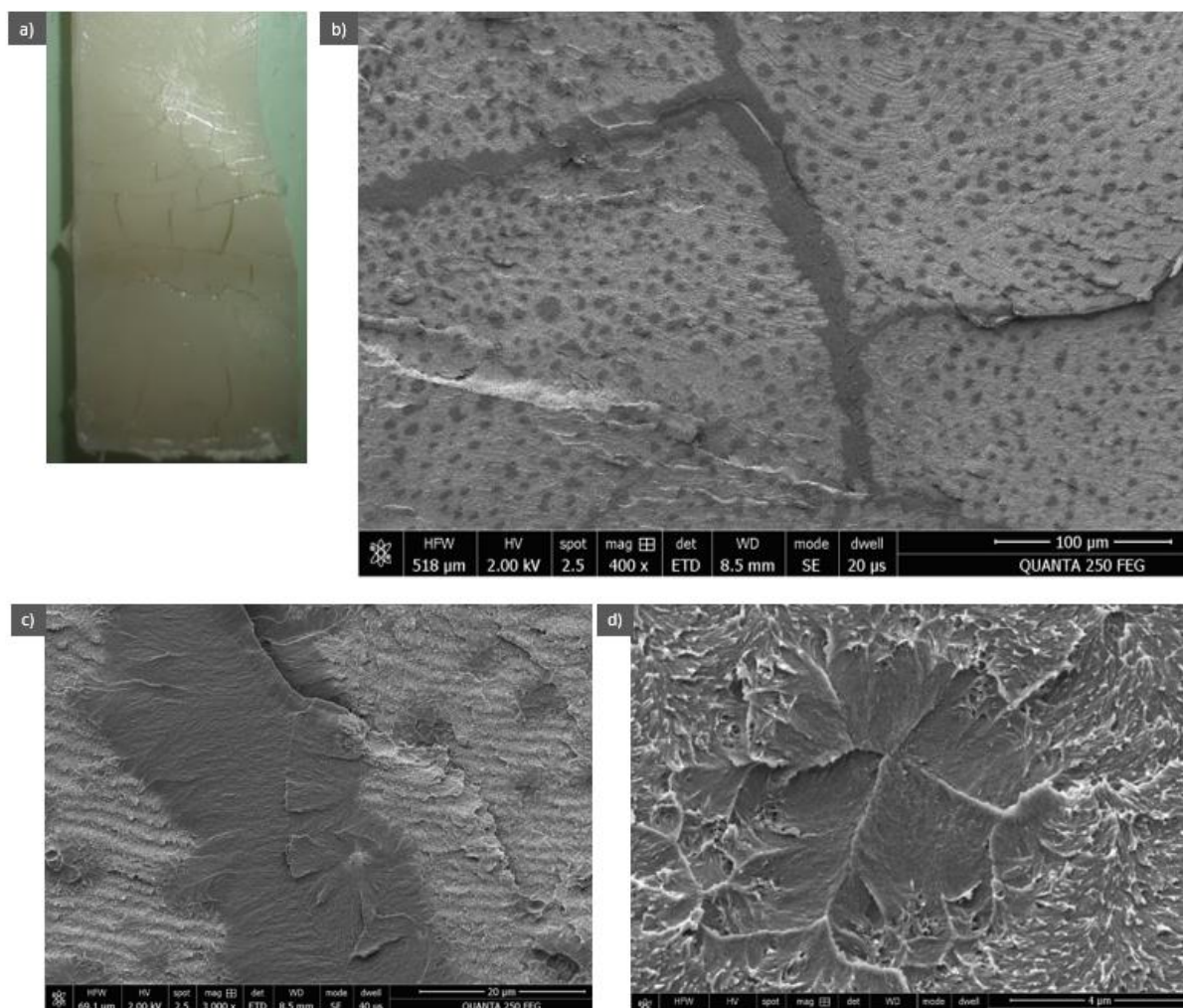
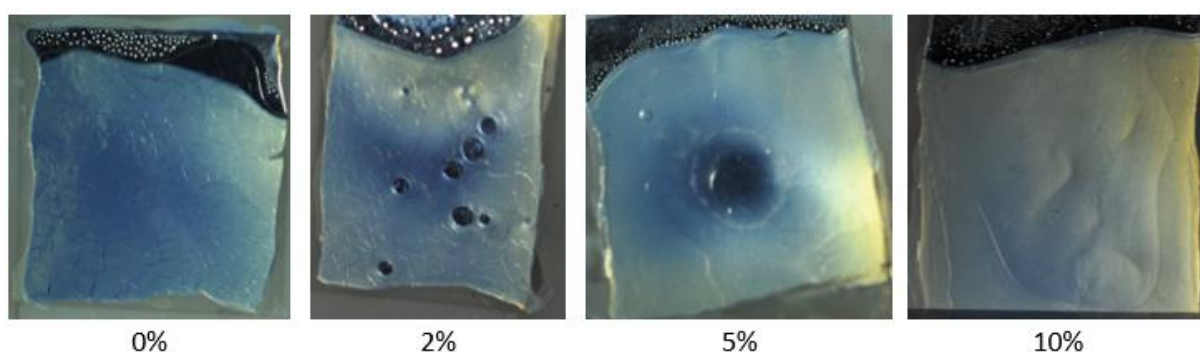


Figure 122 : a) Visual appearance of a CNC-PS composite at 23.9 wt.% CNC loading phase-separated for 3 days and polymerised in a home-made FEP mould. b) Scanning electron microscopy image obtained by fracturing sample of a) by hand in the anisotropic region at room temperature. c-d) Close-ups of the cracks and spherical inclusions visible in b).

In SEM, the cholesteric phase appears continuous around the inclusions: if we mentally merge the cholesteric phase present at one end of an inclusion and the other, they reproducibly fit into one another without any defect creation. From this observation, we may hypothesize that this cholesteric phase used to be unique before the inclusion was created. This would suggest that monomer is expelled from the cholesteric suspension over the course of the polymerisation. A similar mechanism is known in the literature to take place in gels made of loosely cross-linked networks and is referred to as syneresis (Scherer 1989a, 1989b). Shortly after gelling is observed, the medium consists of a chemically cross-linked organogel swollen by a mixture of the monomer and cross-linker left to be polymerised, some remaining initiator and the helical CNC charges. As the reaction continues, this network tightens due to the increasing number of cross-linking points forming inside the network, resulting in an overpressure that tends to expel liquid out of the gel. Depletion interactions involving short

macromolecular chains could also be at play and strengthened by the choice made not to remove inhibitors. It is not straight-forward why the monomer-initiator-crosslinker mixture is expelled but not the helical CNC charges. It may be due to the average pore size of the network, big enough for molecules to travel freely while colloidal objects remain trapped inside the polymeric network. Another possibility is that cholesteric CNC domains have an intrinsic elasticity that is enough to resist the pressure exerted by the surrounding network.

Whatever mechanism is at play at the molecular level, a mean to reduce or suppress syneresis phenomenon consists in tightening the polymer network by adding more cross-linker (Scherer 1989a, 1989b). Figure 123 presents a dose effect of the cross-linker on the optical appearance of anisotropic PS-CNC composites. While real cracks are visible when no cross-linker is added to the reaction mixture, the syneresis phenomenon observable at 2 wt.% disappears to yield homogeneous composites at 5 and 10 wt.%. It is worth noting that suppressing syneresis did not change drastically the intensity of incoherent scattering in the composites.



*Figure 123 : Influence of the dose effect of cross-linker on syneresis and the optical appearance of PS-CNC composites. Thickness are comparable from one sample to another around 400  $\mu\text{m}$ , bubbles at 2 and 5% are due to mould filling.*

#### **5.2.4. Anisotropic CNC-PMMA composites**

By contrast with CNC-PS composites, anisotropic CNC-PMMA composites have shown an iridescent optical response starting from the very first samples in transparent PMMA matrices (made of 0.25 wt.% Irgacure, 10 wt.% TMPTA, cholesteric CNCs and MMA) presented in Figure 124. The evaporation of MMA through the FEP mould and the fast gelation over time of the MMA dispersion only allowed for a window of *ca.* 24 hours between sample filling and gelation. This is why these samples are not fully phase-separated prior to polymerisation nor present fully developed helices, resulting in a polychromatic iridescent optical response.



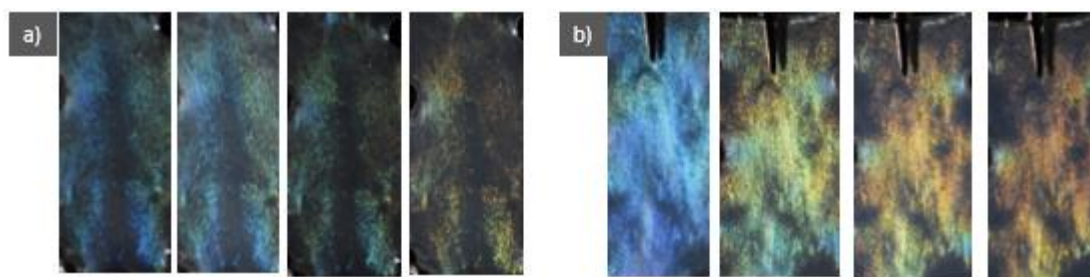


Figure 124 : Optical appearance of two PMMA samples with 0.25 wt.% Irgacure, 10 wt.% TMPTA, MMA and (a) 24.5 wt.% and (b) 27.8 wt.% CNC content without phase-separation and polymerised for 2 hours. Illumination is made with a horizontally offset lamp at increasing angles from left to right, allowing the observation of iridescent light diffraction.

While these first samples are far from perfect, they already show important improvements with respect to PS composites. Their incoherent scattering is greatly reduced compared to PS composites, whereas their coherent iridescent scattering appears stronger. It is not yet clear what physicochemical property differing in both matrices is responsible for such a difference. Because both polymer matrices are completely transparent without CNCs, these differences could be due to the interplay between CNCs and the matrices. Both PS and PMMA have similar refractive index contrast with the ordinary refractive index of cellulose ( $n(\text{PS}) = 1.59$ ,  $n_o(\text{CNC}) = 1.544$ ,  $n(\text{PMMA}) = 1.49$ ) whereas PS index-matches more the extraordinary refractive index of cellulose ( $n_e(\text{CNC}) = 1.618$ ) than PMMA. The obvious differences in the polymerisation times of the two matrices (from minutes for PMMA to hours for PS) could also lead to different samples microstructures. Syneresis is indeed observed in samples that require longer times to develop, whereas PMMA-CNC samples are quickly frozen.

### 5.3. *Field-aligned CNC-polymer composites*

The experimental process has been thought from the beginning to allow for the electric and magnetic field alignment of CNC suspensions prior to polymerisation. It consists in the current process of setting the electric or magnetic field just after moulds are filled, during phase separation and the following polymerisation of the samples.

#### 5.3.1. **Influence of field alignment on the optical response in PS composites**

Figure 125 presents the influence of the electric and magnetic field alignment on the optical response of CNC-PS composites. A cholesteric CNC suspension has been aligned in a horizontal electric field  $E_y = 266 \text{ V/cm}$ , situation in which the helices are expected to reorient in a plane perpendicular to the field according to results of chapter 4, and then polymerised. For

the magnetic field-aligned sample, a cholesteric CNC suspension has been aligned in a 0.65 T, situation in which the helices are expected to reorient in the direction of the field, and then polymerised. One observes a gradual recovery of the iridescent white light diffraction of the composite: while incoherent scattering dominates without field alignment (Figure 125a), coherent scattering becomes visible when CNCs are aligned under an electric field in the form of a very shady iridescent optical response (Figure 125b). Magnetic alignment further strengthens the coherent scattering of the sample compared to the two previous samples, leading to a clearly visible iridescent optical response still in competition with incoherent scattering (Figure 125c). We have seen that the sum of coherent and incoherent scattering is an invariant. What is observed here is the strengthening of the coherent response at the expense of the intensity of incoherent scattering (observed in forward scattering).

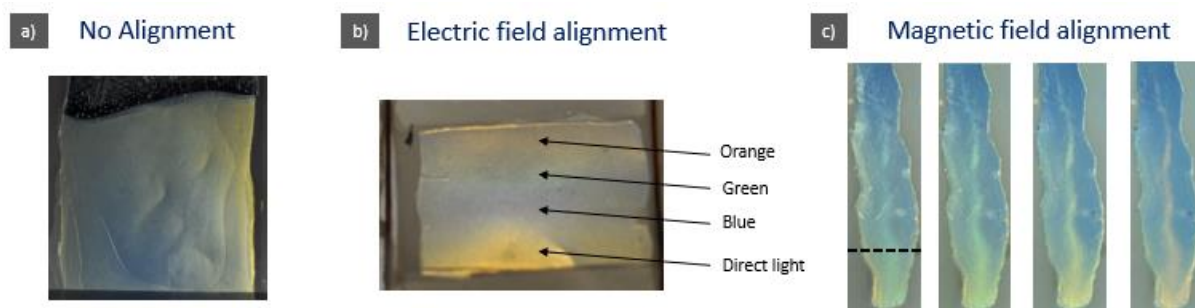


*Figure 125 : Visual appearance of CNC-PS composites made of 0.5 wt.% Irgacure, 10 wt.% DVB, a-b) 28 wt.% and c) 24.5 wt.% CNC content in styrene. Samples have been a) left unaligned b) aligned in a horizontal electric field  $E=266$  V/cm and c) aligned in a horizontal magnetic field  $B=0.65$  T. Samples a) and b) have not been phase-separated whereas sample c) has been phase-separated during 5 days. Samples have been polymerised respectively during a) 8 hours, b) 17 hours and c) 22 hours under field and 9 hours without field. Illumination light is offset with respect to the camera-sample direction a) horizontally, b) vertically and c) horizontally with increasing angles from left to right.*

These results are in very good agreement with the conclusions of chapter 4, where the effect of electric and magnetic fields has been shown to favour the alignment of the cholesteric helical axes, respectively perpendicular and parallel to the field direction. From left to right in Figure 125, samples have 3D, 2D and 1D possible helices orientations. The increasing degree of orientation of cholesteric helices in the direction matching Bragg conditions for the illumination light is thought to be responsible for the iridescence onset from the least to the most oriented sample of this series. From a purely optical point of view, this observation relates directly to observations on Centimetre scale thickness experiments of chapter 4. In this case as well, the recovery of the coherent scattering response is observed when helices are aligned in a single direction (magnetic fields) compared to the case where different helices orientations are allowed (electric fields).

### 5.3.2. Orientation of cholesteric helices in field-aligned PS composites

Polarised optical microscopy, laser diffraction and scanning electron microscopy cross-characterisation has been conducted on field-aligned samples to assess the orientation of cholesteric helices in the materials. SEM interpretations are based on Bouligand and coworkers' works (Leforestier and Livolant 1993) reproduced in the corresponding figures and further detailed in chapter 2.

#### 5.3.2.1.1. *PS-CNC composite oriented in magnetic field*

SEM characterisation of the magnetic field-aligned PS-CNC composite fractured by hand in a plane (almost) containing the magnetic field and in a plane perpendicular to the magnetic field are respectively presented in Figure 126 and Figure 127. Whenever the magnetic field is almost contained in the plane of fracture, vertical stripes with small variability in orientation are observed, corresponding to horizontally oriented helices in the direction of the field according to Bouligand and coworkers. The small variability in the orientation of helices is consistent with the magnetic field intensity of 0.65 T, for which some defects have been observed in aligned suspensions in chapter 4.

The SEM image of a fracture perpendicular to the magnetic field is presented in Figure 127. In this fracture configuration, helical axes of ideal orientation are oriented normal to the surface of the fracture, therefore exposing a layer of individual CNCs beyond the resolution of SEM. However, any significantly misoriented helix will be cut obliquely and therefore display the classical Bouligand arches. One cannot observe any obviously misoriented regions in the transverse fracture, rather a uniform pattern with small features reminding of fish scales. This result confirms a qualitative retention of orientation of the cholesteric domains orientation in the direction of the field. Angular-resolved optical spectroscopy provides additional insights on this topic with the quantitative characterisation of helices orientation that will be discussed in a following section.

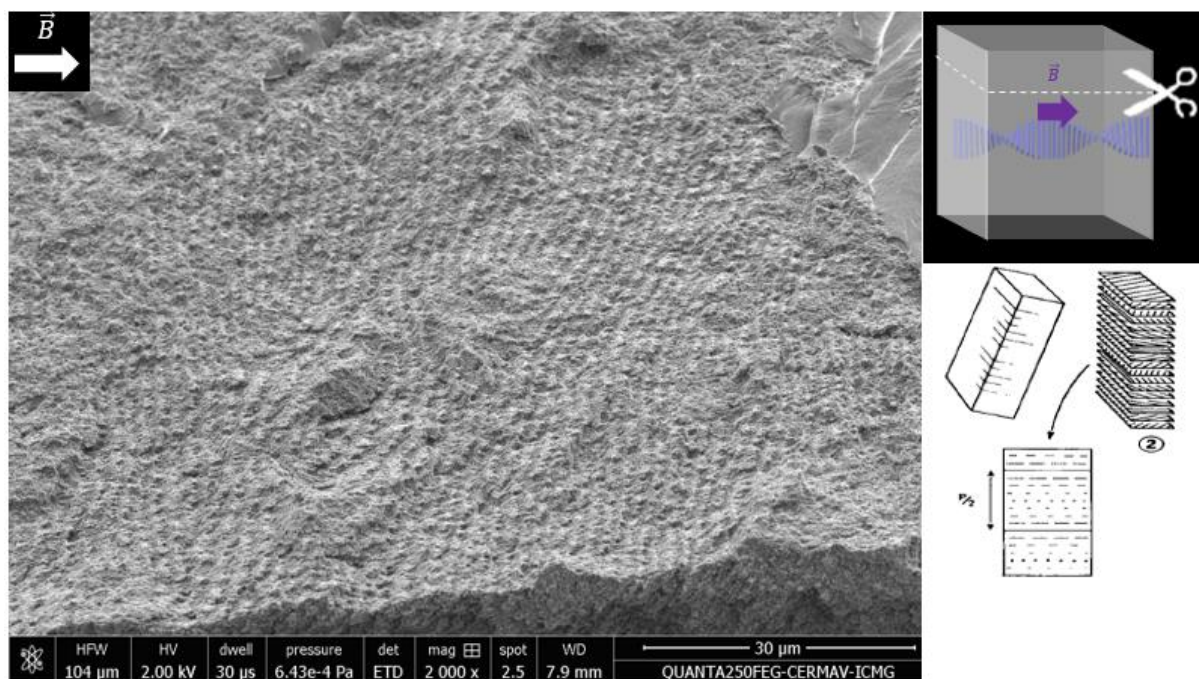


Figure 126 : (left) Scanning electron microscopy image of the CNC-PS composite presented in Figure 125 fractured by hand in the anisotropic domain in a plane almost containing the magnetic field. (right) Schematics of the geometry of the fracture and expected SEM pattern according to Leforestier et Livolant, Biophysical Journal 1993.

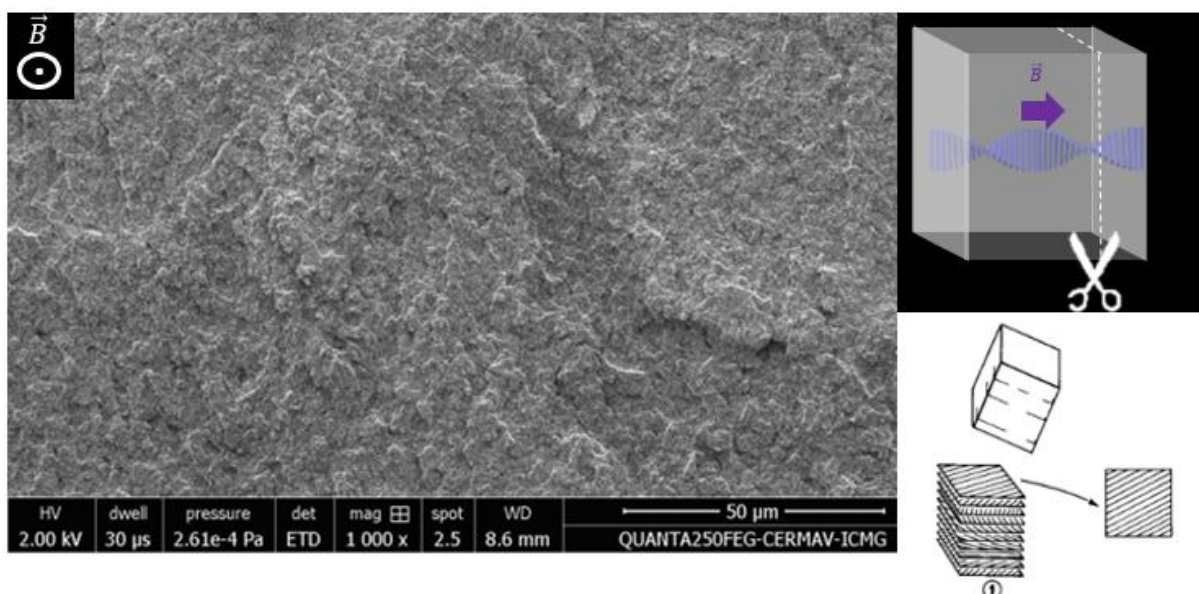
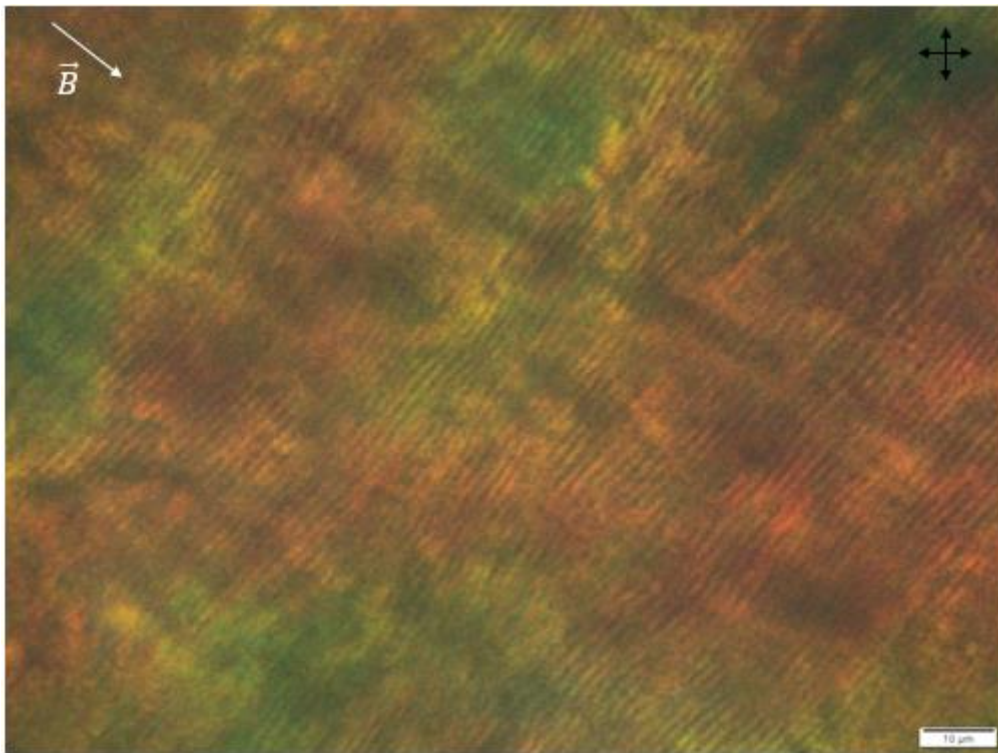


Figure 127 : (left) Scanning electron microscopy image of the CNC-PS composite aligned under magnetic field presented in Figure 125 fractured by hand in the anisotropic domain in a plane perpendicular to the magnetic field. (right) Schematics of the geometry of the fracture and expected SEM pattern according to Leforestier et Livolant, Biophysical Journal 1993.

Interestingly, the material is thin enough to be analysed by polarised optical microscopy in transmission. Observing in a plane containing the magnetic field as in Figure 128, the overwhelming majority of the material display fingerprint patterns whose axes point in the



direction of the magnetic field with the same small variability observed in SEM. Having near 100% of the material display fingerprint patterns in polarised optical microscopy is another indirect indication that helices are preserved during the polymerisation process, as well as their orientation along the field. An out-of-plane orientation would otherwise result in a blank pattern that is not observed here. It is worth noting that the pitch value can be assessed from this image with little projection bias, conversely to usual polarised optical microscopy measurements for which the tilt angle of the helix direction with the plane of observation is not known. Pitch measurements are further developed in a dedicated section.



*Figure 128 : Polarised optical microscopy image of the PS-CNC composite aligned under magnetic field presented in Figure 125 in the anisotropic domain in a plane containing the magnetic field. Scale bar is 10  $\mu\text{m}$ , Obj. x40.*

Finally, laser diffraction can be used to capture the coherent scattering from the anisotropic domain. The pattern obtained in Figure 129 clearly indicates a single diffraction peak corresponding to horizontally aligned helices. Other orientations, if present in the material, are beyond the resolution of this characterisation technique. Notably, the diffraction peaks are less intense and widened compared to suspension diffraction patterns presented in chapter 4. This is interpreted as the contribution of the incoherent scattering of the material that convolutes the coherent scattering signal.

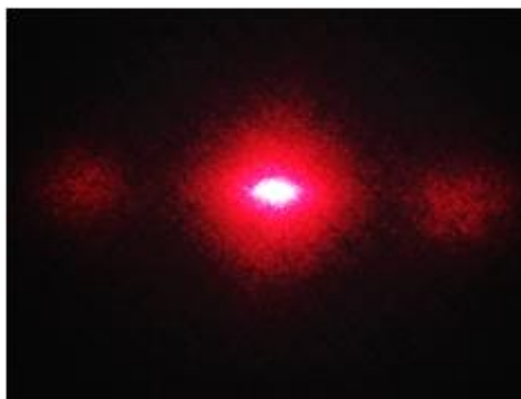


*Figure 129 : Laser diffraction pattern of the CNC-PS composite aligned under magnetic field presented in Figure 125 in the anisotropic region.*

From the cross-analysis of these three techniques, the bulk retention of orientation of helices orientation in CNC-PS composites aligned under magnetic field can be concluded with reasonable confidence.

#### *5.3.2.1.2. PS-CNC composite oriented in electric field*

A similar study has been conducted on the CNC-PS composite aligned under electric field of Figure 125. The electric field is expected to induce a reorientation of the helical axes in the plane perpendicular to the electric field, as previously discussed in chapter 4. SEM characterisation presented in Figure 130 and Figure 131 respectively shows the pattern obtained when fracturing the samples perpendicularly and obliquely with respect to the direction of the electric field. In the first case, the plane of fracture should contain all helical axes of the helices oriented along the field, therefore should yield a pointillist pattern according to Bouligand and coworkers, whereas the second case should correspond to the observation of classical Bouligand arches. In the fracture perpendicular to the field, no Bouligand arches are observed, suggesting that the helical axes are in the plane of the section as expected. Moreover, ribbons of regularly-spaced stripes with random orientation are distinguishable on the image (red stripes are a guide to the eye on Figure 130). Measuring the spacing between the stripes, one finds approximately  $1.25\ \mu\text{m}$ , on the order of magnitude of half a pitch value of the original suspension (Frka-Petesic, Radavidson, et al. 2017). The regularly-spaced white stripes likely correspond to individual CNCs having their long axis pointing normal to the plane of fracture, thus attracting the field of the electron microscope according to a peak effect. No such effect is observed for individual CNCs of other orientations, corresponding to a lower contrast. It would mean that ribbons correspond to non-phase-separated cholesteric domains fractured following a plane containing the helical axis, whose axis points perpendicularly to the stripes. The oblique

fracture displays the classical Bouligand arches pattern corresponding to a section of the cholesteric assembly following a random oblique angle.

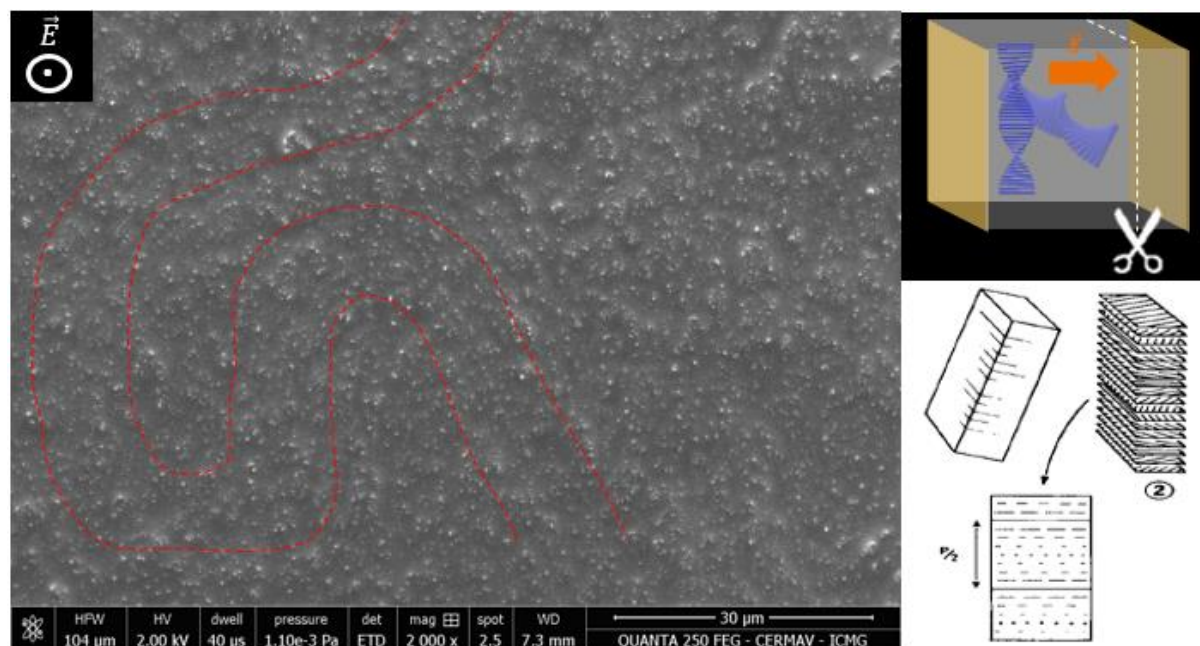


Figure 130 : (left) Scanning electron microscopy characterisation of the CNC-PS composite aligned under electric field presented in Figure 125 fractured by hand in a plane perpendicular to the electric field. (right) Schematic of the plane of fracture and expected SEM pattern according to Leforestier et Livolant, Biophysical Journal 1993.

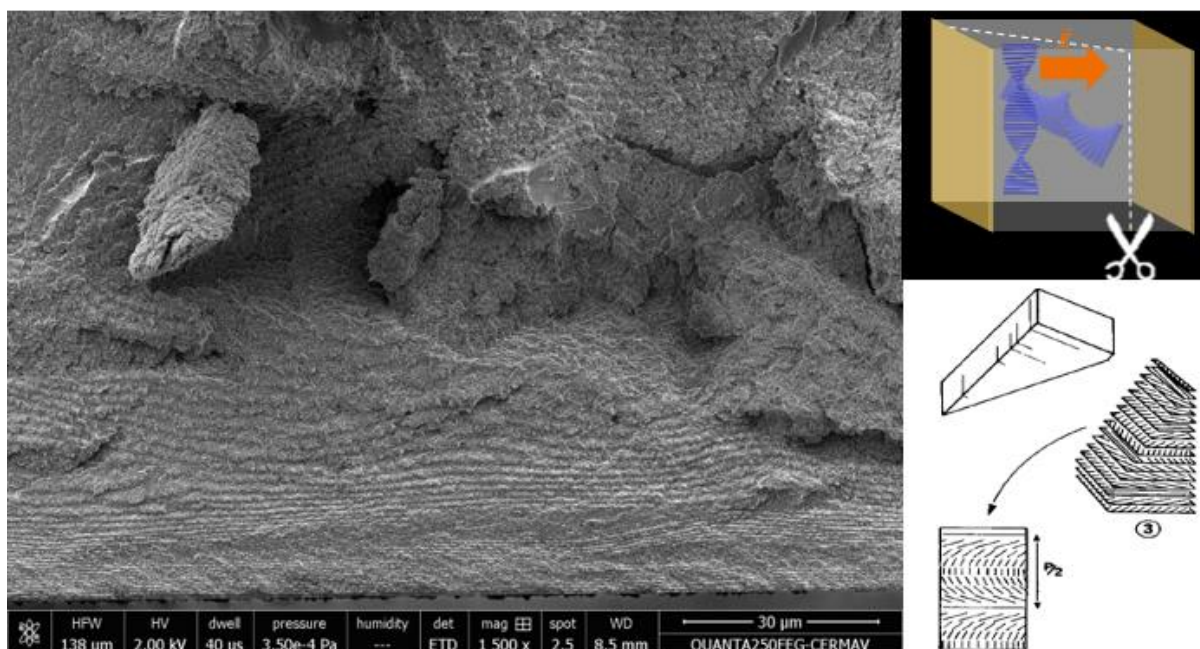
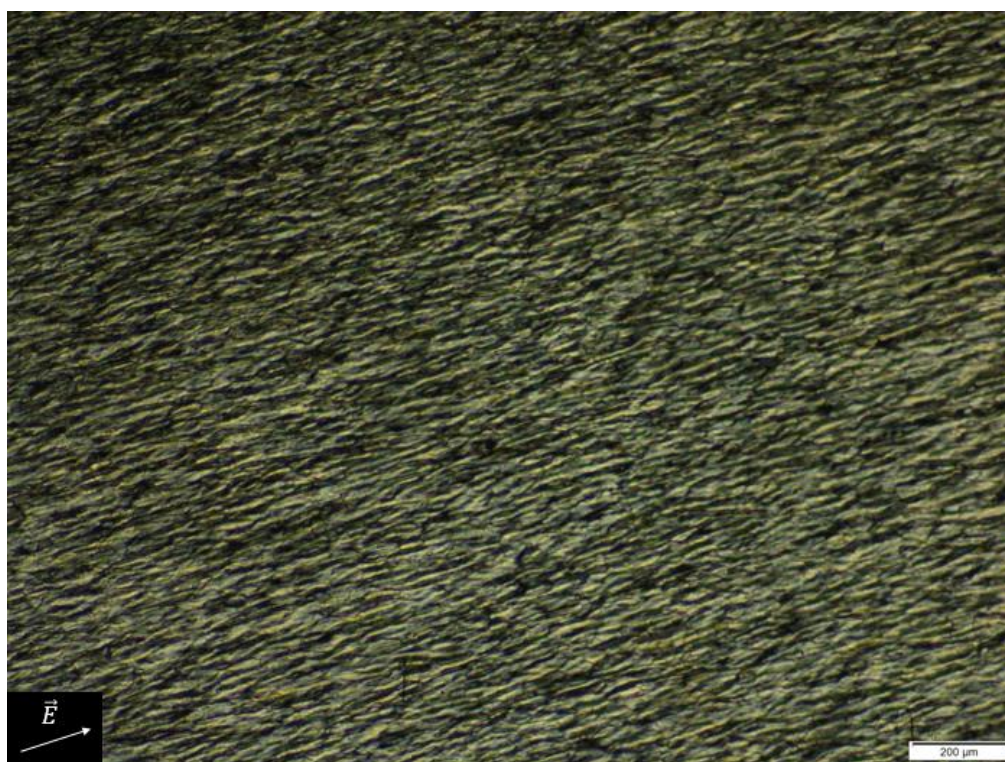
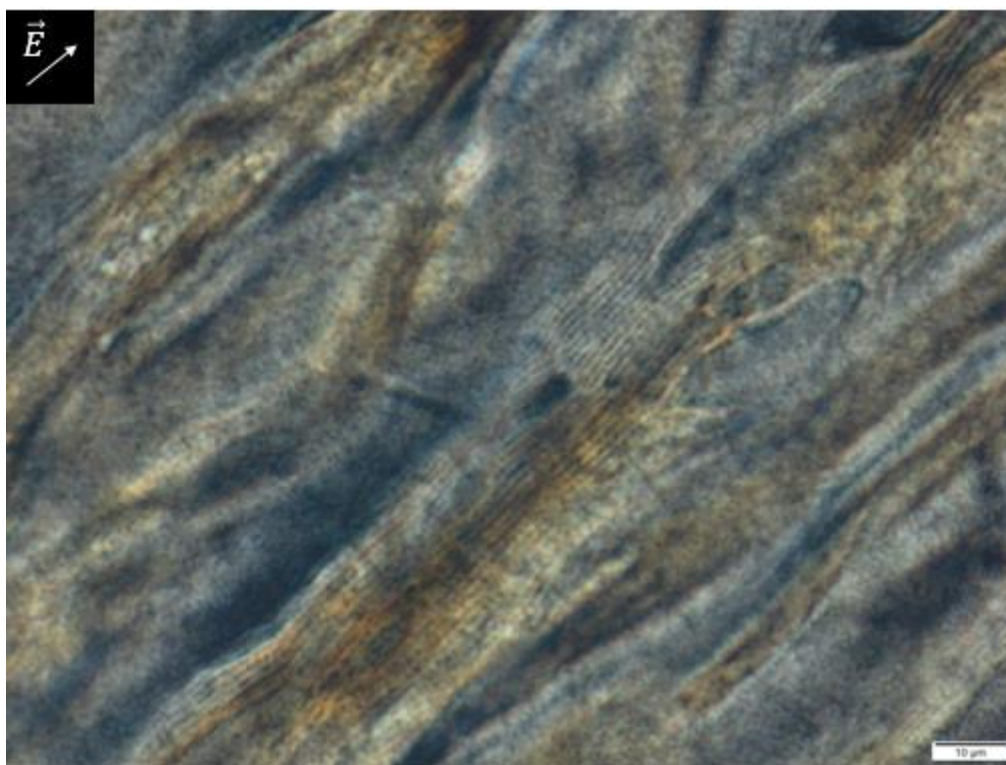


Figure 131 : (left) Scanning electron microscopy characterisation of the CNC-PS composite aligned under electric field presented in Figure 125 fractured by hand in an oblique plane with respect to the electric field. (right) Schematic of the plane of fracture and expected SEM pattern according to Leforestier et Livolant, Biophysical Journal 1993.



Polarised optical microscopy characterisation of the electric field-aligned composites has been performed with the plane of observation of the microscope containing the electric field direction, the perpendicular configuration being not experimentally accessible. According to results of chapter 4, helices are expected to be oriented in a plane perpendicular to the electric field. In the geometry of Figure 132, that would correspond to only a small fraction of the helices orientations being in the plane of observation of the microscope. This is what we observe on Figure 132: at low magnification, a strong anisotropy in the material is visible. At high magnification, the majority of the helices are not in the plane of observation of the microscope because they have a component in the third dimension, and the fingerprint patterns of the visible helices only correspond to helices axes perpendicular to the electric field. Projection bias on pitch measurements are present here.





*Figure 132 : Polarised optical microscopy images of the CNC-PS composite presented in Figure 125 in a plane containing the electric field. (top) Obj. x2.5, scale bar is 200  $\mu\text{m}$ . (bottom) Obj. x40, scale bar is 10  $\mu\text{m}$ .*

Laser diffraction characterisation was not informative: the signal of interest was beyond the resolution of the camera due to a small number of helices scattering coherently in a given direction and a strong competition with multiple incoherent scattering (data not shown).

To conclude, both SEM and optical microscopy showed the retention of orientation of helices in electric field-aligned composites, in the form of a planar distribution of helices axes perpendicular to the field. While laser diffraction is not sensitive enough to capture the coherent scattering signal, characterisation suggests the retention of 2D orientation of cholesteric helices in electric field.

### **5.3.3. Distortion of CNC helices under electric field alignment**

In this section, a PS-CNC composite has been polymerised with partially unwound helices using a stronger electric field, whose value was slightly lower than the critical electric field value for the unwinding (see chapter 4 for more information). Experimentally, a redshift of the iridescent optical response in suspension from blue to orange has been observed, characteristic of the beginning of the unwinding, before polymerising the sample in that state. Ultrathin cryo-cuts of this material and of a reference PS-CNC composite aligned under magnetic fields have

been prepared and observed in TEM, yielding high resolution images of individual CNCs in the composites reproduced in Figure 133.

Interestingly, the TEM images obtained for individual CNCs organised in helices aligned under electric fields (Figure 133a) are quite different from helices aligned under magnetic fields (Figure 133b). While the modulation of the director of CNCs along the helix axis in Figure 133b) describes a near-regular helical trajectory, the modulation of the director of CNCs in Figure 133a) no longer correspond to a helical trajectory. A fraction of the helix corresponding in rough approximation to half of the helical stack is made of CNCs whose director points within  $5\text{-}10^\circ$  in the direction of the electric field.

Image analysis has been performed using the ImageJ software. Since the resolution was not high enough to use shape recognition algorithms to isolate the orientation of the individual crystals, the assessment of the width of the helical stack in which individual CNCs are aligned within  $\pm 10^\circ$  of the electric field direction has been done by eye on a set of approximately 10 images for each sample. One must therefore be cautious with the conclusions because this characterisation procedure is likely biased by its method, and is a local assessment. An average of 39% of the CNCs composing the helical stack are found to be aligned within  $\pm 10^\circ$  of the electric field direction, compared to an average of 18% of the CNCs composing the helical stack in magnetic fields. This result may be the first direct experimental observation of the deformation of the cholesteric stack of CNCs under electric fields. Deforming the helical stack breaks the sinusoidal periodicity of the director rotation, which likely has an influence on the optical response of the material. This influence has however not been directly observed nor modelled in this work.



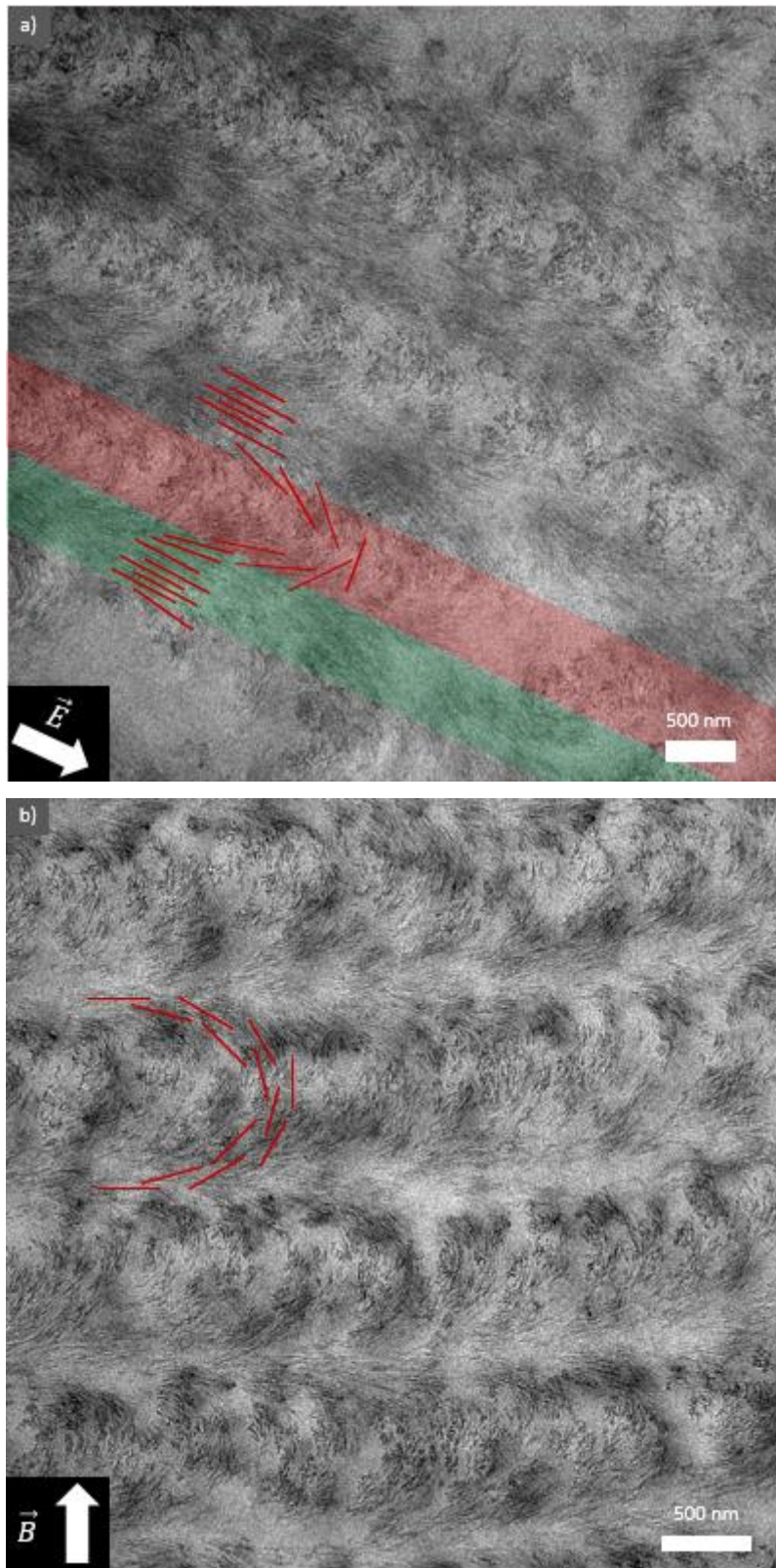


Figure 133 : Transmission electron microscopy images of ultra-thin cryo-cuts of a) a PS-CNC composite partially unwound under electric field and b) a PS-CNC composite aligned under magnetic fields. Individual CNCs tend to align in the electric field, deforming the helical revolution of their directors. Red rods are a guide to the eye that schematically reproduce the orientation of CNCs on the TEM image. The green fraction of the helical assembly corresponds to CNCs near-aligned in the direction of the electric field, whereas CNCs undergo a distorted helical revolution in red regions.

The deformation of the helical stack is possibly observed as well by observing the cryo-cuts in SEM, as shown in Figure 134. In this image, Bouligand arches are not observed, rather regular oblique stripes can be distinguished (red dashed line of Figure 134 is a guide to the eye). These could be the reminiscence of the former helical assembly that has been distorted under electric fields.

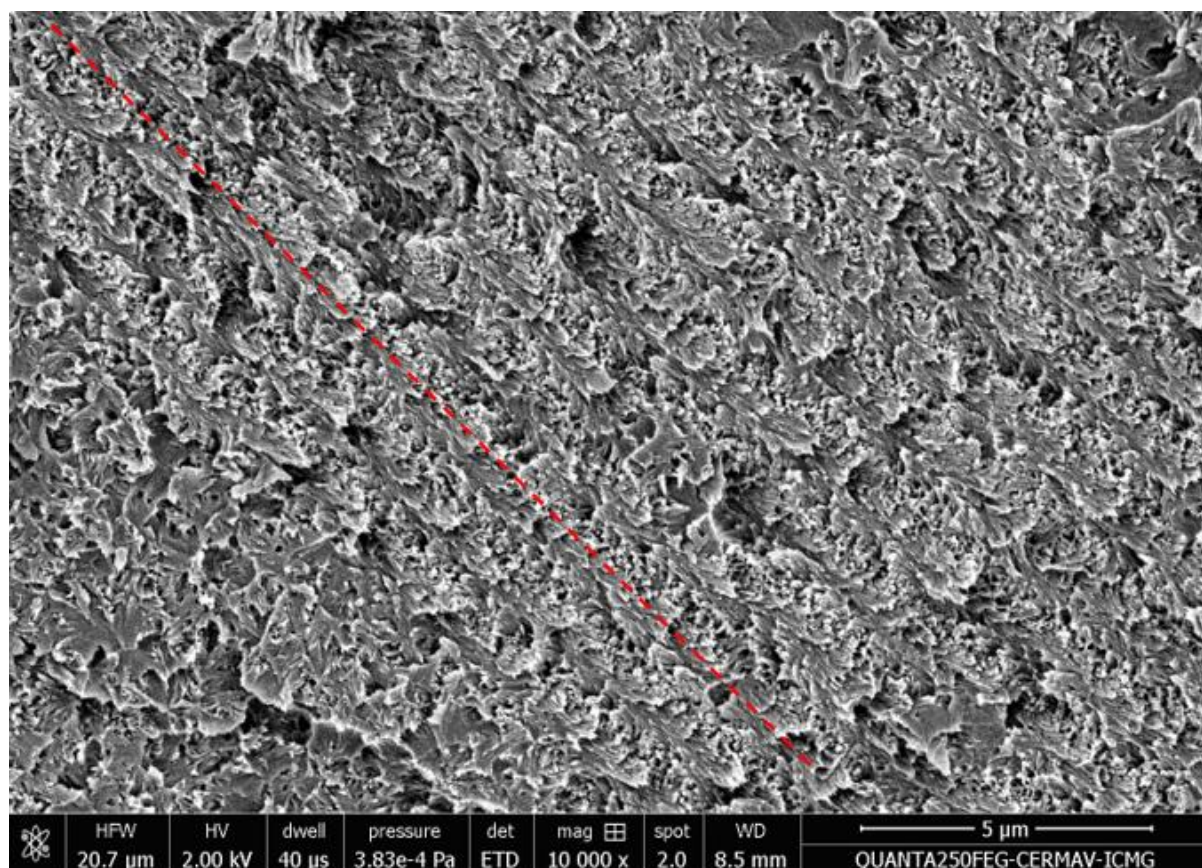


Figure 134 : Scanning electron microscopy characterisation of the cryo-cuts of the CNC-PS composite distorted under electric fields presented in Figure 133. The red dashed line indicates the direction of the stripes (perpendicular to the former helical axis).

#### 5.3.4. Anchored skin layer in field-aligned composites

The previous section described the field orientation of helices in the majority of the material. However, a competition for orientation can take place near the edges of the material, where there is an additional entropic energy gain referred to as anchoring (Schütz et al. 2020) for CNCs to lay parallel to the surface rather than perpendicular in their helical assembly in addition to the field alignment incentive. SEM characterisation performed near the surface of the sample, presented in Figure 135, shows an abrupt transition between two helices orientation. In the immediate vicinity of the surface, helix orientation is observed to be perpendicular to the surface whereas helices orientation favoured by the field – in the plane of the section – are



observed in the bulk. The thickness of the layer in which anchoring rules helices orientation is found to be around 8 to 10  $\mu\text{m}$ . While this is only approximately 5% of the total thickness of the material – approximately 400  $\mu\text{m}$  – that is misoriented with respect to the orientation favoured by the field, this anchored skin layer creates an intermediate defect region that may contribute to the incoherent scattering of the material. It would be interesting to see if the optical response of the material is modified by etching this skin-layer with *e.g.* a microtome tool. While these observations have been made for electric field-aligned PS composites, conclusions are expected to apply to other composite orientations as well.

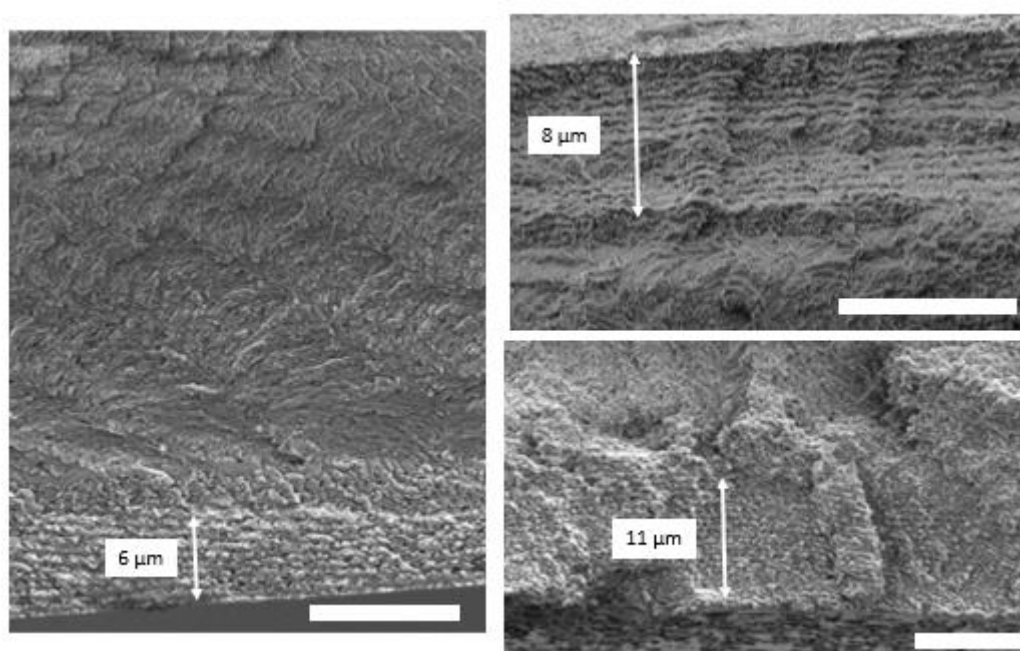


*Figure 135 : Scanning electron microscopy image of the CNC-PS composite aligned under electric field presented in Figure 125 fractured by hand (left) obliquely to the electric field direction and (right) perpendicularly to the electric field direction. Bulk orientation consisting of Bouligand arches is clearly visible in the oblique fracture.*

### **5.3.5. Influence of the magnetic field alignment on the optical response of PMMA composites**

While PS-CNC composites were useful to follow the orientation of the helices axes under external fields, their optical quality is limited to perform advanced optical characterisation. On the other hand, PMMA-CNC composites displayed much better optical performances evidenced in the beginning of this chapter. By aligning CNCs dispersed in MMA under magnetic fields before polymerising, the resulting material displays a strengthened and much more homogeneous iridescent optical response reproduced in Figure 136 compared to non-aligned samples presented in Figure 124. A single colour is scattered over the whole material,

much like PS-CNC composites aligned under magnetic fields. Although no isotropic-cholesteric phase separation has been performed in these samples due to MMA evaporation in the setup, incoherent scattering remains comparatively low compared to the PS equivalent. This is confirmed by angular-resolved spectroscopy results discussed in the following section.

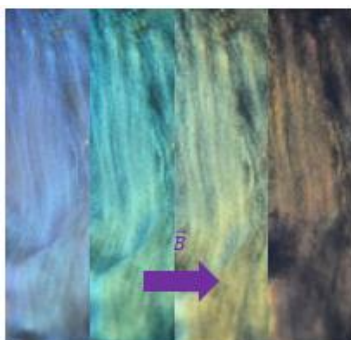


*Figure 136 : Optical appearance of a PMMA-CNC composite with 0.25 wt.% Irgacure, 10 wt.% TMPTA, MMA and 24.5 wt.% CNC loading aligned under magnetic fields during 4h30 and polymerised under field during 1h10. Illumination is made with a horizontally offset lamp allowing the observation of iridescent light diffraction. From left to right, increasing offset angles.*

#### **5.4. Characterisation of the optical response of iridescent CNC-polymer composites**

The characterisation of the colour response of a material involves three components that all have an influence on the observation: the illumination light spectrum, the scattering properties of the sample, and the spectral sensitivity of the detector. To accurately measure the scattering properties of the sample, one must subtract the influence of the illumination light spectrum (which in cold sources often present multiple peaks instead of a black body curve) and the varying sensitivity of the detector to different wavelengths. This is the reason why angular-resolved optical spectroscopy has been used rather than simple camera pictures to characterise the light scattering of the samples. Given the pitch value of the cholesteric assembly, scattering is collected in “transmission”. The signal results from the reflection of light on cholesteric domains at high angles of incidence.

##### **5.4.1. Optical response of the composites**

By recording the spectra presented in Figure 137 of the different polymer-CNC composites introduced in the previous sections, trends observed by naked eye are also observed in goniometry. PS-CNC composites with no alignment do not show any visible iridescent signal but rather incoherent scattering with a wavelength dependency: the intensity of ballistic light in the blue is much lower than in the red, meaning a lot of the original blue intensity has been



scattered in a different direction while travelling through the material. This wavelength dependent scattering behaviour is characteristic of Rayleigh scattering, involving scatterers that are small compared to the wavelength.

As the helices inside the composite align increasingly, incoherent scattering becomes less intense. Aligned under electric or magnetic fields, PS-CNC composites show two oblique lines characteristic of an iridescent optical response. These lines appear broad in width, which means the same wavelength is scattered at different collection angles. This could be either a consequence of the incoherent scattering that broadens the signal of interest, or an indication of pitch polydispersity in the material. Finally, it could be an expression of the bandwidth  $\Delta\lambda = \Delta n \cdot p$  predicted by the theory at normal incidence that is anticipated to be non-negligible for pitches of several microns: for  $\Delta n = 0.06$  and  $p = 2 \mu m$ , we have  $\Delta\lambda \sim 120 \text{ nm}$  which would already have a visible impact on the optical response.

PMMA composites have much better defined optical responses that span the entire visible region. Colour bars of Figure 137 indicates that the optical response of PMMA composites is about 4 times stronger than PS composites. The width of the iridescent signal bands decreases from PS to PMMA, and from non-aligned PMMA to magnetic field-aligned PMMA. This observation excludes a contribution of the theoretically predicted bandgap of cholesteric assemblies as the birefringence and pitch values of the helices do not observe any change from PS to PMMA composites. The two other interpretations remain possible to explain why PMMA composites show a stronger iridescent response than PS composites: the polydispersity in pitch inside all materials is hardly accessible without using optical means as both polarised optical microscopy and scanning electron microscopy have a projection bias in non-aligned composites, which makes it hard to de-correlate the two contributions. Notably, incoherent scattering is largely reduced from PS to PMMA composites.

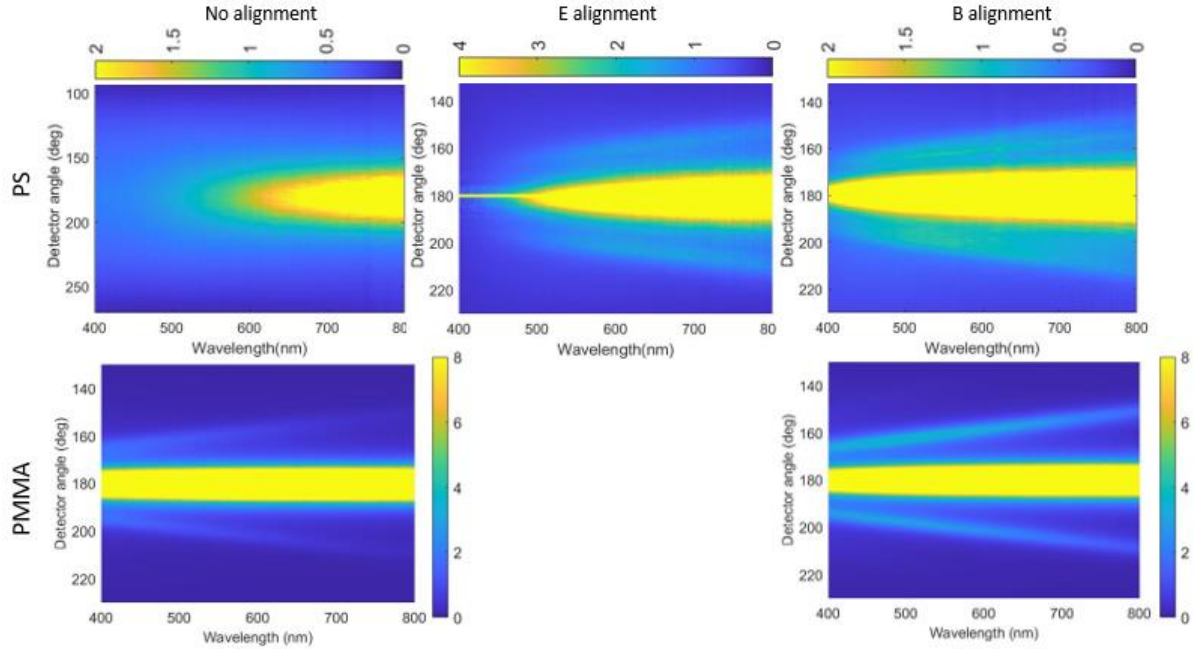


Figure 137 : Angular-resolved spectroscopy plots of PS and PMMA-CNC composites presented in the previous sections: PS-CNC composites of Figure 125, PMMA-CNC composites of Figure 124 and Figure 136. Colour bars range indicates the strength of the intensity signal.

#### 5.4.2. Pitch measurements in the composites

On the example of the magnetic field-aligned PMMA-CNC composite that has the most well-defined optical response, pitch values have been deduced from the iridescent signal by fitting them with the Fergason law. The underlying hypothesis is that the cholesteric assembly behaves as a Bragg multilayer reflector, which is not true to a full extent but still accurately predicts the position of the maximum of the iridescent peak (refer to chapter 1 for more information). Figure 138 presents the fit of the previous plot by the Fergason law with adjusted parameters. The Fergason law matches accurately the experimental data with a volume fraction of 0.25 and a pitch value of  $3.3 \mu\text{m}$ .

An experimental measurement of the polydispersity in pitch can be obtained by plotting the intensity as a function of the detector angle at fixed wavelengths. While the two iridescent peaks are not completely separated from the ballistic light peak, they can be isolated in the residues of a gaussian-lorentzian fitting of the ballistic light peak (Figure 138c and d). The full width at half maximum (FWHM) of the peaks is measured at  $6^\circ$ , which corresponds to a polydispersity in pitch of  $p = 3.3 \pm 0.4 \mu\text{m}$ . This measurement is valid under the hypothesis that only the polydispersity in pitch contributes to the broadening of iridescence peaks. Incoherent scattering has already been mentioned to possibly contribute, also the finite diameter of the optical fibre

of the detector contributes to broaden the peak in angle. Polydispersity in pitch in this measurement is therefore likely overestimated.

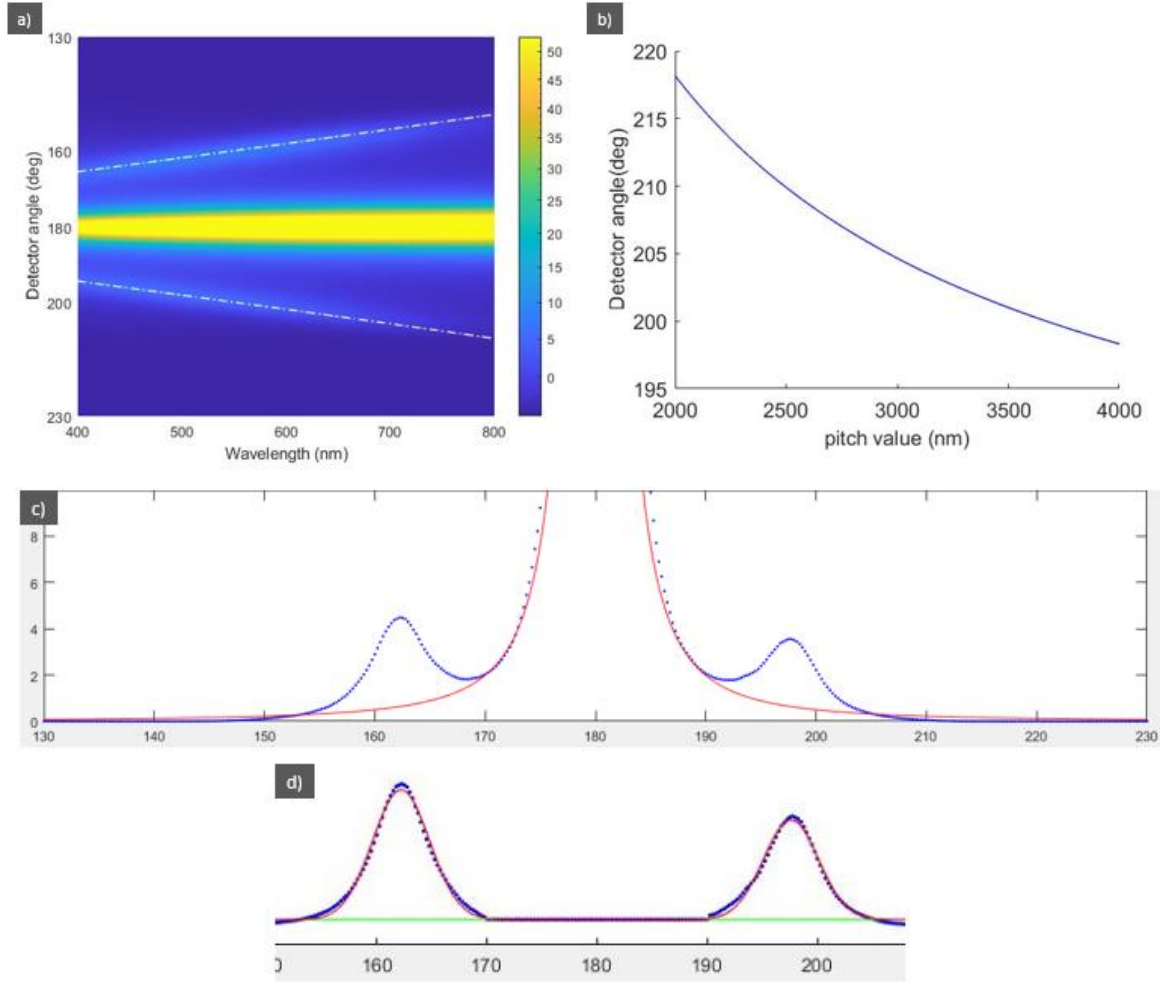


Figure 138 : a) Fit of the iridescent signal of a PMMA-CNC composite aligned under magnetic fields by the Fergason law (in dashed lines) with  $p=3.3 \mu\text{m}$ , the volume fraction  $\phi=0.25$  and  $n=1.49$ . b) Detected angle of the iridescence peak maximum as a function of the pitch value at 632 nm as given by the Fergason law for the calculation of the polydispersity in pitch. c) Ballistic light subtraction by a 70% gaussian/30% lorentzian peakfit.m function in Matlab (red line) from the experimental data (blue dots) of intensity as a function of the detector angle. d) Iridescent peak signals recovered from the residues of ballistic light subtraction.

This value is to be compared with other characterisation techniques, namely laser diffraction, polarised optical microscopy and scanning electron microscopy. Laser diffraction gives a mean pitch value of  $p = 3.5 \pm 0.2 \mu\text{m}$  over 3 measurements in relatively good agreement with goniometry. Measuring the pitch value in polarised optical microscopy gives a mean pitch value of  $p = 3.2 \pm 0.2 \mu\text{m}$  over 23 measurements. Measuring the pitch value in scanning electron microscopy gives a mean pitch value of  $p = 3.35 \pm 0.2 \mu\text{m}$  over 12 measurements. One should note that polarised optical microscopy and SEM pitch measurements are thought to be unbiased by projection in this case.

This value is compared to the pitch value in suspension in the very same conditions of  $p = 3.9 \pm 0.2 \mu\text{m}$ , data obtained from laser diffraction. This small pitch decrease upon polymerisation has also been observed in other samples. The first idea to explain a pitch contraction during polymerisation is to consider the impact of volume shrinkage following the density increase during polymerisation on the pitch value. In PMMA matrices, volume shrinkage is on the order of 19.5%. If we assume isotropic volume contraction, the corresponding pitch contraction is therefore given by  $\frac{p'}{p} = \sqrt[3]{80.5\%} = 93\%$ , to be compared with the *ca.* 15% pitch contraction measured experimentally from suspension to composite materials. Volume shrinkage is thought to contribute to half of the pitch reduction, while the other half is attributed to partial evaporation of the monomer during experimental manipulations.

The pitch values measured on the TEM images of the cryo-cuts are found to be in between 2.3 and 2.5  $\mu\text{m}$ , notably lower than other characterisation methods. The concentration of the starting suspension of 24.5 wt.% does not justify such a value, nor the projection bias of cutting the helices obliquely. Significant evaporation may have taken place in this particular sample.

### 5.4.3. Selectivity in polarisation

At normal incidence, theory predicts that cholesteric assemblies selectively reflect circularly polarised light of the same handedness than the helicity of the stack into a circularly polarised reflected beam. From normal to oblique incidence, the polarisation of the reflected beam is expected to become increasingly elliptical with increasing angles of incidence. What is the polarisation state of reflected light in the composite materials of this work?

Using a polariser and a quarter wave plate mounted on the detector arm, the left circularly polarised (LCP), right circularly polarised (RCP), vertical (s) and horizontal (p) polarisations of reflected light have been measured similarly to Figure 138a) and circular and linear polarisation excesses have been plotted in Figure 139. Circular polarisation excess heat map shows values close to zero, with a slight excess of RCP of 4% in the iridescent bands region. By contrast, there is an important excess of linear horizontal polarisation (p) with respect to the vertical polarisation (s) in the iridescent band regions with an excess of approximately 40% (here, the sample normal is maintained within the horizontal plane where the goniometer operates). The loss of selectivity in circular polarisation is a consequence of the pitch value of several microns leading to Bragg reflection at high angles of incidence. The strong horizontal

linear polarisation selection is ascribed to the favoured horizontal helices axes orientation in this material due to magnetic alignment.

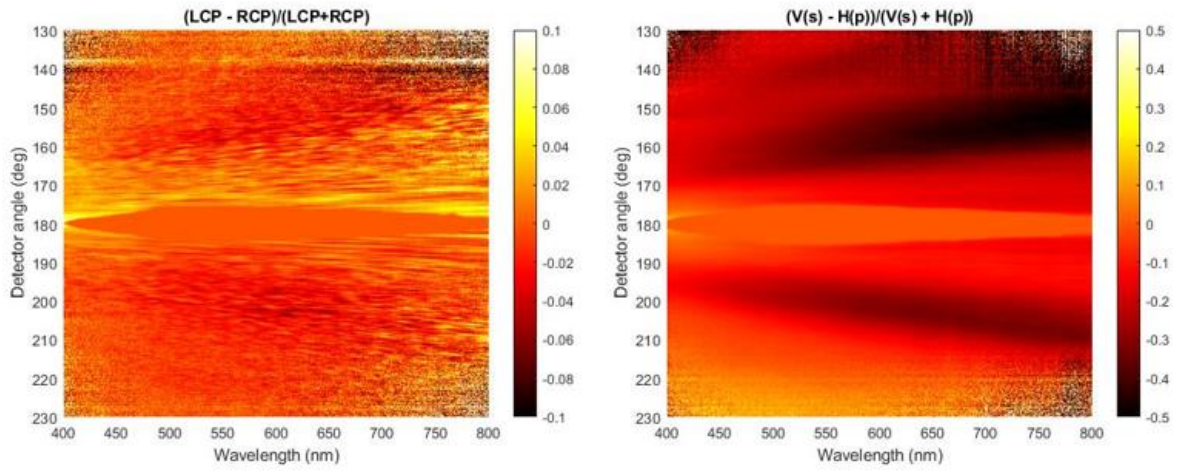


Figure 139 : (left) Circular polarisation excess  $(LCP - RCP)/(LCP + RCP)$  and (right) linear polarisation excess  $(s - p)/(s + p)$  heat map of the PMMA-CNC composite aligned under magnetic fields of Figure 138. Heat map format has been chosen to highlight intensity contrasts.

#### 5.4.4. Quantitative assessment of helices orientation inside the composites

Figure 140 clearly shows that white light scattering occurs preferentially in the horizontal direction, which is consistent with the retention of helices orientation in the direction of the horizontal magnetic field of the sample already suggested by SEM, polarised optical microscopy and laser diffraction data. However, a more quantitative assessment of helices orientation would be beneficial to facilitate comparison of the helical alignments in the composites. By measuring the optical response of the sample in the particular optical configuration of Figure 141, it is possible to quantitatively assess the orientation of helices inside the sample, retrieve the order parameter for helices orientation in the composite and compare this result to the order parameter value measured in suspension in chapter 4 to assess how much helices orientation has been modified by the polymerisation process.



*Figure 140 : White light diffraction of the PMMA-CNC composite aligned under horizontal magnetic fields projected on a screen. Illumination is done with a xenon lamp; detector is the camera of a smartphone. Colours observed are therefore biased by those two apparatuses.*

Let us first clarify the geometry of Figure 141. In the measurement of Figure 141a), the source and the detector initially face each other and are concomitantly moved by an angle  $\alpha$  as described on the schematic, with  $\alpha$  sweeping from  $-90^\circ$  to  $+90^\circ$ . At any angle  $\alpha$ , helices scatter light in the plane defined by their helical axis direction  $\mathbf{h}$ , and the direction of incoming light,  $\mathbf{k}_i$ , defined as parallel to  $\mathbf{z}$ . Whenever the helical axis  $\mathbf{h}$  has a  $x$  component (here vertical), its scattering plane does not cut the detector so this helix does not contribute to the light reaching the detector. Helices with a  $z$  component have their scattering plane cutting the detector, but they typically do not match the Bragg reflection conditions for scattering in the precise direction of the detector. As a result, the scattering that reaches the detector is mainly due to the contribution of helices whose axes are in the  $y$  direction. Among these helices, sweeping  $\alpha$  from  $-90^\circ$  to  $+90^\circ$  allows to measure the contribution of a wide range of pitches: it corresponds to sweeping the  $\cos(\theta)$  value of the Bragg law from 0 to 1. Performing this measurement yields the plot presented in Figure 142, that looks very similar to Figure 137 although both plots do not measure the same scattering signal. Logscale used in Figure 142 is a visualisation trick to enhance the intensity contrasts of the plot and reduce the saturation of ballistic light. It has not been used earlier because the iridescent optical response of PS is not strong enough to do it.

The idea of the measurement detailed schematically in Figure 141b) is to rotate the sample by an angle  $\varphi$  in the (Oxy) plane and repeat the measurement of Figure 141a). By screening  $\varphi$  angles regularly, data will cover the scattering from all helices whose axes point in the (Oxy) plane as they will all be pointing horizontally along  $y$  for a given  $\varphi$  value. Knowing that scattering intensity is directly proportional to the number of helices scattering, this experiment provides a direct measurement of the number of helices in any orientation of the (Oxy) plane.

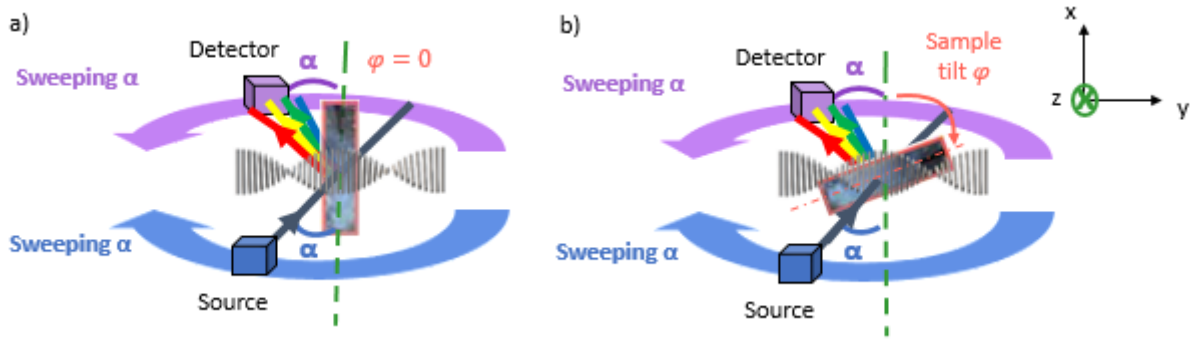


Figure 141 : Schematics of the optical geometry of the experiment conducted to quantitatively assess helices orientation inside the sample. a) In the “mirror” configuration where the illumination light and the detector are concomitantly moved by an angle  $\alpha$  with respect to their original position, only the scattering of strictly horizontal helices along  $y$  reaches the detector at all angles  $\alpha$ . Sweeping  $\alpha$  allow for capturing a broad range of helical pitches. b) Rotation of the sample in the  $(Oxy)$  plane by an angle  $\varphi$  and repetition of the measurement presented in a) allows to measure the scattering intensity contribution of all helices orientation in the plane of the sample  $(Oxy)$ .

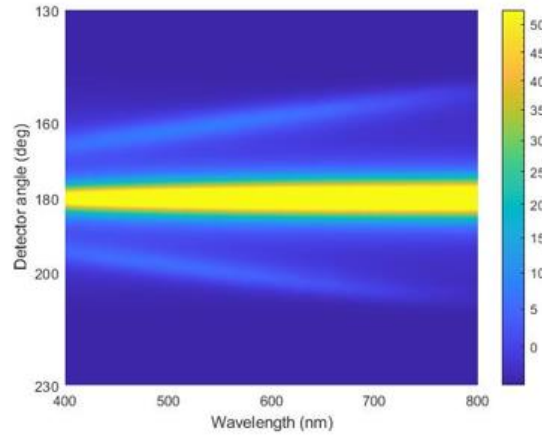


Figure 142 : Angular-resolved spectroscopy plot of the PMMA-CNC composite aligned under magnetic fields measured following the procedure of Figure 141. Logscale is used to enhance intensity contrasts and reduce the saturation of the ballistic beam.

#### 5.4.5. Order parameters determination

One can now gather all the data in one plot presented in Figure 143 showing the number of helices as a function of the tilt angle  $\varphi$ . The reference for  $\varphi$  is chosen such that  $\varphi = 0^\circ$  corresponds to the direction of the magnetic field. From the experimental curve of Figure 143a), one can retrieve an experimental value of the order parameter for helices orientation inside the composite. From symmetry arguments on the magnetic field orientation that are detailed in chapter 2, it is possible to give a simplified expression of the quadrupolar order parameter directly as a function of the sample tilt:



$$S_{2,exp} = \left\langle \frac{3 \cdot \cos^2 \theta - 1}{2} \right\rangle = 1 - 3 \cdot \langle \sin^2(\varphi) \rangle = 1 - 3 \cdot \frac{\int_{\varphi=0}^{360} I(\varphi) \sin^2(\varphi) d\varphi}{\int_{\varphi=0}^{360} I(\varphi) d\varphi}$$

Using data from Figure 143a) for  $I(\varphi)$ , one retrieves an experimental value of  $S_{2,exp} = +0.73$  for 3D helices orientation inside the PMMA composite.

To assess the validity of this value, one can also question whether the experimental distribution fits the theoretical distribution of helices orientation in a magnetic field (details in chapter 2):

$$\gamma = \frac{\mu_0 \cdot \Delta\chi \cdot V \cdot H^2}{2 \cdot k_B \cdot T}$$

$$f = \frac{1}{2\pi \cdot \sqrt{\frac{\pi}{4\gamma}} \cdot \text{erfi}(\sqrt{\gamma})} e^{\gamma(h.H)^2}$$

$$S_{2,th} = \frac{3}{4\gamma} \cdot \left( \sqrt{\frac{4\gamma}{\pi}} \cdot \frac{e^\gamma}{\text{erfi}(\sqrt{\gamma})} - 1 \right) - 1/2$$

By varying the value of  $\gamma$  until the theoretical distribution fits the experimental data as in Figure 143b), we obtain  $\gamma = 7$  and  $S_{2,th} = 0.75$  in very good agreement with the experimental value of the order parameter. This agreement indicates that helices orientation in the PMMA-CNC composite material aligned under magnetic fields is governed by the incentive of helices to align in the direction of the magnetic field as expected.

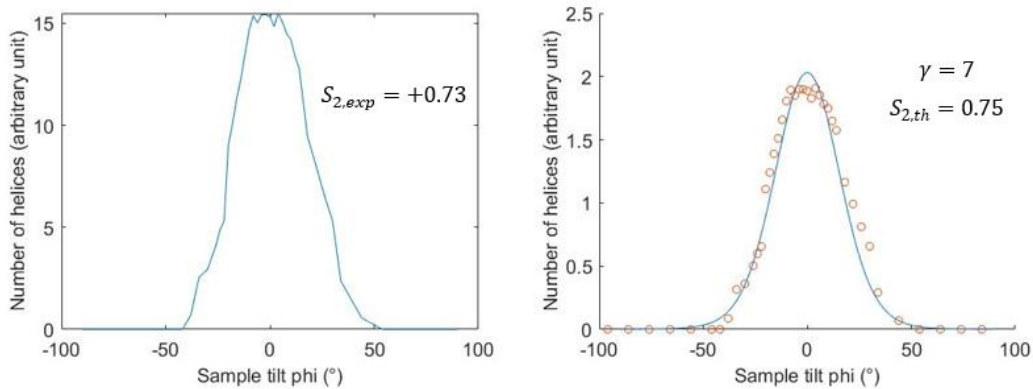


Figure 143 : Plots of the number of helices as a function of the sample tilt  $\varphi$  within the (Oxy) plane constructed from scattering intensity measurements at 500 nm in the configuration of Figure 141. In both plots, one point corresponds to one angular-spectroscopy measurement like the one of Figure 142. (left) Experimental curve. (right) Experimental points in orange and theoretical fit in blue. Ordinary rescaling has been carried out from left to right to match the fit, justified by the fact that the ordinary information is relative.

By comparing the order parameter for helices orientation in PMMA-CNC composites aligned under magnetic fields with the order parameter for helices orientation in suspension obtained in chapter 4, we can observe that helices are slightly less aligned in composites than in suspension. Whether this is due to the polymerisation reaction itself or a slightly different suspension state prior to polymerisation remains an open question at this point. One can assess as well the impact of magnetic field alignment on helices orientation inside the composite by comparing on Figure 144 the order parameters for helices orientation obtained with and without magnetic field alignment. A slight alignment corresponding to an order parameter of  $S_{2,\text{helices}} = +0.16$  is observed without magnetic field possibly due to a mould-filling bias, that is indeed much lower than the order parameter measured in the presence of the magnetic field.

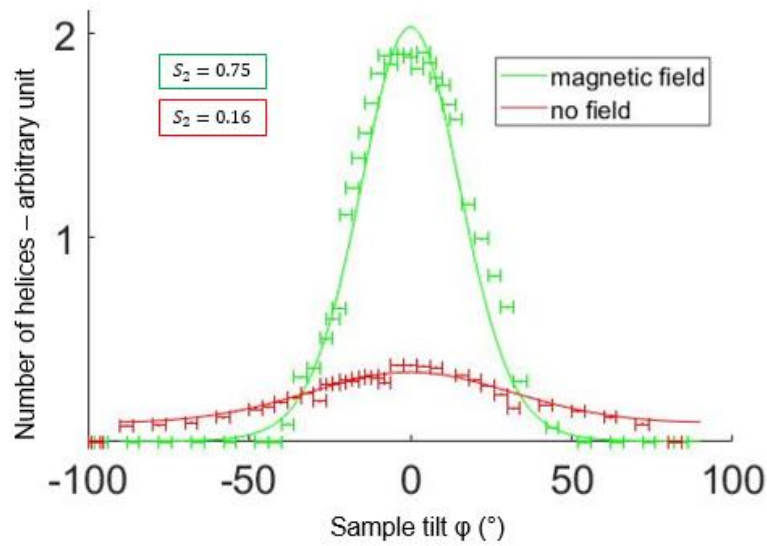


Figure 144 : Number of helices as a function of the sample tilt  $\phi$  of PMMA-CNC composites (green) aligned under a 0.65 T magnetic field and (red) non-aligned. Dots correspond to experimental points with error bars, whereas plain lines correspond to theoretical fits ( $\gamma = 7$  and  $\gamma = 1.5$  respectively).

## 5.5. Conclusions

The original aim of the study discussed in this chapter was to make polymer-CNC composites showing an iridescent colour response. While isotropic polymer-CNC composites scatter light strongly, cholesteric composites by contrast show a partial recovery of transparency due to the coherent scattering arising from helical assemblies. These helical assemblies were not significantly distorted by the polymerisation process, according to SEM observations. Syneresis effects have been observed to strongly impede transparency in loosely cross-linked matrices and have been solved by tightening the polymer network with a higher cross-linker concentration. While PS composites showed no iridescent optical response owing to their strong

incoherent scattering, PMMA composites by contrast immediately showed iridescent optical responses.

Electric and magnetic field alignment allowed to recover the coherent iridescent optical response in PS composites while it strengthened the already existing response of PMMA composites as a consequence of the lower degrees of freedoms given to helices orientation. Using cross characterisation of the materials in SEM, polarised optical microscopy and laser diffraction on the example of PS composites, the expected field-aligned orientation of CNC helices in composites has been observed in the bulk of the sample, with the exception of a skin-layer approximately 10  $\mu\text{m}$  at the sample surface.

The optical response of the composites has been characterised in more detail using angular-resolved optical spectroscopy. By capturing the iridescent optical responses of the materials, this technique allowed to measure the helical pitch and its polydispersity in the composites. Good agreement with the values obtained from SEM, polarised optical microscopy and laser diffraction characterisation has been obtained. Polarisation-filtered measurements showed no excess of circular polarisation, but a predictable excess of linear (p) polarisation in the reflected light. Finally, choosing a particular optical configuration to capture the scattering of helices allowed for a quantitative measurement of the number of helices in a given orientation of space inside the composite on the example of a PMMA-CNC composite aligned under magnetic fields. An experimental measurement of the order parameter for helices orientation  $S_{2,exp} = +0.73$  is deduced from this experiment and found to be in very good agreement with the theoretical order parameter  $S_{2,th} = +0.75$  obtained with a fit of the experimental data by a Boltzmann distribution describing the competition between the incentive of helices to align along the magnetic field and Brownian motion. This leads us to conclude that helices orientation in the composite is mostly determined by their incentive to align in the magnetic field. Comparing these values with order parameters in suspension of chapter 4 suggests a slight influence of the polymerisation process on the quality of helices alignment.

Eventually, some questions remain opened to further investigation. We do not have enough information to date to conclude on why PMMA composites have such a better coherent scattering response compared to PS composites. Even though obtaining iridescent optical response in polymer composites was a real challenge to overcome, the optical responses measured in the composites do not compete with the state of the art CNC materials obtained by controlled drying of aqueous suspensions. However, the photopolymerisation process allowed

for much shorter processing times and additional versatility compared to the slow drying process. Moreover, the manipulation of the helices axes, which allows to explore a variety of geometries, can only be achieved in organic apolar monomers. Additionally, obtaining pitches compatible with iridescence in reflection are still an open question. This last issue is specifically addressed in a different approach in chapter 6. Finally, the versatility of the process opens interesting possibilities to make composites using polymer matrices of radically different properties that are currently under investigation.

## **5.6. *Perspectives on the mechanical reinforcement properties of the composites***

While the primary objective of this work has been to incorporate helical CNC charges into composite polymer matrices to create structural colour effects, it is interesting to take a moment to assess whether these materials are also useful for other applications. These materials are first remarkable because they hold perfectly dispersed fillers content of 25-30 wt.% in CNC+surfactant with a remarkable supra-colloidal organisation. Some of nature's toughest materials are made of helical organisations (Natarajan and Gilman 2018): the snow crab (*Chionoecetes opilio*)'s carapace both mechanically strong and loosely iridescent has been observed to be a porous network of helical chitin (Nguyen and MacLachlan 2019) in which the regularity of pores arrangement both contributes to mechanical reinforcement and structural colour effects. Mantis shrimp (*Odontodactylus scyllarus*) clubs, famous for their ability to crush repeatedly crab shells to provide food, are also made of helical chitin of optimised orientation and pitches that show impressive fracture resistance properties (Weaver et al. 2012; Natarajan and Gilman 2018). Finally, ivory is also a helical assembly of collagen that provides tough mechanical properties to the material (Giraud-Guille, Mosser, and Belamie 2008). These natural structures have impressive fracture resistance properties on top of good mechanical toughness because the supramolecular organisation has the property to stop crack propagation similarly to the salami structure of a man-made polystyrene-IMPACT (Guarín-Zapata et al. 2015).

Notable difference with this work, the pitch value of these natural helical assemblies ranges from tens to thousands of microns whereas the typical pitches measured in this work are 1 to 5 microns. One forecast that the pitch value would need to be increased by an order of magnitude to provide efficient fracture resistance properties to the composite. Another issue comes from the ability of CNC charges to actively participate in the response of the material to mechanical

stress. A previous work in CERMAV (Ljungberg et al. 2005) led a mechanical study on the involvement of CNC fillers in a polypropylene matrix depending on the stabilisation mechanism of CNC charges inside the matrix: neat CNCs, surfactant-stabilised CNCs and grafted CNCs with maleated polypropylene chains. While aggregation of charges has been observed for neat and grafted CNCs, surfactant-stabilised CNCs were well-dispersed on the other hand. However, surfactant-stabilised CNCs were found not to take an active part in responding to the mechanical stress exerted on the matrix (apart from a modulus increase arising from filler-filler interactions).

It is very likely that the surfactant-stabilised CNCs in PS and PMMA composites of this work behave similarly to the ones of Ljungberg et al. In order to make the helical organisation of charges beneficial to mechanical properties, literature on composite materials (François 2008; Legrand and Soulié-Ziakovic 2016) suggests the surface grafting of functional groups that will get involved in forming the polymer network even though this approach seemed not to have been successful for Ljungberg et al. because of CNC aggregation.

To conclude on the usage of the composites of this work for mechanical reinforcement, the helical organisation of fillers can provide interesting mechanical properties such as high charges loading and exceptional fracture resistance. However, natural structures suggest that ideal contribution to mechanical properties would require a pitch value about one order of magnitude higher than the current one. Additionally, the current surfactant stabilisation mechanism of CNCs in the monomer suspension seems to impede strongly the contribution of the fillers to the mechanical properties of the final composite.

# **Chapter 6. Dryings of CNC suspensions in organic solvents**

*« Trois ans. [...] Le prix à payer. [...]   
Trois années qui te forgeront, parfois dans la douleur,   
souvent dans le doute, toujours dans la difficulté. »   
P. Bottero*

This chapter aims at exploring the drying of non-aqueous suspensions of CNCs. Because this field is unexplored in the literature to date, this work has vastly inspired from the dryings of aqueous suspensions of CNCs, in which a significant research effort has been conducted over recent years, unveiling the important features of this process. We will see how these features take place in non-aqueous dryings, although adaptations have often been required to accommodate the specificities of this system. In the first part, we review literature works on the drying of CNC films. We then present the try-and-error iterations that have led to our final experimental setup. The third part presents the drying of sessile droplets of CNC suspensions in toluene. In the fourth part, drying of MMA suspensions is conducted in the scope of being able to stop the drying on-demand by polymerising at intermediate steps. The last part presents the optical response of the dried and polymerised films.

## **6.1. *State of the art: Dryings of CNC suspensions***

Reviewing literature, the most efficient and most explored way of making photonic materials out of cellulose to date is to dry aqueous CNC suspensions. There is a paradox here: while the experiment is as simple as drying a droplet or a film of suspension in a petri dish, understanding the final state of the film and/or what is happening over the course of the drying turns out to be really complex. In this state of the art, we aim to cover the main mechanisms taking place over the course of aqueous dryings and explain why retrieving a homogeneous photonic colour from the drying of CNC suspensions is not straightforward.

### **6.1.1. A timeline of the drying process**

A big picture to bear in mind when discussing dryings is the one summarised by Gray (Gray 2016) and reproduced in Figure 145. Starting from an isotropic suspension of CNCs the concentration of the system will increase as the solvent evaporates. Upon reaching the volume fraction  $\varphi = \varphi_i$ , the anisotropic phase will nucleate in the form of growing tactoids in the system. When  $\varphi = \varphi_a$ , the system is fully composed of anisotropic domains. From here, a concentration increase will result in a decrease in pitch following the power law  $p \sim c^{-1}$  (Gray 2016; Parker et al. 2016) until kinetic arrest is reached. Parker et al provided an experimental measurement of the kinetic arrest for their suspension at  $c \sim 19$  wt. % by observing the change in the power law from  $p \sim c^{-1}$  to  $p \sim c^{-1/3}$  in a system of CNC microfluidic droplets (Parker et al. 2016). After kinetic arrest, the system is trapped in a gelled state where colloidal rods can no longer move to accommodate for the most energetically favourable configuration, but



approximately 80 % of the solvent remains to be evaporated. The cholesteric order, determined by the local pitch and the helical axis orientation, will evolve according to the macroscopic distortion experienced by the drying phase and dictated by the drying geometry. In the example of a film drying in a petri dish, water evaporates upwards leading to a 1D vertical compression. The case of drying droplets is more complex and treated in the next [section](#). Over the course of this final step, the arrested system will need to shrink its volume at kinetic arrest by a factor 5 without being able to rearrange the orientation of the CNCs to accommodate the changes. It is easy to imagine that heavy mechanical constraints will take place inside the film, leading to helices compression, deformation, film cracking and possibly film breakage.

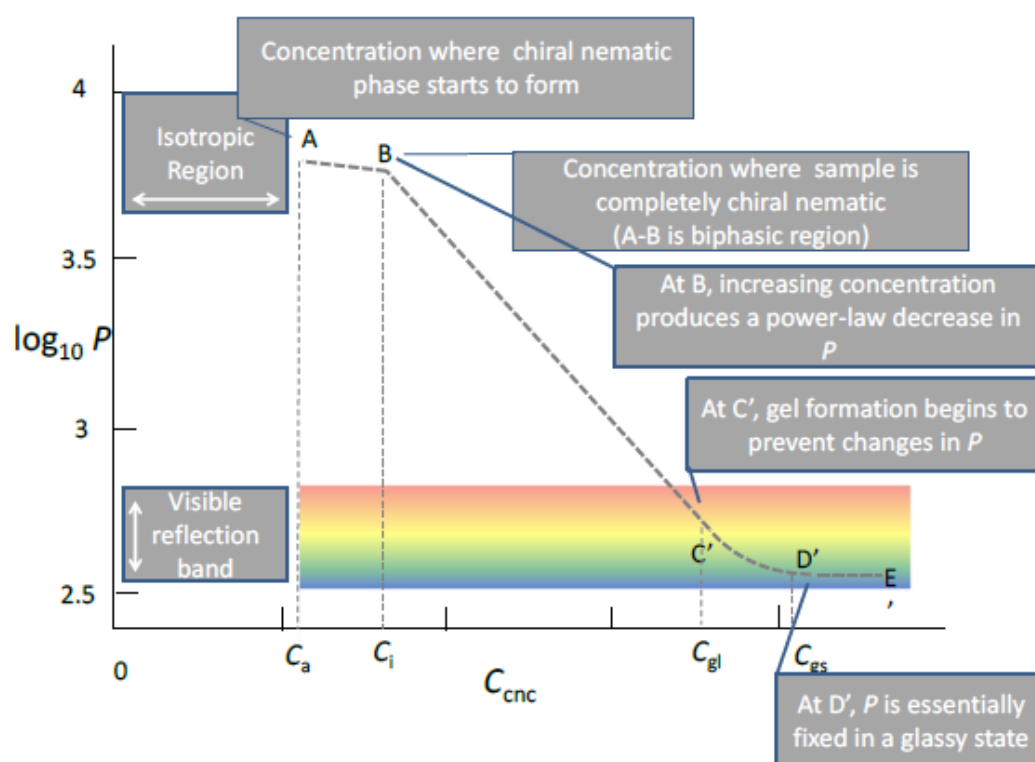
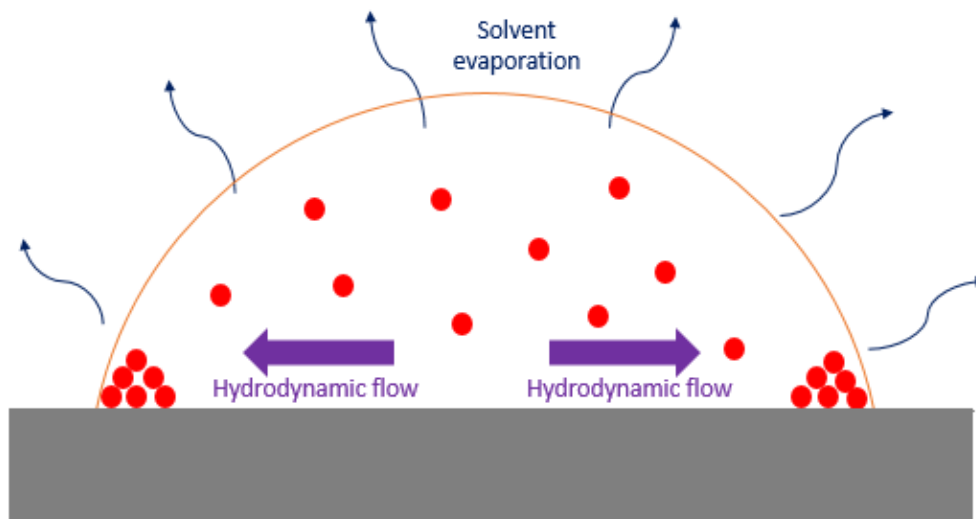


Figure 145 : Schematic visualisation of the drying process proposed by Gray et al. by plotting the helical pitch as a function of the concentration in log-scale. Adapted from Gray, *Nanomaterials* 2016.

### 6.1.2. Drying droplets and coffee-ring effect

In drying droplets, the drying process is more complicated for a purely geometrical reason. While evaporation mainly takes place radially, the higher surface/volume ratio on the droplet edges leads to a faster evaporation of the edges compared to the centre of the droplet. The concentration at the edges increases therefore faster than the concentration at the centre, causing a hydrodynamic flow from the centre to the edges to equilibrate these. This flow of water and colloidal particles leads to the accumulation of colloids on the edge of the droplets and can

eventually empty the centre of the droplet (Deegan 2000; Deegan et al. 1997) just like in drying droplets of coffee. The phenomenon is schematically viewed in Figure 146 and commonly referred to as the “coffee-ring effect”.



*Figure 146 : Schematic view of the coffee-ring effect. The higher evaporation rate on the edge leads to an outwards hydrodynamic flow that cause the accumulation of colloidal particles on the edges of the droplet.*

This hydrodynamic flow can be negated in various ways (Parker et al. 2018):

- Slow-drying gives time to the system to equilibrate during the drying, corresponding to a quasi-static evolution. Zhao et al successfully applied this principle to the drying of CNC suspensions, showing a conserved dome height profile after slow-drying reproduced in Figure 147 (Zhao et al. 2019). They used an intermediate layer of hexadecane on top of the CNC film to slow down water evaporation. Water can no longer evaporate directly, but needs to diffuse through the oil layer in which it has limited solubility, decreasing dramatically the evaporation rate.
- Alternatively, interfacial trapping of colloidal particles ensures they are distributed evenly in the dried film (Anyfantakis et al. 2015). Capron and Cranston’s groups have successfully trapped cellulose nanocrystals at interfaces to stabilise oil-in-water Pickering emulsions (Kalashnikova et al. 2011; Hu et al. 2015). However, their system requires adaptations in order to develop helical CNC organisation inside the droplets upon drying.
- Counter-flows can also be used to counteract the effect of the concentration gradient. In particular, setting a positive gradient of surface tension from the edges to the centre of the droplet will naturally induce a Marangoni counter-flow from the edge to the centre.

Since ethanol has a lower surface tension than water, ethanol vapour can induce such effect. Gençer et al exploited this effect in cast CNC films and obtained a near-even dried film surface using a 50% EtOH atmosphere (Gençer, Schütz, and Thielemans 2017).

- Finally, adding a non-volatile rheology modifier to the system can greatly reduce the hydrodynamic flow towards the edge of the droplet. Yao et al exploited this phenomenon to make uniform photonic CNC-PEG dried films (Yao et al. 2017).

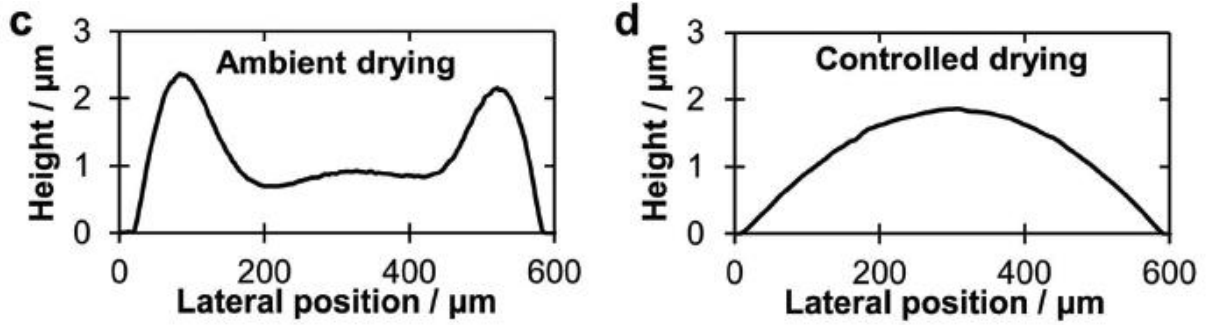


Figure 147 : Standard drying (c) versus controlled drying (d) of CNC suspension droplet profiles reproduced from Zhao et al, *Adv. Funct. Mater.* 2018, 1804531.

### 6.1.3. Optimising the suspension state before kinetic arrest

As discussed earlier, the self-assembled structure becomes kinetically arrested upon solvent evaporation. Therefore, obtaining good control over the final structure requires the ability to manipulate the cholesteric order before this arrest takes place.

Recently unveiled by Frka-Petesic and coworkers (Frka-Petesic et al. 2019), the orientations of CNC helices at kinetic arrest have a direct and significant impact on the final optical appearance of the dried films. The authors consider the deformation of a helical stack of rods, initially tilted by an angle  $\beta$  after vertical compression. For a compression ratio  $\alpha < 1$ , the new pitch  $p'$  after compression is given by:

$$\frac{p'}{p} = \frac{1}{\sqrt{\sin^2 \beta + \alpha^{-2} \cos^2 \beta}}$$

where  $p$  was the pitch at kinetic arrest. Moreover, the authors show that the direction of the helix axis changes during the compression, being significantly reoriented towards the direction of compression. For example, a helix whose axis is tilted by  $\beta = 45^\circ$  with respect to the direction of compression and compressed by  $\alpha = 0.1$  will end up at a new tilt angle of  $\beta' \sim 5^\circ$

and will have a pitch 50% larger than the one of a non-tilted helix undergoing the same compression. Main results are shown in Figure 148.

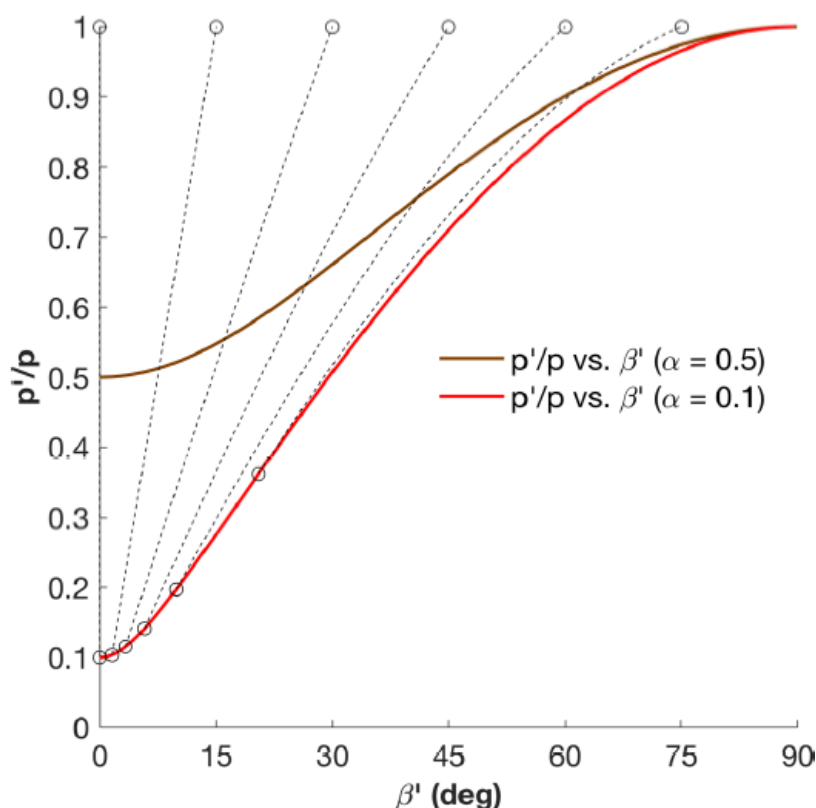


Figure 148 : Evolution of the helical pitch ratio  $p'/p$  after compression as a function of the tilt angle after compression  $\beta'$ . The brown curve corresponds to a 50% compression ( $\alpha=0,5$ ) whereas the red curve corresponds to a 90% compression ( $\alpha=0,1$ ). Dashed lines represent trajectories of pitch values and tilt angles over the course of the compression, demonstrating cholesteric domains reorientation under compression. Adapted from Frka-Petescic et al, PRM 2019.

As a result, even a unique pitch in suspension at kinetic arrest results in a distribution of pitch values in the dried film, due to this anisotropic compression effect (with longer pitch values being observed at larger tilts). As a result, the optical appearance of the film will be polychromatic if the orientation of the initial domains is not controlled.

#### 6.1.4. A toolbox to reorient cholesteric domains

Cholesteric domains need to be oriented in the direction of compression to yield films with homogeneous colour. In that scope, Parker et al recently reviewed different tools to orient CNC cholesteric domains (Parker et al. 2018):

- Interface anchoring is an efficient and widely used method to orient CNC helical axes perpendicular to an interface. Schütz et al recently developed in detail the origin of this stabilisation effect (Schütz et al. 2020): it fundamentally comes from the translational

entropy gain of individual CNCs having their long axis parallel to the interface rather than perpendicular to the interface. While only a tiny amount of CNCs should in this case feel the effect, it does transfer to a significant amount of CNCs in a skin-layer in the vicinity of the interface because arranging differently would mean creating a defect in the chiral-nematic arrangement, which has a significant energy cost. In this work, the thickness of the skin-layer in CNC-polymer composites has been measured in chapter 5 to be approximately 10 microns with an additional field alignment incentive. Given this distance is also the thickness required to make a 100% reflection film, anchoring seems a reliable tool towards this objective. In film geometry, this anchoring would correspond to the vertical direction that is also the direction of compression. In droplets geometry, this anchoring could correspond either to a radial or vertical domain orientation that would depend on the contact angle of the droplet with the substrate. Little droplets are expected to yield radial reorientation owing to a relatively large local droplet curvature whereas large droplets are expected to yield vertical domain reorientation owing to a relatively low local droplet curvature, the droplet-substrate flat interface contributing also towards vertical domain orientation. Whenever droplets are very large, anchoring is not sufficient anymore to yield homogeneous orientation.

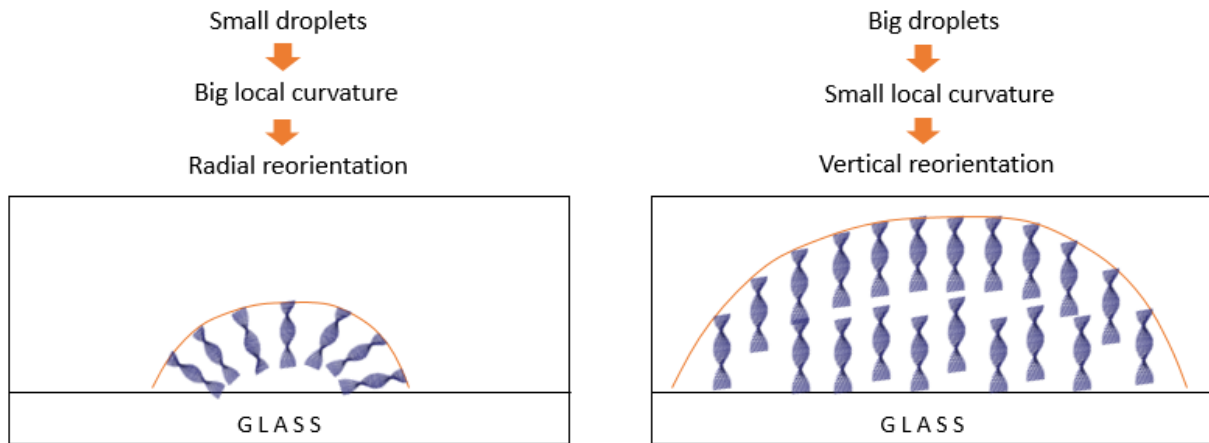


*Figure 149 : Schematic view of the vertical and radial cholesteric domain reorientations taking place in droplets of different sizes on account of interface anchoring.*

- As stated in chapter 4, magnetic field alignment is also an efficient tool to orient CNC helices in the direction of compression. The reorientation takes place within several hours, which can be a limitation to this method. It has been used to successfully tune the orientation of dried CNC films, both in the direction of compression and to induce tilts that shape a different optical response (Frka-Petesic, Guidetti, et al. 2017).

## 6.2. Results

Switching from aqueous to organic apolar solvent dryings – namely toluene and monomers –, we expect the timeline of the drying process to be conserved: an initial isotropic suspension entering the biphasic and subsequently the fully anisotropic regime, the decrease of the pitch with increasing concentration until kinetic arrest is reached and the final evaporation of the solvent. However, the onset of the kinetic arrest is expected to take place at around 30-45 wt.% in dry mass (CNC+surfactant), providing a larger window for the sample to rearrange upon solvent evaporation before kinetic arrest takes place. The inherent viscosity increase over time of the suspensions may prevent the observation of the  $p \sim c^{-1}$  power-law in the fully anisotropic domain. Finally, the starting pitch value in suspension of 2 to 5  $\mu\text{m}$  may lead to lower pitch values compared to aqueous systems.

### 6.2.1. Iterations on the experimental setup

The experimental setup has been built up in a try-and-error fashion. An overview is given in Figure 150. The next sections explain what observations have led to the current experimental setup.

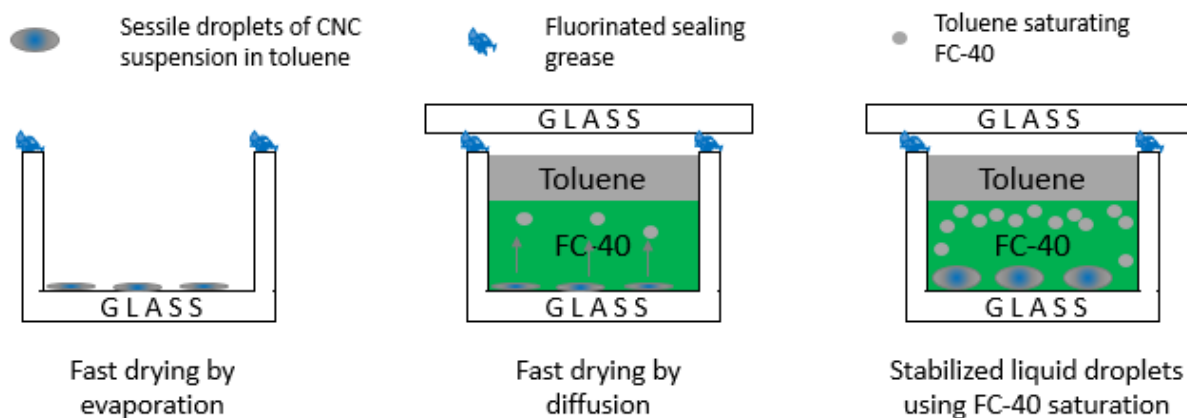


Figure 150 : From left to right, evolution of the experimental setup used for the drying of sessile droplets of CNC suspension in non-aqueous solvents on the example of toluene.

#### 6.2.1.1. Slowing down the evaporation with an intermediate layer

Leaving toluene in open air leads to a very fast evaporation, which is due to the high volatility of toluene compared to water. This fast evaporation does not allow for the development of a cholesteric order and does not produce a film with structural colour.

To slow down the evaporation of toluene, an intermediate layer of immiscible liquid was added on top of the evaporating toluene suspension to enable a much slower toluene evaporation via its diffusion through that liquid, similarly to Zhao et al. However, the choice of a suitable solvent to play this role is not straightforward. Oil-based solvents are often miscible with toluene, and migration of CNC-surfactant objects in this layer will be observed. Any water-based solvent is also problematic because the adsorption of the surfactant on the surface of CNCs is reversible. CNCs being very hydrophilic objects, the surfactant desorbs and migrates at the toluene-water interface while the neat CNCs migrate in the aqueous phase. For this reason, fluorinated solvents appeared as the only class of liquid suitable for this role, being both hydrophobic and lipophobic. The unusually high density of such solvents – *e.g.*  $d = 1.85 \text{ g/mL}$  for FC-40™ – cause an experimental issue, since it is denser than the CNC suspension in toluene. Used as an intermediate layer placed immediately above the CNC suspension in toluene, it requires an additional stabilising force that keeps the CNC suspension at the bottom of the vial. In this work, it has been chosen to pin relatively big ( $V = 10 - 20 \text{ }\mu\text{L}$ ) sessile droplets of CNC suspension at the bottom of the vial using capillary forces.

#### ***6.2.1.2. On the saturation of the intermediate layer***

Whenever sessile droplets are pinned at the bottom of a closed vial containing an intermediate layer of FC-40 and time is given for the cholesteric domains to reorient inside the droplets, what is observed in polarised optical microscopy and reproduced in Figure 151a) is a fast drying of the droplets over approximately 15 min before any cholesteric reorientation takes place. Stick-and-slip is also observed over the course of the drying. More remarkably, the very same phenomenon happens when the vial is sealed with a glass slide and fluorinated grease. It has been concluded that this characteristic time corresponds to the diffusion of toluene from the droplets to the unsaturated intermediate FC-40 layer. Full drying is observed in this case, *i.e.* the amount of toluene present in the droplets is not sufficient to saturate the intermediate layer by itself. Diffusion through the intermediate layer seemed to take place much faster in our system compared to the one of Zhao et al (Zhao et al. 2019).

As a result, the process has been modified to allow for the saturation of the intermediate layer with solvent as a pre-requisite to any drying experiment. Typically, pure toluene and FC-40 have been mildly vortexed together or simply put in contact together in a closed vial for 30 min to several hours before droplets deposition. This modification has been quite successful in preventing fast droplet drying, as liquid droplets with preserved mobility have been observed



after several days in such an experimental setup (Figure 151b). It is worth noting however that saturation had some reproducibility issues especially with low droplets volume.

The other drawback of such a process is that pure solvent deposits on the walls and on the bottom of the vial, due to capillary forces stabilising solvent droplets formation there as well. This mechanism is especially observed using vortex treatments to yield saturation. These droplets can affect the drying process by diluting CNC sessile droplets through diffusion or coalescence at the bottom of the vial (Figure 151c). While this experimental process has been sufficient to lead the experimental study presented hereafter, there are improvements to be made to lower the amount of manipulations and increase the reproducibility of the experiments.

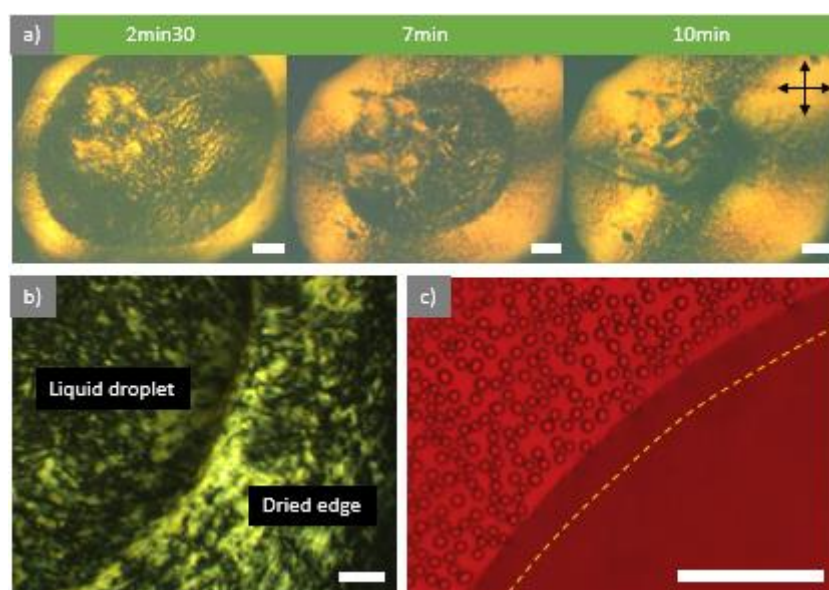


Figure 151 : Polarised optical microscopy images of a) fast-drying of sessile droplets of a 17.9 wt.% CNC suspension in toluene with a non-saturated FC-40 interlayer. Black areas correspond to the drying droplets, whereas yellow regions displaying a maltese cross pattern correspond to dried areas. b) Sessile droplets of a 17.9 wt.% CNC suspension in toluene with a saturated FC-40 interlayer after 24 hours. While an edge layer has fast-dried due to a slight unsaturation, most of the droplet is stabilised in liquid state. c) Toluene deposition at the bottom of the vial following generous vortex treatment. The orange dashed line corresponds to the contact line of the drying droplet one minute before picture is taken, showcasing coalescence events.  $\lambda/4$  retardant plate is inserted in c) (Obj. x5). All scale bars are 200  $\mu\text{m}$ .

### 6.2.2. Evolution of the droplets upon drying

The stabilisation of sessile droplets in a state where cholesteric mobility is conserved over several days allows for key reorientation mechanisms discussed in the state of the art to take place. Once cholesteric domains have been reoriented in the desired state, final drying can be performed. From experimental results and literature, reorienting cholesteric domains in the

direction of compression prior to drying seemed to determine the optical properties of the final film more than carefully slow-drying the suspension until complete evaporation of the solvent.

### 6.2.2.1. Concentration of the starting suspension

In this section, droplets of different starting concentrations in the isotropic (4.5 wt.%, 9 wt.%, 17.9 wt.%, see Figure 152), biphasic (23 wt.%, 25 wt.%) and near-fully anisotropic regime (30.4 wt.%) have been dried using a saturated FC-40 intermediate layer. Drying times are on the order of 15 min. At 4.5 wt.%, the dried films are observed to be essentially in the isotropic state, which means the droplets have been stabilised in the isotropic state by FC-40 saturation, and have been further dried in such way that kinetic arrest took place fast enough to prevent the development of the cholesteric phase inside the droplets. At 9 wt.% the edge of dried droplets displays a cholesteric texture whereas the centre is still isotropic, corresponding to a similar scenario. At 17.9 wt.%, 23 wt.% and 25 wt.%, a cholesteric texture is visible everywhere in the droplet. This result indicates a slight evaporation of the solvent due to under-saturation shortly after CNC droplets deposition, in agreement with dried droplet edges often observed in polarised optical microscopy (Figure 151b). Phase separation by gravity may take place in the height after several days, but cannot be detected in polarised optical microscopy. Mobility inside the droplets allows for tactoid annealing and cholesteric domain reorientation, developed in the next [section](#). At 30.4 wt.%, a cholesteric texture is visible throughout the droplet as well, but cholesteric domains were kinetically arrested before any reorientation could take place (data not shown). The experimental window is therefore defined by a compromise between developing cholesteric domains inside the droplets and keeping their mobility to allow for their reorientation in the saturated state, corresponding to a range of concentrations from approximately 17 wt.% to 25 wt.% in good agreement with literature practices in aqueous droplets (Zhao et al. 2019).

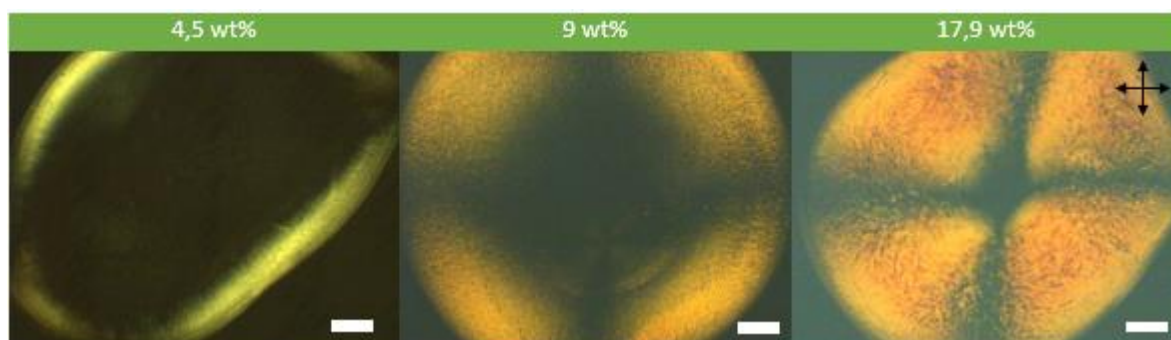


Figure 152 : Optical microscopy images of dried droplets at different starting concentrations (Obj. x5), taken in transmission between crossed polarisers. All scale bars are 200  $\mu\text{m}$ .

#### 6.2.2.2. *Cholesteric domains reorientation inside the droplets*

We have seen in the state of the art that reorienting helices in the direction of compression through anchoring is a major pre-requisite to obtaining homogeneously coloured dried films. By depositing in saturated FC-40 an uncontrolled droplet volume  $V = 10 - 20 \mu\text{L}$  from a 23 wt.% suspension in toluene, tactoid annealing (Tran, Hamad, and MacLachlan 2018) is observed to merge cholesteric domains over several days and lead to two different cholesteric domain reorientation behaviours. Figure 153 presents the evolution of sessile droplets at short times and after 2 days in a sealed and saturated environment. The initially birefringent texture under crossed polarisers disappears completely, indicating either a dilution back to the isotropic domain by toluene migration through the intermediate layer or anchoring reorientation of the helical axes in homeotropic orientation. However, strongly birefringent defects displaying fingerprint patterns can be observed in some samples, corresponding to areas of the sample that have not encountered full reorientation. The observation of these fingerprints strongly suggests the second scenario, namely an almost complete homeotropic reorientation of these droplets. Cholesteric domain reorientation is visible approximately 1 hour after droplet deposition but is still incomplete after 20 hours.

Another type of domain reorientation behaviour has been observed in dried droplets of the same suspension allowed to reorient and fast-dried. Polarised optical microscopy characterisation of Figure 157 indicates a near defect-free radial reorientation of cholesteric domains in the droplets, characterised by a maltese cross pattern that cannot be solely induced by the final drying process.

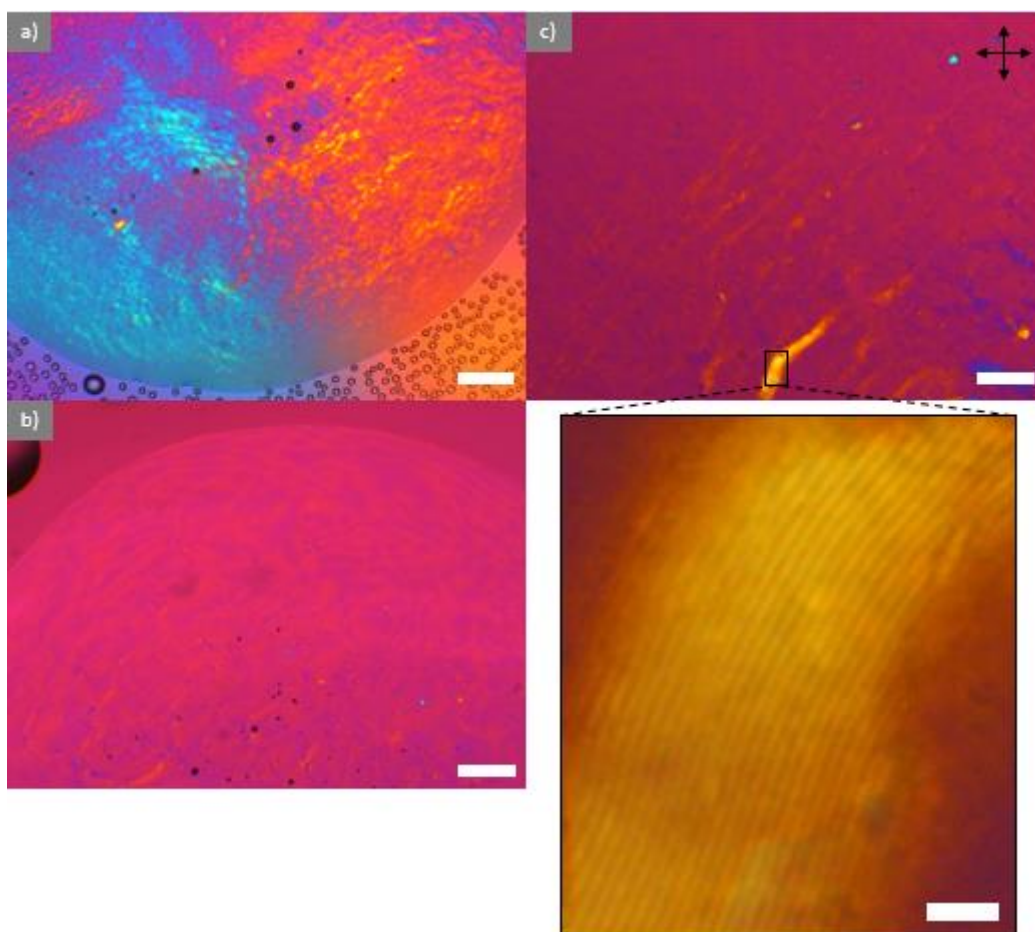


Figure 153 : Optical microscopy images taken between crossed polarisers in transmission with a  $\lambda/4$  retardant plate of a 23 wt.% CNC suspension in toluene after a) 5 min and b-c) 2 days (Obj. x5, scale bar 200  $\mu\text{m}$ ). The inset presents a zoom-in (Obj. x20, scale bar 20  $\mu\text{m}$ ) of the highlighted yellow region of c): a fingerprint pattern is clearly visible.

A similar behaviour made of two possible reorientations is observed with CNC suspensions in MMA, presented in Figure 154. Conducting the same experiment as in toluene with an uncontrolled droplet volume of 10-20  $\mu\text{L}$  from a 25 wt.% CNC-surfactant suspension in MMA containing also 10 wt.% TMPTA (crosslinker) and 0.5 wt.% Irgacure (initiator), a clear maltese cross pattern under cross polarisers is observed 1 day after deposition, corresponding to radial domain reorientation. However, whenever the volume of deposited droplets is reduced down to 0.5  $\mu\text{L}$  while keeping all other experimental parameters unchanged, homeotropic reorientation of cholesteric domains is observed. Variations in droplet volume appear to trigger the change in reorientation behaviour in both systems.

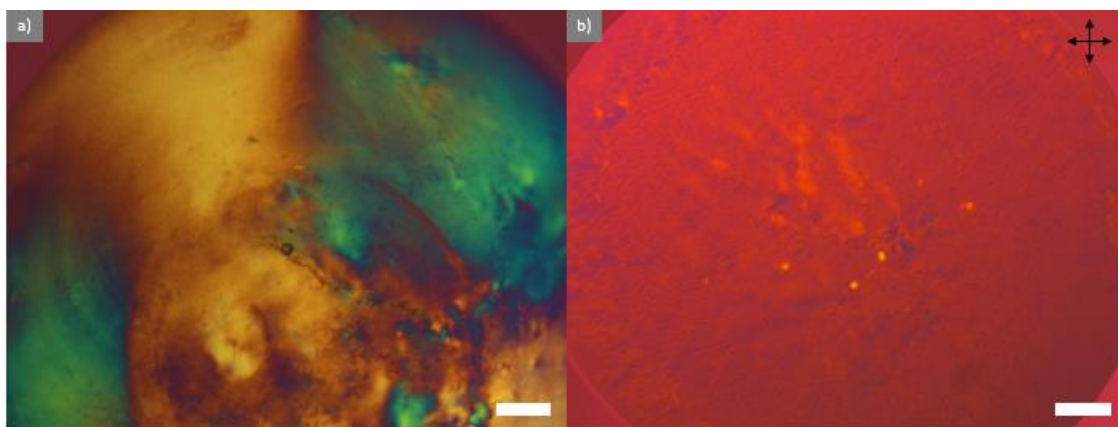


Figure 154 : Polarised optical microscopy images of sessile droplets under cross polars and quarter wave plate containing 25 wt.% CNC-surfactant, 10 wt.% TMPTA and 0.5 wt.% Irgacure 819 in MMA after 24 hours. a) Droplet volume of 10-20  $\mu\text{L}$  shows a maltese cross pattern characteristic of radial reorientation. b) Droplet volume of 0.5  $\mu\text{L}$  shows a homeotropic texture characteristic of vertical cholesteric domain reorientation. Scale bars are 200  $\mu\text{m}$ .

This can be surprising since anchoring reorientation is expected to follow the droplet local curvature, as already discussed in the state of the art. Assuming a sessile droplet with a spherical cap and a given contact angle, the local curvature is expected to be inversely proportional to the droplet dimensions. A smaller volume should then cause higher curvature and a radial reorientation while bigger droplets should favour lower curvature and vertical helical orientation. The opposite trend is observed.

The explanation of this peculiar observation may be found in the shape of the droplets. Using data of Figure 154 on the example of MMA droplets, one can measure a droplet diameter of about 2 mm for a total deposited volume of 0.5  $\mu\text{L}$ . Assuming spherical cap for the droplet, the droplet height can be calculated at  $h = 310 \mu\text{m}$  corresponding to a contact angle of  $\theta = 34^\circ$ . This is indeed a flat droplet as reproduced in Figure 155. For the uncontrolled droplet volume, the diameter of the droplet is measured to be 2.3 mm. Without a precise value of the volume or of the contact angle, one cannot retrieve the precise height of the droplet. The only thing one can tell for sure is that the actual droplet volume is smaller than 6.4  $\mu\text{L}$ , which corresponds to a perfectly round shaped droplet ( $\theta = 180^\circ$ ). A more thorough characterisation would help confirming that the shape of the droplets is indeed responsible for the different cholesteric domains orientation observed. SEM cross-section or contact angle characterisation of the corresponding droplets would also assess how spherical the droplets cap is.

The difference in contact angle between the large and the small droplets is ascribed to the deposition method. The smaller droplets ( $V = 0.5 \mu\text{L}$ ) were deposited using a pipette of 2  $\mu\text{L}$  total capacity with pipette tips of nozzle diameter *ca.* 0.5 mm (20  $\mu\text{L}$  total capacity), whereas



the larger ones ( $V = 10 - 20 \mu\text{L}$ ) were deposited using a pipette of 1 mL total capacity with pipette tips of nozzle diameter *ca.* 1 mm (1 mL total capacity). The nozzle dimensions being of similar range, it is likely that it dictated the surface area of the substrate wet by the suspension and therefore the initial height of the droplet, since FC-40 is non-wetting on most surfaces. It looks like this initial droplet shape has been conserved over time, rather than relax in its thermodynamically favoured state described in the state of the art, however we did not measure the advancing and receding angles of toluene CNC suspensions in FC-40 to confirm this hypothesis. The presence of free surfactant in suspension likely to adsorb on interfaces may also participate in stabilising the observed droplet shapes.

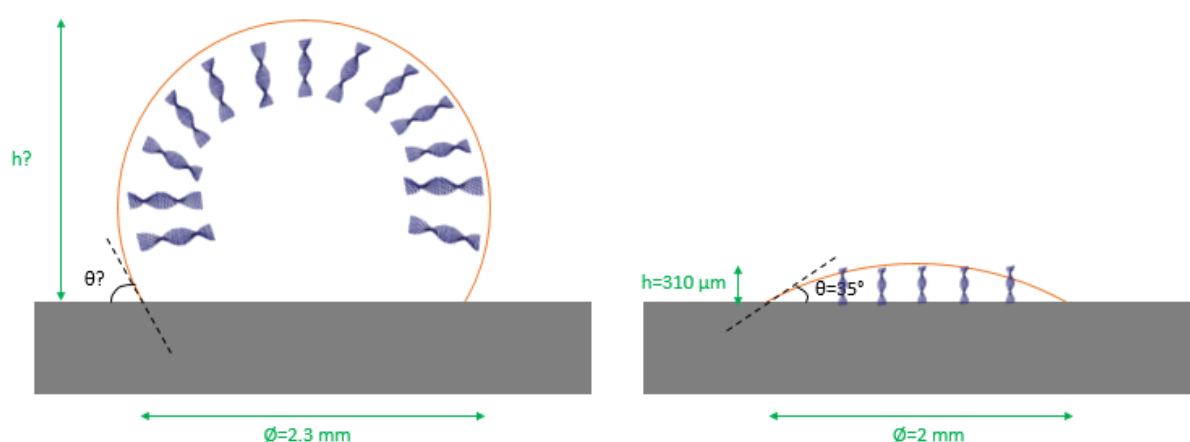


Figure 155 : Schematic view of the likely droplet shape and cholesteric domain orientation resulting from image analysis of Figure 154. (left) Radial domain orientation in large droplets. (right) Vertical domain orientation in small droplets.

### 6.2.2.3. Final drying step and coffee-ring effects

Once favourable anchoring allowed for successful vertical reorientation of the cholesteric domains, the sample is in optimal configuration to produce a uniform structure from further drying. In this work, this final drying step has been performed by opening the samples to open air under a fume cupboard while keeping the FC-40 intermediate layer above the suspension droplets. The precise duration of this final drying step has been found to vary with the amount of solvent left in the vial after solvent removal by pipetting, making on-demand photopolymerisation in MMA samples particularly difficult. An average drying time is thought to be between 10 minutes and 1 hour. Toluene samples have typically been left to dry for minimum one day to ensure complete drying before characterisation.

A majority of the toluene samples present a donut-like deposit as shown in Figure 156 when completely dry, suggesting that a pure coffee-ring effect took place. MMA samples typically

show a crack in the centre of the film which is attributed to TMPTA increasing the viscosity of the MMA suspension, thus modifying how coffee-ring takes place in the droplets. In some samples, accumulation of deposit at the edge is also clearly visible, similarly to the profile Zhao et al describe when drying in ambient conditions (Zhao et al. 2019). Some of the samples also do not present any visible evidence of coffee-ring effects under the microscope.

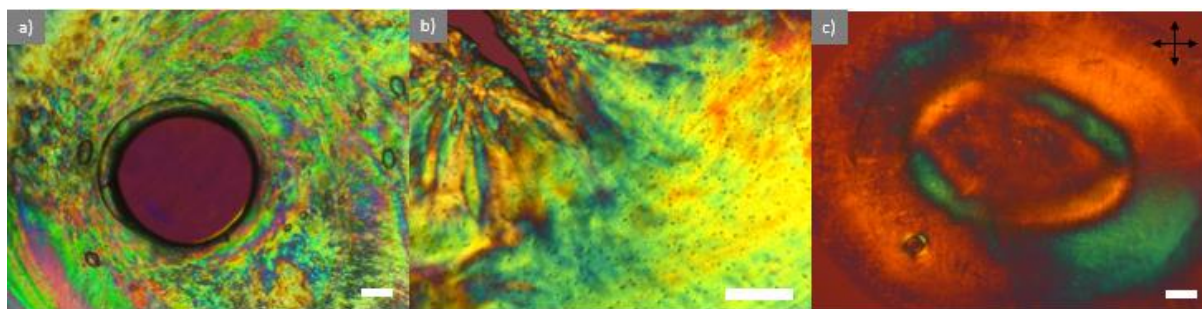


*Figure 156 :Polarised optical microscopy images of coffee-ring effects in dried droplets from a) toluene suspensions and b-c) MMA suspensions. a) presents donut-like shape, b) present a crack in the centre and c) presents an accumulation of deposit. a) and c) Objx5, b) Objx10. All scale bars correspond to 200  $\mu\text{m}$ .*

In isotropic toluene samples, this final drying step has been observed to induce radial nucleation of helices as already presented in Figure 151, possibly corresponding to the nucleation of domains in the preferred direction of orientation induced by the curved suspension/FC40 interface. In anisotropic non-reoriented samples, no significant modification of the orientation of cholesteric domains over the course of the drying has been observed. In anisotropic radially oriented samples, the uniform domain orientation is sometimes hampered by the final drying in the immediate vicinity of the centre of the droplet due to harsh coffee-ring effects, but is largely conserved elsewhere as presented in Figure 157. In anisotropic vertically oriented samples, the cholesteric orientation is observed to be slightly modified especially near the edge of the droplet, as observed in Figure 158.



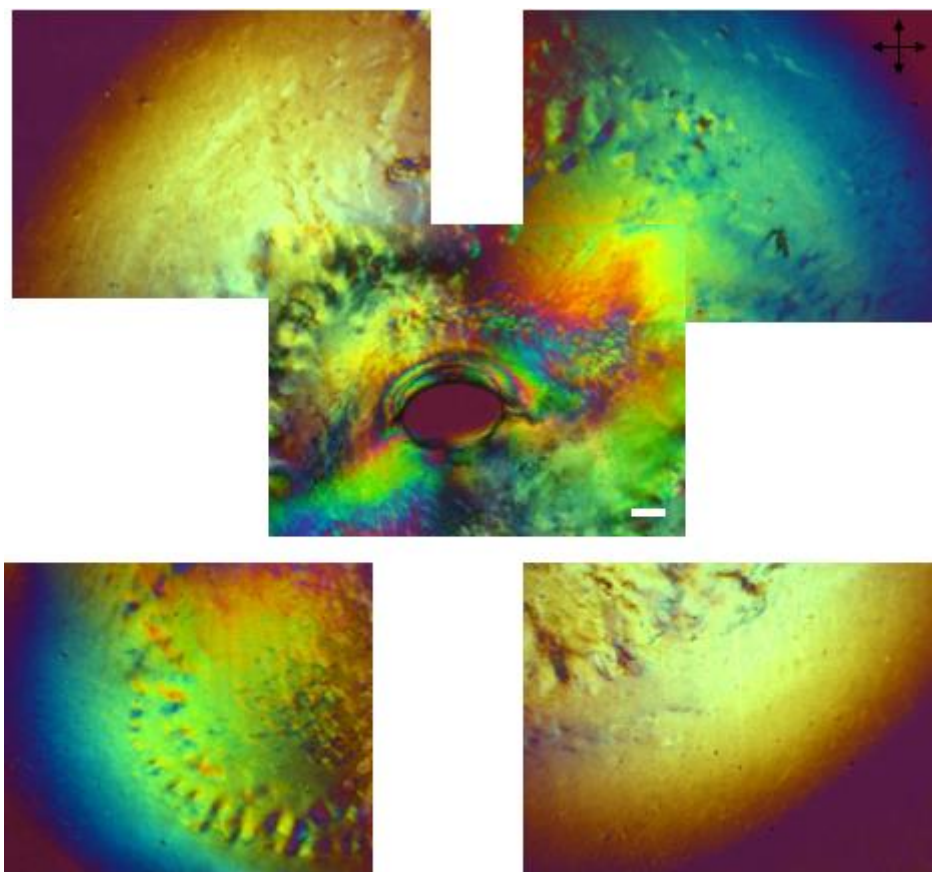


Figure 157 : Reconstitution of the polarised optical microscopy pattern of a large dried droplet from a CNC suspension in toluene at 23 wt.% that has observed radial domain reorientation for 4 days before undergoing a fast drying. Images on the top are continuous, images at the bottom are discontinuous. Cholesteric domain orientation on the edge has been conserved whereas domain orientation has been messed up in the centre of the droplet. Obj. x5, scale bar is 200  $\mu\text{m}$  for all images.

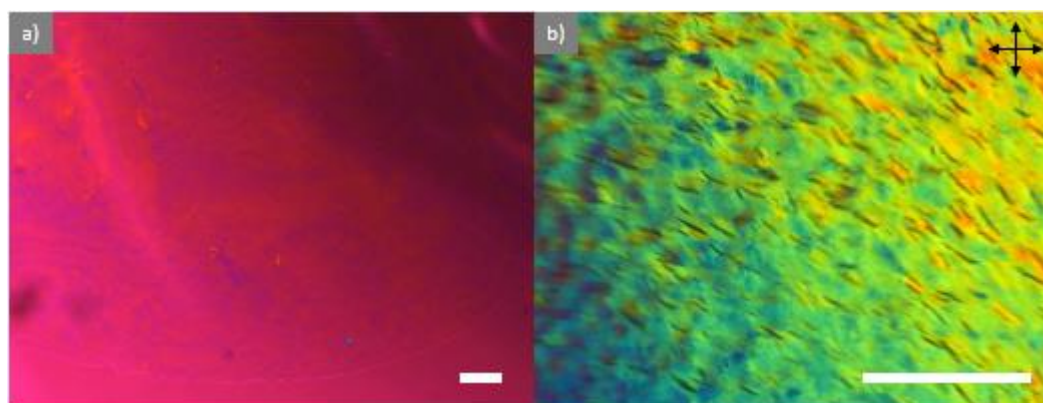


Figure 158 : Polarised optical microscopy patterns of a droplet of CNC suspension at 23 wt.% a) after 2 days of vertical reorientation and b) after the following fast drying. Domain orientation has been modified by the drying process. a) Obj x5 b) Objx20. Scale bars are 200  $\mu\text{m}$ .

#### 6.2.2.4. Iridescence in reflection

CNC films were produced by drying CNC suspensions in toluene. Several films displaying radially reoriented domains displayed a relatively faint iridescence in reflection, as shown in

Figure 159. The colour captured in different sample areas by reflection microscopy in bright field mostly corresponds to red, yellow and green colour. Blue is barely visible. The reflected colour is highly heterogeneous and corresponds to pitch values in the range of 320-500 nm according to the Bragg reflection condition at normal incidence  $\lambda = n \cdot p$ .

The characterisation of the dried iridescent droplets by polarised optical microscopy, provided in Figure 157, directly corresponds to regions described in Figure 159b1). The fast drying has induced coffee-ring effects, which have mainly disrupted the domain orientation in the centre of the droplet. The brightest iridescent response is observed close to the centre of the droplet, in regions that have been slightly impacted by coffee-ring effects whereas regions located at the edge, clearly showing radial symmetry orientation, do not scatter light in the visible. By contrast, the drying of vertically reoriented cholesteric domains from toluene suspensions of Figure 153b) and c) do not yield visible iridescence. However, if the dried droplets are swollen by a drop of toluene, faint iridescence is observed. The process is not fully reversible and toluene destroys the film structure after a few swelling cycles.

According to the state of the art (Frka-Petesic et al. 2019), a radial alignment of the cholesteric domains should lead to inefficient helices compression as well as polydispersity in pitch especially near the edges where a redshift is expected. Polydispersity in pitch is observed according to the highly heterogeneous colour reflected by the film, and the most tilted cholesteric domains near the edges are redshifted out of the visible. Non-tilted cholesteric domains leading to non-visible iridescent reflection that becomes visible upon swelling is also consistent with this result. In aqueous systems, swelling by water has been reported to increase the pitch value, therefore redshifting the reflected colour (Zhao et al. 2019).

These results therefore indirectly suggest that CNC films dried out of organic solvents with vertically aligned domains could have pitches corresponding to the reflection of UV light, although a more thorough characterisation is needed to proof-check this assessment. SEM cross-section of the droplets would be especially useful to assess the quality of helical orientations and pitch values inside the dried droplets.

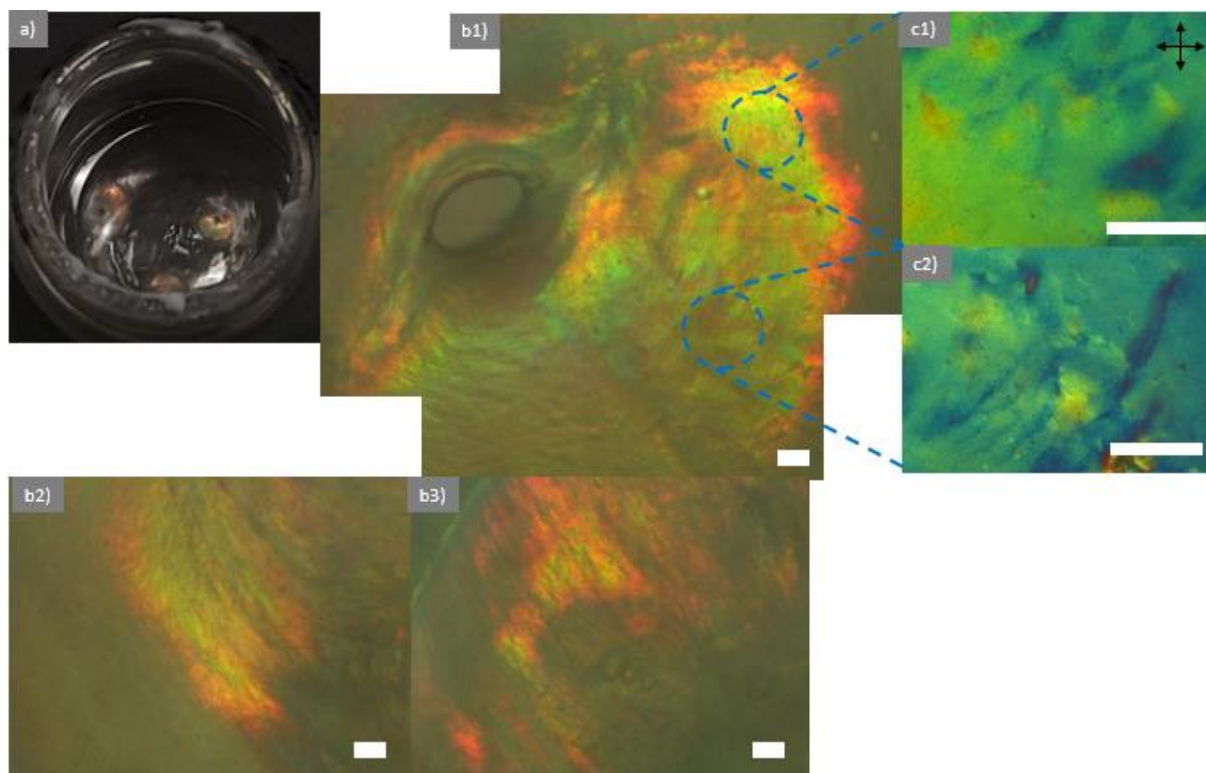


Figure 159 : Iridescence in reflection of dried droplets produced from casting CNC suspension at 23 wt.% in toluene, with an annealing time of 4 days followed by a final fast drying. a) Macroscopic iridescence in reflection in the vial. b) Reflection microscopy of different iridescent droplet patterns (Obj. x5, no polarisers). c) Polarised optical microscopy patterns of the circled iridescent regions presented in b1 (Obj. x20, cross polarisers). Scale bars correspond to 200  $\mu\text{m}$ .

#### 6.2.2.5. Polymerisation of the sample before complete drying

Switching solvent from toluene to MMA monomers enables the polymerisation of the suspension into a solid film at any step of the drying process, increasing its versatility. Polymerisation is performed in a very similar way to the one described in chapter 5, using a PMMA matrix cross-linked by TMPTA (10 wt.%) and initiated by Irgacure (0.5 wt.%). The polymerisation process is fast: kinetic arrest is estimated to occur within the first 5 minutes of UV exposure. This short polymerisation time enables an on-demand lock-in of the sample state.

Initially, we intended to control the domain orientation as in toluene samples and monitor the evolution of the optical response during the final drying step to lock the structure whenever reflection of visible light appears. However, the iridescent optical response of anisotropic MMA suspensions before polymerisation was found to fade very quickly with increasing thickness: reflection was barely visible in 0.5  $\mu\text{L}$  droplets and could not be observed in 10-20  $\mu\text{L}$  droplets. This optical response decay comes from the high scattering of CNCs in MMA, due to the large refractive index contrast between MMA ( $n = 1.41$ ) and cellulose ( $n = 1.55$ ), as shown in

Figure 160. Polymerisation of MMA into PMMA increases the refractive index ( $n_{\text{PMMA}} = 1.49$ ), which results in the reappearance of a reflection peak in the sample, ascribed to the smaller optical index contrast and thus weaker incoherent scattering. Since polymerisation is triggered before the optical response is revealed, the experimenter unfortunately cannot assess the state of the drying process.



*Figure 160 : Optical appearance of (left) an anisotropic suspension of CNCs in MMA and (right) drying droplets of this suspension under FC-40.*

Alternatively, we chose to prepare a series of samples in the same conditions and polymerise them at staggered drying times to retrieve snapshots of what happens at different moments of the drying process, as shown in Figure 161. Samples were first annealed by maintaining them immersed for 11 hours in FC-40 saturated with MMA, then partially evaporated by exposing them to ambient air for various durations noted  $t_{\text{evap}}$  (0 min, 11 min, 20 min, 1 hour, 2 hours, 4 hours and 1 day), and finally UV-polymerised for 1 hour. While the control sample ( $t_{\text{evap}} = 0$  min) displays structural colour in transmission after polymerisation as in CNC suspensions discussed before, samples dried for 11 min, 20 min and 1 hour display structural colour in reflection after polymerisation, but also imperfect radial cholesteric orientation presented in Figure 162 as a consequence of the annealing and drying steps. Samples dried for 2, 4 and 24 hours did not display any structural colour in reflection. It is worth nothing that their cholesteric domain orientation seems to have taken place to a lesser extent according to the polarised optical microscopy characterisation presented in Figure 162. Iridescent samples mostly reflect green and red, similarly to films made from CNC suspensions in toluene. The polychromaticity in reflection is slightly higher for MMA suspensions, possibly due to a less efficient alignment of the cholesteric domains in the vertical direction.



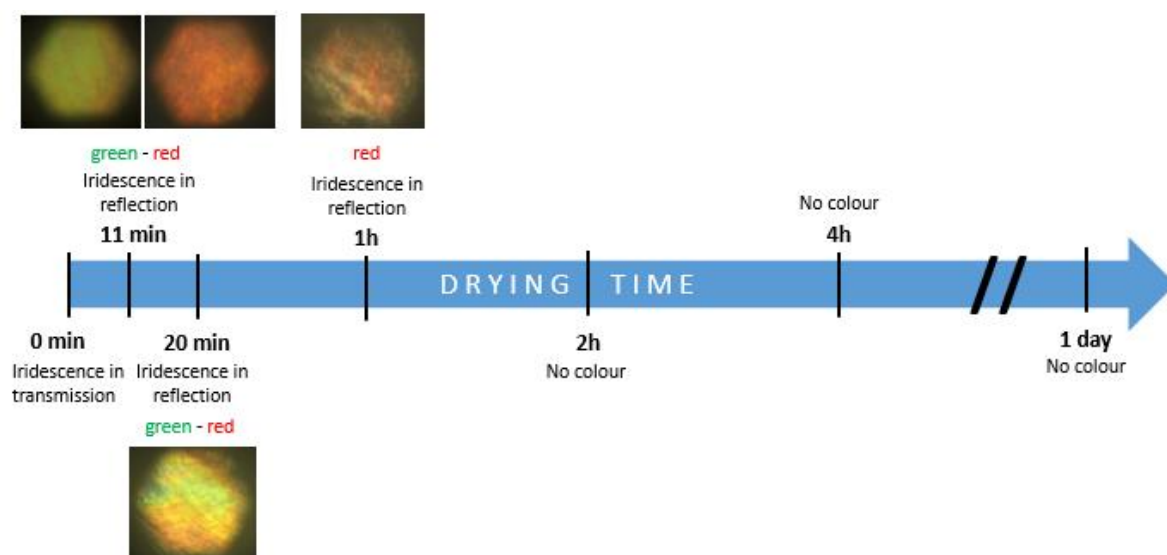


Figure 161 : Iridescent response captured by reflection microscopy (referenced against white diffuser) of the dried and polymerised droplets of CNCs at 25 wt.% in MMA (TMPTA 10 wt.%, Irgacure 0.5 wt.%) as a function of the drying time.

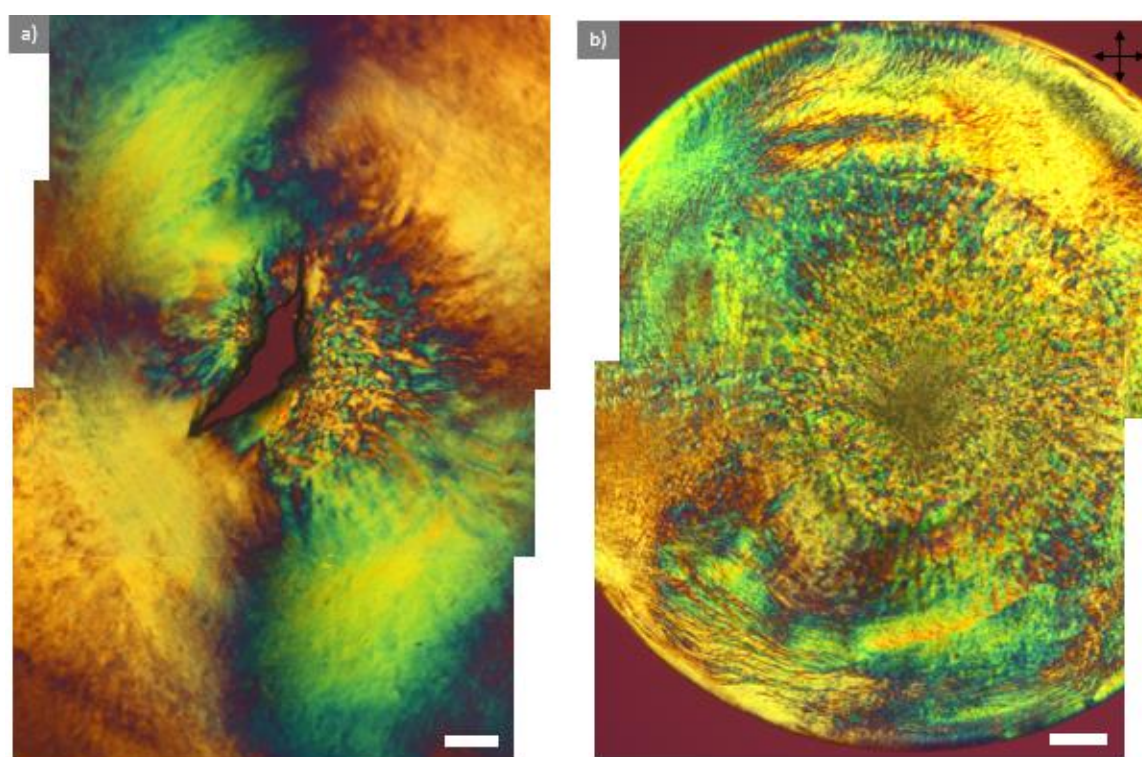


Figure 162 : Polarised optical microscopy reconstituted images of polymerised droplets of suspensions of CNCs in MMA (TMPTA 10 wt.%, Irgacure 0.5 wt.%) after being reoriented for 11 hours and dried for a) 11 min and b) 4 hours.

#### 6.2.2.6. Characterisation of the reflected iridescence

Optical characterisation of the reflected iridescence has been performed by coupling a spectrometer with an optical fibre mounted on the reflection microscope and conjugated with

the sample plane in a small region of the viewing field of view. The reference was taken both against a white diffuser and a silver mirror, since the optimal choice depends on the type of the optical response (rather scattering or metallic). A limitation to the measurement is the presence of an IR filter mounted on the microscope that cut the optical signal above 700 nm. The sample dried from MMA suspensions for 11 min before being polymerised presents the brightest iridescence by eye and is discussed below.

From the reflection peaks normalised against a white diffuser, as shown in Figure 163, the reflection peak appears quite broad, with a full width at half maximum (FWHM) spanning over 150 nm in the green area and more than 200 nm in the multicolour area. It suggests an important variation of pitch values that is expected from literature works (Frka-Petescic et al. 2019) on the compression of radially oriented cholesteric domains. From scanning different areas of the sample, reflection peaks ranging from 500 to 800 nm are observed, in good agreement with the observed green, yellow and red colour.

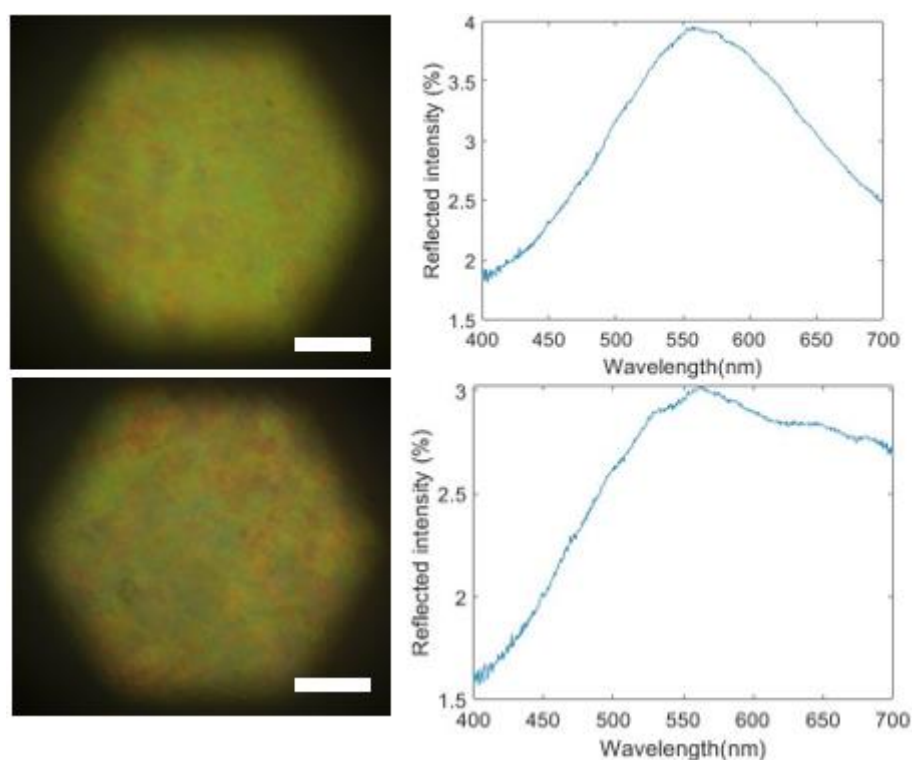


Figure 163 : Qualitative iridescent optical response of MMA dryings by coupled reflection microscopy and spectroscopy (unpolarised light) against a white diffuser reference of (top) a green region with its corresponding spectrum and (bottom) a multi-colour region with its corresponding spectrum. Spectra are cut at 700 nm due to the presence of an IR filter mounted on the microscope; the multi-colour spectrum likely present a significant reflection above 700 nm. Scale bars correspond to 100  $\mu\text{m}$ .

Using the mirror as reference, the reflected spectrum can be quantitatively expressed as a percentage of the incoming light. The signal is measured through a layer of glass back and forth

corresponding to the bottom of the vial. The signal of the empty glass vial is then measured and subtracted from the original data. The signal obtained is therefore:

$$reflected\ intensity = \frac{signal_{vial+film} - background}{reference - background} - \frac{signal_{empty\ vial} - background}{reference - background}$$

The result is plotted for a green and multicolour sample areas in Figure 164. In both areas, about 5% of the incoming light is reflected by the dried film with an error of approximately 1%, probably mainly coming from the subtraction of the glass layer. Spanning across different sample areas, the reflected intensity is relatively constant around this value, corresponding to weakly reflecting multi-layer films in good agreement with the faint colour observed macroscopically.

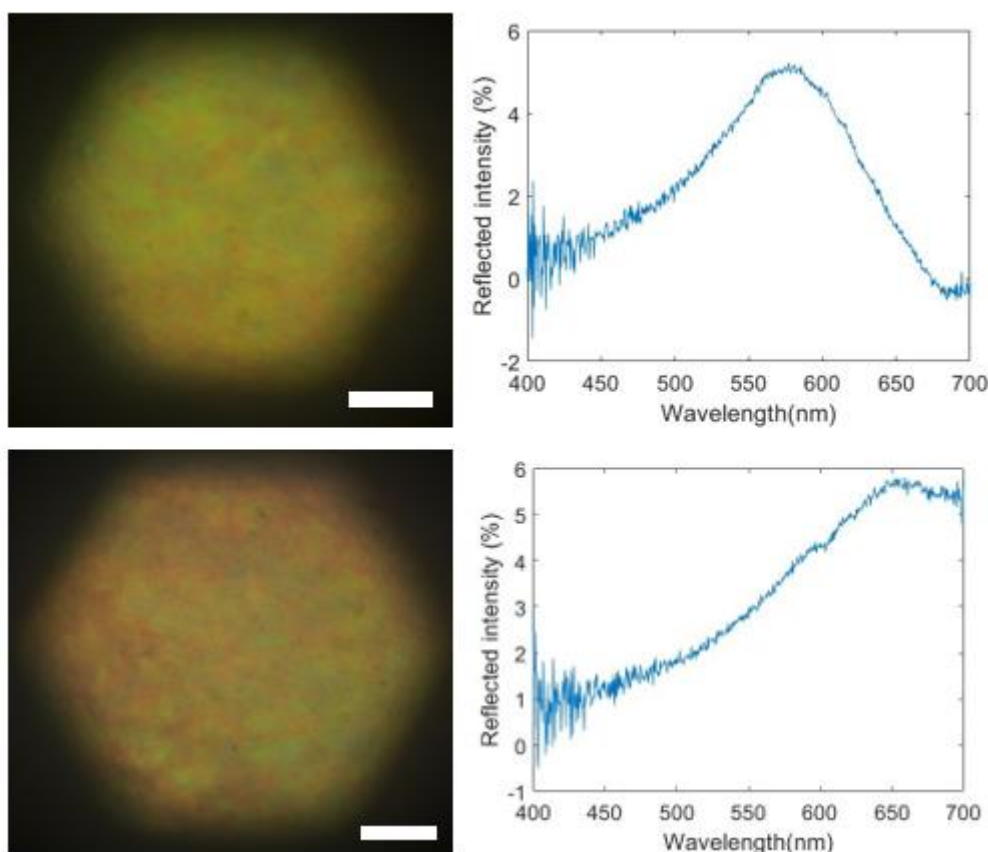


Figure 164 : Quantitative iridescent optical response of MMA dryings by reflection microscopy coupled with spectroscopy (unpolarised light) using a mirror reference of a green region with its corresponding spectrum (top) and a multi-colour region with its corresponding spectrum. Reflected intensity in Y axis is directly expressed as a percentage of the incoming light. Spectra are cut at 700 nm due to the presence of an IR filter mounted on the microscope that probably cuts the multi-colour signal.



### 6.2.3. Conclusions

In this chapter, an exploratory study on the drying of CNC films out of suspensions dispersed in organic apolar solvents on the example of toluene and MMA has been conducted. It has largely inspired from the acquired knowledge and experimental practices of aqueous systems that highlights the importance of reorienting cholesteric domains in the direction of compression before kinetic arrest takes place through interface anchoring or magnetic field alignment and provides several tools to counteract the coffee-ring effect in drying sessile droplets. Adaptations to the experimental setup have been necessary to deal with the specificities of organic solvents, leading to an intermediate layer of fluorinated oil that proved to require solvent saturation to efficiently play its role. Similarly to reported observations in aqueous CNC suspensions, cast suspensions of CNCs in apolar solvents worked best when their initial concentration spanned from the end of the isotropic domain to the first half of the biphasic domain in order to develop cholesteric helices while preserving their mobility inside the droplets. Using a closed system with an intermediate layer of fluorinated solvent saturated with the solvent (toluene or MMA), we enabled the interruption of solvent evaporation for a controlled duration, which effectively allowed for a controlled annealing of the cholesteric structure during which cholesteric domains can reorient. In toluene and MMA, both radial and vertical domain reorientation have been observed and found to depend on the deposition volume or, more fundamentally, on sessile droplet shape and wetting configuration: vertical domain reorientation has been observed for small deposition volumes whereas radial domains reorientation has been observed for large deposition volumes. The similar pipette tip nozzle diameter for both deposition volumes is thought to be responsible for the observed droplets shape.

Coffee-ring effect in drying droplets have proved to induce non-negligible domain orientation disruption over the course of the drying. While this work has not focused specifically on counteracting this effect, we have seen that slow-drying was not an option because of the higher evaporation rate of toluene and MMA compared to water. The vial had to be sealed and saturated to stop the fast evaporation of organic solvents. The addition of a rheology modifier is thought to be what reduces coffee-ring effects in MMA systems compared to toluene ones through the viscosity increase provided by TMPTA.

Iridescence in reflection has been observed from the drying of radially reoriented domains in both toluene and MMA systems. Reflection microscopy provided precise information on the

optical response of these samples: reflection peaks span from 500 to at least 700 nm corresponding to the observation of green, yellow and red colours. In the example of MMA samples, optical spectroscopic characterisation has been performed. The optical response consisted of broad peaks of 150-200 nm in width, corresponding to the reflection of about 5% of the incoming light, indicating poor cholesteric organisation along with a polydispersity in the pitch values in the sample. From an optical point of view, these multi-layer reflectors show rather low quality. Noteworthy, it has not been possible to yield visible structural colour out of the drying of vertically aligned domains in toluene and MMA in this work. According to literature, such a drying should present increased pitch compression and homogeneity, corresponding to a strengthened optical response in the samples at lower wavelengths. Pitches corresponding to near-UV reflections are suggested by the observation of visible iridescence from the solvent swelling of a dried droplet.

On a more general note, this work suffers from insufficient characterisation. While a likely scenario has been developed accounting for all experimental results, precise characterisation of the droplet profiles and microstructure of the final films are missing to confirm this results, via *e.g.* contact angle characterisation and/or SEM cross-section images. The on-demand polymerisation provided by the MMA system appears promising to yield CNC-polymer composite films displaying structural colour in reflection with significant polymer content, but important information is lacking such as the pitch value resulting from the drying of vertical domains and the polymer content in polymerised dryings.



## **General conclusion**

In this work, we have found a new surfactant molecule able to disperse CNCs in toluene and styrene but not in MMA, bringing additional insights on what could be a suitable surfactant molecule in this process. We investigated the origin of gelation effects in these systems, identifying the loosely attractive colloidal interactions as being responsible for the viscosity increase over time. Dispersing CNCs in low permittivity solvents allowed to perform an extensive study of the alignment of cholesteric CNCs under electric and magnetic fields. We show that electric field alignment of CNCs leads in fact to a plane of possible cholesteric domains orientation conversely to magnetic field alignment that align domains in a unique direction. This feature of the electric field alignment appeared as a limitation on the quality of the optical response, especially noticeable at high thicknesses and in composite materials. The threshold for cholesteric domains alignment in weak magnetic fields is found to be between 0.5 and 0.65 T, yielding already excellent alignment qualities at 0.65 T corresponding to an order parameter of  $S_2 = 0.96$  when the anisotropic phase is grown under field. Electric field domain orientation also yields excellent anti-alignment quality, corresponding to an order parameter of  $S_2 = -0.44$  with respect to a direction perpendicular to the electric field. Alignment experiments with electric and magnetic fields together show the dominance of the electric field alignment incentive over the magnetic field one.

In parallel, working on the chemical composition of two polymer matrices, PS and PMMA, allowed to retain cholesteric CNC assemblies in composite materials with no visible deformation of the fillers organisation. After overcoming several issues affecting the transparency of the polymer matrices, an iridescent optical response is observed in PMMA-CNC composites. Re-using our knowledge on the field alignment of cholesteric CNCs, we proved the alignment of cholesteric CNC fillers under electric and magnetic fields in PS and PMMA composites using laser diffraction, scanning electron microscopy and polarised optical microscopy cross-characterisation, away from a skin layer close to the surface of the material where anchoring dominates. The alignment of cholesteric domains leads to the recovery of the iridescent optical response in PS composites and a strengthened optical response in PMMA composites. Precise characterisation of the iridescent optical response of the composites has been performed using angular-resolved optical spectroscopy. By choosing a particular configuration for the measurement, one is able to measure an average order parameter for the helices orientation of  $S_2 = 0.74$  on the example of a PMMA-CNC composite aligned under magnetic fields. The pitch is slightly lower in composites compared to suspensions and its polydispersity is not significantly modified.

While these composite materials show a conserved iridescent optical response, they are a bit underwhelming compared to the best optical responses of CNC materials in the literature and their pitch value of several microns still leads to light reflection at high angles of incidence. This issue has been tackled last by studying the drying of CNC suspensions in organic solvents and monomers. Several modifications to the experimental setup have been necessary to account for the specificities of the system. The reorientation of cholesteric domains has been observed to yield both radial and homeotropic orientations, likely depending on the shape of the droplet. Subsequent fast drying led to a faint iridescent optical response in reflection of approximately 10% of the incoming LCP light with radially reoriented samples. Vertically reoriented samples, which are thought to yield a better optical response on account of literature reports, only display iridescence upon swelling, which suggests UV reflection of light.

Considering the initial objectives of this work, the main goal of making iridescent polymer composite films with cholesteric CNC fillers has been attained with PS and PMMA. The field alignment of the cholesteric CNC fillers has been shown to work as well. This work proves the viability of optical quality composite material-making using sterically stabilised cholesteric CNCs in organic apolar solvents, which unveils a broad range of possibilities for future works. Optimisation of the optical response of the composites remain to be investigated in more detail. Our second approach of drying CNC suspensions in organic solvents showed some potential in yielding CNC films iridescent in reflection with significant non-cellulose content, but the experimental process is not totally mastered yet. A hybrid approach consisting of polymerising a composite with solvent content inside to be evaporated afterwards could be a potential successful approach to yield iridescent optical responses in reflection in composites. Finally, the versatility in the choice of the polymer matrix for the process opens up possibilities. Choosing a flexible polymer matrix could for example yield iridescent CNC-elastomers with interesting mechanochromic effects.

## References

*In alphabetical order*

- Albéric, Marie, Aurélien Gourrier, Wolfgang Wagermaier, Peter Fratzl, and Ina Reiche. 2018. 'The three-dimensional arrangement of the mineralized collagen fibers in elephant ivory and its relation to mechanical and optical properties', *Acta biomaterialia*, 72: 342-51.
- Almeida, Ana PC, João P Canejo, Susete N Fernandes, Coro Echeverria, Pedro L Almeida, and Maria H Godinho. 2018. 'Cellulose-based biomimetics and their applications', *Advanced Materials*, 30: 1703655.
- Anyfantakis, Manos, Zheng Geng, Mathieu Morel, Sergii Rudiuk, and Damien Baigl. 2015. 'Modulation of the coffee-ring effect in particle/surfactant mixtures: the importance of particle–interface interactions', *Langmuir*, 31: 4113-20.
- Araki, Jun, and Shigenori Kuga. 2001. 'Effect of trace electrolyte on liquid crystal type of cellulose microcrystals', *Langmuir*, 17: 4493-96.
- Araki, Jun, Masahisa Wada, and Shigenori Kuga. 2001. 'Steric stabilization of a cellulose microcrystal suspension by poly (ethylene glycol) grafting', *Langmuir*, 17: 21-27.
- Araki, Jun, Masahisa Wada, Shigenori Kuga, and Takeshi Okano. 1998. 'Flow properties of microcrystalline cellulose suspension prepared by acid treatment of native cellulose', *Colloids and Surfaces A: Physicochemical and Engineering Aspects*, 142: 75-82.
- Asakura, Sho, and Fumio Oosawa. 1954. 'On interaction between two bodies immersed in a solution of macromolecules', *The Journal of chemical physics*, 22: 1255-56.
- Astruc, J. 2014. "Les matériaux composites biomimétiques." In, edited by CERMAV.
- Battista, OA, Sydney Coppick, JA Howsmon, FF Morehead, and Wayne A Sisson. 1956. 'Level-off degree of polymerization', *Industrial & Engineering Chemistry*, 48: 333-35.
- Beck, Stephanie, and Jean Bouchard. 2014. 'Auto-catalyzed acidic desulfation of cellulose nanocrystals', *Nordic Pulp & Paper Research Journal*, 29: 6-14.
- Belamie, E, P Davidson, and MM Giraud-Guille. 2004. 'Structure and chirality of the nematic phase in  $\alpha$ -chitin suspensions', *The Journal of Physical Chemistry B*, 108: 14991-5000.
- Belyakov, VA, Vladimir E Dmitrienko, and VP Orlov. 1979. 'Optics of cholesteric liquid crystals', *Soviet Physics Uspekhi*, 22: 64.
- Berreman, DW, and TJ Scheffer. 1970. 'Bragg reflection of light from single-domain cholesteric liquid-crystal films', *Physical Review Letters*, 25: 577.
- Boluk, Yaman, Roya Lahiji, Liyan Zhao, and Mark T McDermott. 2011. 'Suspension viscosities and shape parameter of cellulose nanocrystals (CNC)', *Colloids and Surfaces A: Physicochemical and Engineering Aspects*, 377: 297-303.
- Bonini, Céline, Laurent Heux, Jean-Yves Cavallé, Peter Lindner, Charles Dewhurst, and Pierre Terech. 2002. 'Rodlike cellulose whiskers coated with surfactant: a small-angle neutron scattering characterization', *Langmuir*, 18: 3311-14.
- Boott, Charlotte E, Andy Tran, Wadood Y Hamad, and Mark J MacLachlan. 2020. 'Cellulose Nanocrystal Elastomers with Reversible Visible Color', *Angewandte Chemie International Edition*, 59: 226-31.
- Bordel, Damien, Jean-Luc Putaux, and Laurent Heux. 2006. 'Orientation of native cellulose in an electric field', *Langmuir*, 22: 4899-901.
- Brecher, Peter, John Chobanian, Donald M Small, and AV Chobanian. 1976. 'The use of phospholipid vesicles for in vitro studies on cholesteryl ester hydrolysis', *Journal of lipid research*, 17: 239-47.
- Brown Jr, R Malcolm. 1996. 'The biosynthesis of cellulose', *Journal of Macromolecular Science, Part A: Pure and Applied Chemistry*, 33: 1345-73.
- Bruckner, Johanna R, Anja Kuhnhold, Camila Honorato-Rios, Tanja Schilling, and Jan PF Lagerwall. 2016. 'Enhancing self-assembly in cellulose nanocrystal suspensions using high-permittivity solvents', *Langmuir*, 32: 9854-62.



- Camarero Espinosa, Sandra, Tobias Kuhnt, E Johan Foster, and Christoph Weder. 2013. 'Isolation of thermally stable cellulose nanocrystals by phosphoric acid hydrolysis', *Biomacromolecules*, 14: 1223-30.
- Cao, Yuanyuan, Lev Lewis, Wadood Y Hamad, and Mark J MacLachlan. 2019. 'Pressure-responsive hierarchical chiral photonic aerogels', *Advanced Materials*, 31: 1808186.
- Cao, Yuanyuan, Pei-Xi Wang, Francesco D'Acierno, Wadood Y Hamad, Carl A Michal, and Mark J MacLachlan. 2020. 'Tunable Diffraction Gratings from Biosourced Lyotropic Liquid Crystals', *Advanced Materials*.
- Carlmark, Anna, and Eva Malmström. 2002. 'Atom transfer radical polymerization from cellulose fibers at ambient temperature', *Journal of the American Chemical Society*, 124: 900-01.
- Chanzy, H. 1990. "Aspects of cellulose structure." In.
- Chen, Liheng, JY Zhu, Carlos Baez, Peter Kitin, and Thomas Elder. 2016. 'Highly thermal-stable and functional cellulose nanocrystals and nanofibrils produced using fully recyclable organic acids', *Green Chemistry*, 18: 3835-43.
- Chen, Pan, Yu Ogawa, Yoshiharu Nishiyama, Ahmed E Ismail, and Karim Mazeau. 2018. 'I $\alpha$  to I $\beta$  mechano-conversion and amorphization in native cellulose simulated by crystal bending', *Cellulose*, 25: 4345-55.
- Chen, Xianyi, Bo Gao, Jørgen Kops, and Walther Batsberg. 1998. 'Preparation of polystyrene-poly (ethylene glycol) diblock copolymer by 'living' free radical polymerisation', *Polymer*, 39: 911-15.
- Cheung, Clement CY, Michael Giese, Joel A Kelly, Wadood Y Hamad, and Mark J MacLachlan. 2013. 'Iridescent chiral nematic cellulose nanocrystal/polymer composites assembled in organic solvents', *ACS Macro Letters*, 2: 1016-20.
- Collman, JP, T Kodadeck, and JI Brauman. 1986. 'J Am Chem Soc 108: 2588 (b) Collman JP', *Brauman JI, Meunier B, Hayashi T, Kodadeck T, Raybuck SA (1985) J Am Chem Soc*, 107: 2000.
- Cowley, Alexandra Christina, NL Fuller, RP Rand, and VA Parsegian. 1978. 'Measurement of repulsive forces between charged phospholipid bilayers', *Biochemistry*, 17: 3163-68.
- Davankov, VA, and MP Tsyurupa. 1990. 'Structure and properties of hypercrosslinked polystyrene—the first representative of a new class of polymer networks', *Reactive Polymers*, 13: 27-42.
- De France, Kevin J, Kevin G Yager, Todd Hoare, and Emily D Cranston. 2016. 'Cooperative ordering and kinetics of cellulose nanocrystal alignment in a magnetic field', *Langmuir*, 32: 7564-71.
- De Gennes, PG. 1968. 'Calcul de la distorsion d'une structure cholesterique par un champ magnetique', *Solid State Communications*, 6: 163-65.
- De Gennes, Pierre-Gilles, and Jacques Prost. 1993. *The physics of liquid crystals* (Oxford university press).
- De Vries, Hill. 1951. 'Rotatory power and other optical properties of certain liquid crystals', *Acta Crystallographica*, 4: 219-26.
- Deegan, Robert D. 2000. 'Pattern formation in drying drops', *Physical Review E*, 61: 475.
- Deegan, Robert D, Olga Bakajin, Todd F Dupont, Greb Huber, Sidney R Nagel, and Thomas A Witten. 1997. 'Capillary flow as the cause of ring stains from dried liquid drops', *Nature*, 389: 827-29.
- Derjaguin, B, and L Landau. 1941. 'The theory of stability of highly charged lyophobic sols and coalescence of highly charged particles in electrolyte solutions', *Acta Physicochim. URSS*, 14: 58.
- Derjaguin, BV, and M Kussakov. 1939. 'Anomalous properties of thin polymolecular films', *Acta Physicochim. URSS*, 10: 25-44.
- Dinand, Elizabeth, Michel Vignon, Henri Chanzy, and Laurent Heux. 2002. 'Mercerization of primary wall cellulose and its implication for the conversion of cellulose I  $\rightarrow$  cellulose II', *Cellulose*, 9: 7-18.
- Dong, Xue Min, and Derek G Gray. 1997. 'Effect of counterions on ordered phase formation in suspensions of charged rodlike cellulose crystallites', *Langmuir*, 13: 2404-09.

- Dong, Xue Min, Tsunehisa Kimura, Jean-François Revol, and Derek G Gray. 1996. 'Effects of ionic strength on the isotropic– chiral nematic phase transition of suspensions of cellulose crystallites', *Langmuir*, 12: 2076-82.
- Dorris, Annie, and Derek G Gray. 2012. 'Gelation of cellulose nanocrystal suspensions in glycerol', *Cellulose*, 19: 687-94.
- Dreher, R, and G Meier. 1973. 'Optical properties of cholesteric liquid crystals', *Physical Review A*, 8: 1616.
- Earl, William L, and D-L\_ VanderHart. 1980. 'High resolution, magic angle sampling spinning carbon-13 NMR of solid cellulose I', *Journal of the American Chemical Society*, 102: 3251-52.
- Elazzouzi-Hafraoui, Samira, Yoshiharu Nishiyama, Jean-Luc Putaux, Laurent Heux, Frédéric Dubreuil, and Cyrille Rochas. 2008. 'The shape and size distribution of crystalline nanoparticles prepared by acid hydrolysis of native cellulose', *Biomacromolecules*, 9: 57-65.
- Elazzouzi-Hafraoui, Samira, Jean-Luc Putaux, and Laurent Heux. 2009. 'Self-assembling and chiral nematic properties of organophilic cellulose nanocrystals', *The Journal of Physical Chemistry B*, 113: 11069-75.
- Elazzouzi, Samira. 2006. 'Auto-organisation de whiskers de cellulose en suspension dans l'eau ou dans les solvants organiques apolaires'.
- Epstein, Benjamin. 1947. 'The mathematical description of certain breakage mechanisms leading to the logarithmico-normal distribution', *Journal of the Franklin Institute*, 244: 471-77.
- Espinha, André, Giulia Guidetti, María C Serrano, Bruno Frka-Petesic, Ahu Gümrah Dumanli, Wadood Y Hamad, Álvaro Blanco, Cefe López, and Silvia Vignolini. 2016. 'Shape memory cellulose-based photonic reflectors', *ACS Applied Materials & Interfaces*, 8: 31935-40.
- Evans, R, and D-H\_ Napper. 1973. 'Steric stabilization II', *Kolloid-Zeitschrift und Zeitschrift für Polymere*, 251: 329-36.
- Favier, V, H Chanzy, and JrY Cavaillé. 1995. 'Polymer nanocomposites reinforced by cellulose whiskers', *Macromolecules*, 28: 6365-67.
- Felix, Johan M, Paul Gatenholm, and HP Schreiber. 1993. 'Controlled interactions in cellulose-polymer composites. 1: Effect on mechanical properties', *Polymer Composites*, 14: 449-57.
- Feng, Kai, Xiaobin Gao, Zehao Gu, and Zhaoxia Jin. 2019. 'Improving homogeneity of iridescent cellulose nanocrystal films by surfactant-assisted spreading self-assembly', *ACS Sustainable Chemistry & Engineering*, 7: 19062-71.
- Ferguson, James L. 1966. 'Cholesteric structure-1 optical properties', *Molecular Crystals and Liquid Crystals*, 1: 293-307.
- Findenegg, GH. 1986. 'JN Israelachvili: Intermolecular and Surface Forces (With Applications to Colloidal and Biological Systems). Academic Press, London, Orlando, San Diego, New York, Toronto, Montreal, Sydney, Tokyo 1985. 296 Seiten, Preis: \$65.00', *Berichte der Bunsengesellschaft für physikalische Chemie*, 90: 1241-42.
- Fink, Hans-Peter, Burkart Philipp, Dieter Paul, Ritva Serimaa, and Timo Paakkari. 1987. 'The structure of amorphous cellulose as revealed by wide-angle X-ray scattering', *Polymer*, 28: 1265-70.
- Foster, E Johan, Robert J Moon, Umesh P Agarwal, Michael J Bortner, Julien Bras, Sandra Camarero-Espinosa, Kathleen J Chan, Martin JD Clift, Emily D Cranston, and Stephen J Eichhorn. 2018. 'Current characterization methods for cellulose nanomaterials', *Chemical Society Reviews*, 47: 2609-79.
- Fourier\_square. <https://mathworld.wolfram.com/FourierSeriesSquareWave.html>.
- François, Lequeux. 2008. 'Elastomères renforcés modèles: effet de la physico-chimie d'interface à structure constante sur les propriétés viscoélastiques', Paris 6.
- Frka-Petesic, Bruno. 2010. 'Agrégats de nanoparticules magnétiques auto-assemblées'.
- Frka-Petesic, Bruno, Bruno Jean, and Laurent Heux. 2014. 'First experimental evidence of a giant permanent electric-dipole moment in cellulose nanocrystals', *EPL (Europhysics Letters)*, 107: 28006.

- Frka-Petescic, Bruno, Gen Kamita, Giulia Guidetti, and Silvia Vignolini. 2019. 'Angular optical response of cellulose nanocrystal films explained by the distortion of the arrested suspension upon drying', *Physical Review Materials*, 3: 045601.
- Frka-Petescic, Bruno, Junji Sugiyama, Satoshi Kimura, Henri Chanzy, and Georg Maret. 2015. 'Negative diamagnetic anisotropy and birefringence of cellulose nanocrystals', *Macromolecules*, 48: 8844-57.
- Frka-Petescic, Bruno, Giulia Guidetti, Gen Kamita, and Silvia Vignolini. 2017. 'Controlling the photonic properties of cholesteric cellulose nanocrystal films with magnets', *Advanced Materials*, 29: 1701469.
- Frka-Petescic, Bruno, Harisoa Radavidson, Bruno Jean, and Laurent Heux. 2017. 'Dynamically controlled iridescence of cholesteric cellulose nanocrystal suspensions using electric fields', *Advanced Materials*, 29: 1606208.
- Fumagalli, Matthieu, Julien Berriot, Benoit de Gaudemaris, Anne Veyland, Jean-Luc Putaux, Sonia Molina-Boisseau, and Laurent Heux. 2018. 'Rubber materials from elastomers and nanocellulose powders: filler dispersion and mechanical reinforcement', *Soft Matter*, 14: 2638-48.
- Gençer, Alican, Christina Schütz, and Wim Thielemans. 2017. 'Influence of the particle concentration and marangoni flow on the formation of cellulose nanocrystal films', *Langmuir*, 33: 228-34.
- Giraud-Guille, Marie Madeleine, Gervaise Mosser, and Emmanuel Belamie. 2008. 'Liquid crystallinity in collagen systems in vitro and in vivo', *Current Opinion in Colloid & Interface Science*, 13: 303-13.
- Goerlitzer, ESA, and Klupp Taylor. 2018. 'RN; Vogel, N. Bioinspired photonic pigments from colloidal self-assembly', *Adv. Mater.*, 30: 1706654.
- Gray, Derek G. 2016. 'Recent advances in chiral nematic structure and iridescent color of cellulose nanocrystal films', *Nanomaterials*, 6: 213.
- Grelet, Eric, and Seth Fraden. 2003. 'What is the origin of chirality in the cholesteric phase of virus suspensions?', *Physical Review Letters*, 90: 198302.
- Guarín-Zapata, Nicolás, Juan Gomez, Nick Yaraghi, David Kisailus, and Pablo D Zavattieri. 2015. 'Shear wave filtering in naturally-occurring Bouligand structures', *Acta biomaterialia*, 23: 11-20.
- Guidetti, Giulia, Siham Atifi, Silvia Vignolini, and Wadood Y Hamad. 2016. 'Flexible photonic cellulose nanocrystal films', *Advanced Materials*, 28: 10042-47.
- Habibi, Youssef, Thomas Heim, and Roger Douillard. 2008. 'AC electric field-assisted assembly and alignment of cellulose nanocrystals', *Journal of Polymer Science Part B: Polymer Physics*, 46: 1430-36.
- Habibi, Youssef, Lucian A Lucia, and Orlando J Rojas. 2010. 'Cellulose nanocrystals: chemistry, self-assembly, and applications', *Chemical reviews*, 110: 3479-500.
- Heux, L, G Chauve, and C Bonini. 2000. 'Nonflocculating and chiral-nematic self-ordering of cellulose microcrystals suspensions in nonpolar solvents', *Langmuir*, 16: 8210-12.
- Hiemenz, Paul C. 1972. 'The role of van der Waals forces in surface and colloid chemistry', *Journal of Chemical Education*, 49: 164.
- Honorato-Rios, Camila, and Jan PF Lagerwall. 2020. 'Interrogating helical nanorod self-assembly with fractionated cellulose nanocrystal suspensions', *Communications Materials*, 1: 1-11.
- Hu, Zhen, Tyler Patten, Robert Pelton, and Emily D Cranston. 2015. 'Synergistic stabilization of emulsions and emulsion gels with water-soluble polymers and cellulose nanocrystals', *ACS Sustainable Chemistry & Engineering*, 3: 1023-31.
- Huang, Dafang, Jiayang Wu, Chaoji Chen, Xinxin Fu, Alexandra H Brozena, Yan Zhang, Ping Gu, Chen Li, Changsheng Yuan, and Haixiong Ge. 2019. 'Precision Imprinted Nanostructural Wood', *Advanced Materials*, 31: 1903270.
- Inhibitor\_remove.  
<https://www.sigmaaldrich.com/catalog/product/aldrich/306320?lang=en&region=GB>.
- Irgacure\_supplier\_data.  
[https://www.alibaba.com/product-detail/I-G-M-Omnirad-Former-Irgacure\\_60764058920.html](https://www.alibaba.com/product-detail/I-G-M-Omnirad-Former-Irgacure_60764058920.html).

- Jewell, SA. 2011. 'Living systems and liquid crystals', *Liquid Crystals*, 38: 1699-714.
- Kalashnikova, Irina, Hervé Bizot, Bernard Cathala, and Isabelle Capron. 2011. 'New Pickering emulsions stabilized by bacterial cellulose nanocrystals', *Langmuir*, 27: 7471-79.
- Kalidindi, Sanjay, Zoubeida Ounaies, and Hamid Kaddami. 2010. 'Toward the preparation of nanocomposites with oriented fillers: electric field-manipulation of cellulose whiskers in silicone oil', *Smart materials and structures*, 19: 094002.
- Kimura, F, and T Kimura. 2009. "Three-dimensional orientation of cellulose crystals under dynamic elliptic magnetic field." In *Journal of Physics: Conference Series*, 012002. IOP Publishing.
- Kimura, Fumiko, Tsunehisa Kimura, Moritaka Tamura, Asako Hirai, Masaya Ikuno, and Fumitaka Horii. 2005. 'Magnetic alignment of the chiral nematic phase of a cellulose microfibril suspension', *Langmuir*, 21: 2034-37.
- Kimura, Satoshi, Walairat Laosinchai, Takao Itoh, Xiaojiang Cui, C Randal Linder, and R Malcolm Brown. 1999. 'Immunogold labeling of rosette terminal cellulose-synthesizing complexes in the vascular plant *Vigna angularis*', *The Plant Cell*, 11: 2075-85.
- Kinoshita, S, Shinya Yoshioka, and J Miyazaki. 2008. 'Physics of structural colors', *Reports on Progress in Physics*, 71: 076401.
- Kose, Osamu, Charlotte E Boott, Wadood Y Hamad, and Mark J MacLachlan. 2019. 'Stimuli-responsive anisotropic materials based on unidirectional organization of cellulose nanocrystals in an elastomer', *Macromolecules*, 52: 5317-24.
- Kose, Osamu, Andy Tran, Lev Lewis, Wadood Y Hamad, and Mark J MacLachlan. 2019. 'Unwinding a spiral of cellulose nanocrystals for stimuli-responsive stretchable optics', *Nature communications*, 10: 1-7.
- Kostritskii, Andrei Yu, Dmitry A Tolmachev, Natalia V Lukasheva, and Andrey A Gurtovenko. 2017. 'Molecular-level insight into the interaction of phospholipid bilayers with cellulose', *Langmuir*, 33: 12793-803.
- Kruger, Kathleen, Klaus Tauer, Yusuf Yagci, and Norbert Moszner. 2011. 'Photoinitiated Bulk and Emulsion Polymerization of Styrene—Evidence for Photo-Controlled Radical Polymerization', *Macromolecules*, 44: 9539-49.
- Kvien, Ingvild, and Kristiina Oksman. 2007. 'Orientation of cellulose nanowhiskers in polyvinyl alcohol', *Applied Physics A*, 87: 641-43.
- Lamps\_details. [www.luzchem.com](http://www.luzchem.com), [www.hoenle.com](http://www.hoenle.com).
- Leforestier, Amilie, and F Livolant. 1993. 'Supramolecular ordering of DNA in the cholesteric liquid crystalline phase: an ultrastructural study', *Biophysical journal*, 65: 56-72.
- Legrand, Aurélie, and Corinne Soulié-Ziakovic. 2016. 'Silica–epoxy vitrimer nanocomposites', *Macromolecules*, 49: 5893-902.
- Lettinga, M Paul, Kyongok Kang, Peter Holmqvist, Arnout Imhof, Didi Derks, and Jan KG Dhont. 2006. 'Nematic-isotropic spinodal decomposition kinetics of rodlike viruses', *Physical Review E*, 73: 011412.
- Lettinga, M Paul, Kyongok Kang, Arnout Imhof, Didi Derks, and Jan KG Dhont. 2005. 'Kinetic pathways of the nematic–isotropic phase transition as studied by confocal microscopy on rod-like viruses', *Journal of Physics: Condensed Matter*, 17: S3609.
- Li, Tian, Yao Zhai, Shuaiming He, Wentao Gan, Zhiyuan Wei, Mohammad Heidarinejad, Daniel Dalgo, Ruiyu Mi, Xinpeng Zhao, and Jianwei Song. 2019. 'A radiative cooling structural material', *Science*, 364: 760-63.
- Li, Yuanyuan, Qiliang Fu, Shun Yu, Min Yan, and Lars Berglund. 2016. 'Optically transparent wood from a nanoporous cellulosic template: combining functional and structural performance', *Biomacromolecules*, 17: 1358-64.
- Lin, Fangbo, Fabrice Cousin, Jean-Luc Putaux, and Bruno Jean. 2019. 'Temperature-Controlled Star-Shaped Cellulose Nanocrystal Assemblies Resulting from Asymmetric Polymer Grafting', *ACS Macro Letters*, 8: 345-51.
- Lipatov, Yu S, AE Nesterov, TM Gritsenko, and RA Veselovskii. 1971. "Polymer chemistry handbook." In.: Naukova Dumka, Kiev.

- Ljungberg, N, C Bonini, F Bortolussi, C Boisson, L Heux, and Jean-Yves Cavaillé. 2005. 'New nanocomposite materials reinforced with cellulose whiskers in atactic polypropylene: effect of surface and dispersion characteristics', *Biomacromolecules*, 6: 2732-39.
- Louie, Brian M, Gregory M Carratt, and David S Soong. 1985. 'Modeling the free radical solution and bulk polymerization of methyl methacrylate', *Journal of applied polymer science*, 30: 3985-4012.
- Lydon, John. 2006. 'Microtubules: Nature's smartest mesogens—a liquid crystal model for cell division', *Liquid Crystals Today*, 15: 1-10.
- Mao, Yimin, Markus Bleuel, Yadong Lyu, Xin Zhang, Doug Henderson, Howard Wang, and Robert M Briber. 2018. 'Phase separation and stack alignment in aqueous cellulose nanocrystal suspension under weak magnetic field', *Langmuir*, 34: 8042-51.
- Meddeb, Amira Barhoumi, Inseok Chae, Aijie Han, Seong H Kim, and Zoubeida Ounaies. 2020. 'Magnetic field effects on cellulose nanocrystal ordering in a non-aqueous solvent', *Cellulose*, 27: 7901-10.
- Mitov, Michel. 2017. 'Cholesteric liquid crystals in living matter', *Soft Matter*, 13: 4176-209.
- Moad, Graeme, and David Henry Solomon. 2006. *The chemistry of radical polymerization* (Elsevier).
- Montesanti, Nicole. "Rapport de stage, Master Polymères et technologies avancées." In, edited by CERMAV.
- Morbidelli\_ETH\_Zürich\_course. [https://ethz.ch/content/dam/ethz/special-interest/chab/icb/morbidelli-dam/documents/Education/PRCE/DOC\\_2016/Chapter6.pdf](https://ethz.ch/content/dam/ethz/special-interest/chab/icb/morbidelli-dam/documents/Education/PRCE/DOC_2016/Chapter6.pdf).
- Moyroud, Edwige, Tobias Wenzel, Rox Middleton, Paula J Rudall, Hannah Banks, Alison Reed, Greg Mellers, Patrick Killoran, M Murphy Westwood, and Ullrich Steiner. 2017. 'Disorder in convergent floral nanostructures enhances signalling to bees', *Nature*, 550: 469-74.
- Natarajan, Bharath, and Jeffrey W Gilman. 2018. 'Bioinspired Bouligand cellulose nanocrystal composites: a review of mechanical properties', *Philosophical Transactions of the Royal Society A: Mathematical, Physical and Engineering Sciences*, 376: 20170050.
- Neville, AC, and S Caveney. 1969. 'Scarabaeid beetle exocuticle as an optical analogue of cholesteric liquid crystals', *Biological Reviews*, 44: 531-62.
- Nguyen, Thanh-Dinh, and Mark J MacLachlan. 2019. 'Double Twisted Photonic Honeycomb Frameworks with Mesoporous Structures', *Advanced Optical Materials*, 7: 1801275.
- Nickerson, RF, and JA Habrle. 1947. 'Cellulose intercrystalline structure', *Industrial & Engineering Chemistry*, 39: 1507-12.
- Nishiyama, Yoshiharu, Paul Langan, and Henri Chanzy. 2002. 'Crystal structure and hydrogen-bonding system in cellulose I $\beta$  from synchrotron X-ray and neutron fiber diffraction', *Journal of the American Chemical Society*, 124: 9074-82.
- O'Shaughnessy, Ben, and Jane Yu. 1994a. 'Autoacceleration in free radical polymerization. 1. Conversion', *Macromolecules*, 27: 5067-78.
- . 1994b. 'Autoacceleration in free radical polymerization. 2. Molecular weight distributions', *Macromolecules*, 27: 5079-85.
- Onelli, Olimpia D, Thomas van de Kamp, Jeremy N Skepper, Janet Powell, Tomy dos Santos Rolo, Tilo Baumbach, and Silvia Vignolini. 2017. 'Development of structural colour in leaf beetles', *Scientific reports*, 7: 1-9.
- Onsager, Lars. 1949. 'The effects of shape on the interaction of colloidal particles', *Annals of the New York Academy of Sciences*, 51: 627-59.
- Orts, WJ, L Godbout, RH Marchessault, and J-F Revol. 1998. 'Enhanced ordering of liquid crystalline suspensions of cellulose microfibrils: a small angle neutron scattering study', *Macromolecules*, 31: 5717-25.
- Oseen, Carl Wilhelm. 1929. *Die anisotropen Flüssigkeiten: tatsachen und Theorien* (Gebrüder Borntraeger).
- Parker, Richard M, Bruno Frka-Petesic, Giulia Guidetti, Gen Kamita, Gioele Consani, Chris Abell, and Silvia Vignolini. 2016. 'Hierarchical self-assembly of cellulose nanocrystals in a confined geometry', *ACS nano*, 10: 8443-49.

- Parker, Richard M, Giulia Guidetti, Cyan A Williams, Tianheng Zhao, Aurimas Narkevicius, Silvia Vignolini, and Bruno Frka-Petescic. 2018. 'The Self-Assembly of Cellulose Nanocrystals: Hierarchical Design of Visual Appearance', *Advanced Materials*, 30: 1704477.
- Peddireddy, Karthik R, Isabelle Capron, Taco Nicolai, and Lazhar Benyahia. 2016. 'Gelation kinetics and network structure of cellulose nanocrystals in aqueous solution', *Biomacromolecules*, 17: 3298-304.
- Pérez-Juste, Jorge, Isabel Pastoriza-Santos, Luis M Liz-Marzán, and Paul Mulvaney. 2005. 'Gold nanorods: synthesis, characterization and applications', *Coordination chemistry reviews*, 249: 1870-901.
- Philipp, B, V Jacopian, F Loth, W Hirte, and G Schulz. 1979. "Hydrolysis of cellulose: mechanisms of enzymatic and acid catalysis." In, 127. American Chemical Society: Washington.
- Preston, RD, AB Wardrop, and E Nicolai. 1948. 'Fine structure of cell walls in fresh plant tissues', *Nature*, 162: 957-59.
- Private\_communication.
- Qu, Dan, Guang Chu, Patrick Martin, Gleb Vasilyev, Rita Vilensky, and Eyal Zussman. 2019. 'Modulating the Structural Orientation of Nanocellulose Composites through Mechano-Stimuli', *ACS Applied Materials & Interfaces*, 11: 40443-50.
- Qu, Dan, and Eyal Zussman. 2020. 'Electro-responsive Liquid Crystalline Nanocelluloses with Reversible Switching', *The journal of physical chemistry letters*, 11: 6697-703.
- Querejeta-Fernández, Ana, Grégory Chauve, Myriam Methot, Jean Bouchard, and Eugenia Kumacheva. 2014. 'Chiral plasmonic films formed by gold nanorods and cellulose nanocrystals', *Journal of the American Chemical Society*, 136: 4788-93.
- Querejeta-Fernández, Ana, Bernd Kopera, Karen S Prado, Anna Klinkova, Myriam Methot, Grégory Chauve, Jean Bouchard, Amr S Helmy, and Eugenia Kumacheva. 2015. 'Circular dichroism of chiral nematic films of cellulose nanocrystals loaded with plasmonic nanoparticles', *ACS nano*, 9: 10377-85.
- Ranby, BG. 1949. "Aqueous colloidal solutions of cellulose micelles." In, 649-50. MUNKSGAARD INT PUBL LTD 35 NORRE SOGADE, PO BOX 2148, DK-1016 COPENHAGEN ....
- Revol, J-F, H Bradford, J Giasson, RH Marchessault, and DG Gray. 1992. 'Helicoidal self-ordering of cellulose microfibrils in aqueous suspension', *International journal of biological macromolecules*, 14: 170-72.
- Revol, Jean-François, Louis Godbout, Xue-Min Dong, Derek G. Gray, Henri Chanzy, and Georg Maret. 1994. 'Chiral nematic suspensions of cellulose crystallites; phase separation and magnetic field orientation', *Liquid Crystals*, 16: 127-34.
- Rofouie, Pardis, Elizabeth Galati, Lu Sun, Amr S Helmy, and Eugenia Kumacheva. 2019. 'Hybrid Cholesteric Films with Tailored Polarization Rotation', *Advanced Functional Materials*, 29: 1905552.
- Rol, Fleur, Bruno Vergnes, Nadia El Kissi, and Julien Bras. 2019. 'Nanocellulose production by twin-screw extrusion: simulation of the screw profile to increase the productivity', *ACS Sustainable Chemistry & Engineering*, 8: 50-59.
- Sadeghifar, Hasan, Ilari Filpponen, Sarah P Clarke, Dermot F Brougham, and Dimitris S Argyropoulos. 2011. 'Production of cellulose nanocrystals using hydrobromic acid and click reactions on their surface', *Journal of materials science*, 46: 7344-55.
- Saha, Partha, and Virginia A Davis. 2018. 'Photonic properties and applications of cellulose nanocrystal films with planar anchoring', *ACS Applied Nano Materials*, 1: 2175-83.
- Salami-Kalajahi, M, V Haddadi-Asl, and H Roghani-Mamaqani. 2012. 'Study of kinetics and properties of polystyrene/silica nanocomposites prepared via in situ free radical and reversible addition-fragmentation chain transfer polymerizations', *Scientia Iranica*, 19: 2004-11.
- Sassi, Jean-François, and Henri Chanzy. 1995. 'Ultrastructural aspects of the acetylation of cellulose', *Cellulose*, 2: 111-27.
- Scarangella, Adriana, Vanessa Soldan, and Michel Mitov. 2020. 'Biomimetic design of iridescent insect cuticles with tailored, self-organized cholesteric patterns', *Nature communications*, 11: 1-10.

- Scherer, George W. 1989a. 'Mechanics of syneresis I. Theory', *Journal of Non-Crystalline Solids*, 108: 18-27.
- . 1989b. 'Mechanics of syneresis II. Experimental study', *Journal of Non-Crystalline Solids*, 108: 28-36.
- Schütz, Christina, Johanna R Bruckner, Camila Honorato-Rios, Zornitza Tosheva, Manos Anyfantakis, and Jan PF Lagerwall. 2020. 'From Equilibrium Liquid Crystal Formation and Kinetic Arrest to Photonic Bandgap Films Using Suspensions of Cellulose Nanocrystals', *Crystals*, 10: 199.
- Seago, Ainsley E, Parrish Brady, Jean-Pol Vigneron, and Tom D Schultz. 2009. 'Gold bugs and beyond: a review of iridescence and structural colour mechanisms in beetles (Coleoptera)', *Journal of the Royal Society Interface*, 6: S165-S84.
- Shopsowitz, Kevin E, Hao Qi, Wadood Y Hamad, and Mark J MacLachlan. 2010. 'Free-standing mesoporous silica films with tunable chiral nematic structures', *Nature*, 468: 422-25.
- Sonin, AS. 1998. 'Inorganic lyotropic liquid crystals', *Journal of Materials Chemistry*, 8: 2557-74.
- Steiner, Lisa Maria, Yu Ogawa, Villads Egede Johansen, Clive R Lundquist, Heather Whitney, and Silvia Vignolini. 2019. 'Structural colours in the frond of *Microsorium thailandicum*', *Journal of the Royal Society Interface Focus*, 9: 20180055.
- Stroobants, A, HNW Lekkerkerker, and Th Odijk. 1986. 'Effect of electrostatic interaction on the liquid crystal phase transition in solutions of rodlike polyelectrolytes', *Macromolecules*, 19: 2232-38.
- Sugiyama, J, H Chanzy, and G Maret. 1992. 'Orientation of cellulose microcrystals by strong magnetic fields', *Macromolecules*, 25: 4232-34.
- Sugiyama, Junji, Takeshi Okano, Hiroyuki Yamamoto, and Fumitaka Horii. 1990. 'Transformation of Valonia cellulose crystals by an alkaline hydrothermal treatment', *Macromolecules*, 23: 3196-98.
- Tanaka, Hajime, Jacques Meunier, and Daniel Bonn. 2004. 'Nonergodic states of charged colloidal suspensions: Repulsive and attractive glasses and gels', *Physical Review E*, 69: 031404.
- Tatsumi, Mio, Fumiko Kimura, Tsunehisa Kimura, Yoshikuni Teramoto, and Yoshiyuki Nishio. 2014. 'Anisotropic polymer composites synthesized by immobilizing cellulose nanocrystal suspensions specifically oriented under magnetic fields', *Biomacromolecules*, 15: 4579-89.
- Teyssier, Jérémie, Suzanne V Saenko, Dirk Van Der Marel, and Michel C Milinkovitch. 2015. 'Photonic crystals cause active colour change in chameleons', *Nature communications*, 6: 6368.
- Tran, Andy, Wadood Y Hamad, and Mark J MacLachlan. 2018. 'Tactoid annealing improves order in self-assembled cellulose nanocrystal films with chiral nematic structures', *Langmuir*, 34: 646-52.
- Van Blaaderen, Alfons. 1998. 'Opals in a new light', *Science*, 282: 887-88.
- Van Bruggen, MPB, JKG Dhont, and HNW Lekkerkerker. 1999. 'Morphology and Kinetics of the Isotropic– Nematic Phase Transition in Dispersions of Hard Rods', *Macromolecules*, 32: 2256-64.
- Vanderfleet, Oriana M, Michael S Reid, Julien Bras, Laurent Heux, Jazmin Godoy-Vargas, Mohan KR Panga, and Emily D Cranston. 2019. 'Insight into thermal stability of cellulose nanocrystals from new hydrolysis methods with acid blends', *Cellulose*, 26: 507-28.
- Verwey, Evert Johannes Willem, Jan Theodoor Gerard Overbeek, and K Van Nes. 1948. *Theory of the stability of lyophobic colloids: the interaction of sol particles having an electric double layer* (Elsevier Publishing Company).
- Vignolini, Silvia, Edwige Moyroud, Thomas Hingant, Hannah Banks, Paula J Rudall, Ullrich Steiner, and Beverley J Glover. 2015. 'The flower of *Hibiscus trionum* is both visibly and measurably iridescent', *New Phytologist*, 205: 97-101.
- Vignolini, Silvia, Paula J Rudall, Alice V Rowland, Alison Reed, Edwige Moyroud, Robert B Faden, Jeremy J Baumberg, Beverley J Glover, and Ullrich Steiner. 2012. 'Pointillist structural color in Pollia fruit', *Proceedings of the National Academy of Sciences*, 109: 15712-15.
- Wang, Dexiu, Tiantian Yang, Jinyang Li, Jinming Zhang, Jian Yu, Xiaocheng Zhang, and Jun Zhang. 2020. 'Thermostable and Redispersible Cellulose Nanocrystals with Thixotropic Gelation Behavior by a Facile Desulfation Process', *ACS Sustainable Chemistry & Engineering*, 8: 11737-46.



- Wang, Mingsheng, Le He, and Yadong Yin. 2013. 'Magnetic field guided colloidal assembly', *Materials Today*, 16: 110-16.
- Wang, Ruibin, Liheng Chen, JY Zhu, and Rendang Yang. 2017. 'Tailored and integrated production of carboxylated cellulose nanocrystals (CNC) with nanofibrils (CNF) through maleic acid hydrolysis', *ChemNanoMat*, 3: 328-35.
- Weaver, James C, Garrett W Milliron, Ali Miserez, Kenneth Evans-Lutterodt, Steven Herrera, Isaias Gallana, William J Mershon, Brook Swanson, Pablo Zavattieri, and Elaine DiMasi. 2012. 'The stomatopod dactyl club: a formidable damage-tolerant biological hammer', *Science*, 336: 1275-80.
- Woon, TC, C Michael Dicken, and Thomas C Bruce. 1986. 'The kinetics and mechanisms of oxygen transfer in the reaction of p-cyano-N, N-dimethylaniline N-oxide with metalloporphyrin salts. 4. Catalysis by meso-[tetrakis (2, 6-dimethylphenyl) porphinato] iron (III) chloride', *Journal of the American Chemical Society*, 108: 7990-95.
- Wu, Tianhang, Jiada Li, Juntao Li, Simin Ye, Jie Wei, and Jinbao Guo. 2016. 'A bio-inspired cellulose nanocrystal-based nanocomposite photonic film with hyper-reflection and humidity-responsive actuator properties', *Journal of Materials Chemistry C*, 4: 9687-96.
- Xu, Yuan, Aleks D Atrens, and Jason R Stokes. 2018. "'Liquid, gel and soft glass" phase transitions and rheology of nanocrystalline cellulose suspensions as a function of concentration and salinity', *Soft Matter*, 14: 1953-63.
- Yamamoto, Hiroyuki, and Fumitaka Horii. 1993. 'CPMAS carbon-13 NMR analysis of the crystal transformation induced for Valonia cellulose by annealing at high temperatures', *Macromolecules*, 26: 1313-17.
- Yao, Kun, Qijun Meng, Vincent Bulone, and Qi Zhou. 2017. 'Flexible and responsive chiral nematic cellulose nanocrystal/poly (ethylene glycol) composite films with uniform and tunable structural color', *Advanced Materials*, 29: 1701323.
- Yoshiharu, Nishiyama, Kuga Shigenori, Wada Masahisa, and Okano Takeshi. 1997. 'Cellulose microcrystal film of high uniaxial orientation', *Macromolecules*, 30: 6395-97.
- Yu, Houyong, Somia Yassin Hussain Abdalkarim, Heng Zhang, Chuang Wang, and Kam Chiu Tam. 2019. 'Simple process to produce high-yield cellulose nanocrystals using recyclable citric/hydrochloric acids', *ACS Sustainable Chemistry & Engineering*, 7: 4912-23.
- Zhang, Yu Ping, Vamsy P Chodavarapu, Andrew G Kirk, and Mark P Andrews. 2013. 'Structured color humidity indicator from reversible pitch tuning in self-assembled nanocrystalline cellulose films', *Sensors and Actuators B: Chemical*, 176: 692-97.
- Zhao, Tianheng H, Richard M Parker, Cyan A Williams, Kevin TP Lim, Bruno Frka-Petesic, and Silvia Vignolini. 2019. 'Printing of responsive photonic cellulose nanocrystal microfilm arrays', *Advanced Functional Materials*, 29: 1804531.
- Zhou, Qi, Harry Brumer, and Tuula T Teeri. 2009. 'Self-organization of cellulose nanocrystals adsorbed with xyloglucan oligosaccharide– poly (ethylene glycol)– polystyrene triblock copolymer', *Macromolecules*, 42: 5430-32.
- Zhu, Bonan, Villads E Johansen, Gen Kamita, Giulia Guidetti, Mélanie M Bay, Thomas G Parton, Bruno Frka-Petesic, and Silvia Vignolini. 2020. 'Hyperspectral Imaging of Photonic Cellulose Nanocrystal Films: Structure of Local Defects and Implications for Self-Assembly Pathways'.
- Zocher, H, and C Török. 1960. 'Neuere Beiträge zur Kenntnis der Taktosole', *Kolloid-Zeitschrift*, 173: 1.

Cellulose nanocrystals are bio-sourced rod-like nanoparticles showing a remarkable iridescent optical response owing to their ability to self-assemble into cholesteric liquid crystalline phases above a threshold concentration. In the literature, 100% cellulose films and composite materials capable of impressive colour responses have been prepared respectively from aqueous suspensions by controlled drying and/or using organic and inorganic precursors. In this PhD work, we prepare materials from polymerizable cholesteric suspensions with the aim of developing a photonic optical response for a range of composite materials, including flexible and stimuable ones. In that extent, cellulose nanocrystals are compatibilised with organic apolar solvents and monomers using the steric stabilisation of a surfactant. The modification of colloidal interactions in apolar suspensions reduces the cholesteric pitch compared to aqueous suspensions, leading to an optical response at high angles of incidence already in suspension. The optical response in suspension is tuned by the control of the orientation of the cholesteric helices by electric (reorientation and unwinding) and magnetic (alignment) fields before being locked into polymer composites. The retention of the cholesteric assembly of fillers and their field-aligned orientation preserves an iridescent optical response in the composites that is characterised in detail by angular-resolved spectroscopy. In a complementary approach, cellulose and composite films are prepared by drying an organic solvent CNC suspension to yield a slight iridescent optical response in reflection at normal incidence.

Les nanocristaux de cellulose sont des nanoparticules biosourcées anisotropes qui présentent une réponse optique iridescente spectaculaire de par leur capacité à s'auto-assembler en phases cristallines liquides cholestériques au-delà d'une certaine concentration. Dans la littérature, des films 100% cellulose et des composites aux effets de couleurs structuraux parfois impressionnants sont préparés respectivement par séchage contrôlé de suspensions aqueuses et/ou en présence de précurseurs organiques et inorganiques. Ce travail de thèse développe des matériaux fabriqués à partir de suspensions cholestériques polymérisables, avec l'objectif de développer une réponse optique photonique pour une gamme de matériaux, notamment souples et stimulables. Pour cela, les nanocristaux de cellulose sont dispersés en solvant organique apolaire grâce à la stabilisation stérique d'un tensioactif. La modification des interactions colloïdales en suspension conduit à un pas cholestérique proche du visible, induisant des couleurs structurales aux grands angles d'incidence directement en suspension. Cette réponse optique en suspension est modulée par la manipulation des hélices cholestériques en champ électrique (réorientation et déroulement) et magnétique (alignement) avant d'être figée dans des composites polymères. L'organisation cholestérique et son orientation dans le champ sont conservées dans les composites, conduisant à une réponse optique caractérisée en détail par spectroscopie résolue en angle. Dans une approche complémentaire, des films de cellulose et composite sont préparés par séchage de suspensions en solvant organique et présentent de légers effets de couleur en réflexion en incidence normale.